

# EXPERIMENTAL AND ANALYTICAL INVESTIGATION OF VOID FRACTION AND HEAT TRANSFER DURING EVAPORATION IN HORIZONTAL TUBES

THÈSE N° 2978 (2004)

PRÉSENTÉE À LA FACULTÉ SCIENCES ET TECHNIQUES DE L'INGÉNIEUR

Institut des sciences et de l'énergie

SECTION DE GÉNIE MÉCANIQUE

ÉCOLE POLYTECHNIQUE FÉDÉRALE DE LAUSANNE

POUR L'OBTENTION DU GRADE DE DOCTEUR ÈS SCIENCES

PAR

**Leszek WOJTAN**

ingénieur mécanicien, Université de Cracovie, Pologne  
et de nationalité polonaise

acceptée sur proposition du jury:

Prof. J. Thome, directeur de thèse

Prof. D. Favrat, rapporteur

Dr N. Kattan, rapporteur

Prof. P. von Rohr, rapporteur

Lausanne, EPFL  
2004



# Acknowledgements

This study has been carried out at the Laboratory of Heat and Mass Transfer (LTCM), Swiss Federal Institute of Technology in Lausanne, under the direction of Prof. John Richard Thome. The project has been supported financially by the Fond National Swiss (FNS) contract number 21-57210.99 and by the Air-Conditioning and Refrigeration Technology Institute (ARTI) contract number 605-20040, which are gratefully acknowledged.

I would like to express my sincere gratefulness to Prof. John Richard Thome for his total confidence and for the position of responsibility he granted me throughout this work. I am very grateful to him for extensive discussions, his careful reading of this manuscript and excellent working climate he was creating as the laboratory's director.

Many thanks to Dr. Thierry Ursenbacher for his contribution in the development of a new void fraction measurement system. His encouragement in research, optimism and constant helpfulness gave me the pleasure to discover more than a collaborator.

I would like to express my gratitude to all my colleges of the LTCM for their cooperation and friendship. Among them, my special gratitude to Jesus Moreno Quiben for fruitful collaboration and his help in computer science. Many thanks also for our secretary Monique Barraud-Plummer for her politeness and administrative work concerning this thesis.

I also acknowledge our technicians Laurent Chevalley and Alfred Thomas for their creative work in the rebuilding of the flow boiling test facility.

Last, but not least many thanks to my family and my beautiful wife Magda for their support and encouragement during this work.



# Abstract

A new optical void fraction measurement system has been coupled to the existing LTCM flow boiling test facility to obtain dynamic and time-averaged void fractions, simultaneously with measurements of the local heat transfer coefficients. A series of evaporation tests have been run for R-22 and R-410A in 13.84 *mm* and 8.00 *mm* ID tubes. Using our newly developed image processing system for processing laser illuminated cross-sectional views of the flow, about 310 000 images have been analysed in this study to provide the same number of dynamic void fraction measurements. From these images, 238 and 87 time-averaged void fraction values have been obtained for the 13.60 *mm* and 8.00 *mm* diameter glass tubes, respectively. The same number of time-averaged dry angles has been obtained. The measured void fractions have been compared to the principal prediction models, showing good agreement to the Steiner version of Rouhani-Axelsson drift flux model. Based on analysis of the void fraction evolution as a function of time, several modifications of the Kattan *et al.* flow pattern map [30] (1998a) have been made to improve the heat transfer prediction model in stratified-wavy flow and to extend its application to vapor qualities below 0.15. Over 1250 new flow boiling heat transfer points have been acquired at mass velocities from 70 to 700  $kg/m^2s$  and heat fluxes from 2.0 to 57.5  $kW/m^2$ . Based on the 368 heat transfer points obtained in dryout and mist flow conditions, new boundaries for the transitions (from/to) annular/dryout and dryout/mist flow have been defined and integrated into the flow pattern map of Kattan *et al.* A new heat transfer model for dryout and mist flow conditions has also been proposed, extending the flow pattern oriented model of Kattan *et al.* to these flow regimes.



## Version abrégée

Un nouveau système de mesure optique du taux de vide a été développé et couplé au stand biphasé du LTCM afin d'obtenir des mesures de taux de vide dynamiques et moyennées dans le temps, simultanément avec les mesures locales de coefficients de transfert de chaleur. Des campagnes de mesures portant sur l'évaporation des réfrigérants R-22 et R-410A ont été ainsi réalisées dans des tubes de diamètre intérieur de 13.84 mm et de 8.00 mm. En utilisant ce nouveau système de mesure, basé sur le traitement d'images issues de l'illumination par faisceau laser plan d'une mince couche transversale de l'écoulement au travers de tube en verre, quelques 310 000 images ont été analysées pour produire autant de mesures instantanées du taux de vide. De ces images ont pu être extraites 238, respectivement 87 valeurs moyennes de taux de vide, pour les deux types de tubes. Un nombre équivalent de mesures de l'angle sec a également été obtenu. Les mesures de taux de vide ont été comparées aux principaux modèles de prédiction existants, démontrant en particulier une très bonne concordance avec la version modifiée de Steiner du modèle à flux relatif de Rouhani-Axelsson. D'autre part, sur la base de l'analyse de l'évolution du taux de vide en fonction du temps, plusieurs modifications ont été apportées à la carte d'écoulement proposée par Kattan *et al.* [30] (1998a) afin d'améliorer le modèle de prédiction de transfert de chaleur pour écoulements de type stratifiés à vague et en étendre le champ d'application à des titres de vapeur inférieur à 0.15. En outre, plus de 1250 points de mesures du coefficient de transfert de chaleur par évaporation ont été enregistrés pour des débits massiques allant de 70 à 700  $kg/m^2s$  et des flux de chaleur situés entre 2.0 et 57.5  $kW/m^2$ . Parmi ceux-ci, 368 points de mesures, caractéristiques des écoulements de type *dryout* et *mist flow*, ont permis d'établir de nouvelles frontières dans les transitions *annular/mist flow* et *dryout/mist flow*, lesquelles ont été intégrées dans la carte d'écoulement de Kattan *et al.* Un nouveau modèle de transfert de chaleur pour écoulements de type *dryout* et *mist flow* a également été proposé, élargissant ainsi la carte de Kattan à ces deux types de régime d'écoulement.





# Contents

<b>Acknowledgements</b>	<b>3</b>
<b>Abstract</b>	<b>5</b>
<b>Version abrégée</b>	<b>7</b>
<b>Introduction</b>	<b>15</b>
<b>1 Definition of main terms</b>	<b>19</b>
1.1 Multiphase flow . . . . .	19
1.2 Geometrical parameters . . . . .	20
1.3 Void fraction . . . . .	20
1.4 Vapor quality . . . . .	23
1.5 Velocities . . . . .	24
1.6 Non-dimensional numbers . . . . .	26
1.6.1 Reynolds number . . . . .	26
1.6.2 Prandtl number . . . . .	28
1.6.3 Liquid Froude number . . . . .	29
1.6.4 Liquid Weber number . . . . .	29
1.6.5 Nusselt number . . . . .	30
1.6.6 Boiling number . . . . .	30

1.6.7	The Martinelli Parameter . . . . .	30
<b>2</b>	<b>Flow pattern maps and heat transfer models</b>	<b>33</b>
2.1	Flow regimes in horizontal two-phase flows . . . . .	33
2.2	Flow pattern maps . . . . .	36
2.2.1	Flow pattern map of Kattan-Thome-Favrat . . . . .	36
2.2.2	Flow pattern map of Zürcher . . . . .	41
2.2.3	Flow pattern map of Thome and El Hajal . . . . .	43
2.3	Flow boiling . . . . .	46
2.3.1	Heat transfer mechanisms . . . . .	46
2.3.2	Convective boiling . . . . .	48
2.3.3	Nucleate boiling . . . . .	49
2.4	Flow boiling heat transfer models . . . . .	52
2.4.1	The enhancement model . . . . .	53
2.4.2	The superposition model . . . . .	53
2.4.3	The asymptotic model . . . . .	53
2.4.4	The flow pattern oriented model of Kattan-Thome-Favrat . . . . .	54
2.4.5	The onset of nucleate boiling criterion . . . . .	56
2.5	Conclusion . . . . .	58
<b>3</b>	<b>Void fraction measurements</b>	<b>61</b>
3.1	Review of the void fraction measurement methods . . . . .	61
3.1.1	Monofiber optical probe technique . . . . .	61
3.1.2	Radiation attenuation techniques . . . . .	62
3.1.3	Electrical techniques . . . . .	64
3.1.4	Comparison of the existing methods . . . . .	66

<i>CONTENTS</i>	11
3.2 A new optical method to measure void fraction . . . . .	67
3.2.1 Measurement strategy . . . . .	67
3.2.2 Transformation of distorted images . . . . .	69
3.2.3 Vapor-liquid interface detection technique . . . . .	76
3.2.4 Comparison of technique to static void fraction measurements . . . . .	81
3.2.5 Conclusions . . . . .	82
<b>4 Experimental flow boiling test facility</b>	<b>83</b>
4.1 Description of the flow boiling test facility . . . . .	83
4.1.1 Refrigerant loop . . . . .	84
4.1.2 Heating water loop . . . . .	89
4.2 Heat transfer measurements . . . . .	90
4.2.1 Waterside wall temperature . . . . .	91
4.2.2 Temperature of refrigerant . . . . .	93
4.2.3 Local heat flux . . . . .	95
4.2.4 Local heat transfer coefficient determination . . . . .	96
4.3 Vapor quality calculation . . . . .	98
4.4 Void fraction determination . . . . .	99
4.5 Accuracy of measurements . . . . .	100
4.5.1 Vapor quality measurement inaccuracy . . . . .	102
4.5.2 Local heat transfer measurement inaccuracy . . . . .	103
4.5.3 Dynamical void fraction measurement inaccuracy . . . . .	106
<b>5 Dynamic void fraction and dry angles</b>	<b>107</b>
5.1 Void fraction models . . . . .	108
5.1.1 Homogeneous model . . . . .	108

5.1.2	Velocity ratio models . . . . .	109
5.1.3	Geometric model of Taitel-Dukler . . . . .	110
5.1.4	Correlations based on the drift flux model . . . . .	113
5.2	Dynamic void fraction measurements . . . . .	118
5.2.1	Experimental conditions . . . . .	119
5.2.2	Results and discussion . . . . .	119
5.3	Dynamic dry angle measurements . . . . .	132
5.4	Conclusions . . . . .	135
<b>6</b>	<b>Heat transfer coefficient in stratified-wavy flow</b>	<b>137</b>
6.1	New approach to dry angle in stratified-wavy flow . . . . .	138
6.2	Heat transfer results for stratified-wavy flow . . . . .	143
6.3	Comparison of the new model to independent data . . . . .	147
6.4	Conclusions . . . . .	149
<b>7</b>	<b>Dryout and mist flow heat transfer</b>	<b>151</b>
7.1	Heat transfer mechanisms in post dryout . . . . .	152
7.2	Departure from thermodynamic equilibrium . . . . .	154
7.3	Mist flow heat transfer models . . . . .	158
7.3.1	Thermal equilibrium correlations . . . . .	158
7.3.2	No evaporation after dryout - "frozen droplets" model . . . . .	160
7.3.3	Models predicting non-equilibrium effects . . . . .	161
7.4	A new heat transfer model for dryout and mist flow . . . . .	168
7.4.1	Heat transfer for high mass velocities and high heat fluxes . . . . .	169
7.4.2	New transitions: Annular-Dryout and Dryout-Mist flow . . . . .	178
7.4.3	Updating of flow pattern map of Thome-El Hajal for dryout effects . . . . .	184

<i>CONTENTS</i>	13
7.4.4 New heat transfer model for mist flow and dryout zone . . . . .	187
7.5 Heat transfer results at high mass velocities . . . . .	191
7.6 Conclusions . . . . .	201
<b>8 General conclusions</b>	<b>203</b>
<b>9 Nomenclature</b>	<b>205</b>
9.1 Latin . . . . .	205
9.2 Greek . . . . .	210
<b>Bibliography</b>	<b>213</b>
<b>Curriculum Vitae</b>	<b>221</b>



# Introduction

The continuous depletion of the atmospheric ozone layer that protects the Earth's surface from the UV radiation has produced international treaties, requiring a gradual phase-out of halogenated fluids. As a direct consequence, chlorofluorocarbons (CFCs), which have been used as working fluids in air-conditioning and refrigeration systems, were phased out at the end 1995 under EEC Regulation 3093/94. The production of hydrochlorofluorocarbons (HCFCs) was frozen at the same time, and will completely phased out by the end of 2020, being in the meantime gradually replaced by hydrofluorocarbons (HFC). The increasing costs of new replacement refrigerant due to their production costs and increased taxes, call for a reduction of refrigerant charges and an increasing in efficiency of thermal cycles, all which requires extensive knowledge of flow boiling heat transfer phenomena.

Over the years, numerous attempts have been made to predict heat transfer coefficients during evaporation in horizontal tubes. Many correlations tried to empirically describe the very complex process of flow boiling by combining convective and nucleate boiling models. Kattan [29] (1996) analysed three main existing heat transfer models, *i.e.* enhancement, superposition and asymptotic, and showed that without distinguishing between the appropriate two-phase flow pattern, it was not possible to precisely predict local heat transfer coefficients. He observed the largest errors at the high vapor qualities where the dryout effect was not taken into account by any of the previous methods. As a response to this, Kattan *et al.* [30], [31], [32] (1998a-c) proposed a new flow pattern oriented model. In their work, a new two-phase flow pattern map was developed for adiabatic and evaporating flows together with a completely new heat transfer model that represents the local two-phase structure as a function of the local flow pattern. The new heat transfer model was a significant step ahead, improving significantly the predictive accuracy of the local flow boiling heat transfer coefficient.

Because of the complexity of two-phase evaporation and its flow structure, numerous aspects of this flow pattern based heat transfer model remain to be investigated. Currently, the flow pattern map and its transition boundaries have been verified experimentally only for vapor qualities above 0.15 for the following transitions: fully stratified/stratified-wavy flows, stratified-wavy/intermittent-annular flows, intermittent/annular flows and annular/annular with partial dryout flows. Flow pattern transitions for intermittent/bubbly flow and most importantly annular/mist flow must still be investigated experimentally, *i.e.* their current transition threshold prediction methods have yet to be verified.

The onset of dryout is a limiting point for the maximum flow boiling heat transfer coefficients obtainable in an evaporator tube, where the annular liquid film disappears or disrupts on the internal tube surface. The knowledge of the dryout conditions and the heat transfer coefficient in the region beyond the onset of dryout is required for the design and performance evaluations of an evaporator. Thus, the definition of the annular/mist flow transition boundary and a new heat transfer model for the post dryout region is a particular interest in this study.

Even if the flow pattern oriented model of Kattan *et al.* was a big improvement in the flow boiling heat transfer prediction, it has been pointed out by Zürcher [70] (2000) that the predicted heat transfer coefficient for stratified-wavy flow was not as accurate as for annular flow. To improve our scientific approach on the flow structure in stratified-wavy flow, new information concerning dynamic void fraction, dry angle and interfacial flow structure are required.

Thus, the main experimental objectives of this study are to: (i) extend the existing heat transfer database to several new fluids and additional tube diameters, (ii) measure local void fractions simultaneously with the heat transfer coefficient, (iii) extend our knowledge about flow structures, (iv) measure dry angles in stratified/stratified-wavy flow and (v) investigate the annular/mist flow transition. The analytical objectives are to: (i) extend the flow pattern map to annular/mist flow transitions, (ii) developed a new heat transfer model for the post dryout regime, (iii) verify void fraction models used for the flow structure calculations based on direct measurements, (iv) extend the heat transfer model of Kattan *et al.* to vapor qualities below 0.15 and (v) improve the heat transfer model of Kattan *et al.* for the stratified-wavy flow regime.

This manuscript is organised as follows:



- Chapter 1 - defines the main terms and non-dimensional numbers used in two-phase flow analysis.
- Chapter 2 - presents the state of the art of existing flow pattern maps and heat transfer models.
- Chapter 3 - reviews the existing void fraction measurements methods and describes a new optical technique for cross-sectional void fraction measurements.
- Chapter 4 - describes the details of the modified flow boiling test facility.
- Chapter 5 - shows main existing void fraction models and the results of dynamic void fraction and dry angles measurements.
- Chapter 6 - presents modifications of the flow pattern map in the stratified-wavy regime and a new approach of the dry angles prediction in this zone.
- Chapter 7 - introduces new boundaries for the transitions: annular/dryout, dryout/mist flow and a new heat transfer model for these two flow regimes.
- Chapter 8 - presents the general conclusions of this study.



# Chapter 1

## Definition of main terms

In this chapter, the main terms used in two-phase flow analysis will be explained. The geometrical parameters will be described on a cross-section of stratified flow to explain a means of modelling two-phase flow. Such parameters include the dry angle, wetted perimeters and the length of interface. The flow geometry in two-phase flow analysis is usually determined using void fraction. This essential parameter characterizing the two-phase flow structures will be explained here. Since both phases flow with different velocities, it is very important to also define all true and relative velocities. In the last section of this chapter, non-dimensional numbers used in the analysis will be discussed to clarify some literature inconsistencies.

### 1.1 Multiphase flow

A phase is a thermodynamic definition for the state of the matter, which can be either solid, liquid or gas. Multiphase flow is the case when several phases flow simultaneously in a conduit. By two-phase flow, normally, we mean a mixture of two phases, which is not extremely dilute. It means that in the macro scale, both phases can be discerned. The term two-component is used to describe the flow of two chemical species. Thus, a refrigerant liquid/vapor mixture is two-phase, one component, while a liquid refrigerant-oil mixture is one phase, two component. This study deals only with one component saturated liquid/vapor flows.

## 1.2 Geometrical parameters

Figure 1.1 shows an instantaneous cross-section of a stratified two-phase flow in a circular horizontal tube.

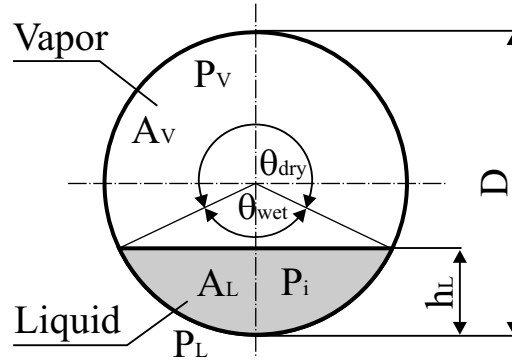


Figure 1.1: Stratified two-phase flow cross-section.

The areas described by  $A$  are cross-sectional surfaces and  $P$  refers to the characteristic lengths (perimeter and interface). The subscripts refer to liquid (L), vapor (V) and interface (i).  $\theta_{dry}$  - is the **dry angle** corresponding to the angular fraction of the tube perimeter in contact with the vapor phase.  $\theta_{wet}$  - is the **wetted angle** defining to the angular fraction of the tube perimeter in contact with the liquid phase. The internal diameter is  $D$  and  $h_L$  is the liquid height. Even if this flow pattern configuration is simplified, some very important works cited in this study are based on this approach.

## 1.3 Void fraction

The void fraction  $\varepsilon$  describes the portion of the channel which is occupied by the vapor phase at any instant. Normally the instantaneous value is integrated over a time period to give a time-averaged value (dynamic void fraction). There are four geometrical definitions of void fraction, corresponding to four different experimental measurements: a local value, a chordal value, a cross-sectional value and a volumetric value. All four are briefly described below.

**Local void fraction** is defined as the fraction of time in which the vapor phase occupies a given point in space, *i.e.* this is the point-wise void fraction. The presence (or absence) of phase  $k$  ( $k=V, L$ ) at a given point  $r$  and at a given time  $t$  is characterized by the binary

function  $P_k(r, t)$  as:

$$P_k(r, t) = \begin{cases} 1 & \text{if point } r \text{ is in phase V} \\ 0 & \text{if point } r \text{ is in phase L} \end{cases}$$

The local void fraction is the time-averaged phase density function, given as

$$\varepsilon_k(r, t) = \frac{1}{t} \int_t P_k(r, t) dt \quad (1.1)$$

This is the time-average of phase k, where k=V, L. Thus the time averaged local void fraction equals:

$$\varepsilon_V = \varepsilon_V(r, t) \quad (1.2)$$

The local void fraction shown in Figure 1.2a is measured principally using U-shaped fiber-optical sensors (see subsection 3.1.1) and miniature resistive probes (see subsection 3.1.3).

**Chordal void fraction** is defined as:

$$\varepsilon_{Ch} = \frac{L_V}{L_V + L_L} \quad (1.3)$$

where  $L_V$  is an instantaneous cumulative length of the vapor phase at any given chord of length  $L_V + L_L$ . This is best illustrated in Figure 1.2b. The best method to measure the chordal void fraction is based on radiation absorption methods (see subsection 3.1.2).

**Cross-sectional void fraction** is defined as:

$$\varepsilon = \frac{A_V}{A_V + A_L} \quad (1.4)$$

where  $A_V$  is the total area occupied by the vapor and  $A_L$  is the total area occupied by the liquid. These parameters are depicted in Figure 1.2c.

The definition of the liquid interface and consequently cross-sectional void fraction is of particular interest in two-phase flow analysis and is the type of void fraction through this thesis. In this study, a new optical method to measure void fraction in stratified type of flows has been developed (see section 3.2) and applied in experimental tests. Existing methods,

such as integrating of chordal-average measurements over the cross-section, by using the "one-shot" technique, or by a neutron scattering technique give only the area average void fraction value over the cross-section without any information about the geometry of the liquid-vapor interface.

**Volumetric void fraction**, also called channel average void fraction, shown in Figure 1.2d is defined as:

$$\langle \varepsilon \rangle = \frac{V_V}{V_V + V_L} \quad (1.5)$$

where  $V_V$  is the volume occupied by vapor and  $V_L$  is the volume occupied by liquid in a certain part of the channel. Naturally, the sum of  $V_V$  and  $V_L$  is equal to the volume of the channel. The average void fraction over a full channel length can be obtained by integrating many local or cross-sectional averages or by the quick-closing-valve technique. In this method, two valves (which can be simultaneously and quickly operated) are placed at the two ends of the test section. At the appropriate time, the two valves are actuated and the volume of the void is established by subtraction of the measured liquid volume from the total volume.

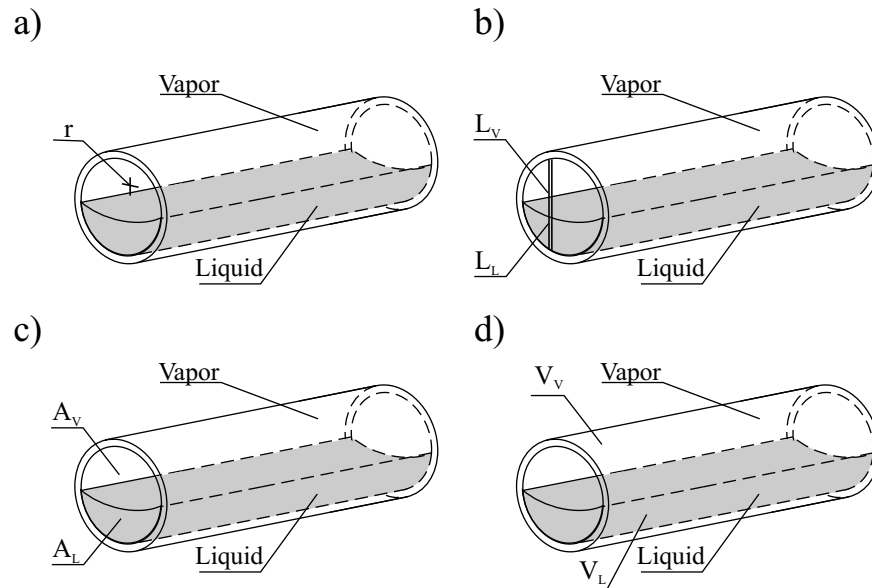


Figure 1.2: Four principal void fraction representations a) local void fraction, b) chordal void fraction, c) cross-sectional void fraction, d) volumetric void fraction.

It should be mentioned here that the cross-sectional void fraction cannot be determined using the quick-closing-valve technique. The volumetric void fraction is equal to the cross-sectional void fraction only when the two phases travel at the same velocity, *i.e.* the homogeneous

case. The relationship between the cross-sectional void fraction  $\varepsilon$  and the volumetric void fraction  $\langle \varepsilon \rangle$  is

$$\langle \varepsilon \rangle = \frac{\varepsilon}{\frac{1}{S}(1 - \varepsilon) + \varepsilon} \quad (1.6)$$

where  $S$  is the velocity ratio defined later in equation 5.2.

## 1.4 Vapor quality

The vapor quality is defined as the ratio of the vapor mass-flow rate  $\dot{M}_V$  [kg/s] to the total mass flow rate  $\dot{M} = \dot{M}_L + \dot{M}_V$  [kg/s]:

$$x = \frac{\dot{M}_V}{\dot{M}} \quad (1.7)$$

In the case where a phase change does not take place in the channel, one needs to measure the mass flow rate of each phase if possible, and the quality is then determined for the entire channel. In the case where the channel is heated and boiling takes place, the quality increases downstream with the flow. Only thermodynamic equilibrium vapor quality can be calculated by assuming that both phases are saturated as their temperatures are equal to the saturation temperature corresponding to their common pressure. The thermodynamic equilibrium vapor quality can be calculated as:

$$x = \frac{h(z) - h_L}{h_{LV}} \quad (1.8)$$

where  $h_L$  is the enthalpy of saturated liquid [J/kg],  $h_{LV}$  is the latent heat of vaporization [J/kg] and  $h(z)$  is the enthalpy at a cross-section  $z$  [J/kg] calculated from:

$$h(z) = h_{in} + \frac{1}{\dot{M}} \int_0^z q'(z) dz \quad (1.9)$$

where  $h_{in}$  is the enthalpy of the fluid at the inlet [J/kg] and  $q'(z)$  is the heat input from the wall per unit length [W/m].

## 1.5 Velocities

There are a number of velocities which can be defined in a two-phase flow. In general, the two phases will not have the same velocity, and there will be a relative velocity between them, as discussed below.

The **mass velocity** is defined to be the mass flow rate divided by the total cross-sectional area:

$$G = \frac{\dot{M}}{A} \quad (1.10)$$

The principal unit of the mass velocity is  $[kg/m^2s]$ . Considering the continuity law, the mass velocity is also the expression of the mean flow velocity multiplied by the mean density.

The **true mean velocities** (or actual velocities) of the phases  $u_V$  and  $u_L$  are the mean velocities at which the phases actually travel. The cross-sectional velocities are determined by the volumetric flow rates  $\dot{Q}_V$  and  $\dot{Q}_L$   $[m^3/s]$  and divided by the cross-sectional areas which are actually occupied by the phases as:

$$u_V = \frac{\dot{Q}_V}{A_V} = \frac{\dot{Q}_V}{\varepsilon A} \quad (1.11)$$

$$u_L = \frac{\dot{Q}_L}{A_L} = \frac{\dot{Q}_L}{(1 - \varepsilon)A} \quad (1.12)$$

From the continuity law, it is possible to define both liquid and vapor true mean velocities as:

$$u_V = \frac{x}{\varepsilon} \cdot \frac{\dot{M}}{\rho_V A} = \frac{G}{\rho_V} \cdot \frac{x}{\varepsilon} \quad (1.13)$$

$$u_L = \frac{1 - x}{1 - \varepsilon} \cdot \frac{\dot{M}}{\rho_L A} = \frac{G}{\rho_L} \cdot \frac{1 - x}{1 - \varepsilon} \quad (1.14)$$

The **superficial velocities** (called also volumetric flux densities)  $j_V$  and  $j_L$  are the velocities of the phases as if they were each flowing alone in the channel, occupying the total cross-sectional area. They are defined as:



$$j_V = \frac{\dot{Q}_V}{A} = \varepsilon u_V \quad (1.15)$$

$$j_L = \frac{\dot{Q}_L}{A} = (1 - \varepsilon)u_L \quad (1.16)$$

The **total superficial velocity** is the sum of the vapor and liquid superficial velocities:

$$j = j_V + j_L \quad (1.17)$$

The **local drift velocities** are defined as the local true velocity of the vapor (or liquid) in relation to the local total superficial velocity, namely:

$$V_{Vj} = u_V - j \quad (1.18)$$

$$V_{Lj} = u_L - j \quad (1.19)$$

and the **drift fluxes**  $j_{Vj}$  and  $j_{Lj}$  are defined as:

$$j_{Vj} = \varepsilon V_{Vj} = \varepsilon(u_V - j) \quad (1.20)$$

$$j_{Lj} = (1 - \varepsilon)V_{Lj} = (1 - \varepsilon)(u_L - j) \quad (1.21)$$

The drift flux of the vapor relative to the liquid can be calculated as follows:

$$j_{VL} = (1 - \varepsilon)j_V - \varepsilon j_L \quad (1.22)$$

and similarly

$$j_{LV} = \varepsilon j_L - (1 - \varepsilon)j_V \quad (1.23)$$

In view of above two equations and equation 1.17, superficial velocities of the vapor and liquid phase can be calculated also as:

$$j_V = \varepsilon j + j_{VL} \quad (1.24)$$

$$j_L = (1 - \varepsilon)j - j_{VL} \quad (1.25)$$

## 1.6 Non-dimensional numbers

The principal non-dimensional numbers encountered in former and current studies of the two-phase flow are defined below. Different definitions of certain non-dimensional numbers exist in the literature. This concerns especially the Reynolds and Froude numbers of the liquid.

### 1.6.1 Reynolds number

The Reynolds number represents the ratio between the inertia forces and the viscosity forces. For forced convection inside a tubular channel, the **liquid Reynolds** number is calculated as:

$$Re_L = \frac{\rho_L u_L D_h}{\mu_L} \quad (1.26)$$

where  $D_h$  is the hydraulic diameter defined as the ratio of the cross-section  $A$  of the fluid to the wetted perimeter  $P_L$ .

$$D_h = \frac{4A}{P_L} \quad (1.27)$$

In the case of a circular tube,  $D_h = D$ .

The transition criterion between laminar and turbulent flow is based on the Reynolds number. In a fully developed flow in a circular tube, the critical Reynolds number corresponding to the onset of turbulence is  $Re_L = 2300$ , although much larger Reynolds numbers  $Re_L \approx 10000$  are needed to achieve fully turbulent conditions.

Considering one-dimensional flow and using the definition of the true mean velocity from equation 1.14, the **Reynolds number of the liquid phase** in a two-phase flow can be

expressed in the following form:

$$Re_L = \frac{GD_h}{\mu_L} \cdot \frac{1-x}{1-\varepsilon} \quad (1.28)$$

where

$$D_h = \frac{4A_L}{P_L} = \frac{4(1-\varepsilon)A}{P_L} \quad (1.29)$$

After substituting equation 1.29 into 1.28 the liquid Reynolds number is defined as:

$$Re_L = \frac{4G(1-x)A}{\mu_L P_L} \quad (1.30)$$

A similar approach can be used for the **Reynolds number of the vapor phase**. Using the definition of the true mean vapor velocity,  $Re_V$  can be calculated in the following form:

$$Re_V = \frac{GD_h}{\mu_V} \cdot \frac{x}{\varepsilon} \quad (1.31)$$

After substituting  $D_h$  related to the vapor phase, equation 1.31 becomes:

$$Re_V = \frac{4GxA}{\mu_V P_L} \quad (1.32)$$

Kattan *et al.* [30, 31, 32] (1998a-c) assumed that the hydraulic diameter  $D_h$  of the vapor phase equals to the tube diameter  $D$  like in a tubular single-phase flow. As the void fraction increases very rapidly with increasing of the vapor quality to nearly 1, this assumption seems to be reasonable. In this study the same definition will be used.

$$Re_V = \frac{GD}{\mu_V} \cdot \frac{x}{\varepsilon} \quad (1.33)$$

For the liquid phase in the Kattan-Thome-Favrat two-phase flow heat transfer model, the Reynolds number referred to a liquid layer. The configurations of the stratified and liquid film flow are shown in Figure 1.3.

If we assume that both configurations are equivalent (both areas occupied by the liquid are the same), the hydraulic diameter can be calculated as:

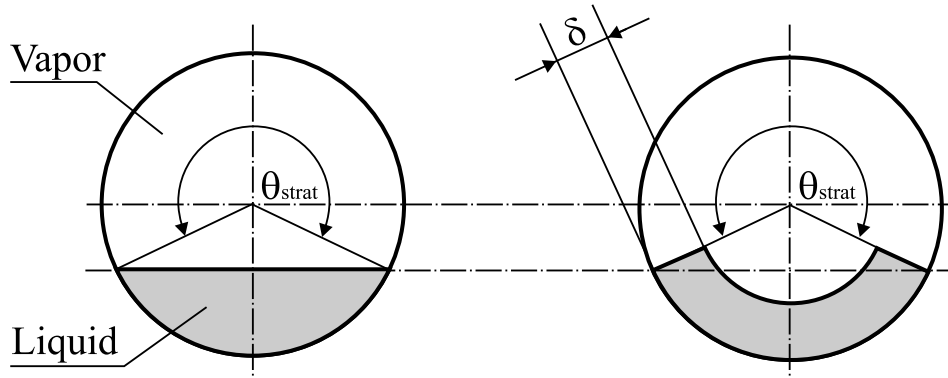


Figure 1.3: Equivalent configurations of stratified flow and liquid film flow.

$$D_h = \frac{4\delta P_L}{P_L} \quad (1.34)$$

Substituting equation 1.34 into equation 1.28, the **Reynolds number based on a liquid layer** is defined as follows:

$$Re_\delta = \frac{4G\delta}{\mu_L} \cdot \frac{1-x}{1-\varepsilon} \quad (1.35)$$

This form of the Reynolds number is used in the modelling of the heat transfer coefficient in stratified and stratified-wavy flow regimes. For the intermittent and annular flows  $Re_\delta$  becomes:

$$Re_\delta = \frac{G(1-x)D}{\mu_L} \quad (1.36)$$

The film flow is wavy-free laminar when  $Re_\delta < 30$  and the transition to turbulent flow through laminar-wavy flow is complete when  $Re_\delta \approx 1800$ .

## 1.6.2 Prandtl number

The Prandtl number is the ratio between the momentum and the thermal diffusivity. For the liquid and vapor phase it is expressed respectively as:

$$Pr_L = \frac{c_{pL}\mu_L}{\lambda_L} \quad (1.37)$$

$$Pr_V = \frac{c_{pV}\mu_V}{\lambda_V} \quad (1.38)$$

### 1.6.3 Liquid Froude number

The Froude number represents the ratio between the inertial and the gravitational forces. The general expression is:

$$Fr = \frac{u^2}{gL} \quad (1.39)$$

In the flow boiling correlation of Shah [49] (1982), the liquid Froude number is used to define if the tube perimeter is all wet or partially dry (see subsection 2.4.1). Chen [9] (1963), Gungor and Winterton [22] (1986) and Jung [28] (1989) used the liquid Froude number for calculation of empirical factors for flow boiling heat transfer prediction. All of them used the following form of the liquid Froude number:

$$Fr_L = \frac{G^2}{\rho_L^2 g D} \quad (1.40)$$

Zürcher [70] (2000) pointed out that this expression is not completely consistent. Firstly, the velocity respective to the real liquid cross-sectional area is not applied. Secondly, the tube diameter is used as the characteristic length in equation 1.40. This does not necessarily make sense for the liquid phase. It is more realistic to express the characteristic length ( $L$  in equation 1.39) as the height of the liquid  $h_L$  in the flow cross-section. Finally, Zürcher proposed defining the Froude number taking into account the real velocity of the liquid and the liquid height of following form:

$$Fr_L = \frac{G^2(1-x)^2}{\rho_L^2(1-\varepsilon)^2 g h_L} \quad (1.41)$$

### 1.6.4 Liquid Weber number

The Weber number describes the ratio of inertia to surface tension forces. In forced convection, the reference length is also the tube diameter:

$$We_L = \frac{\rho_L u_L^2 D}{\sigma} \quad (1.42)$$

### 1.6.5 Nusselt number

The Nusselt number describes the ratio of the convective to conduction temperature gradient. In internal forced convection, the reference length is the tube diameter:

$$Nu = \frac{hD}{\lambda} \quad (1.43)$$

where  $h$  is the heat transfer coefficient,  $D$  is the tube diameter and  $\lambda$  is the thermal conductivity.

### 1.6.6 Boiling number

The boiling number describes the ratio between the heat flux and the potential heat flux that would have to be applied for complete evaporation:

$$Bo = \frac{q}{h_{LV}G} \quad (1.44)$$

Zürcher [70] (2000) pointed out that the boiling number is only consistent when the vapor quality is zero and when the considered heat flux is the mean heat flux during evaporation. He proposed a new boiling number referring only to the real potential heat flux that could be applied for complete evaporation as:

$$Bo = \frac{q(1 - \varepsilon)}{h_{LV}(1 - x)G} \quad (1.45)$$

### 1.6.7 The Martinelli Parameter

The Martinelli parameter [40] (1949) is the ratio of the theoretical pressure drops that would occur if each fluid could flow separately in the complete cross-section with the original flow rate of each phase. In general form the Martinelli parameter is calculated as:

$$X_{tt} = \left[ \frac{\left(\frac{\Delta P}{\Delta L}\right)_{LS}}{\left(\frac{\Delta P}{\Delta L}\right)_{VS}} \right]^{0.5} \quad (1.46)$$

$X_{tt}$  can be also defined as a measure of the degree to which the two-phase mixture is closer to being a liquid ( $X_{tt} \gg 1$ ), or to being a gas ( $X_{tt} \ll 1$ ).

If we model the pressure drop of each phase with its superficial velocity and friction factors as:

$$f_L = c_L Re_L^{-n} \quad (1.47)$$

$$f_V = c_V Re_V^{-m} \quad (1.48)$$

assuming the same friction model for both phases (both turbulent or both laminar), what means that  $m = n$  and  $c_L = c_V$ , equation 1.46 can be reduced to:

$$X_{tt} = \left( \frac{1-x}{x} \right)^{(-n+2)/2} \cdot \left( \frac{\mu_L}{\mu_V} \right)^{n/2} \cdot \left( \frac{\rho_V}{\rho_L} \right)^{1/2} \quad (1.49)$$

Based on equation 1.47 Lockhart-Martinelli [40] (1949) and then Taitel and Dukler [53] (1976) used  $n=m=0.2$  for a smooth pipe. Steiner [58] (1993), Kattan [29] (1996) and Zürcher [70] (2000) used  $n=m=0.25$  for a smooth pipe. In this work, the general expression of the Martinelli parameter will be the same as Steiner, Kattan, Zürcher used:

$$X_{tt} = \left( \frac{1-x}{x} \right)^{0.875} \cdot \left( \frac{\mu_L}{\mu_V} \right)^{0.125} \cdot \left( \frac{\rho_V}{\rho_L} \right)^{0.5} \quad (1.50)$$





## Chapter 2

# Flow pattern maps and heat transfer models

One of the most important aspects in two-phase flow analysis is the study of flow patterns, *i.e.* how do the phases distribute themselves in the conduit. Without knowing the flow regime (pattern) one cannot calculate correctly the design parameters for defined flow conditions such as heat transfer and pressure drop. The flow patterns depend on many parameters, such as the inclination of the conduit, geometry, pressure, surface roughness, type of liquid, *etc.* In the two first sections of this chapter, the main flow regimes and flow pattern maps encountered in a horizontal two-phase flow will be characterized. The last section describes the principal heat transfer mechanisms in flow boiling and the state-of-the-art of flow boiling heat transfer models.

### 2.1 Flow regimes in horizontal two-phase flows

The main physical forces controlling the distribution of the phases in horizontal two-phase flows are surface tension and gravity. The surface tension forces act to keep the tube wall of the tube wetted and the gravity force pulls the liquid downwards and makes the vapor buoyant. The generally accepted flow patterns in internal flow in a horizontal tube, are shown in Figure 2.1 and described below.

**Bubbly flow** - Bubbles are dispersed in the continuous liquid, though their concentration tends to be higher in the upper part of the tube. At higher velocity, the bubbles tend to be

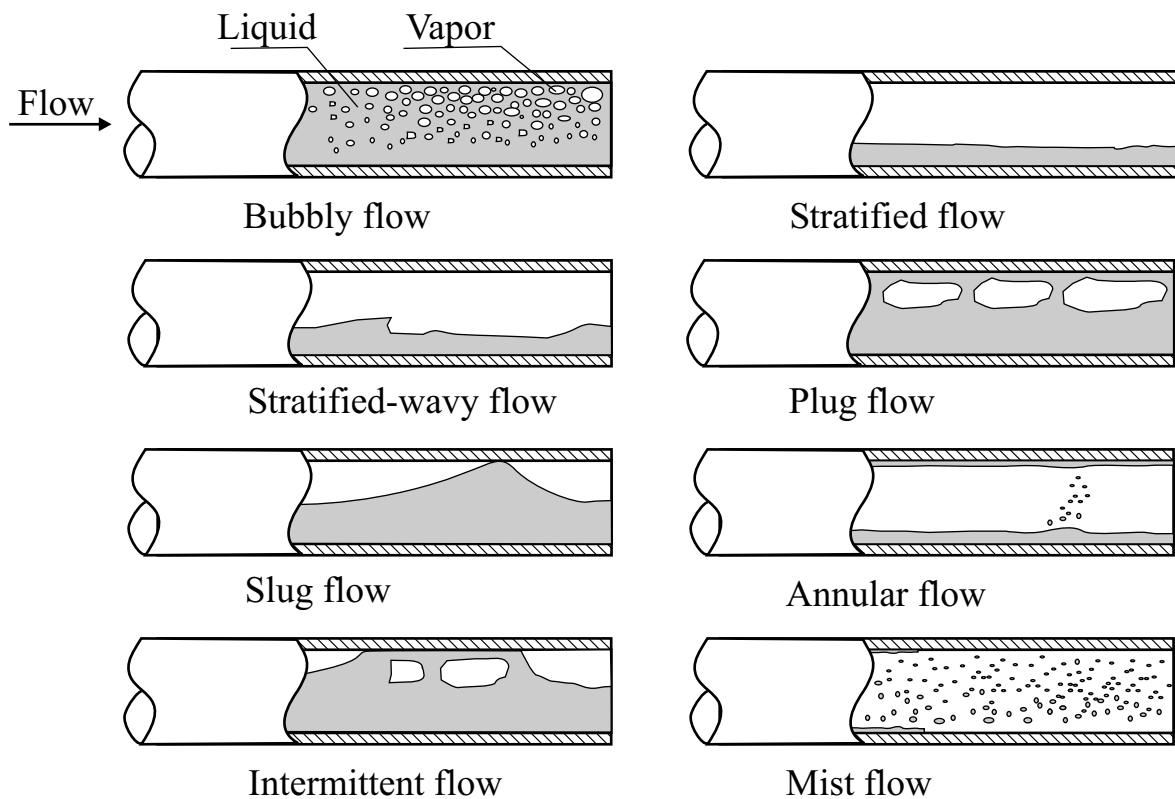


Figure 2.1: Flow regimes in internal two-phase flow.

more dispersed in the tube such that their distribution is more uniform.

**Stratified flow** - The two-phases are separated with liquid at the bottom of the tube (under normal gravity conditions) and gas at the top. This flow pattern occurs at low liquid and gas velocities.

**Stratified-wavy flow** - As the gas velocity in stratified flow is increased, waves are formed on the liquid-gas interface and they travel in the direction of fluid flow. The amplitude of the waves depends on the relative velocity between the phases and the properties of the fluids, such as their density and surface tension.

**Plug flow** - This is an intermittent flow that occurs at low gas flow rates and a moderate liquid rate. In this regime, zones of elongated gas bubbles separate liquid plugs, free of entrained gas bubbles. Plug flow is also termed elongated bubble flow.

**Slug flow** - when the gas velocity is increased in a plug flow, the liquid forms slugs, which pass frequently through the flow channel. The flow is more chaotic compared with plug flow and the interface between gas and liquid is not clearly defined.

**Annular flow** - Higher gas flow rates cause liquid to form a film on the tube wall. Usually, the liquid film at the bottom of the tube is much thicker than the film at the top. The distribution of the film thickness depends on the gas velocity. Also some droplets of entrained liquid are encountered in the gas core. The flow pattern is considered to be annular as soon as the motion of the liquid flowing at the top of the tube is comparable to the one of the liquid at the bottom of the tube.

**Intermittent flow** - This groups unsteady flow patterns like the plug and the slug flows. Due to the unsteadiness of the flow, all the tube periphery is frequently wetted.

**Mist flow** - This is encountered when all the liquid is entrained in a gas core by the high velocity gas. The vapor phase is the continuous phase and the liquid flows in the form of droplets (atomized droplets that may be too small to be seen).

This study will deal only with diabatic flow conditions, *i.e.* a saturated liquid/vapor mixture is heated during the flow. Flow patterns formed during the generation of vapor in horizontal tubular channels are influenced by departures from thermodynamic and hydrodynamic equilibrium. Figure 2.2 from Collier and Thome [11] depicts a schematic representation of a horizontal tubular channel heated by a uniform heat flux and fed with liquid just below the saturation temperature. The sequence of flow patterns shown corresponds to a relatively low inlet velocity ( $< 1 \text{ m/s}$ ). Important phenomena from a heat transfer point of view are: intermittent drying and rewetting of the upper surfaces of the tube in slug and stratified-wavy flow as well as the progressive drying out over long tube lengths of the upper circumference of the tube wall in annular flow. At higher inlet liquid velocities, the influence of gravity is less obvious and the phase distribution becomes more symmetrical.

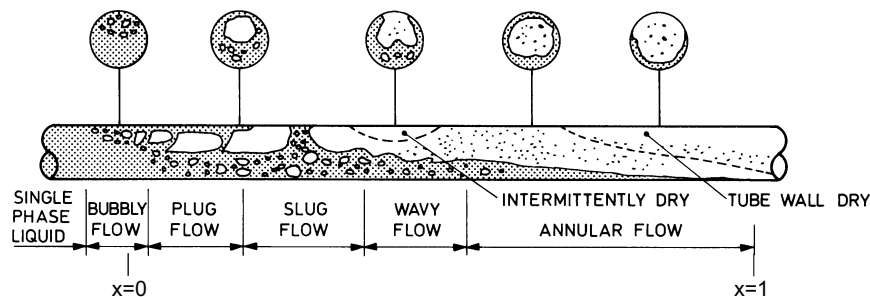


Figure 2.2: Flow regimes in co-current two-phase flow.

## 2.2 Flow pattern maps

Many flow pattern maps are available for predicting adiabatic two-phase flow regimes in horizontal tubes, such as Baker [4] (1954), Taitel and Dukler [53] (1976), Hashizume [26] (1983), Steiner [58] (1993). Very important factors for the flow during evaporation, which have an effect on transition between flow regimes, are nucleate boiling, evaporation of liquid films and acceleration of the flow due to the phase change. It is desirable to define for this type of flow a flow pattern map that includes the influences of heat flux and dryout on the flow pattern transition boundaries and one which is also easier to implement than the frequently used log-log format. As a first step in this direction, Kattan *et al.* [30] (1998a) proposed a modification of the Steiner map, which in turn is a modified Taitel-Dukler map, and which includes a method for predicting the onset of dryout at the top of the tube in evaporating annular flow. In the study of Kattan *et al.*, stratified (S), stratified-wavy (SW), intermittent (I) and annular (A) flows were encountered. The bubbly (B) and mist flow (M), which can be observed at very high mass velocities, were not reached in their study. The transition between stratified and stratified-wavy flow will be designated as "S - SW", between stratified-wavy and intermittent/annular as "SW - I/A", between intermittent and annular as "I-A", between annular and mist flow as "A-M" and between intermittent and bubbly as "I-B".

### 2.2.1 Flow pattern map of Kattan-Thome-Favrat

To better identify flow patterns during the evaporation process at different mass velocities and to make the map a more useful research and design tool, Kattan *et al.* [30] (1998a) converted the axes of the Steiner flow pattern map to mass velocity  $G$  versus vapor quality  $x$ . With this new representation, it is feasible to follow the change in flow pattern during the evaporation of a refrigerant at a fixed mass velocity. Compared to the original Steiner map, the transition boundary curve between stratified-wavy and intermittent/annular region (SW - I/A) was raised to better describe their large flow pattern observation database. It was also adjusted to take into account the influence of the heat flux on the onset of dryout at high vapor quality. The annular to mist flow transition curve (A-M) has been modified as well to make a more realistic boundary.

To calculate flow pattern transition curves using their method, the following six dimensionless geometrical variables must first be defined:

$$P_{LD} = \frac{P_L}{D}; \quad P_{VD} = \frac{P_V}{D} \quad (2.1)$$

$$P_{iD} = \frac{P_i}{D}; \quad h_{LD} = \frac{h_L}{D} \quad (2.2)$$

$$A_{LD} = \frac{A_L}{D^2}; \quad A_{VD} = \frac{A_V}{D^2} \quad (2.3)$$

As shown in Figure 1.1,  $P_L$  is the wetted perimeter while,  $P_V$  is the complementary perimeter in contact with vapor. Similarly,  $A_L$  and  $A_V$  are the corresponding cross-sectional areas, and  $P_i$  is the phase interface.

The dimensionless peripheral and cross-sectional area variables that are required for analysis can be derived from the geometry for a given liquid height  $h_L$  or for a reference liquid level  $h_{LD}$ .

For  $h_{LD} \leq 0.5$

$$P_{LD} = (8(h_{LD})^{0.5} - 2(h_{LD}(1 - h_{LD}))^{0.5})/3 \quad (2.4)$$

$$P_{VD} = \pi - P_{LD} \quad (2.5)$$

$$A_{LD} = (12(h_{LD}(1 - h_{LD}))^{0.5} + 8(h_{LD})^{0.5})h_{LD}/15 \quad (2.6)$$

$$A_{VD} = \frac{\pi}{4} - A_{LD} \quad (2.7)$$

For  $h_{LD} > 0.5$

$$P_{VD} = (8(1 - h_{LD})^{0.5} - 2(h_{LD}(1 - h_{LD}))^{0.5})/3 \quad (2.8)$$

$$P_{LD} = \pi - P_{VD} \quad (2.9)$$

$$A_{VD} = (12(h_{LD}(1 - h_{LD}))^{0.5} + 8(1 - h_{LD})^{0.5})(1 - h_{LD})/15 \quad (2.10)$$

$$A_{LD} = \frac{\pi}{4} - A_{VD} \quad (2.11)$$

For  $0 \leq h_{LD} \leq 1$

$$P_{iD} = 2(h_{LD}(1 - h_{LD}))^{0.5} \quad (2.12)$$

An iterative method of resolution, on the basis of the following equation, is necessary to calculate the reference liquid level  $h_{LD}$ :

$$X_{tt}^2 = \left[ \left( \frac{P_{VD} + P_{iD}}{\pi} \right)^{0.25} \left( \frac{\pi^2}{64A_{VD}^2} \right) \left( \frac{P_{VD} + P_{iD}}{A_{VD}} + \frac{P_{iD}}{A_{LD}} \right) - \frac{1}{T_v^2} \right] \left( \frac{\pi}{P_{LD}} \right)^{0.25} \left( \frac{64A_{LD}^3}{\pi^2 P_{LD}} \right) \quad (2.13)$$

where the inclination angle  $\varphi = 0^\circ$ ,  $T_v^2 \rightarrow \infty$  and  $1/T_v^2$  in equation 2.13 goes to zero.  $X_{tt}$  is calculated from equation 1.50 for each vapor quality  $0 \leq x \leq 1$ . This iteration with respect to  $h_{LD}$  is de facto the determination of void fraction based on the model of Taitel-Dukler described in Chapter 5.

Knowing the geometrical parameters and the thermodynamical properties of the liquid, the flow pattern transition curves can be calculated as follows:

### S-SW transition

$$G_{strat} = \left\{ \frac{226.3^2 A_{LD} A_{VD}^2 \rho_V (\rho_L - \rho_V) \mu_L g \cos \varphi}{x^2 (1-x) \pi^3} \right\}^{1/3} \quad (2.14)$$

### SW-I/A transition

$$G_{wavy} = \left\{ \frac{16 A_{VD}^3 g D \rho_L \rho_V}{x^2 \pi^2 (1 - (2h_{LD} - 1)^2)^{0.5}} \left[ \frac{\pi^2}{25 h_{LD}^2} (1-x)^{-F_1(q)} \cdot \left( \frac{We}{Fr} \right)_L^{-F_2(q)} + \frac{1}{\cos \varphi} \right] \right\}^{0.5} + 50 \quad (2.15)$$

where

$$\left( \frac{We}{Fr} \right)_L = \frac{g D^2 \rho_L}{\sigma_L} \quad (2.16)$$

$$F_1(q) = 48.24 \left( \frac{q}{q_{crit}} \right) \quad (2.17)$$

$$F_2(q) = 9.65 \left( \frac{q}{q_{crit}} \right) + 1.053 \quad (2.18)$$

The exponents  $F_1(q)$  and  $F_2(q)$  modify the "SW-I/A" transition curve by taking into account the diabatic effect of dryout encountered for the higher vapor qualities. Above,  $F_1(q)$  and  $F_2(q)$  were defined for the outlet vapor quality of the test section (where the sight glass is located). However, the experimental heat transfer coefficient in the test of Kattan was based

on the mean vapor quality of the test zone. Consequently, Kattan proposed to use the mean vapor quality of the test section instead of the outlet vapor quality; the exponents  $F_1(q)$  and  $F_2(q)$  become:

$$F_1(q) = 646.0 \left( \frac{q}{q_{crit}} \right)^2 + 64.8 \left( \frac{q}{q_{crit}} \right) \quad (2.19)$$

$$F_2(q) = 18.8 \left( \frac{q}{q_{crit}} \right) + 1.023 \quad (2.20)$$

$q_{crit}$  is the critical heat flux obtained from Kutateladze [37] (1948) as:

$$q_{crit} = 0.131 \rho_V^{0.5} h_{LV} (g(\rho_L - \rho_V) \sigma)^{0.25} \quad (2.21)$$

### A-M transition

$$G_{mist} = \left\{ \frac{7680 A_{VD}^2 g D \rho_L \rho_V}{x^2 \pi^2 \zeta_{Ph}} \left( \frac{Fr}{We}_L \right) \right\}^{0.5} \quad \text{at } x < x_{min} \quad (2.22)$$

$$G_{mist} = G_{min} \quad \text{at } x > x_{min}$$

$x_{min}$  is the vapor quality at which  $G_{mist}$  reaches its minimum value.

### I - A transition

For turbulent flow of both the vapor and the liquid phase, the transition curve of the intermittent to annular flow is defined by a fixed Martinelli parameter  $X_{tt} = 0.34$ . By extracting the vapor quality from equation 1.50, the transition between intermittent and annular flows is calculated as:

$$x_{IA} = \left\{ \left[ 0.34^{1/0.875} \left( \frac{\rho_V}{\rho_L} \right)^{-1/1.75} \left( \frac{\mu_V}{\mu_L} \right)^{-1/7} \right] + 1 \right\}^{-1} \quad (2.23)$$

### I-B transition

$$G_{bubbly} = \left\{ \frac{256 A_{VD} A_{LD}^2 D^{1.25} \rho_L (\rho_L - \rho_V) g \cos \varphi}{0.3164 (1-x)^{1.75} \pi^2 P_{iD} \mu_L^{0.25}} \right\}^{1/1.75} \quad (2.24)$$

As has been mentioned, this transition curve was not verified during experimental work in the frame of this study and previous by Kattan [29] (1996) and Zürcher [70](2000).

Figure 2.3 shows the flow pattern map of Kattan compared to Steiner for the refrigerant R-410A at  $T_{sat} = 5^\circ\text{C}$ . All transition curves were obtained using the above equations with  $F_1(q)$  and  $F_2(q)$  defined for the mean vapor quality in equations 2.17 and 2.18.

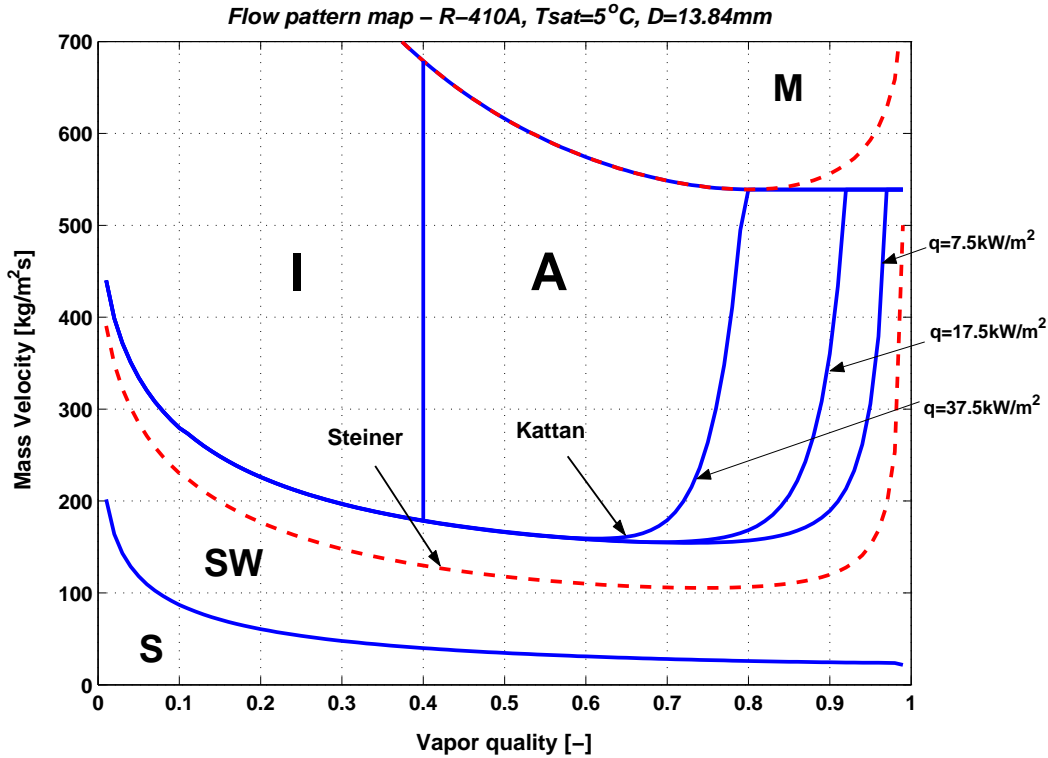


Figure 2.3: Flow pattern map of Kattan compared to Steiner for R-410A at  $T_{sat} = 5^\circ\text{C}$  in 13.84 mm internal diameter tube.

As can be seen, the transition curves "SW-I/A" of Kattan (solid lines) are strongly influenced by the effect of onset of dryout compared to the adiabatic curve of Steiner (dashed line). Based on Kattan's flow pattern observations, his "SW-I/A" curve was also raised by  $50 \text{ kg/m}^2\text{s}$ . To the "A-MF" transition curve, Kattan added a criterion to avoid the possibility of a mist flow reverting back again to annular flow with increasing vapor quality. Therefore, once the minimum value of mass velocity is reached with equation 2.22, this minimum value is then applied for all higher vapor qualities. Thus, at the end of the evaporation the "A-M" transition curve remains flat. It must be noted that this transition boundary has not been investigated experimentally in the work of Kattan. Two other transition curves "S-SW" and "I-A" were not modified and are the same as the original ones of Steiner. Note that annular flow with partial dryout at the top of the tube is classified as a stratified-wavy flow by the map. Kattan verified his flow pattern map for 702 experimental points for five refrigerants tested over a wide range of pressures, vapor qualities and mass velocities representative of



direct-expansion evaporator conditions. These observations showed that 96.2% of the flow pattern data were identified correctly with his diabatic flow pattern map.

### 2.2.2 Flow pattern map of Zürcher

Regarding improvements to the Kattan *et al.* [30] (1998a) flow pattern map, Zürcher *et al.* [71] (1999) proposed small changes to the "S-SW" and "SW-A/I" transition curves based on new observations for ammonia that targeted these two transitions. In particular, the transition curve "S-SW" was found to be too low based on flow pattern observations at  $G = 20 \text{ kg/m}^2\text{s}$  which were in the fully stratified regime. Hence, the  $G_{strat}$  boundary equation was modified empirically by adding the additional term of  $20x$  as follows:

#### S-SW transition

$$G_{strat} = G_{strat,Kattan} + 20x \quad (2.25)$$

$$G_{strat} = \left\{ \frac{226.3^2 A_{LD} A_{VD}^2 \rho_V (\rho_L - \rho_V) \mu_L g \cos \varphi}{x^2 (1-x) \pi^3} \right\}^{1/3} + 20x \quad (2.26)$$

In addition, the transition curve "SW-I/A" at high vapor qualities was observed by Zürcher to be too high, which had also been noted earlier in some previous tests with other refrigerants. Hence, an additional empirical term was added to the  $G_{wavy}$  equation as:

#### SW - I/A transition

$$G_{wavy} = G_{wavy,Kattan} - 75e^{-[(x^2-0.97)^2/x(1-x)]} \quad (2.27)$$

$$G_{wavy} = \left\{ \begin{array}{l} \left\{ \frac{16A_{VD}^3 g D \rho_L \rho_V}{x^2 \pi^2 (1-(2h_{LD}-1)^2)^{0.5}} \left[ \frac{\pi^2}{25h_{LD}^2} (1-x)^{-F_1(q)} \cdot \left( \frac{We}{Fr} \right)_L^{-F_2(q)} + \frac{1}{\cos \varphi} \right] \right\}^{0.5} \\ +50 - 75e^{-[(x^2-0.97)^2/x(1-x)]} \end{array} \right\} \quad (2.28)$$

Zürcher noted that the heat flux effect of the Kattan *et al.* flow pattern map on the onset of dryout is too strong and predicts transition from annular flow to stratified-wavy flow at vapor quality values that are too low. The original data used to determine the heat flux correction to this curve in Kattan *et al.* [32] (1998c) had only a few values above  $20 \text{ kW/m}^2$  and applying it to the high heat flux conditions of Zürcher represents an extrapolation of the method. Based on a large number of new ammonia data at high heat fluxes, Zürcher proposed to reduce the heat flux effect to about one-half using the new exponent  $F_1(q)$  and  $F_2(q)$  defined as:

$$F_1(q) = 24.12 \left( \frac{q}{q_{crit}} \right) \quad (2.29)$$

$$F_2(q) = 4.825 \left( \frac{q}{q_{crit}} \right) + 1 \quad (2.30)$$

Note that the heat flux relaxation effect has been done with respect to  $F_1(q)$  and  $F_2(q)$  defined by Kattan for the outlet vapor quality of the test section divided by two. However, Kattan used much higher values of exponents  $F_1(q)$  and  $F_2(q)$  based on the mean vapor quality of the test zone. In consequence the onset of dryout is relaxed much more than one-half. This can be observed in Figure 2.4, which illustrates differences between "S-SW" and "SW-I/A" transition curves of Zürcher and Kattan.

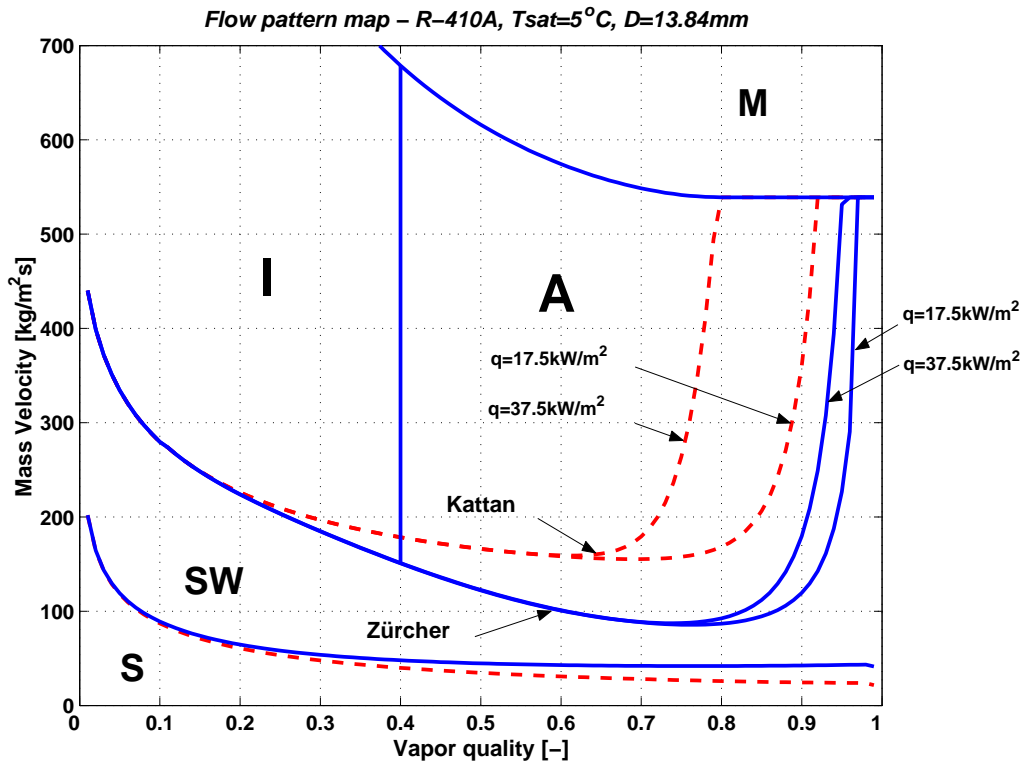


Figure 2.4: Flow pattern map of Zürcher compared to Kattan for R-410A at  $T_{sat} = 5^\circ C$  in 13.84 mm internal diameter tube.

Zürcher [70] (2000) and Zürcher *et al.* [73] (2002) described a new more advanced version of a flow pattern map that better respects the ammonia flow pattern observation but is in fact quite complex to implement. It used the Taitel-Dukler void fraction model (equation 5.11) for fully stratified flows, the Rouhani-Axelsson void fraction model (equation 5.47) for intermittent and annular flows and interpolates between these two for void fractions in

stratified-wavy flows. Also, it includes a dissipation function in "SW-I/A" transition curve. Essentially, the entire set of equations of the flow pattern map must be iteratively solved to find the transition curves, which is physically logical but difficult to implement for general practice.

### 2.2.3 Flow pattern map of Thome and El Hajal

As a practical option, a new, easier to implement version of the above maps was proposed by Thome and El Hajal [55](2002). In both previously presented flow pattern maps, dimensionless variables  $A_{LD}$ ,  $A_{VD}$ ,  $h_{LD}$  and  $P_{iD}$  were calculated in an iterative way using *de facto* a void fraction model of Taitel-Dukler. On the other hand, the flow boiling heat transfer model of Kattan *et al.* [32] (1998c) uses instead the Rouhani-Axelsson drift flux model presented in equation 5.47.

This model can be easily applied and gives the void fraction as a function of total mass flux, something the method of Taitel-Dukler does not do. Hence it makes sense to use the same void fraction model in both the flow pattern map and the flow boiling heat transfer model, for which the Rouhani-Axelsson model is a better choice as a general method.

Then, from the sectional area of the tube A and after calculating  $\varepsilon$ , the values  $A_{LD}$  and  $A_{VD}$  are directly determined by:

$$A_{LD} = \frac{A(1 - \varepsilon)}{D^2} \quad (2.31)$$

$$A_{VD} = \frac{A\varepsilon}{D^2} \quad (2.32)$$

The dimensionless liquid height  $h_{LD}$  and the dimensionless length of the liquid interface  $P_{iD}$  can be expressed as a function of stratified angle  $\theta_{strat}$ :

$$h_{LD} = 0.5 \left( 1 - \cos \left( \frac{2\pi - \theta_{strat}}{2} \right) \right) \quad (2.33)$$

$$P_{iD} = \sin \left( \frac{2\pi - \theta_{strat}}{2} \right) \quad (2.34)$$

Avoiding any iteration, the stratified angle  $\theta_{strat}$  can be calculated from an expression evaluated in terms of void fraction proposed by Biberg [5] (1999) as follows:

$$\theta_{strat} = 2\pi - 2 \left\{ \begin{array}{l} \pi(1 - \varepsilon) + \left(\frac{3\pi}{2}\right)^{1/3} \left[1 - 2(1 - \varepsilon) + (1 - \varepsilon)^{1/3} - \varepsilon^{1/3}\right] \\ -\frac{1}{200}(1 - \varepsilon)\varepsilon[1 - 2(1 - \varepsilon)][1 + 4((1 - \varepsilon)^2 + \varepsilon^2)] \end{array} \right\} \quad (2.35)$$

The error of this explicit method is about 0.00005 radians for  $2\pi \geq \theta_{strat} \geq 0$  compared to the original implicit expression.

The above described method recommends using the equations of Zürcher *et al.* [71] (1999) for the "S-SW" and "SW-I/A" transition boundaries with the exponents  $F_1(q)$  and  $F_2(q)$  of the form:

$$F_1(q) = 646.0 \left(\frac{q/2}{q_{crit}}\right)^2 + 64.8 \left(\frac{q/2}{q_{crit}}\right) \quad (2.36)$$

$$F_2(q) = 18.8 \left(\frac{q/2}{q_{crit}}\right) + 1.023 \quad (2.37)$$

The "A-M", "I-A" and "I-B" transition boundaries have not been changed by Zürcher *et al.* [71] (1999) and it is recommended to use them in the form proposed by Kattan.

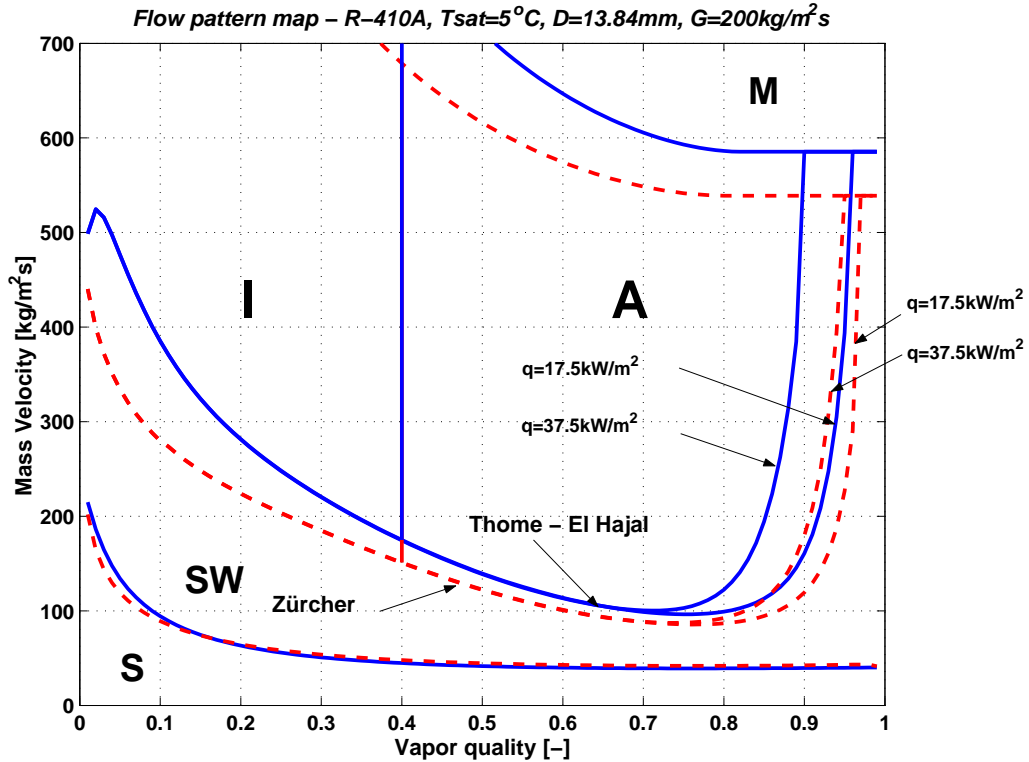


Figure 2.5: Flow pattern map of Thome-El Hajal compared to Zürcher for R-410A at  $T_{sat} = 5^\circ C$  in 13.84 mm internal diameter tube (graph was prepared assuming a fixed value of  $G = 200 \text{ kg/m}^2 \text{ s}$ ).

Figure 2.5 shows a comparison of transition curves obtained by Thome-El Hajal and by Zürcher. In the non-iterative method of Thome-El Hajal, the void fraction was calculated for the mass velocity  $G = 200 \text{ kg/m}^2\text{s}$ . The above approach at a fixed  $G$  is only to simplify the generation of the flow pattern map. The main differences are observed between the "SW-I/A" and "A-M" transition curves. The curves predicted by Thome-El Hajal are significantly above the boundaries of Zürcher. The effect of heat flux on the onset of dryout has been magnified as well. As the void fraction is the function of the mass velocity, in the presented model it influences the position of transition curves. The effect of mass velocity on the prediction of flow transition is shown in Figure 2.6.

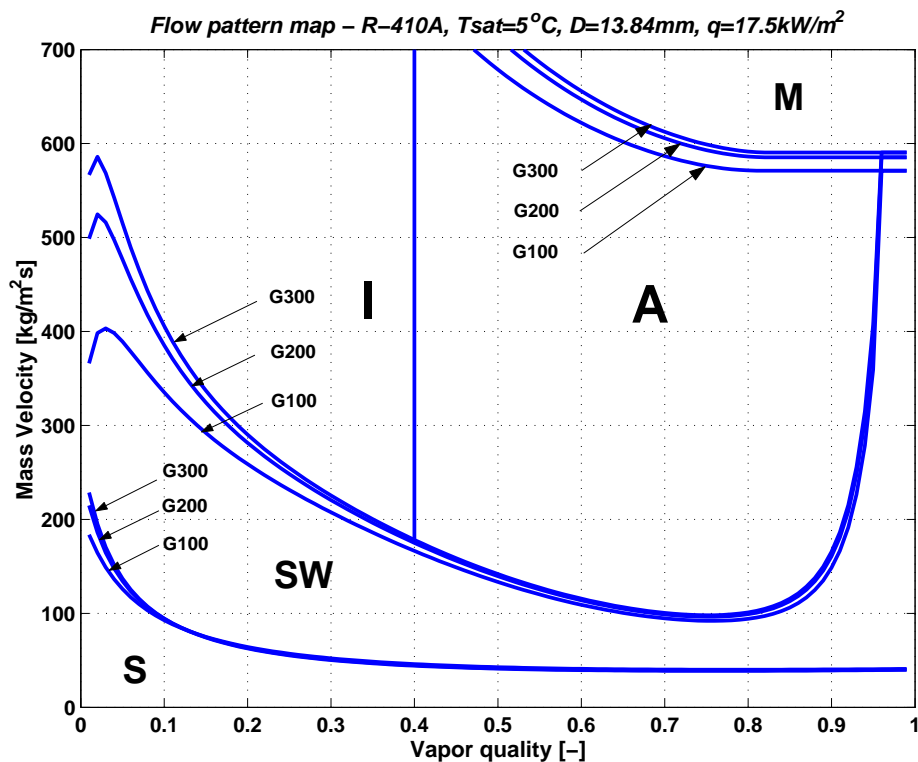


Figure 2.6: Flow pattern map of Thome-El Hajal for R-410A at  $T_{sat} = 5^{\circ}\text{C}$  in 13.84 mm internal diameter tube at three mass velocities  $G = 100, 200$  and  $G = 300 \text{ kg/m}^2\text{s}$ .

The strongest effect of mass velocity is observed for the "SW-I/A" transition curve for vapor qualities below 0.1. The transition curve goes up with increasing mass velocity. This divergence becomes less significant as the vapor quality increases. The boundary curve "A-M" moves up with increasing mass velocity.

## 2.3 Flow boiling

Flow boiling is a very complex process in which numerous phenomena are superimposed. The saturated liquid generates vapor, which flows with much higher velocity than the liquid phase. The flow geometry varies due to the shear forces of accelerating vapor, bubble agitation from the nucleate boiling and evaporation of the liquid film. The variation in void fraction causes changes in flow patterns. Therefore, the prediction of heat transfer in such a complicated continuously developing process is a big challenge. Many prediction methods can be found in literature. The main methods will be described here with the most recent one based on the flow pattern map in flow boiling heat transfer prediction.

### 2.3.1 Heat transfer mechanisms

Heat transfer mechanisms encountered in flow boiling will be analysed based on the pool boiling curve presented in Figure 2.7.

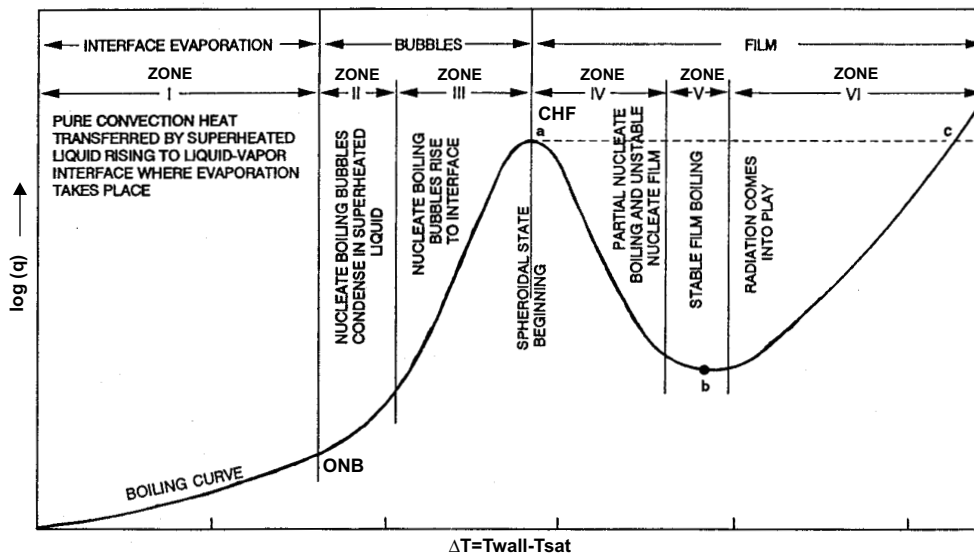


Figure 2.7: Flow boiling curve taken from ASHRAE Handbook [2].

This curve shows a variation of heat flux  $q$  as a function of the wall and saturation temperature difference  $\Delta T$ . The curves can be divided and analysed into six zones as follows:

**Natural convection** - zone I in the Figure 2.7, exists for the lowest temperature differences

$\Delta T$ . In this regime there is no boiling at heated surface and instead superheated liquid rises to the liquid-vapor interface where the evaporation takes place (see Figure 2.8a).

As the excess temperature is increased, bubble inception will occur at the point called **onset of nucleate boiling (ONB)**. In **nucleate boiling**, two different regimes may be distinguished. In zone II, isolated bubbles form at nucleation sites and separate from the surface (see Figure 2.8c). This separation induces considerable fluid mixing near the surface, substantially increasing the heat transfer coefficient -  $h$  and heat flux -  $q$ . In this regime, most of the heat is transferred through direct transfer from the surface to liquid in motion at the surface, and not through the vapor bubbles. They rise from the surface and condense in superheated liquid. As  $\Delta T$  is increasing, more nucleation sites become active and increased bubble formation causes bubble interference and coalescence. In this region, heat is transferred mostly by the vapor formed as jets or columns, which subsequently merge into slugs and rise to interface (see Figure 2.8d). Interference between the densely populated bubbles inhibits the motion of liquid near the surface.

The maximum heat flux is obtained at the (**CHF**) point and is usually termed **critical heat flux**. At this point, considerable vapor is being formed, making it difficult for the liquid to continuously wet the surface (see Figure 2.8e). The region corresponding to zone IV in Figure 2.7 is termed **transition boiling, unstable film boiling, or partial film boiling**. Bubble formation is now so rapid that a vapor film or blanket begins to form on the surface (see Figure 2.8f). At any point on the surface, conditions may oscillate between the film and nucleate boiling, but the fraction of surface covered by the film increases with augmentation of  $\Delta T$ . Because the thermal conductivity of the vapor is much less than that of the liquid, the heat transfer coefficient  $h$  decrease dramatically beyond the **CHF** with increasing  $\Delta T$ . **Stable film boiling** exists for zone V and VI as depicted in Figure 2.7 and as shown in Figure 2.8g. Heat transfer from the surface to the liquid occurs by conduction through the vapor. As the surface temperature is increased, radiation through the vapor film becomes significant and the heat flux increases with increasing  $\Delta T$ .

The present study will deal only with the flow boiling heat transfer below the critical heat flux. Thus, the phenomena encountered will be the convective and nucleate boiling. The prediction methods for these two heat transfer mechanisms will be presented below.

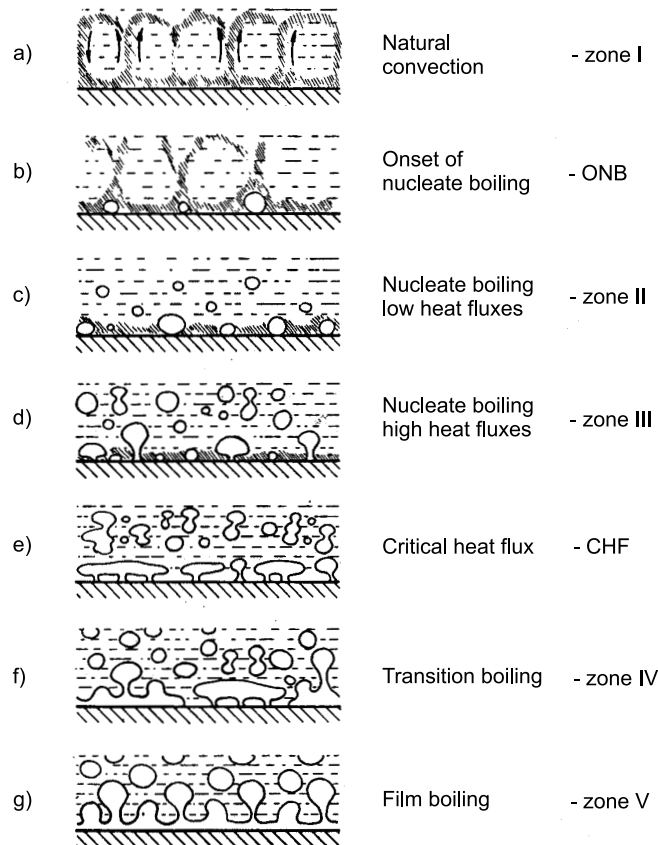


Figure 2.8: Various stages in flow boiling according to Collier and Thome [11].

### 2.3.2 Convective boiling

Most of the convective heat transfer correlations are related to the well-known Dittus Boellter correlation (1930) and are expressed as a product of Reynolds and Prandtl numbers with some empirical parameters. Taking into consideration the definition of Reynolds and Prandtl numbers, it can be said that the convection heat transfer coefficient is a function of the momentum and thermal diffusivities and the inertia and viscosity forces. In a two-phase flow, the convective heat transfer coefficient has to be defined separately for each phase.

For the **liquid convective heat transfer coefficient**, the following film form of equation has been proposed by Kattan *et al.* [31](1998b):

$$h_{L,cb} = C \cdot \text{Re}_\delta^m \cdot \text{Pr}_L^{0.4} \cdot \frac{\lambda_L}{\delta} \quad (2.38)$$



$Re_\delta$  and  $Pr_L$  are calculated from equation 1.35 and equation equation 1.37, respectively.

Annular liquid film thickness  $\delta$  shown in Figure 1.3 is determined by:

$$\delta = \frac{A_L}{R(2\pi - \theta_{dry})} = \frac{A(1 - \varepsilon)}{R(2\pi - \theta_{dry})} = \frac{\pi D(1 - \varepsilon)}{2(2\pi - \theta_{dry})} \quad (2.39)$$

where  $\varepsilon$  is the void fraction calculated from the Rouhani-Axelsson correlation - equation 5.47 and  $\theta_{dry}$  is the dry angle calculated iteratively by Kattan [29] (1996) with assumption that  $\theta_{dry} = \theta_{strat}$  from following equation:

$$A_L = 0.5R^2[(2\pi - \theta_{strat}) - \sin(2\pi - \theta_{strat})] \quad (2.40)$$

$\theta_{strat}$  can be also calculated non-iteratively from expression of Biberg, - equation 2.35.

Empirical values were found to be equal to  $m=0.69$  and  $C=0.0133$ . They have been obtained by Kattan [29] (1996) based on the study of 1141 experimental points for five refrigerants and four flow patterns. Note that the presented model is based on turbulent liquid film flow rather than on tubular flow.

To calculate the **vapor convective heat transfer coefficient**, Kattan proposed using the tubular, turbulent equation in the form:

$$h_V = 0.023 \cdot Re_V^{0.8} \cdot Pr_V^{0.4} \cdot \frac{\lambda_V}{D} \quad (2.41)$$

where  $Re_V$  and  $Pr_V$  are calculated from equation 1.33 and equation 1.38, respectively.

He assumed tubular flow conditions, since the vapor cross-section is nearly circular for a thin annular liquid film flow with partial dryout and  $h_V$  is much lower than for the wetted part.

### 2.3.3 Nucleate boiling

The nucleate boiling is related to the nucleation and growing of vapor bubbles on the heated surface. For nucleation to occur, a given amount of heat is needed to overcome surface tension forces. This heat can be calculated from the equation used by Steiner and Taborek [52](1992) as:

$$q_{ONB} = \frac{2\sigma T_{sat} h_{L,cbo}}{r_{crit} \rho_V h_{LV}} \quad (2.42)$$

where  $r_{crit} = 0.3 \cdot 10^{-6}$  m is the critical bubble radius recommended for usual extruded tube materials and  $h_{L,cbo}$  is the all liquid convective heat transfer coefficient.

The principal heat transfer mechanisms involved in the process of nucleate boiling are as follows:

**Bubble agitation** - Convection in the liquid phase is induced by the lateral pumping motion imparted on the liquid by numerous growing and departing bubbles. Essentially, the liquid is pushed back and forth across the heater surface by neighbouring bubbles and this transforms the natural convection process into a localised forced convection process. Thus, the more intense the boiling activity, the stronger this mechanism is. Sensible heat is carried away from the surface in the form of superheated liquid.

**Vapor-liquid exchange** - Transient conduction of heat from the wall into liquid forms a superheated layer, and its subsequent removal by the wake of departing bubbles gives rise to a cyclic thermal boundary layer stripping phenomenon. The sensible heat transported away depends on the rate of superheated liquid removal, which is proportional to the layer thickness, its mean temperature, the area of influence of a departing bubble and its departure frequency, and finally the density of active boiling sites.

**Evaporation** - Vapor bubbles grow by virtue of the heat conducted first into the thermal boundary layer and then by diffusion to the bubble interface, where it is converted to latent heat and generation of vapor. Since bubbles rise much faster than liquid natural convection currents and contain a large quantity of energy due to the latent heat absorbed by the bubble, this is an efficient heat transport mechanism. Macro-evaporation occurs over the top of the bubble surrounded by the thermal boundary layer while micro-evaporation occurs underneath the bubble across the thin layer of liquid trapped between a rapidly growing bubble and the surface, the latter being often referred to as microlayer evaporation. The latent heat transported by this mechanism is determined by the volumetric flow rate of vapor per unit area from the surface.

The above mechanisms are not exclusive in that they are the function of the same heat flux and hence the mechanisms in some ways compete with one another. For instance, the evaporation mechanism tries to remove enthalpy from the thermal boundary layer in the form of latent heat while the other two mechanisms try to transport the same enthalpy to

the bulk liquid as sensible heat, which allows rising bubbles to continue to grow.

The analysis of nucleate boiling requires prediction of the number of nucleation sites on the heated surface and the rate at which bubbles grow from each site. To date, no analytical method is capable of accurately and reliably describing the complex process of nucleate pool boiling heat transfer. The first who showed the influence of nucleation sites on the heat flux was Yamugata [66](1955). He proposed following relation.

$$q = C\Delta T^a n^b \quad (2.43)$$

where  $n$  is the site density (active nucleation sites per unit area) and the exponents are approximately  $a = 1.2$  and  $b = 0.33$ . Although  $C$  and  $n$  vary for different fluid-surface combinations, it has been found that the number of active nucleation sites for most commercial surfaces is proportional to  $\Delta T^5$  or  $\Delta T^6$ . Hence, from (2.43) it follows that  $q$  is approximately proportional to  $\Delta T^3$ .

The foregoing dependence of  $q$  and  $\Delta T$  characterizes the first widely used correlation for nucleate boiling developed by Rohsenow [45](1962).

$$q = \mu_L h_{LV} \left[ \frac{g(\rho_L - \rho_V)}{\sigma} \right]^{0.5} \left( \frac{c_{pL} \Delta T}{C_{sf} h_{LV} \text{Pr}_L^n} \right)^3 \quad (2.44)$$

Very often the correlation of Rohsenow is shown in the following form:

$$\frac{c_{pL} \Delta T}{h_{LV}} = C_{sf} \left[ \frac{q}{\mu_L h_{LV}} \sqrt{\frac{\sigma}{g(\rho_L - \rho_V)}} \right]^{0.33} \left( \frac{c_{pL} \mu_L}{\lambda_L} \right)^n \quad (2.45)$$

The last experimental evaluation of  $C_{sf}$  and  $n$  constants for four working fluids (water, ethanol, R-113 and R-11) and various heated surfaces has been published by Pioro [42](1998). He analysed 42 previous experimental works over the last 70 years and extended the existing database with his own experiments.

Cooper [12](1984) presented a different method to predict nucleate boiling heat transfer coefficients. He proposed a simple type of correlation, using only the reduced pressure  $P_r$ , molecular weight  $M$  and surface roughness  $R_p$ . He showed that properties like  $p_{sat}$ ,  $T_{sat}$ ,  $\rho_L$ ,  $\rho_V$ ,  $h_{LV}$ ,  $\sigma$ ,  $\lambda_L$ ,  $\mu_L$ ,  $c_{pL}$  can be expressed as a product of powers of  $P_r$ ,  $T_r$  and  $(1 - T_r)$ , each with an accuracy typically about  $\pm 3\%$  for  $0.001 < P_r < 0.9$ . Furthermore, the variation of  $T_r$  and  $(1 - T_r)$  has been transformed using Clapeyron equation in the logarithmic form of  $P_r$  and the final version of the correlation is as follows:

$$h_{nb} = 55(P_r)^{0.12-0.2 \log R_p} (-\log P_r)^{-0.55} M^{-0.5} q^{0.67} \quad (2.46)$$

When the value of  $R_p$  is unknown, it is set to  $1.0 \mu\text{m}$  and the equation can be shown as:

$$h_{nb} = 55(P_r)^{0.12} (-\log P_r)^{-0.55} M^{-0.5} q^{0.67} \quad (2.47)$$

This correlation is based on over 6000 experimental points related to over 100 publications. It was also selected by Kattan and Zürcher in their models to predict the nucleate boiling contribution to the flow boiling heat transfer coefficient.

## 2.4 Flow boiling heat transfer models

In flow boiling, the nucleate and the convective components are superimposed by a very complex mechanism, which so far is not well understood. As can be seen in Figure 2.7 the nucleate and convective boiling components are dominant at high and at low  $\Delta T$ , respectively. The effect of nucleate boiling depends strongly on the surface roughness and the thickness of the liquid film, while the contribution of convective boiling depends strongly on the mass velocity.

Over the years, many correlations tried to empirically describe the very complex process of flow boiling by combining convective and nucleate boiling models. The three main type of models are enhancement, superposition and asymptotic models. They will be shortly presented below. Kattan [29] (1996) analysed all three models and compared them with his experimental results for his five test liquids. He showed that without distinguishing between the appropriate two-phase flow pattern, it was not possible to precisely predict the heat transfer coefficient. He observed the highest errors in the partial dryout zone, where all three reviewed methods do not account for this phenomenon, which has an enormous influence on the heat transfer. Finally, Kattan [29] (1996) proposed a new flow pattern oriented model, which has been extended by Zürcher [70] (2000) with an onset of nucleate boiling criterion.

### 2.4.1 The enhancement model

The enhancement model assumes that the local flow boiling heat transfer coefficient is a function of an enhancement factor  $E$  and the liquid convective boiling heat transfer coefficient  $h_{cb}$ .

$$h_{tp} = E \cdot h_{cb} \quad (2.48)$$

This type of model has been proposed by Shah [49], where the enhancement factor  $E$  is an empirical function of the liquid Froude number  $Fr_L$  and the boiling number  $Bo$  defined in equation 1.40 and equation 1.44, respectively. The convective boiling heat transfer coefficient  $h_{cb}$  is calculated from the Dittus Boelter correlation.

Generally speaking, the method is based on the consideration that the surface is fully wetted for vertical tubes at any value of  $Fr_L$ , while for horizontal tubes only if  $Fr_L \geq 0.4$ . For the value of  $Fr_L < 0.4$ , the top part of the horizontal tube surface is defined to be partially dry and the heat transfer coefficient is lower than in vertical tubes.

### 2.4.2 The superposition model

The superposition model assumes that the local flow boiling heat transfer coefficient  $h_{tp}$  is the sum of nucleate and convective boiling components. This relation can be expressed in following form:

$$h_{tp} = E_1 h_{cb} + E_2 h_{nb} \quad (2.49)$$

Such a model has been developed by Chen [9] (1963) and afterwards modified by Gungor and Winterton [22] (1986). A similar type of correlation has been proposed by Jung [28] (1989). In all mentioned models, both multiplying factors have been empirically correlated with the boiling number, the Reynolds number, the Martinelli parameter and the liquid Froude number.

### 2.4.3 The asymptotic model

The asymptotic model assumes that the local flow boiling heat transfer coefficient  $h_{tp}$  is a function of the relative dominance of nucleate boiling and convective boiling. It can be

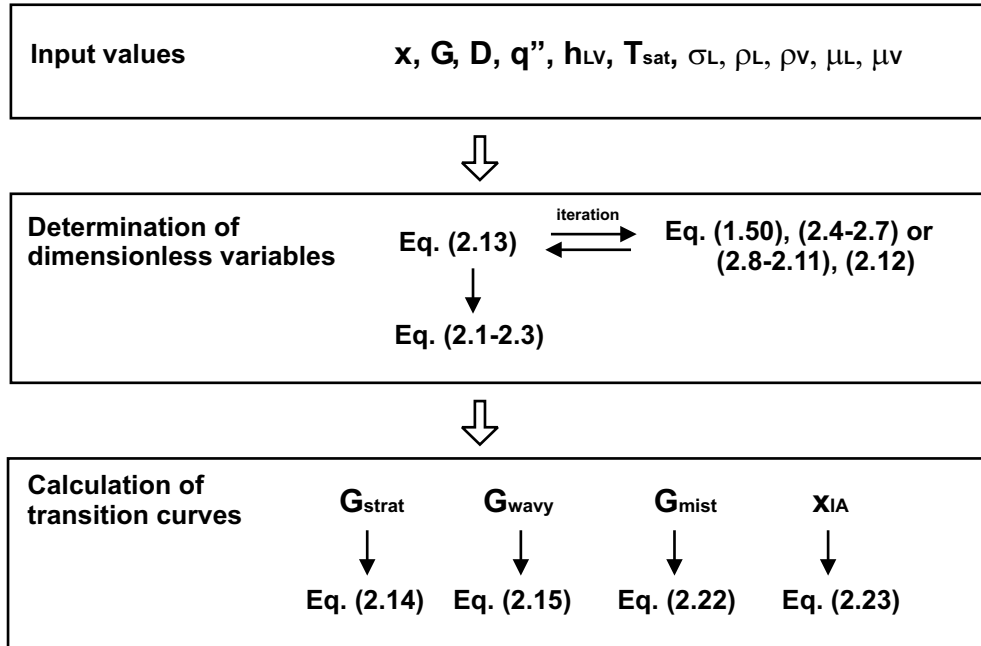
expressed as:

$$h_{tp} = [(h_{cb})^n + (h_{nb})^n]^{1/n} \quad (2.50)$$

Steiner and Toborek [52] (1992) proposed  $n = 3$  based on parametric tests on their database for evaporation in vertical tubes. From indications to date, it is the most accurate vertical tube boiling correlation currently available.

#### 2.4.4 The flow pattern oriented model of Kattan-Thome-Favrat

As a first step in the heat transfer model of Kattan [29] (1996), flow regimes transition curves  $G_{strat}$ ,  $G_{wavy}$ ,  $G_{mist}$  and  $x_{IA}$  have to be calculated according to the scheme presented below:



After determination of the flow pattern map (see section 2.2.1), actual flow regimes can be determined for the specified combination of  $x$  and  $G$ . In the heat transfer model, Kattan *et al.* took into account the fact that in stratified, stratified-wavy and annular flow with partial dryout, heat is transferred partially to the vapor phase on the dry perimeter of the tube. Therefore, they proposed to calculate the heat transfer coefficient for the wet and dry perimeter separately, as:

$$h_{tp} = \frac{\theta_{dry} h_V + (2\pi - \theta_{dry}) h_{wet}}{2\pi} \quad (2.51)$$

where  $h_V$  is the heat transfer coefficient for the dry perimeter defined in the equation (2.41), and  $h_{wet}$  is the heat transfer coefficient for the wet perimeter calculated from the asymptotic model with the exponent  $n=3$  as:

$$h_{wet} = [(h_{L,cb})^3 + (h_{nb})^3]^{1/3} \quad (2.52)$$

Convective boiling heat transfer coefficient  $h_{L,cb}$  is calculated from (2.38) and  $h_{nb}$  is obtained using the Cooper correlation described in equation (2.47).

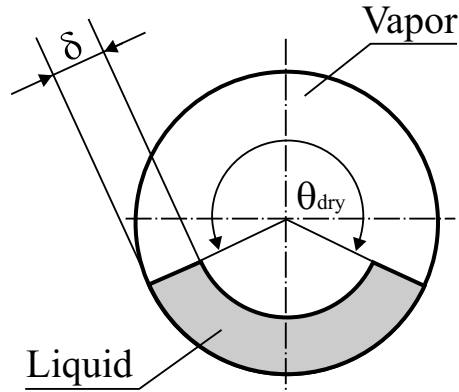


Figure 2.9: Annular flow with partial dryout configuration - Kattan *et al.* [32] (1998c).

The parameter, which takes into account the existence of different flow patterns in equation 2.51, is the dry angle  $\theta_{dry}$  shown in Figure 2.9.  $\theta_{dry}$  defines the flow structure and the ratio of the tube perimeter in contact with the liquid and gas. In stratified flow  $\theta_{dry}$  equals the stratified angle  $\theta_{strat}$  and was calculated by Kattan iteratively from equation 2.40. In this study, the expression of Biberg, equation - 2.35, is used for the  $\theta_{strat}$  calculation, which gives the same results as the prior method and does not require any iteration. It is obvious that for annular and intermittent flows, where the tube perimeter is continuously wetted, that  $\theta_{dry} = 0$ . A more complicated approach is used for prediction of  $\theta_{dry}$  for stratified-wavy flows. For the fixed vapor quality  $x$ ,  $\theta_{dry}$  varies between 0 for  $G_{wavy}(x)$  and  $\theta_{strat}$  for  $G_{strat}(x)$ . Kattan assumed a linear variation of  $\theta_{dry}$  between the annular and stratified flow and proposed the following equation:

$$\theta_{dry} = \theta_{strat} \frac{(G_{wavy} - G)}{(G_{wavy} - G_{strat})} \quad (2.53)$$

The model of Kattan was developed from a database including results for five refrigerants, containing over 1100 new experimental points for tube diameters of 12.00 and 10.92 *mm* in

a vapor quality range varying from 15 to 100%. The mean deviation of the new plain tube correlation of Kattan is 13.3%, the standard deviation is 16.8% and the average deviation is 2%. The correlation was confronted with five different existing correlations being particularly more accurate for the flow regimes with partially wetted tube walls.

### 2.4.5 The onset of nucleate boiling criterion

Zürcher [72] (2000) proposed to calculate an onset value of the heat flux at which boiling nucleation occurs. He modified the Steiner-Taborek criterion by introducing a more realistic convective boiling heat transfer coefficient as:

$$q_{ONB} = \frac{2\sigma T_{sat} h_{cb,crit}}{r_{crit} \rho_V h_{LV}} \quad (2.54)$$

where  $h_{cb,crit}$  is the convective heat transfer coefficient occurring during evaporation at the current vapor quality, and at the most advantageous location in the liquid cross-section. As convective boiling is inversely proportional to the liquid thickness, the onset of the nucleate pool boiling should occur at the location where the liquid thickness is the largest. Thus, the critical convective boiling heat transfer coefficient is defined as:

$$h_{cb,crit} = C \cdot \text{Re}_\delta^m \cdot Pr_L^{0.4} \cdot \frac{\lambda_L}{\delta_{crit}} \quad (2.55)$$

where the values of the two components  $C=0.01361$  and  $m=0.6965$  are based on experimental results of pure convective heat transfer in annular flow (only slightly different than those found by Kattan *et al.*). Based on the geometrical representation of the flow patterns, the critical layer thicknesses are as follows:

- for stratified flow:

$$\delta_{crit,Strat} = \frac{D}{2} \left( 1 - \cos \frac{\theta_{wet}}{2} \right) \quad (2.56)$$

where all parameters of stratified configurations are defined in Figure 2.10



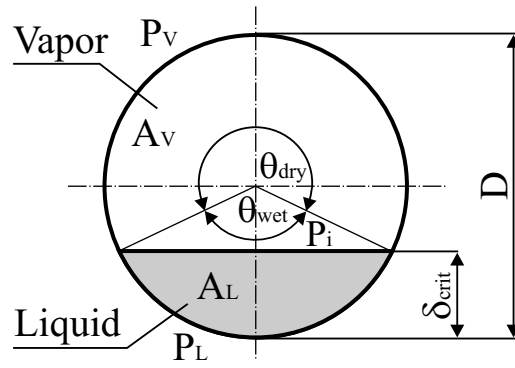


Figure 2.10: Cross-section of stratified configurations.

- for stratified-wavy flow:

$$\delta_{crit,Wavy} = \frac{D}{2} \left( 1 - \frac{\cos \psi + \cos \varphi}{1 + \cos(\psi - \varphi)} \right) \quad (2.57)$$

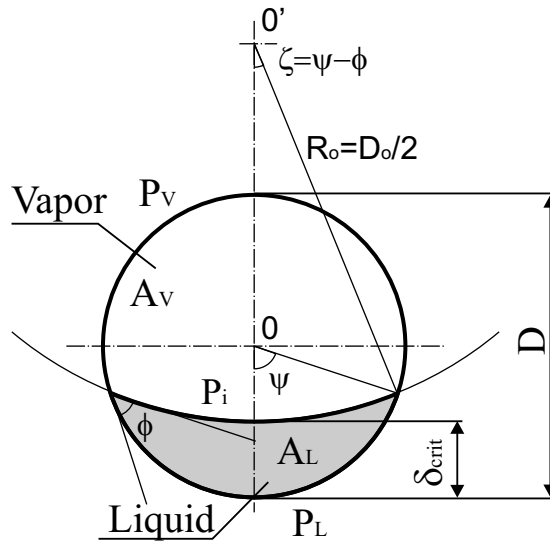


Figure 2.11: Modeling of the stratified-wavy flow pattern.

As shown in Figure 2.11 the liquid cross-sectional area is modeled using two circles which are parameterised as a function of half wetting angle  $\psi$  and the moon angle  $\varphi$ . The difference between those two angles is called stratified-wavy angle  $\xi$ .

- for annular flow:

$$\delta_{crit,Annular} = D - d = D (1 - \sqrt{\varepsilon}) \quad (2.58)$$

According to the configuration shown in Figure 2.12 twice the mean liquid layer is chosen as it corresponds to the thickest liquid layer in annular horizontal flow. But

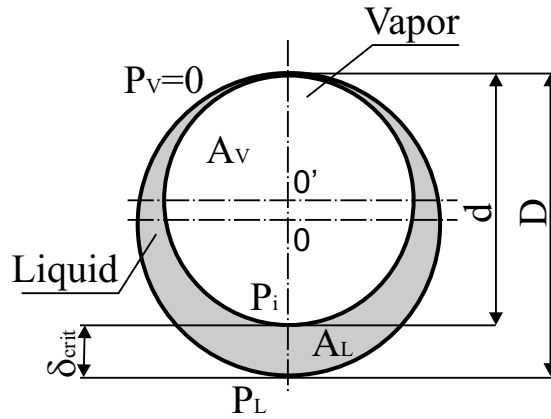


Figure 2.12: Cross-section of ideal annular configuration.

still with twice the liquid layer, the calculated onset of nucleate boiling value was higher than most experimental heat fluxes of Zürcher.

- for intermittent flow Zürcher proposed to use the same approach as for stratified flow for the critical liquid layer thickness determination.

Based on the experimental database, Zürcher set the critical bubble radius to  $r_{crit} = 0.38 \cdot 10^{-6} \text{ m}$ .

When the onset of nucleate boiling heat flux is obtained, the liquid heat transfer coefficient can be calculated from the asymptotic model defined in equation 2.52

With these considerations, the onset of the nucleate boiling value is easily reached for stratified, stratified-wavy and partially for intermittent flow patterns.

## 2.5 Conclusion

The main flow regimes encountered in adiabatic and diabatic horizontal two-phase flow have been presented. To predict transition between the individual flow regimes, Kattan *et al.* [30] (1998a) modified the flow pattern map of Steiner [58] (1993) taking into account the diabatic effect of heat flux. The map of Kattan *et al.* has been verified by Zürcher *et al.* [73] (2002) for the lower mass velocities in stratified and stratified-wavy flows. The final version of the map, proposed by Thome and El Hajal [55](2002), recommends use of Rouhani-Axelsson void fraction model for all transition curves and to use the expression of Biberg defined in equation - 2.35, instead iteration of equation 2.40 for  $\theta_{strat}$  calculation. The effect of heat

flux in the prediction of the onset of dryout varies for each presented map and needs to be further investigated.

Principal heat transfer mechanisms and models have been described. Extensive comparison of existing models to a complete database covering different flow types done by Kattan [29] (1996) shows that only flow pattern map based heat transfer models can be seriously considered. The new model proposed by Kattan was a major improvement over previous two-phase flow heat transfer predictions. This approach has been continued by Zürcher, who with his study also covered the stratified flow zone and verified a flow pattern oriented model for R-717. He also proposed a new onset of nucleate boiling criterion for flow boiling heat transfer calculations. Even if the method proposed by Kattan greatly improves the prediction of the flow boiling heat transfer, it has not been tested extensively for high mass velocities. He was not able to obtain a heat transfer database covering the mist flow region nor the transition between annular and mist flow. The method also shows some inaccuracies for the stratified-wavy flow conditions. Hence, further work is called for to more thoroughly investigate these points and they are the objectives of this thesis.



# Chapter 3

## Void fraction measurements

For the further development of the two-phase flow heat transfer model based on the flow pattern map, we need to extend our knowledge about flow structures. Our particular interest is focused on stratified types of flows where the existing model of Kattan *et al.* shows more inaccuracies compared to tests results than other regimes. This model is based on some assumptions concerning the flow geometries. The heat transfer coefficient is calculated separately for the wetted and dry perimeter of the tube. For stratified-wavy flow, which is encountered between intermittent/annular and stratified flow, a linear variation of the mean dry angle is assumed. To improve our scientific approach on the two-phase flow, new information concerning dynamic void fraction, dry angle, liquid interface and wave frequencies are required. In view of this need, the evaporator test section has been equipped with a dynamic void fraction measurement system, which allows us to obtain the definition of flow structures simultaneously with the heat transfer measurements. Before presenting a newly developed method to measure void fraction, the other used techniques will be reviewed.

### 3.1 Review of the void fraction measurement methods

#### 3.1.1 Monofiber optical probe technique

An optical probe is sensitive to the change in the refractive index of the surrounding medium and is thus responsive to liquid-vapor interfacial passages enabling measurements of local void fraction and of interface passage frequencies even in non conducting fluids.

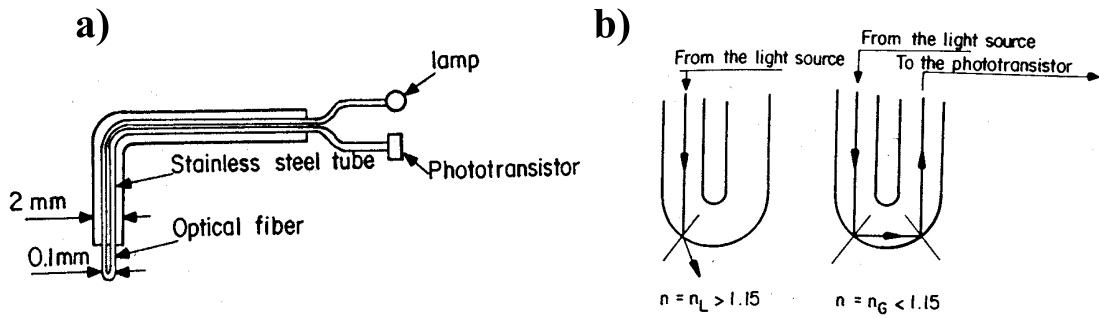


Figure 3.1: a) U-shaped fiber optical sensor; b) Active part of the fiber optical sensor.

A tiny optical sensor was first proposed by Danel and Delhaye in 1971. The overall configuration of the U-shaped optical probe and its active part is shown on Figure 3.1. Signals from the probe are analysed through an adjustable threshold that enables the signal to be transformed into a binary signal.

Fiber optical probes are used in experimental studies of the void fraction distribution in two-phase flow, multi-phase-fluid discrimination and gas velocity measurements. Spindler and Hahne [51](1998) used a fiber optical probe to measure the radial distribution of void fraction and bubble frequency of adiabatic water/air two-phase flow in an inclined tube. Fordham et al [17] (1999) demonstrated the use of a novel design of a fibre-optic sensor for immiscible-fluid discrimination in multi-phase flows. Characterisation of the performance of optical probes in void fraction measurements is shown by Cartellier [6] (1990). Cartellier [7] (1998) also presented measurements of the gas phase characteristics in air/water flows, where he obtained the void fraction with a relative error less than 10%.

### 3.1.2 Radiation attenuation techniques

Phonon attenuation methods measure the chordal and area void fraction. They are frequently used in void-fraction and film thickness measurements and can provide information on the flow pattern. A beam of monochromatic collimated phonons of incident intensity  $I_o$ , traversing a substance of thickness  $\delta$  and density  $\rho$ , has an emerging intensity  $I$  given by the following exponential absorption law:

$$I = I_o \exp \left( -\frac{\mu}{\rho} \rho \delta \right) \quad (3.1)$$

where  $\rho/\mu$  is the specific absorption coefficient of the material. To have a reference, it is necessary to measure intensities  $I_V$ , and  $I_L$ , corresponding to the channel filled with gas and liquid, respectively. The instantaneous line void fraction is then easily obtained from the following relation:

$$\varepsilon_{Ch} = \frac{\log(I/I_L)}{\log(I_V/I_L)} \quad (3.2)$$

Figure 3.2 and 3.3 show the practical application of the neutron attenuation technique to measure liquid height and cross section void fraction.

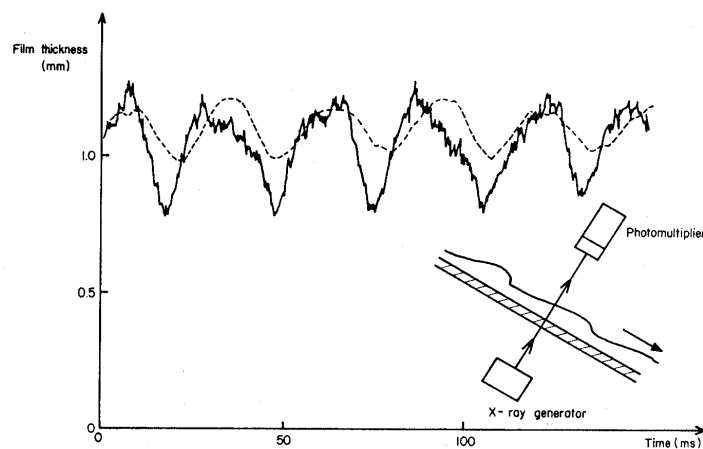


Figure 3.2: Measurements of instantaneous liquid height with the X-ray absorption technique.

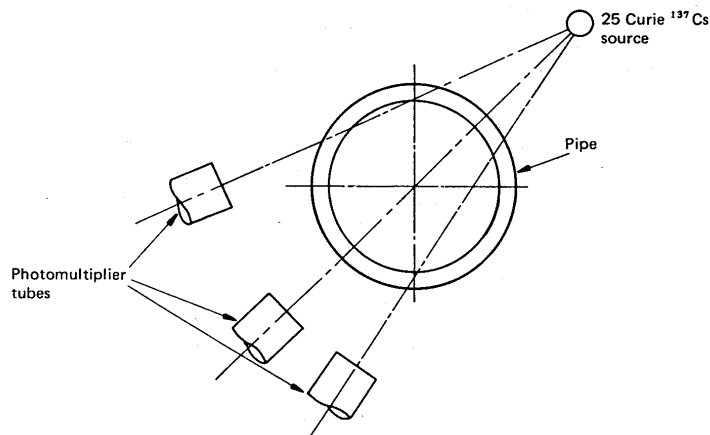


Figure 3.3: Area void fraction measurements with three-beam gamma densitometer.

Radiation techniques are nonintrusive options for improving our understanding of the details of transient two-phase flow structure. Static tests for a water/air mixture made by Kendoush [34] (2001) show that the uncertainty in the radiation technique is a function of X-ray energy. The relative error for the different X-ray energies for the reference void fraction is shown in Figure 3.4.

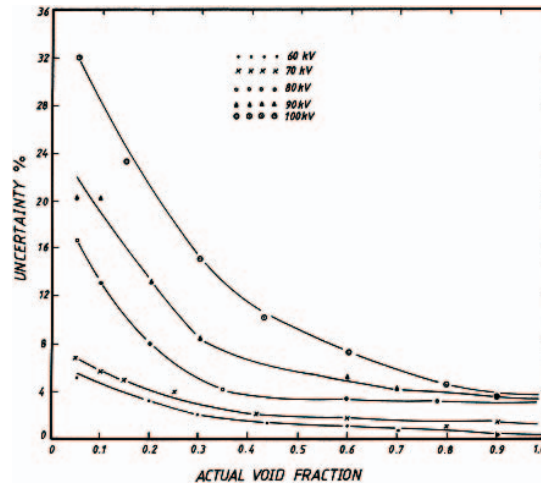


Figure 3.4: The uncertainty in void fraction for various X-ray energies and a fixed tube current of 4 mA from Kendoush [34] (2001).

As can be seen in the Figure 3.4, the best accuracy was obtained for the X-ray energy 60kV. The relative error is 5% for void fractions lower than 0.1. For higher void fractions the relative error is about 2%. The recent studies utilise more advanced radiation techniques, such as a real time neutron radiography (RTNR) and X-ray computed tomography (X-CT). Both of these methods were used by Harvel [25] (1999) to obtain a two-dimensional void fraction distribution.

### 3.1.3 Electrical techniques

The first requirement to be met when using an electrical probe in a two-phase flow is that one phase has a significantly different electrical conductivity from the other. Consequently, variations in conductance permit the measurement of the local void fraction and the arrival frequency of the bubbles at a given point in a continuous, conducting fluid. Figure 3.5 shows the classical electrical diagram of a resistive probe and a typical probe geometry. To identify the cross-sectional void fraction, a wire-mesh sensor can be used. This method is based on the local conductivity measurement of the mixture between the gap of a crossed electrode



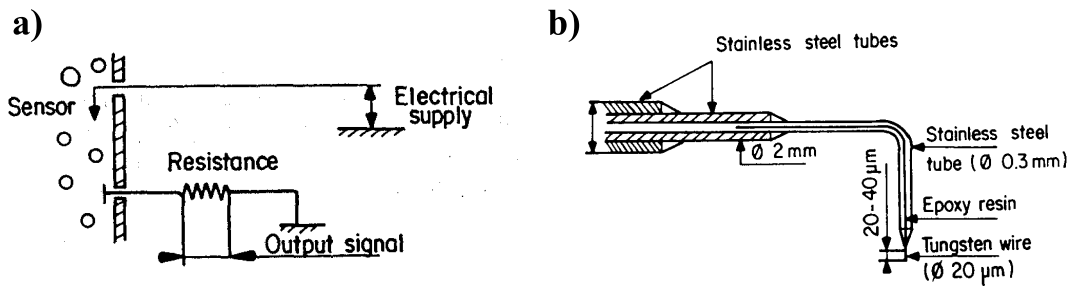


Figure 3.5: a) Electrical diagram of a resistive probe, b) Miniature probe geometry.

pair  $90^\circ$ . Richter [44] (2002) used a wire mesh sensor to measure the local instantaneous gas velocity and void fraction in a rectangular channel. This method was also used by Krepper *et al.* [36] (1999). They used a matrix of fine wires (0.120 mm diameter) extended as a grid across a 51.20 mm internal diameter tube, to obtain 242 local measurements points. Using this method, they achieved maximum errors of  $\pm 0.05$  over the entire range of void fraction. The void fraction in a two-phase mixture can be determined by measuring the impedance of a mixture if a significant difference in the electrical properties exists between two-phases. This nonintrusive technique was used by Costigan and Whalley [13] (1997) and by Song [50] (1998). Costigan and Whalley obtained particularly good agreement at void fractions below 0.30 in a 32.00 mm internal diameter acrylic tube for water/air flow. For a void fraction range between 0.3 and 0.6 the meter indicated values from 0.01 to 0.05 higher than the measured value. The most uncertain zone was the void fraction range between 0.6 and 0.8 where the inaccuracy was higher than 0.1. Figure 3.6 shows the impedance probe arrangement used by Costigan and Whalley.

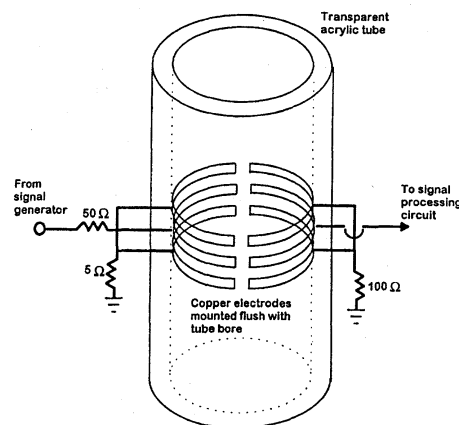


Figure 3.6: Void fraction impedance probe arrangement of Costigan and Whalley [13] (1997).

### 3.1.4 Comparison of the existing methods

Void fraction measurements techniques can be classified as intrusive and nonintrusive. Intrusive methods may adversely disturb the flow field and induce imperfect identification of the liquid interface. This is the main problem in using the monofiber optical technique and electrical resistive probe measurements. For the tests with high pressure refrigerants like R-410A, it would be very difficult to seal numerous intrusive parts in the test section. In our evaporation tests, undisturbed flow pattern observation is required. Also, the information obtained from local probes would not be sufficient to reconstruct the interface between gas and liquid. Nonintrusive methods like radiation techniques and impedance measurements yield mean void fraction values of the cross-section. Using these results we can not determine neither the dry angle nor the shape of the interface between gas and liquid. More sophisticated nonintrusive methods such as a real time neutron radiography (RTNR) and X-ray computed tomography (X-CT) allow the measurement of the distribution of void fraction. These two methods seem to be the most appropriate for our evaporating tests of all presented techniques. The high speed X-CT enables reconstruction of two-dimensional cross-sectional images taken at frequencies up to 250  $Hz$ . The results obtained by Harvel et al [25] (1999) using X-CT system for a slug flow are presented in Figure 3.7. The RTNR technique allows

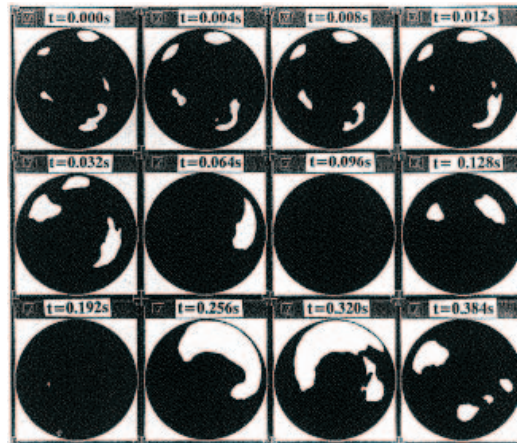


Figure 3.7: Real-time void distribution of developing slug flow for a gas flow rate at 10 l/min by an X-CT method from Harvel et al [25] (1999).

determination of lateral void fraction with respect to time. The accuracy of RTNR and X-CT methods is dependent upon many factors including source strength and geometry. Harvel et al [24](1996) showed that the two techniques agreed to within 4%. However, both methods require enhanced radiation protection systems. A lead shielding has to be used in

the case of X-rays and water/concrete in the case of neutrons. Hence, this method is not appropriate for application to our flow boiling test facility.

## 3.2 A new optical method to measure void fraction

### 3.2.1 Measurement strategy

As has been mentioned in the introduction, the main objective of the new optical technique is to measure cross-sectional void fraction by determination of the ratio of area occupied by gas to the total area of the channel. For this purpose, a borosilicate glass tube has been installed at the end of the heat transfer measurement test section. The external diameter of the glass tube is  $16.00\text{ mm}$  and the wall thickness is  $1.20\text{ mm}$  (with a very uniform thickness and roundness, *i.e.*  $\pm 0.02\text{ mm}$ ). Before installation, the glass tube was tested up to an internal pressure of  $5\text{ MPa}$  (one-half of its maximum recommended working pressure). The optical set-up scheme is presented in the Figure 3.8. A perpendicular cross-section of the glass tube and fluid within are illuminated by a laser sheet (using a Spectra Physics laser, Millennium II), and the images are recorded by a digital camera (Panasonic CCD camera type GP-LM7/TA) located above the glass tube with a vision angle of  $40^\circ$  with respect to the axis of the tube. The laser sheet is about  $0.50\text{ mm}$  thick. The wavelength emitted by the laser is  $532\text{ nm}$  and interlaced images are recorded on a Pentium 3 PC through a Targa Video card.

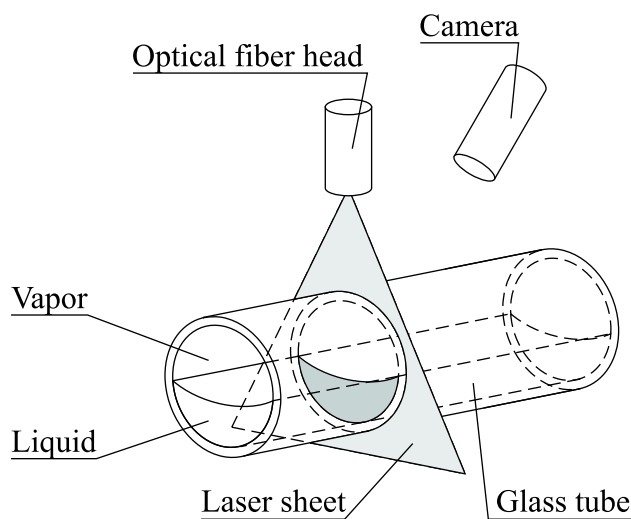


Figure 3.8: Schematic of the optical set-up.

The recorded image, representing a cross-sectional view of the two-phase flow, is distorted by the refraction of the light through both sides of the glass (internal and external surfaces). Thus for void fraction measurements to be made, this technique requires reconstruction of field of the vision to obtain a non-deformed, orthogonal view of the illuminated cross-section. This reconstruction is based on the optical distortion of a regular grid placed inside the glass tube in the same plane as the laser sheet during preliminary tests without any liquid in the tube. The process consists of extracting an inverse transformation function, which is applied to the distorted grid image in order to obtain an image of a regular grid (see next section). This function is applied in the same way to the video images of the two-phase refrigerant flowing in the tube. The transformation, however, is only valid for the cross-sectional fraction occupied by a gas under the condition that the gas-phase is in direct contact with the upper wall of the tube. Therefore, for a fully annular flow the optical deformation of the gas area no longer corresponds to the one on the grid. The presence of a liquid film on the upper wall induces a new deformation of the image depending on the refractive index of the liquid. For this reason, the new technique is only applicable to stratified types of flow. Furthermore, the transformation is only valid in the gas phase above the vapor-liquid interface and not below into the liquid phase (where the light is again refracted). Finally, the locus of the interface is detected using image processing, giving the ratio of the area occupied by the vapor phase with the total cross-sectional area, *i.e.* the instantaneous void fraction as a function of time.

From a practical point of view, the grid is printed on a glossy paper, which is fixed on a stopper introduced inside the glass tube. To avoid regularly opening the refrigerant circuit, a calibration set-up has been manufactured (Figure 3.9). This set-up is made of the same material and has the same geometry and dimensions as the void fraction measurement set-up installed on the flow boiling test facility ( $\pm 0.01$  mm for the machined pieces and both tubes have an internal diameter of  $13.60 \pm 0.02$  mm). It is used to model the optical distortion and to calibrate the interface detection procedure between the gas and liquid (see section 3.4). In order to assure the same conditions during the image acquisition for both test set-ups (illumination and relative position), the optic fiber head and the camera are fixed on the upper support structure of the test facility. Owing to this particular conception and independence, the upper support is positioned along the tube axis. Once the optical alignment of the laser and the camera set-up are made, it remains unchanged whether the upper support is mounted on the calibration set-up or on the flow boiling test facility. The last step is to assure that the upper support structure is precisely horizontal. The image processing program is coded with LabView (version 6i). This particular language provides a

powerful visual interface to the user (graphic and image) allowing a continuous interaction on processing the image. The human eye remains the most useful tool and allows one to quickly focus on the pertinent zones needing further improvement during the development of the image processing technique.

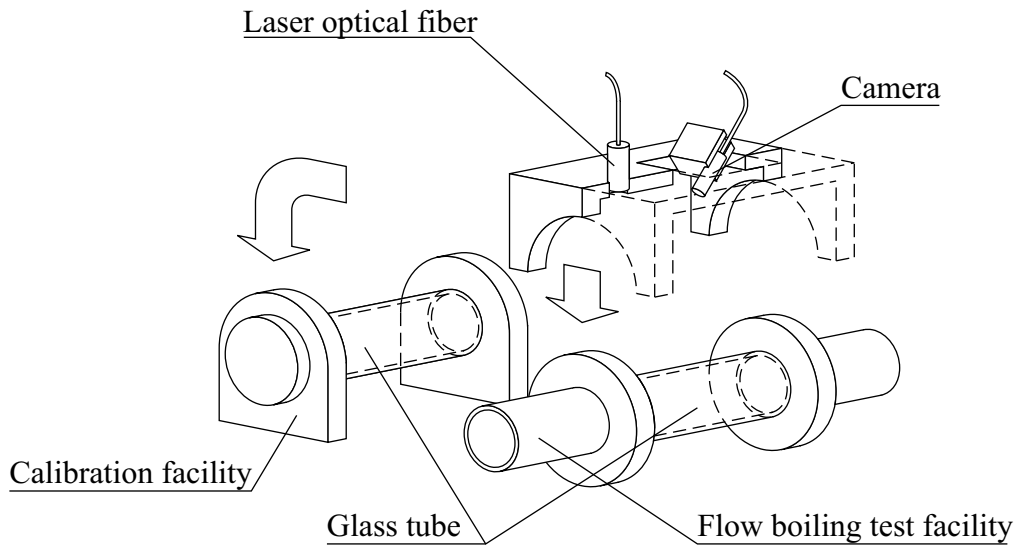


Figure 3.9: Image calibration and video acquisition system set-ups.

### 3.2.2 Transformation of distorted images

#### Detection of the distorted grid

The distorted grid image is converted into an 8-bits encoded image with 256 levels of grey. Due both to the small distance between the camera and the grid (about 3 *cm*) and the vision angle of  $40^\circ$ , the depth of focus is weak, making it impossible to obtain a well-focused image on the total surface of the grid. The focal plane is thus adjusted on the horizontal grid axis in such a way that the lines above and below the axis do not become too blurred. The zones outside of the grid are eliminated by limiting the image size (from 720 x 576 pixels to 430 x 370 pixels) and by adding an elliptical mask to focus only on the internal surface of the glass tube (Figure 3.10). Before adding the mask, the image is inverted (in terms of gray levels) allowing an easier distinction of the grid border. In this way, a black line appears as a white one and vice versa. Optically, two types of distortion can be distinguished on the deformed grid image. Firstly, the bottom part of the grid (under the axis) is vertically compressed (diminution of the space between the horizontal lines), and secondly, the upper

part is horizontally elongated (increasing space between the vertical lines).

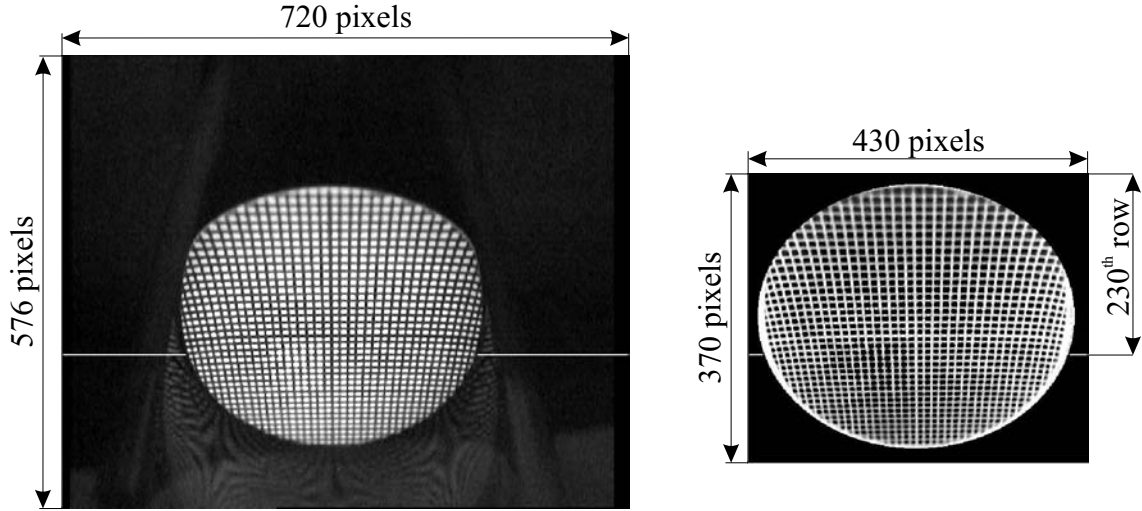


Figure 3.10: Original (left) and limited (right) grid image (the white transversal line corresponds to the 230<sup>th</sup> line, counted from the top on the limited image).

To model the optical deformation, each grid line (vertical and horizontal), must be individually detected. This detection is based on the grey level signal evolution over each pixel row and each pixel column of the image. This signal depends directly both on the line spacing and the line thickness. Numerous grids were thus tested and the choice of a grid having a line spacing of  $0.35\text{ mm}$  (*i.e.* 37 vertical and 37 horizontal lines) and a line thickness of  $0.12\text{ mm}$  ( $0.35\text{ point}$ ) was selected. Figure 3.11 illustrates the variation in the light signal intensity along the 230<sup>th</sup> pixel row ( $1.00\text{ mm}$  above the grid centerline axis). At each extremity the signal is equal to zero, which corresponds to the presence of the mask (black zone). In the center, the signal evolves in a sinusoidal way: each peak corresponds to a vertical line of the grid cut almost perpendicularly by the current pixel row. Therefore by detecting a peak position, one detects a local point of a grid line. Proceeding in this way on each pixel row/column, a collection of spatial points is obtained, which describes all the grid lines. The points of each line are sorted both by proximity and on the *a priori* knowledge of the spatial shape of each line (mainly vertical or mainly horizontal). Qualitatively, the peak thickness is proportional to the line thickness. With the current grid, the peak thickness is between 3 and 5 pixels wide. A thicker line would increase the number of the successive pixels with a high grey level; however, this would not bring more information about the position of one line. Concerning the grid mesh size (line spacing), it fixes the spatial frequency of the signal. A finer size than the one used would risk affecting the difference between the neighboring maximum and minimum values in the grey level signal evolution (*i.e.* diminution of the

sinusoidal amplitude); exaggerating, it means that two successive lines would not be distinguished from each other. Another particular case visible in Figure 3.11 is where a section of the pixel row of the image falls directly on a horizontal line of the grid; in this section, the signal is dominated by the white color of the grid line, yielding small differences between the neighboring maximum and minimum values, and thus does not allow one to distinguish the vertical lines. This implies the introduction of an amplitude threshold, which fixes the minimum difference between a successive maximum and minimum value (experimentally fixed at 40 bits) and below which the peak is considered as useless.

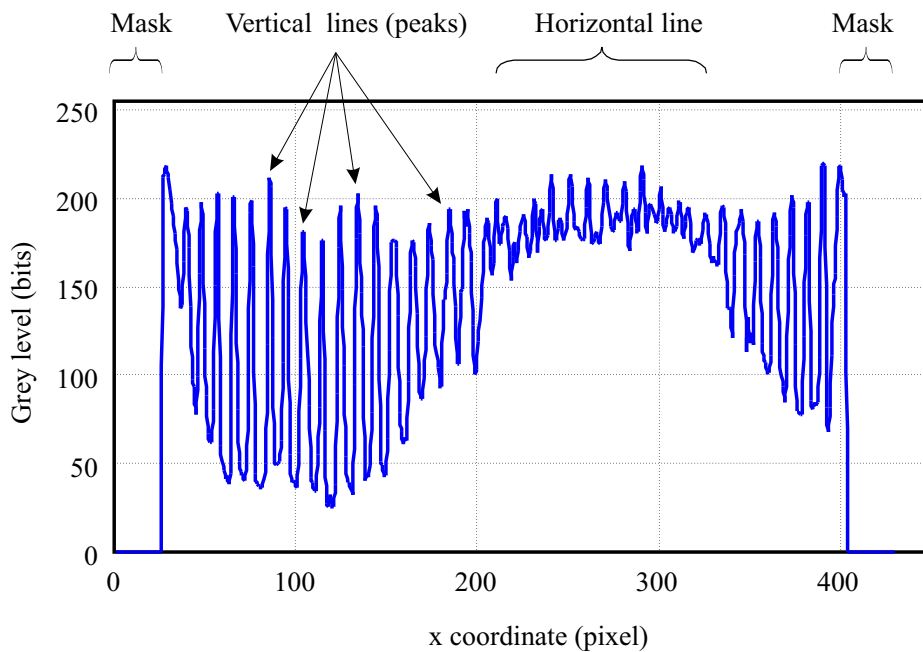


Figure 3.11: Evolution of the grey level intensity along the 230th row of pixels (1.00 mm below the horizontal centerline axis of the grid).

Concerning the detection of the position of a peak, the techniques used in the field of DPIV (Digital Particle Image Velocimetry) for the detection of the correlation peak are used. Thus, according to Westerweel [60] (1997), if the position of the peak is known *a priori* only up to 1 pixel in resolution, the use of the gaussian interpolation functions on the first neighbors of a peak allow the estimation of the peak center to approximately to within  $\pm 0.1$  pixel. However, the extraction of the points describing the different lines can be difficult at the circumference of the grid (the lower differences between the neighboring maximum and the minimum values for  $25 < x < 50$  as in Figure 3.11 and in the bottom part of the grid (small distance between lines due to optical compression as in Figure 3.10). In order to maintain a high quality in modeling the distortion field, a simulation of the camera vision field has

been made. This simulation is based on several hypotheses. Firstly, the refraction of an optical beam passing from one medium to another is perfectly described by the law of sines (Descartes law):

$$n_1 \sin i_1 = n_2 \sin i_2 \quad (3.3)$$

where  $n_1$  and  $n_2$  are the respective refraction indices of the first and second medium,  $i_1$  is the incident angle and  $i_2$  is the refracted angle respectively to the normal component of the plane. Secondly, the digital camera is represented by a table of pixels (having an equivalent or superior size than the effective CCD cell) and is equipped only with a spherical convergent lens. Finally, the path of the light beam is not considered as going from its source point (on the grid) to the receptor (a pixel), but in the inverse direction. Thus, there are two changes in the medium: from air to glass and then from glass to refrigerant vapor. The result of such a simulation is represented in Figure 3.12 and is called a synthetic grid. The resemblance between the real distorted grid and the synthetic distortion is evident: there is a convergence of the horizontal lines below the symmetry axis and a divergence of vertical lines in the upper half.

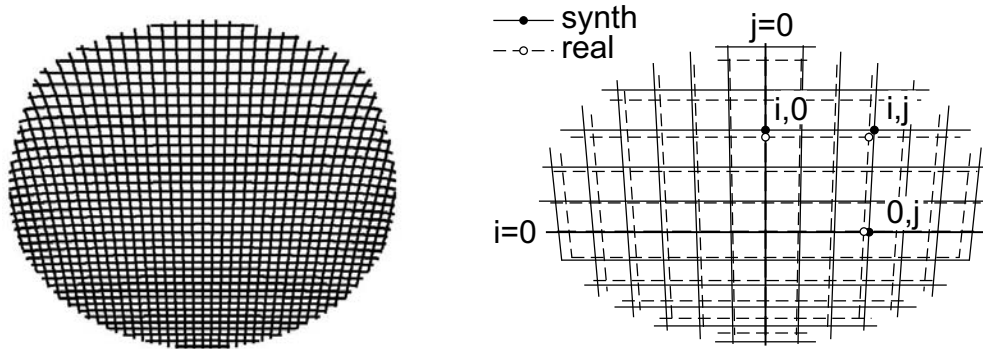


Figure 3.12: Synthetic grid (on the left) and coordinate system (on the right).

Next, the information from both grids is coupled comparing the coordinates of each intersection point with respect to the vertical and horizontal symmetry axis. Isolating the evolution of x-coordinates on a horizontal line and the evolution of y-coordinates on a vertical line, it can be seen that the relationship between the real and the synthetic grid can be described as a second order polynomial function. Now, defining  $i$  as the horizontal line index and  $j$  the vertical line index, one obtains:

$$(x_{synth\ i,j}) - (x_{synth\ i,0}) \cdot [a_0(i) + a_1(i)j + a_2(i)j^2] = x_{real\ i,j} - x_{real\ i,0} \quad (3.4)$$

$$(y_{synth\ i,j}) - (y_{synth\ 0,j}) \cdot [a_0(j) + a_1(j)i + a_2(j)i^2] = x_{real\ i,j} - x_{real\ 0,j} \quad (3.5)$$



where for example,  $x_{real,i,0}$  is the x-coordinate of the intersection point formed by the  $i^{th}$  horizontal line crossing the vertical symmetry axis (line  $j=0$ ). The coordinates  $x_{real}$  and  $y_{real}$  refer to the real image but they are measured values as previously described. The variables set  $a_k(i)$  where  $k = 1, 2$  and  $3$  corresponds to each horizontal line  $i$ , and respectively, each vertical line  $j$  has a variables set  $a_k(j)$ . These variables are extracted by linear regression using a least squares fit. The parameters  $a_k(i)$  and  $a_k(j)$  are thus coupled by tracing the evolution of these variable sets as functions of the horizontal line index, respectively of the vertical line's index. Considering Figure 3.13, it can be stated that each of the three parameters  $a_k(i)$  can be approximated by a first order polynomial function over most of its range. For index values inferior to -10 and greater than +10 (*i.e.* for the 8 first and 8 last horizontal lines), the real/synthetic comparison shows a clearly different behavior. This results directly from the difficulty to detect the lines close to the grid circumference, which was noted previously above. Using a linear regression in the least squares sense with a gaussian weight function (where the width parameter is fixed at 8 to attenuate the extremity influence), we obtain for each parameter  $a_k(i)$  and  $a_k(j)$  a continuous function to describe the geometrical difference between the synthetic and the real grids. From these parameters, the real coordinates of the intersection points can be re-estimated using equations 3.4 and 3.5. This approach acts like a smoothing function without losing the original information and generates a spatial distribution function of intersection points without any inflexion point. The vertical and horizontal lines can thus be described mathematically through new intersection points with cubic spline functions.

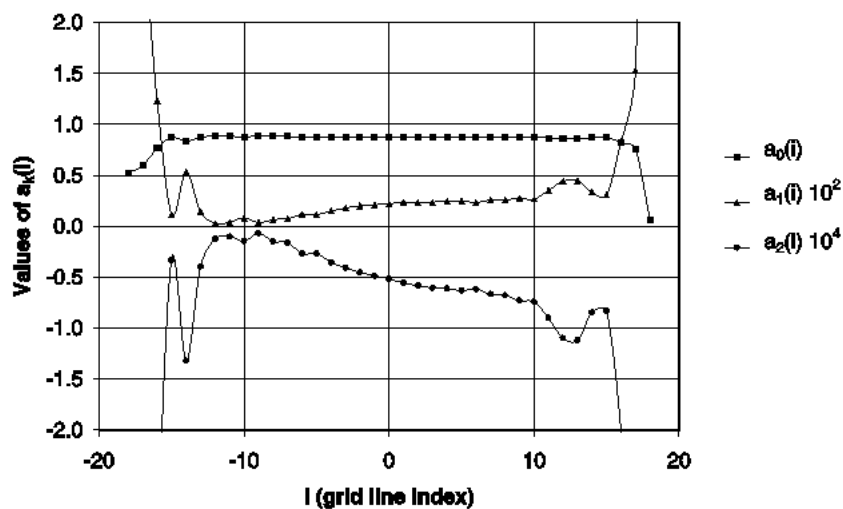


Figure 3.13: "Synthetic-to-real" grid coupling parameters as function of grid line index  $i$ .

The result of these successive operations is illustrated in Figure 3.14. The lines generated from these cubic spline functions correspond visually perfectly to the image of the distorted grid.

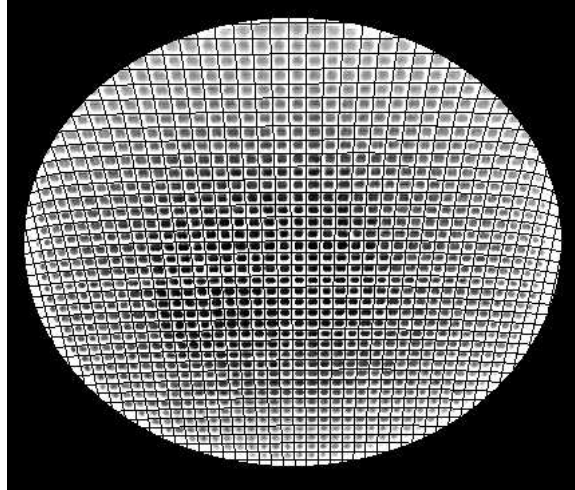


Figure 3.14: Cubic spline functions based on intersection points describing horizontal and vertical grid lines.

Before describing the image mapping process, one can remark that the similarity between the real distorted image and the synthetic grid image also validates the experimental part of the calibration process. As previously specified, the maximum geometrical difference between the glass tube used in the calibration set-up and the glass tube in flow boiling test facility is on the order of  $0.02\text{ mm}$ . Using the simulation and applying it with an internal and external diameter of  $13.58\text{ mm}$  and  $16.02\text{ mm}$ , respectively (instead of  $13.60\text{ mm}$  and  $16.00\text{ mm}$ ), the maximum difference in terms of coordinates is less than  $0.01\text{ mm}$  (*i.e.* less than 0.4 pixel on the image, which is less than the resolution). This confirms that both the glass tube used for calibration and that on the flow boiling facility can be considered identical.

### Image mapping

The transformation of the distorted grid image into one with parallel vertical and horizontal lines is performed in two distinct steps. This first consists of mapping of the points (each point from the distorted space should correspond to a point on the transformed area). The second phase is the reconstruction of the image itself (reconstruction pixel-by-pixel of the grey level signal from the distorted image with respect to the mapping). For the first step, the technique consists in associating the intersection points of the deformed grid to

the intersection points of the regular grid, which should have the characteristic  $y_{transf} = \text{constant}$  on each horizontal line and  $x_{transf} = \text{constant}$  on each vertical line. To simplify, the transformed grid lines are positioned in a way that the coordinates of their intersection points are expressed as integer values (in order to correspond directly to the pixel coordinates). The choice of these coordinates is such that the global size of the transformed image is the same as the original one. In this way, magnification of the image is avoided, which would amplify any defects (for example, crystalline imperfections in the glass tube). Shrinkage of the image, which would induce a loss of resolution in the void fraction measurement, is also avoided. Having fixed the vertical and horizontal coordinates of the transformed grid along with knowledge of the real size of the grid line spacing yields the conversion ratio in pixel/mm. The pixel size of a circular mask corresponding to the internal tube diameter can thus be directly deduced and added to the transformed image. Based on these considerations, the grid is artificially refined to a higher density such that the new grid lines (vertical and horizontal) correspond in size to the pixel grid of the transformed image (the grey level of each pixel can now be determined). Hence, consider the x-coordinates of the intersection points on the distorted lines as a function of the associated x-coordinates of the intersection points on the regular grid. For each horizontal line, a cubic spline function can be constructed. For each intermediate integer value of  $x_{transf}$  (*i.e.* for each pixel), this allows estimation of the corresponding value  $x_{real}$  Figure 3.15.

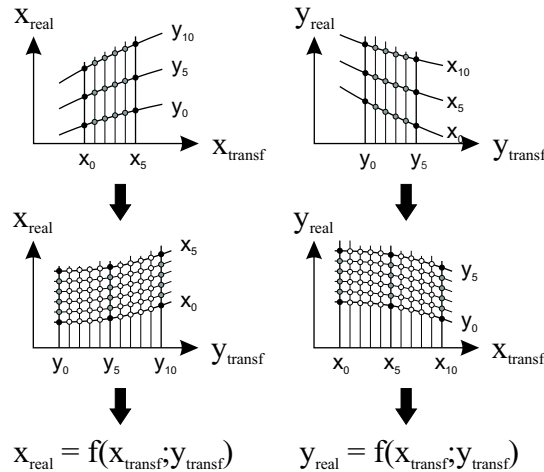


Figure 3.15: Mapping of the coordinates.

In this way, the number of vertical lines is increased. Consider now the same coordinates  $x_{real}$ , but as a function of  $y_{transf}$  coordinates. New cubic spline functions can be constructed for each vertical line, which for each integer value of  $y_{transf}$  allows the estimation of a value

$x_{real}$  on the deformed image. This is the number of horizontal lines, which is increased. Thus, each coordinate couple  $(x_{transf}; y_{transf})$  is associated to an  $x_{real}$  value. Proceeding in a similar way for the coordinates  $y_{real}$ , it is possible to associate each pixel  $(x_{transf}; y_{transf})$  to a corresponding  $y_{real}$  value.

Finally, the simplest technique is used to reconstruct the image pixel by pixel. A pixel  $(x_{transf}; y_{transf})$  receives the intensity of the distorted image pixel containing the corresponding point  $(x_{real}; y_{real})$ , which are not integer values. More sophisticated techniques have been tested, such as the weighted surface mapping technique proposed by Huang *et al.* [27] (1993), without improving accuracy (void fraction measurement error was not influenced by the mapping technique). In addition, through its simplicity, this technique is the fastest one. Taking into account the large number of images to process, this choice is totally justified. The result of this new operation is illustrated in Figure 3.16. Looking in the plane of the drawing, the horizontal and vertical lines in the transformed grid image are nearly perfectly straight and parallel to one another.

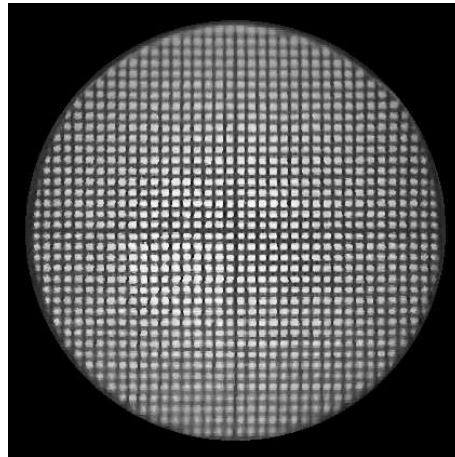


Figure 3.16: Transformed grid image.

### 3.2.3 Vapor-liquid interface detection technique

To detect the vapor-liquid interface, two problems need to be resolved. The first one concerns the optical highlighting of the interface (in the visible domain) and the second one is the strategy to systematically detect this interface with image processing.

### Interface highlighting

As specified in the Measurement strategy section, a laser sheet is used to illuminate the cross-section of the two-phase fluid flowing in the tube. Due to the transparency of the refrigerants tested (R-22 and R-410A), the laser light is absorbed neither by the vapor phase nor the liquid phase and there is no luminescence in the cross-section. Therefore, the presence of a fluorescent in the liquid phase is required to obtain a satisfactory illumination effect. The term luminescence refers to the light emitted by molecules when returning from an electronically excited state to the ground state. In our case, the excited state is produced by the laser light with a wavelength of 532 *nm*. The excited state of a molecule decays to the ground state under emission of light typically within 0.1 to 20 *ns*. Because the period of time during which a molecule remains in its excited state is relatively long, numerous interactions with other species can occur within its lifetime. These include vibrational relaxation and re-orientation in the dielectric field of the solvent, both causing energy to be partially lost. As a result, the luminescence of all organic molecules occurs at longer (less energetic) wavelengths than excitation. For our tests, rhodamineB (produced by Fluka) has been chosen as the fluorescent powder. This fluorescent, when brought to an excited state by the laser light, emits a wavelength of about 627 *nm* for a maximum absorption at 554 *nm*. The refrigerant properties at flow boiling conditions should not be influenced by the presence of the fluorescent powder and thus only a trace amount of rhodamineB is added to the refrigerant. This means that the minimum concentration of the fluorescent for the image processing procedure has to be determined. Both the calibration set-up (static tests) and the flow boiling facility (dynamic tests) are used to fix this concentration, but dynamic tests are more important: firstly, the fluorescent molecules are excited for a shorter time period than in a static conditions (the excitation duration is the time for the molecules to flow across the laser sheet) and secondly, the concentration in the flow boiling test facility is not constant (due to partial evaporation of the liquid in the test section and the consequent concentrating of rhodamineB in the remaining liquid). Based on trials with different amounts of fluorescent powder, the minimum concentration was defined to be about 1 molecule of rhodamineB per 100 million molecules of refrigerant and its potential influence on the refrigerant properties was tested during the calibration procedure (described in next section). Concerning the experimental set-up during the tests, many rays of the laser sheet were reflected by the tube. Moreover, the dynamic tests include a flow induced roughness at the vapor-liquid interface, which produced overexposed images due to the laser light reflections. To reduce the negative effect of excess reflections, an optical filter is directly fixed on the CCD camera. This optical filter is

a combination of six filters especially used for eye-protection glasses for working with Nd:Yag lasers (in terms of Optical Density:  $OD > 9$  at  $190 - 520 \text{ nm}$ ,  $OD > 7$  at  $520 - 532 \text{ nm}$ ,  $OD > 3$  at  $710 - 750 \text{ nm}$ ,  $OD > 5$  at  $750 - 850 \text{ nm}$ ,  $OD > 7$  at  $850 - 1080 \text{ nm}$  and  $OD > 7$  at  $5000 - 11000 \text{ nm}$ ).

### Calibration procedure

To calibrate the new optical measurement technique, a reference measurement of the void fraction  $\varepsilon_{ref}$  is needed. As indicated above, the calibration set-up is used for this purpose and is equipped with a pressure transducer and a thermocouple (both calibrated inhouse). A micro-valve is also installed allowing for the introduction or removal of a precise quantity of the tested refrigerant mixed beforehand with rhodamineB. Each new quantity corresponds to a new reference void fraction. Considering the whole volume of the system (glass tube + circuit through pressure transducer and micro-valve), the void fraction of the system can be expressed as:

$$\varepsilon_T = \frac{\rho_L - \rho_T}{\rho_L - \rho_V} \quad (3.6)$$

where  $\rho_T$  is the density of the saturated mixture,  $\rho_L$  is the density of the saturated liquid phase and  $\rho_V$  is the density of the vapor. The pressure transducer allows the calculation of the densities  $\rho_L$  and  $\rho_V$  and is used to estimate the saturated temperature, which is compared to the thermocouple measurement. A maximum difference of  $\pm 0.1^\circ C$  was observed over the total range of the reference void fraction measurements (from 0.05 to 0.95). This simple test confirms that the refrigerant properties do not change in presence of the fluorescent powder. Then, by measuring the total volume of the enclosure  $V_T$  and the mass of the refrigerant  $m_T$  using a gravimetric balance (Mettler Toledo model PR8002, accuracy of  $\pm 0.02 \text{ g}$ ), equation 3.6 can be rewritten as:

$$\varepsilon_T = \frac{\rho_L - \frac{m_T}{V_T}}{\rho_L - \rho_V} \quad (3.7)$$

to give the measured void fraction in terms of  $m_T$  and  $V_T$ . The total volume  $V_T$  is determined by completely filling the internal volume of the calibration set-up with water (after having pulled a high vacuum), and then measuring the temperature of the water (to accurately determine the density) and its mass. The optical measurement of the void fraction concerns

only the level of liquid in the horizontal glass tube. Thus, with respect to the glass tube, the void fraction  $\varepsilon_{ref}$  is given as:

$$\varepsilon_{ref} = 1 - \frac{\rho_L - \frac{m_T}{V_T}}{\rho_L - \rho_V} \cdot \frac{V_T}{V} \quad (3.8)$$

where  $V$  is the internal volume of the glass tube. At each void fraction value, a series of 8 to 10 images of the illuminated cross-section is acquired. The aim is not to take several images of the same state but to vary the laser beam intensity level in order to artificially take into account the changes in concentration of rhodamineB in the flow boiling test facility at the static state (to emulate the dynamic situation). The resulting images are in color and the chosen encoding system is the DSH system (Density, Saturation and Hue) also called HSL (Hue, Saturation and Luminance). The interest of such a transformation is in the simple and intuitive interpretation of the intensity values  $D$  and the two variables of chrominance  $S$  and  $H$ . Considering the present situation, an optical filter is used to eliminate the light reflections from the tube walls and from the free surface, resulting in images where the principal colour is orange. The extraction of the luminance plane yields a sharp contrast between the vapor zone and the liquid zone. It would be quite important if one were using the red plane from the classical RGB encoding system. But concentrating only on the liquid zone, the luminance component is more sensitive to the laser intensity than the red component. Moreover, the variance of the luminance value is weaker than the one of the red values (less than 20 bits for the luminance against 40 bits for the red). However, the contrast between the liquid and vapor zone is not represented by a discontinuous function of the luminance. A typical evolution of a luminance signal is represented in Figure 3.17, with information extracted from the median pixel column of a transformed image corresponding to a void fraction of 55% and a laser intensity level of 61%. The transition from the gas zone in which the luminance  $L$  is on the order of 50 bits to the liquid zone where  $L \cong 200$  bits occurs over 10 to 15 pixels. It is necessary to fix a luminance threshold above which a gas phase is considered present, and inversely, below which there is a liquid phase. In terms of image processing, selecting only one pixel with a luminance above the threshold is sufficient to consider all the contiguous pixels also with a luminance above the threshold as belonging to the liquid cross-sectional area (this corresponds to the well known function called *magic wand*). Thus the upper border of this zone represents the liquid-vapor interface. Selecting all the pixels above this limit but inside the mask, we obtain the representative surface of the vapor phase. Finally, dividing the number of pixels, which represents this vapor phase with the total number of pixels that are inside the mask, one finds the void fraction. Thus, for each luminance threshold selected

(*e.g.*, in the current image shown the luminance threshold ranges from about 50 to 200) there corresponds an unique void fraction value. In fact, changing the luminance threshold controls the height of the interface.

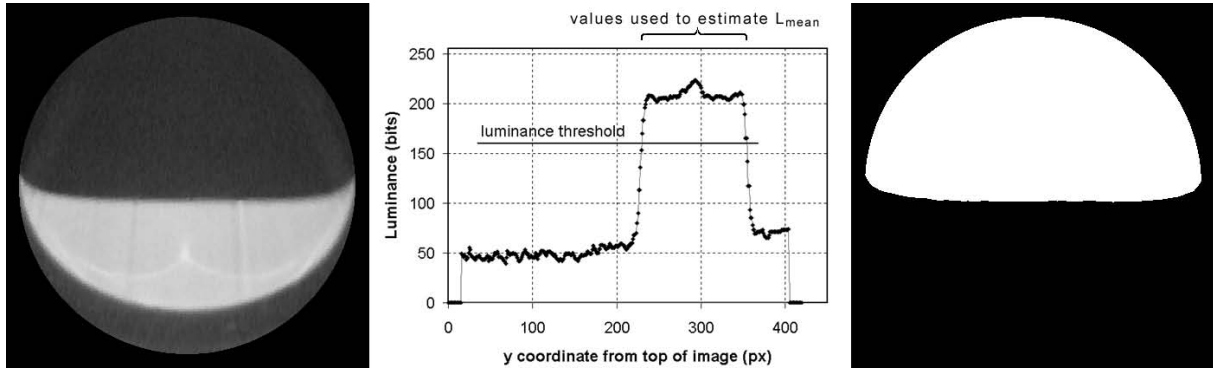


Figure 3.17: Transformed image (luminance plane) of the illuminated cross-section (left), luminance intensity over the median vertical line (center) and extracted vapor zone corresponding to a fixed threshold value (right).

On this basis, considering the reference void fraction as being an exact value, one can study the evolution of the void fraction measured by image processing  $\varepsilon_{ip}$  as a function of the luminance threshold. Thus the luminance threshold to impose on an image is the one that will give  $\varepsilon_{ip}$  equal to  $\varepsilon_{ref}$  (Figure 3.18, on the left). This diagram shows a possible variation in void fraction from  $-0.027$  to  $+0.017$  as a function of the luminance threshold if no calibration procedure was used. However, the image processing program must be able to determine the void fraction no matter the intensity of the image (*i.e.* the intensity of the liquid phase on the image). To distinguish two images in which the void fraction is identical but where the luminance level is different, the program measures the mean luminance  $L_{mean}$  over the liquid phase area for a given threshold (*i.e.* over all contiguous pixels with a luminance value higher than the threshold). Therefore, the calibration technique consists of determining the luminance threshold as a function of both the reference void fraction and the mean luminance over the liquid zone (Figure 3.18, on the right). This is the calibration diagram. During the process, the search of the optimum luminance threshold is determined iteratively. An initial threshold (on the order of 80 bits) allows a first estimation of void fraction and mean luminance. These two parameters are introduced again into the calibration diagram from which a new threshold is taken. A third iteration is necessary and sufficient to achieve a good estimation of the void fraction (see next section). Generally, a fourth iteration only increases processing time without bringing a significant improvement to the measurement.



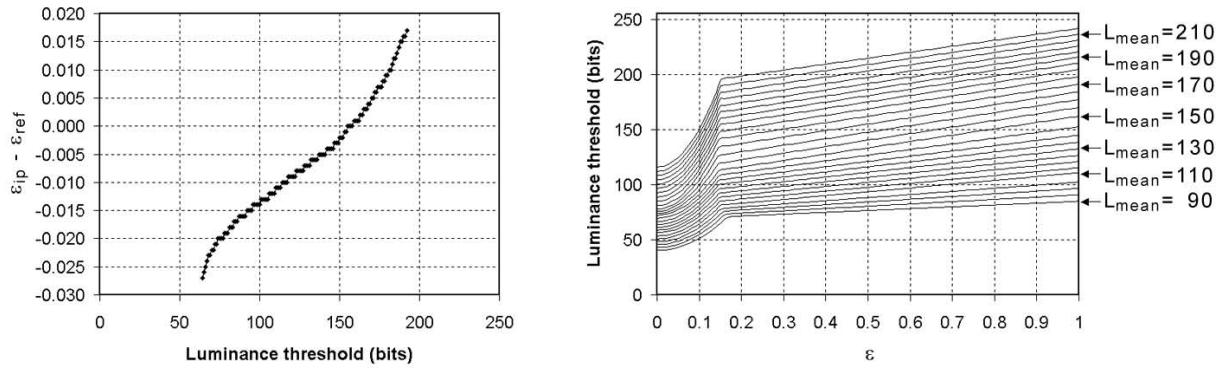


Figure 3.18: Void fraction error in function of the luminance threshold (left) and calibration diagram (right) for the 13.60 mm glass tube.

### 3.2.4 Comparison of technique to static void fraction measurements

Assuming that the static measurement errors are representative of those with flow to determine the characteristic error of this measurement technique, the static calibration images for the glass tube are introduced into the image processing program and analyzed. The differences between  $\varepsilon_{ip}$  and  $\varepsilon_{ref}$  are determined and shown on the Figure 3.19 (on the left). Consequently, the maximum difference between the measured void fraction and the reference void fraction is  $\pm 0.004$ . Statistically, the distribution of the measured errors is slightly biased towards negative values; however, this is not systematically the case. For certain void fractions, the mean error is positive (*e.g.*, for  $\varepsilon_{ref} = 0.05$  or  $\varepsilon_{ref} = 0.40$ ). It must also be mentioned that the reference void fraction also has a certain measurement error,  $\Delta\varepsilon_{ref}$ . As shown in equation 3.8, it depends on five parameters, which are measured experimentally, and two of which depend on the pressure (the saturated vapor density and the saturated liquid density of the refrigerant). Considering these parameters to be linearly independent, an error calculation shows that  $\Delta\varepsilon_{ref}$  does not exceed in its absolute value 0.005 for  $\varepsilon_{ref} = 0.05$  and that  $\Delta\varepsilon_{ref}$  tends to 0.001 for  $\varepsilon_{ref} = 0.95$  (Figure 3.19, on the right). In summary, defining  $\Delta\varepsilon_{ref}$  as the error of the void fraction measured by image processing, it can be said that in the worst case the void fraction measurement error of this new optical technique can be estimated to be  $\Delta\varepsilon = \Delta\varepsilon_{ref} + \Delta\varepsilon_{ip}$  and is on the order of  $\pm 0.01$  over the entire range of void fractions measurable ( $0.05 < \varepsilon < 0.95$ ) for the 13.60 mm glass tube. Applying the same procedure to a 8.00 mm glass tube, the error of the void fraction -  $\Delta\varepsilon$  is on the order of  $\pm 0.03$ .

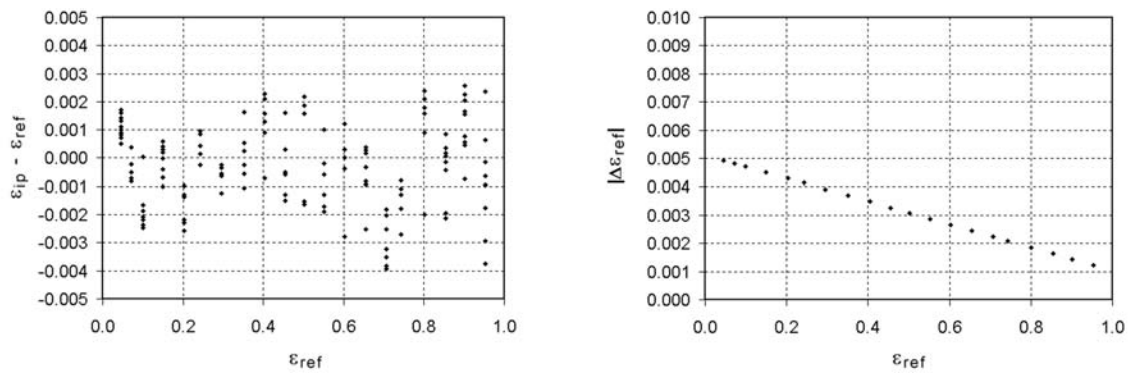


Figure 3.19: Error measurements on calibration images (on the left) and error measurement on  $\varepsilon_{ref}$  (on the right) for the 13.60 mm glass tube.

### 3.2.5 Conclusions

A new optical measurement technique to dynamically measure the cross-sectional void fraction in two-phase flow in horizontal tubes has been proposed, with a description of the practical and theoretical approach of the method, from the realization of an experimental set-up to the image analysis system. This work was developed in parallel with measurements of flow boiling heat transfer coefficients for two refrigerants (R-22 and R-410A). The new method is nonintrusive and allows measurements of the void fraction through a glass tube in a cross-sectional view perpendicular to the flow. It is based on the recording of images of the biphasic fluid illuminated by a laser sheet. With an image processing program, it is possible to compensate for the distortion of the vision area (due to the presence of the tube glass wall) and to reconstruct an orthogonal, non-distorted view of the illuminated section. This reconstruction was developed based on a simulation of the deformation area of the acquired images. The use of a trace concentration of a fluorescent powder in the refrigerant to highlight the interface allows the image processing system to determine the interface vapor-liquid of the refrigerant in order to extract the cross-sectional void fraction. This technique has been optimized for stratified types of flow and yields void fractions with a measured precision in absolute value on the order of  $\pm 0.01$  and  $\pm 0.03$  over the vapor quality range from 0.05 to 0.95 for the 13.60 mm and 8.00 mm glass tube, respectively. This new measurement technique together with void fraction and dry angle measurements are also described in Ursenbacher *et al.* [57] (2004) and Wojtan *et al.* [64] (2004).

# Chapter 4

## Experimental flow boiling test facility

The different test conditions and new measurement methods required the reconstruction of the existing flow boiling test facility used most recently by Zürcher [70] (2001). Two new test sections have been successively implemented into the existing test rig. The present study concerns evaporation in 8.00 *mm* and 13.84 *mm* plain horizontal copper tubes. For both tube diameters, optical set-ups to measure void fraction have been built. To determine the pressure drop separately for each flow regime, an adiabatic section has been installed at the outlet of evaporators. For better accuracy, more thermocouples have been added to determine more precisely the heating-water temperature profile along the test section. A new acquisition system and data processing subroutines written specially for this set-up enabled on-line calculation of the heat transfer coefficient and the vapor quality. This allows the test conditions to be controlled in a more efficient and more precise way. The mist flow tests required higher mass velocities of the refrigerant. Therefore the piping system has been modified to enable the appropriate flow conditions. All modifications have been made on the original test rig developed by Kattan [29] (1996) and modified afterwards by Zürcher [70] (2001).

### 4.1 Description of the flow boiling test facility

The objective of this study was to run in-tube evaporation tests for the following conditions:

Tested fluids	R-410A and R-22	
Heating medium	water	
Internal tube diameter	8.00, 13.84	<i>mm</i>
Saturation temperature	5.0	<i>°C</i>
Vapor quality ( $x$ )	0-1.0	–
Void fraction ( $\varepsilon$ )	0-1.0	–
Mass velocities ( $G$ )	70-700	<i>kg/m<sup>2</sup>s</i>
Heat fluxes ( $q$ )	6.0-57.5	<i>kW/m<sup>2</sup></i>

The measurements of such a large mass velocity range required two pump-to-preheater channels of different diameters. Also, to obtain a satisfactory accuracy it was necessary to use two different sizes of flow meters. The maximum operating pressures were much higher than in previous tests. For the saturation temperature of  $5^{\circ}C$ , the saturation pressure is  $9.30\text{ bar}$  and  $5.84\text{ bar}$  for R-410A and R-22 respectively. Like in the tests of Kattan [29] (1996) and Zürcher [70] (2001), the test facility consists of a refrigerant loop and a heating water loop enabling intube evaporation for the conditions specified above.

### 4.1.1 Refrigerant loop

Figure 4.1 shows a simplified layout of the refrigerant test loop. The refrigerant first passes through a series of horizontal electrical preheaters and then through an insulated tube without any sharp elbows. Then, the refrigerant enters the tubular test section and is heated by a counter-current flow of hot water in the annulus of the double pipe system. The void fraction is measured at the outlet of the test section as shown, and the refrigerant then goes through a condenser, a magnetically driven gear type of pump (oil free) and finally, a Coriolis mass flow meter together with its inlet and outlet temperatures. There are two pump-to-preheater channel diameters, which can be chosen depending on the required mass velocity in the test section. The choice of two diameters also provides more flexibility to reach steady state conditions over the range of mass velocities. As can be seen in the Figure 4.1, there are also two flow meters, which can be independently used to obtain better accuracy for the required operating flow rates. The circuit also includes a vapor-liquid reservoir for controlling the amount of refrigerant in the circuit and thus the operating pressure.

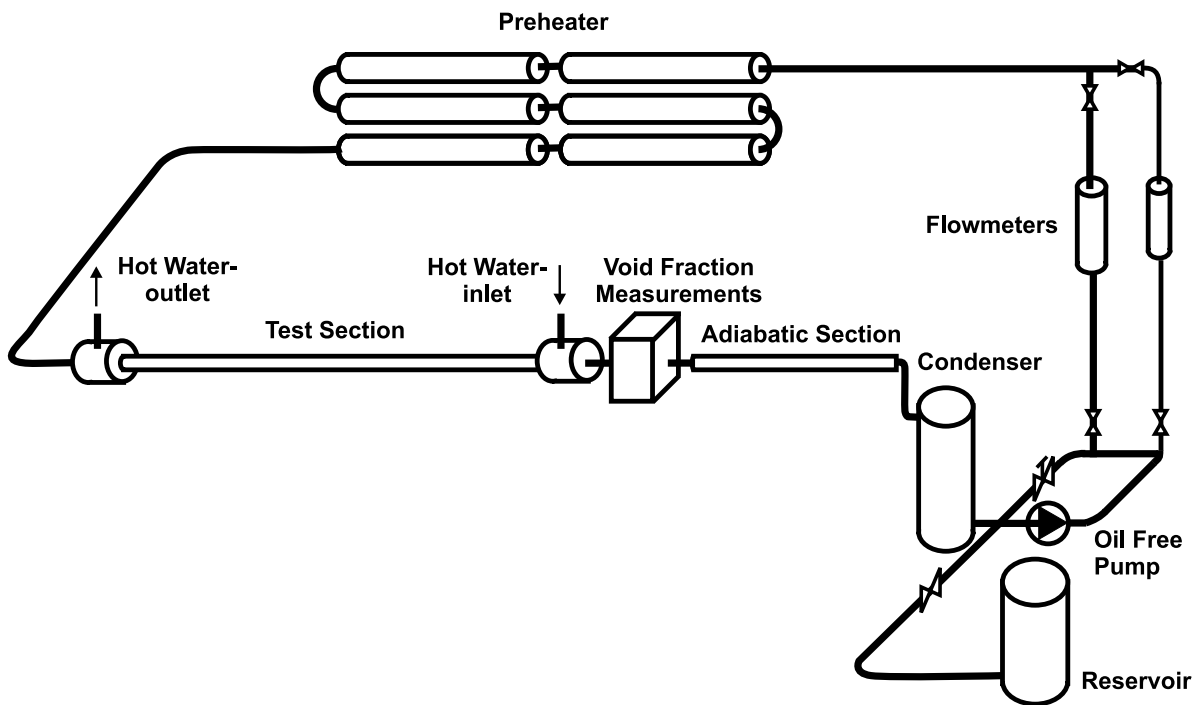


Figure 4.1: Simplified layout of the refrigerant test loop.

### Gear pump and piping

The gear pump provided stable flow of the refrigerant in the range from  $0.15 \text{ kg/min}$  to  $10 \text{ kg/min}$ . The regulation of the flow can be done either by the by-pass of the pump or by pump motor frequency variation. Both gears are made of the nickel-molybdenum-chromium alloy (HASTELLOY C-276). To avoid the presence of any oil in the installation, a magnetic drive has been used. There are two channels to choose from, which connect the pump with the preheater. The internal diameters of the pump-to-preheater channels are  $6.00 \text{ mm}$  and  $10.00 \text{ mm}$ . For the flows below  $1 \text{ kg/min}$ , the  $6.00 \text{ mm}$  channel was used. On each pump-to-preheater channel there is a precise Coriolis flowmeter. The accuracy of the flow meters is  $0.15\%$  of the measured value. The nominal measurement points are  $1.5 \text{ kg/min}$  and  $10 \text{ kg/min}$  for the small and the big flowmeter, respectively. All channels are thoroughly insulated to avoid heat gain from surroundings. The pump-to-preheater channels are fixed according to the flowmeter manuals to maintain steady measurement conditions. Refrigerant temperature is measured at the preheater inlet for the purpose of vapor quality calculation at the outlet of the preheater.

### Preheater

The electrical preheater is composed of six horizontal stainless steel tubes with a hot wire 10.00 *m* long and 3.00 *mm* in diameter coiled around each tube. The internal and external diameters of the tubes are 13.00 *mm* and 16.00 *mm* respectively. The length of each tube is 1.40 *m*. To guarantee an uniform heat transfer, the hot wires are covered with a sprayed copper layer. Each hot wire of the preheater tube supplies 3.5 *kW*, which results in a maximum heat flux of 61.2 *kW/m<sup>2</sup>*. The preheater was constructed and used by Zürcher [70] (2001), in his tests, which required high heat fluxes due to the large latent heat of ammonia. The preheater was not changed from to his experimental work. Thermocouples are installed on each tube of the preheater to prevent operation in critical heat flux (CHF) conditions. Thus, the power supply is shut down when the wall temperature exceeds 25°C. The values of the critical heat flux were calculated from the correlation of Katto [33] (1984) for each test condition and are presented in the Tables 4.1 and 4.2.

Mass Flow ( <i>kg/m<sup>2</sup>s</i> )	CHF for R-22 ( <i>kW/m<sup>2</sup></i> )	CHF for R-410A ( <i>kW/m<sup>2</sup></i> )
70	7.16	7.06
150	14.46	14.28
300	27.42	27.13
500	43.96	43.64
700	54.29	46.85

Table 4.1: Critical heat flux for the measurements in the 13.84 *mm* test section.

Mass Flow ( <i>kg/m<sup>2</sup>s</i> )	CHF for R-22 ( <i>kW/m<sup>2</sup></i> )	CHF for R-410A ( <i>kW/m<sup>2</sup></i> )
100	3.62	3.59
200	6.86	6.76
350	11.49	11.34

Table 4.2: Critical heat flux for the measurements in the 8.00 *mm* test section.

The values of the critical heat flux were not exceeded in our evaporation tests. For more technical details of the preheater, please refer to Zürcher [70](2001).

### Test sections

Two new test sections have been constructed for the intube evaporation tests. The small and large test sections have internal diameters of 8.00 and 13.84 *mm*, respectively. Both tubes

are made of copper and have plain, smooth interiors. The heated lengths are 2.035 *m* and 2.026 *m* for the 8.00 *mm* and 13.84 *mm* evaporator, respectively. The outer stainless steel annulus has an internal diameter of 14.00 *mm* for the small test section and 20.00 *mm* for the large test section. The internal tubes are perfectly centered within the outer annulus tube in five positions using centering screws. The external surface of annulus was well insulated for both test configurations to prevent heat gains from the surroundings. The main properties and geometrical dimensions of the constructed tubular evaporators are shown in Table 4.3.

	Test Tube					Outer Annulus Tube			
	Mat.	$D_{ext}$ (mm)	$D$ (mm)	$z_t$ (mm)	$\lambda$ (W/mK)	Mat.	$D_{ext}$ (mm)	D (mm)	$\delta_{wat}$ (mm)
small section	Cu	9.53	8.00	2035	339	SS	17.40	14.00	2.235
large section	Cu	15.87	13.84	2026	339	SS	23.00	20.00	2.065

Table 4.3: Main properties and geometrical dimensions of the test section.

where:  $D$  is the internal diameter of the tube,  $D_{ext}$  is the external diameter of the tube,  $z_t$  is the total heated length,  $\lambda$  is the thermal conductivity and  $\delta_{wat}$  is the annular gap for the heating water.

A complete schematic diagram of the heat transfer test section is shown in Figure 4.2. The refrigerant enters the copper tube at the left and leaves at the right, and flows into the sight glass. The hot water enters the annulus at the right of Figure 4.2 and leaves at the left. Four thermocouples at the inlet (123, 124, 125, 126) and four thermocouples at the outlet (101, 102, 103 and 104) are placed in the heads of the test section and are used to measure the respective mean inlet (T1water) and outlet temperatures of the water (T5water). There are eighteen more thermocouples (from 105 to 122) creating three additional measurement positions of the mean temperature of the water in the annular channel. These are T2water, T3water and T4water in Figure 4.2. The thermocouples have a diameter of 0.5 *mm* and the thermocouple tips are fixed 0.3 *mm* radially from the wall of the tested tube. Five mean water temperatures form four measurement zones ( $z_1, z_2, z_3, z_4$ ) of the length as specified in Table 4.4. These temperatures allow calculation of the enthalpy profile over the whole length of the tube used in the local heat transfer measurement.

The inlet and outlet temperatures and pressures of the refrigerant are obtained as well. Energy balances over the preheater and test section give the vapor quality at the position of the local heat transfer measurement and at the entrance of the sight glass. All thermocouples

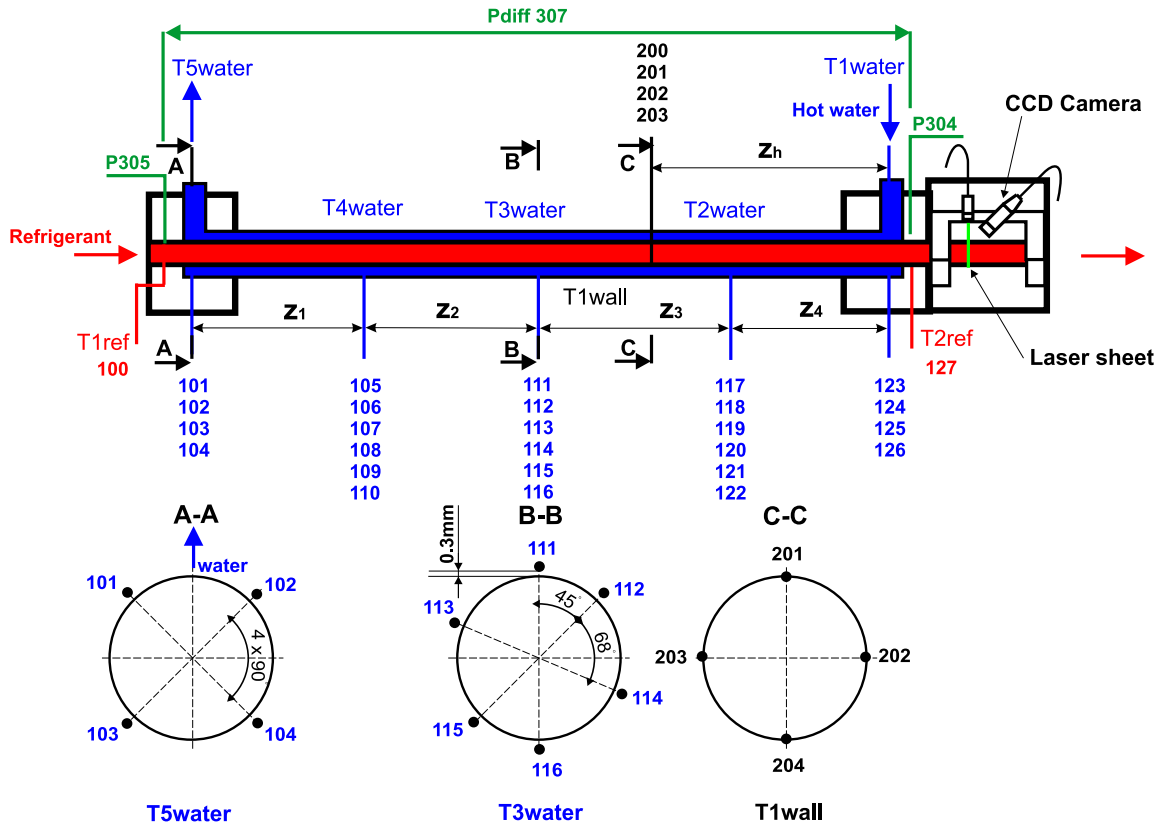


Figure 4.2: Test section of the flow boiling test facility with the void fraction measurement set-up (cross-section A-A: water thermocouple alignment in heads of test section; cross-section B-B: water thermocouple alignment in the three central positions; cross-section C-C: wall thermocouple alignment in the heat transfer measurement position).

were carefully and accurately calibrated *insitu* to an accuracy of  $\pm 0.02^\circ\text{C}$  compared to two precision thermometers of Omega Engineering, model DP251, placed at the entrance and out of the channel during calibrations. The saturation temperature was calculated from the measured saturation pressure using the EES (Engineering Equation Solver) thermophysical property subroutine program and verified with two thermocouples that measure the refrigerant temperature at the inlet and outlet of the test section. A computerised data acquisition system was used to record all data and to insure that steady-state conditions were reached. The criterion for steady-state conditions is the refrigerant saturation temperature, which should not change more than  $\pm 0.05^\circ\text{C}$  during an acquisition. Differential pressure is measured over the test section. To ensure that the results are not influenced by the exit piping, an adiabatic test section has been installed after the void fraction measurement set-up (see Figure 4.1). The length of this test section is 1.0 m and its internal diameter corresponds to that of the tested tube.



	$z_1$ (mm)	$z_2$ (mm)	$z_3$ (mm)	$z_4$ (mm)	$z_h$ (mm)
8.00 mm test section	610	570	500	355	510
13.84 mm test section	600	570	504	357	500

Table 4.4: Main geometrical dimensions of the test section.

### Condenser and cooling group

After evaporation in the test section, the refrigerant enters a stainless-steel shell and tube condenser, where it is condensed and subcooled. Condensation takes place inside the stainless steel tubes and the chilled liquid receives the heat. The main dimensions of the condenser are specified in the Table 4.5.

Number of tubes	165
Tube length	1.5 m
External diameter of tube	6.35 mm
Internal diameter of tube	4.55 mm
Total area of heat exchange	5 m <sup>2</sup>
Internal diameter of the shell	175 mm
Total length of the shell	800 mm

Table 4.5: Main geometrical dimensions of the condenser

### 4.1.2 Heating water loop

The hot water flows counter-currently to the evaporating refrigerant in the annulus of the test section. The water is reheated after it passes through the test section to maintain a constant heat flux during evaporation. The operating pressure of the water is 2 bar. As has been pointed out in the objectives of this experimental work, local heat fluxes range from 6.0 to 57.5 kW/m<sup>2</sup>. The heat flux is directly dependent on the inlet water temperature, which is controlled by two secondary water circuits using two plate heat exchangers. They are connected with a hot water circuit from the heater and an industrial cold water circuit. The layout of the water circuit is presented in Figure 4.3.

During evaporation tests at  $T_{sat} = 5^\circ C$ , the inlet water temperature varied from 7°C to 21°C for the heat fluxes 6.0 to 57.5 kW/m<sup>2</sup>, respectively. To maintain the mixing of the heating

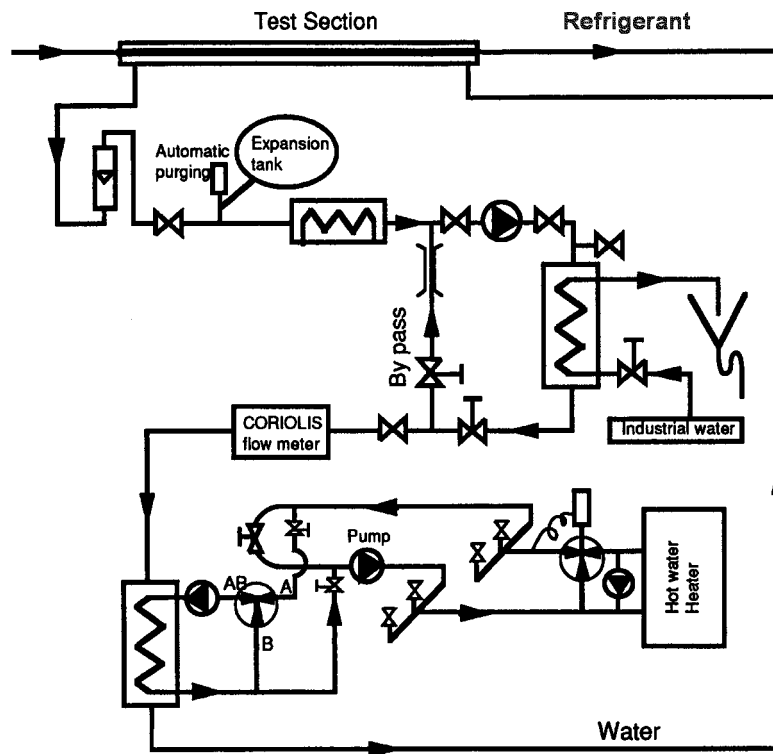


Figure 4.3: Layout of the heating water loop.

liquid in the annular chamber, the laminar flow condition has been avoided. The values of the Reynolds numbers for water flow at the two extreme temperatures are presented in the Table 4.6

	$T_{wat} = 7^{\circ}C$	$T_{wat} = 21^{\circ}C$
8.00 mm test section	7738	11230
13.84 mm test section	4500	6531

Table 4.6: The values of Reynolds number for the heating water in the annulus.

The heating water circuit has not been changed since the evaporation tests of Kattan [29] (1996) and was successfully used during these experimental studies.

## 4.2 Heat transfer measurements

One of the main objectives of this work is to determine the local convective heat transfer coefficient over the vapor qualities range from 0 to 1. The ideal situation would be to

measure the heat transfer coefficient directly at the required position without any intrusive elements in the test section. To accomplish this, the external temperature of the tube wall was measured to avoid additional calculation of the waterside heat transfer coefficient. With knowledge of the temperature of the refrigerant and the value of the local heat flux at the inner wall of the tube, the refrigerant local heat transfer coefficient was determined from Newton's law of cooling:

$$h = \frac{q}{T_{wall} - T_{sat}} \quad (4.1)$$

### 4.2.1 Waterside wall temperature

Four thermocouples have been installed on the external wall of each tested tube (200, 201, 202, 203 as shown in Figure 4.2 cross-section C-C) to measure the mean wall temperature  $T_{wall}$ . The local heat transfer measurement location was located 1.525 m and 1.526 m from the refrigerant inlet for the 8.00 mm and 13.84 mm test section, respectively. The wall thermocouples were only 0.25 mm in diameter. They were placed in 15.00 mm long and 0.25 mm deep grooves on the outside surface of the tube. Figure 4.4 shows the details of the waterside wall thermocouples alignment. As can be seen, the thermocouples are situated in the intersection points of horizontal and vertical axes with the external tube perimeter. They are brazed into the grooves of the tube to assure precise contact with the tested tube. The surface is then polished so as not to disturb the water flow. The local heat transfer coefficient was measured in the axial position of cross-section A-A.

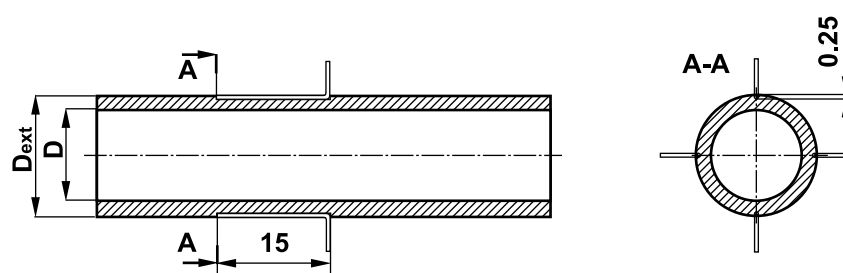


Figure 4.4: Waterside wall thermocouples alignment in the heat transfer measurement position.

Like the water thermocouples, the waterside wall thermocouples were calibrated to an accuracy of  $\pm 0.02^\circ C$  compared to the reference thermometer (again *insitu*). To determine a local mean temperature value of the tube, it is very important to apply numerous thermocouples at different perimeter positions of the tube wall since the temperatures around the

circumference of the tube can vary significantly depending on the particular two-phase flow regime. Figure 4.5 shows the evolution of the temperature difference between the top and the bottom of the tube for three mass velocities. At the mass velocity  $G = 300 \text{ kg/m}^2\text{s}$ , the evaporation occurs under annular flow conditions, where the whole tube perimeter is wet. The mean temperature difference around the circumference of these tube for this conditions equals to  $0.12^\circ\text{C}$  and is not significant.

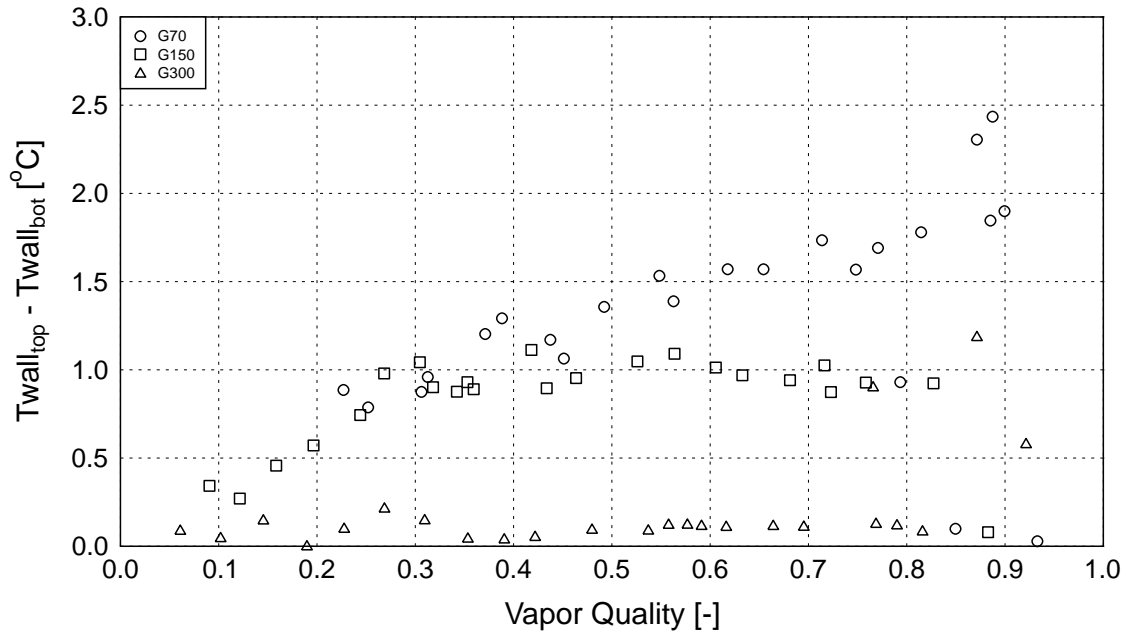


Figure 4.5: The difference between temperature of the top and bottom tube wall thermocouple for R-22 tests,  $D = 13.84 \text{ mm}$ ,  $T_{sat} = 5^\circ\text{C}$  for three mass velocities  $G = 70, 150$  and  $300 \text{ kg/m}^2\text{s}$ .

In the evaporation tests at mass velocities  $G = 70 \text{ kg/m}^2\text{s}$  and  $G = 150 \text{ kg/m}^2\text{s}$  the refrigerant flows in a stratified-wavy flow regime. The top part of the tube remains dry and is intermittently wetted by the high amplitude waves. This phenomenon is encountered with the mass velocity  $G = 150 \text{ kg/m}^2\text{s}$ , where the mean difference in temperature between the top and the bottom tube equals to  $1^\circ\text{C}$  for the vapor quality ranging from 0.25 to 0.9. At the mass velocity  $G = 70 \text{ kg/m}^2\text{s}$ , the temperature difference changes almost linearly over the vapor quality range of 0.2 to 0.95. It equals  $1^\circ\text{C}$  for the vapor quality 0.2 and rises to  $2.5^\circ\text{C}$  for vapor quality of 0.9. This increase of temperature difference is caused by the increasing value of the dry angle as a function of the vapor quality. Even if some low amplitude waves occur, the amount of the tube perimeter that is wetted decreases as the refrigerant vapor quality increases. This confirms that for the stratified types of flows, the mean wall temper-

ature value can not be determined accurately with the single wall thermocouple alignment. Thus, using four 0.25 mm thermocouples around the circumference of the tube at the heat transfer measurement cross-section gives well-defined local mean wall temperature value over whole tube perimeter.

Figure 4.6 shows the test tube with the installed wall thermocouples. At the local wall temperature measurement position, the annular chamber is split into two parts so the thermocouple leads pass through the water and out past the O-ring seal. Only the left part of the annulus is shown in Figure 4.6. Both parts are connected using six screws, where an O-ring maintains a leak-free seal.

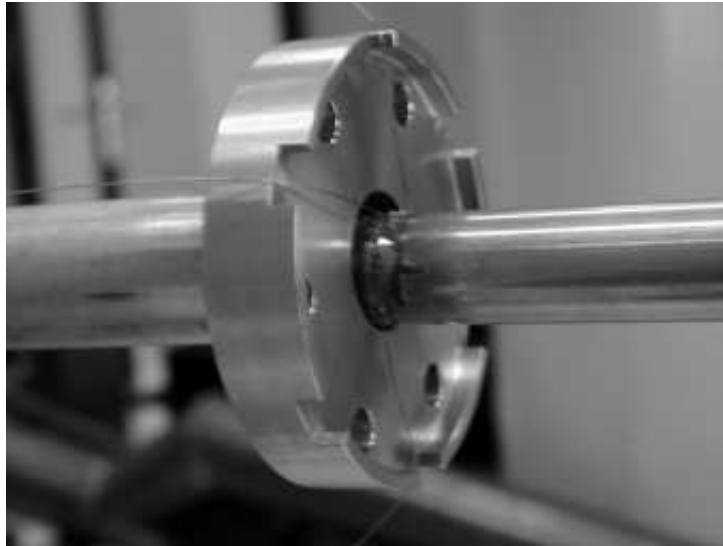


Figure 4.6: Tested tube with the waterside wall thermocouples in the annular chamber of the test section.

### 4.2.2 Temperature of refrigerant

The saturation temperature of the refrigerant core  $T_{sat}$  is calculated using the pressure measurements at the inlet (P305) and the outlet (P304) of the test tube. Figure 4.2 shows the pressure transducer arrangement in the test section. As can be seen in Figure 4.7, the saturation pressure  $P_{local}$  of the refrigerant in the heat transfer measurement position is determined by the assumption of a linear pressure distribution over the length of the test section as is typical in such tests and is calculated using equation 4.2.

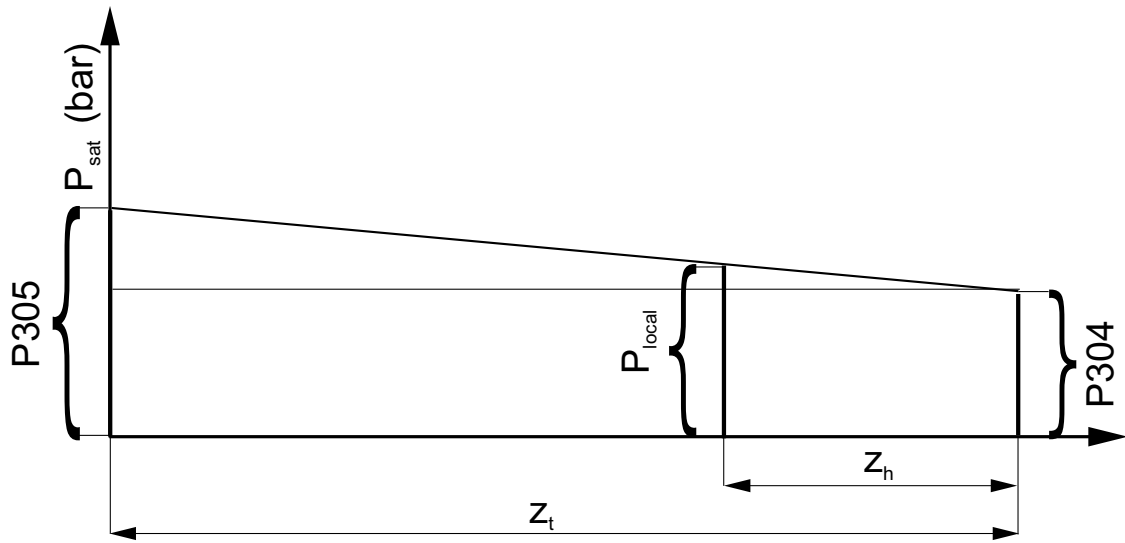


Figure 4.7: Distribution of the pressure over the test section.

$$P_{local} = \frac{z_h}{z_t}(P305 - P304) + P304 \quad (4.2)$$

where:  $z_h$  is the heat transfer measurement position,  $z_t$  is the total test section length,  $P305$  is the absolute pressure at the inlet of the test section and  $P304$  is the absolute pressure at the outlet of the test section.

Finally, the saturation temperature  $T_{sat}$  is obtained for the calculated  $P_{local}$  based on the thermodynamical properties calculated using EES (linked to REFPROP 6.0 of NIST).

The saturation pressures  $P305$  and  $P304$  are measured using precise pressure transducers, which were calibrated with a very accurate balance over the range from 1 to 25 *bars*. After calibration, the values of both pressure transducers installed in the test section were compared in a static pressure test. The pressure was varied from 1 to 13 *bars* and the absolute difference in the measured values between of both transducers was always less than 20 *mbar*.

The saturation temperatures of the refrigerant at the inlet and the outlet of the test section were measured with two probe thermocouples (100, 127), the tips of which were centered within the tube, measuring the refrigerant temperature directly. These values agreed closely with those obtained from the measured inlet and outlet absolute pressures.

### 4.2.3 Local heat flux

The heat is transferred from the hot water to the refrigerant. The temperature of the water is measured in five positions with 26 thermocouples giving five mean water temperatures values  $T_{wat}$ . The water thermocouples arrangement is shown in the cross-sections A-A and B-B in Figure 4.2. As can be seen, the inlet and the outlet mean water temperatures are measured by four thermocouples in each position and the mean water temperatures in the water annulus by six thermocouples (multiple thermocouples are used to get an accurate mean value). The enthalpy of the water, assuming that the pressure drop along the annular chamber is negligible, is given for any location along the tube by equation 4.3:

$$h_{wat} = c_{p wat} \cdot T_{wat} \quad (4.3)$$

where  $h_{wat}$  is the enthalpy of water,  $c_{p wat}$  the water specific heat and  $T_{wat}$  is the mean water temperature.

From equation 4.3, five discrete enthalpy values were obtained for the five measurements points. These points were used to determine the enthalpy profile over the whole test section length. Figure 4.8 shows the enthalpy profile for R-22 evaporation tests at four different mass velocities ( $G = 70, 150, 300$  and  $500 \text{ kg/m}^2\text{s}$ ), for  $x = 0.5$ ,  $T = 5^\circ\text{C}$  and  $q = 7.5 \text{ kW/m}^2$ . For the enthalpy profile determination, a second order polynomial fit has been used. It shows a good agreement with the experimental points.

The heat transferred from the water between two points of the test section can be defined as:

$$Q_{12} = (h_{wat2} - h_{wat1})\dot{M}_{wat} \quad (4.4)$$

The derivative with respect to axial position of equation 4.4 divided by the tube perimeter gives the external heat flux  $q_{ext}$  along an elementary length  $dz$ .

$$q_{ext}(z) = \frac{1}{\pi D_{ext}} \frac{dQ}{dz} = \frac{\dot{M}_{wat}}{\pi D_{ext}} \left( \frac{dh_{wat}(z)}{dz} \right) \quad (4.5)$$

Thus, knowing the enthalpy profile  $h_{wat}(z)$ , the external heat flux can be calculated at any point along the tested tube. For the calculation of the local heat transfer coefficient on the refrigerant side, an internal heat flux is used. The internal local heat flux provided to the

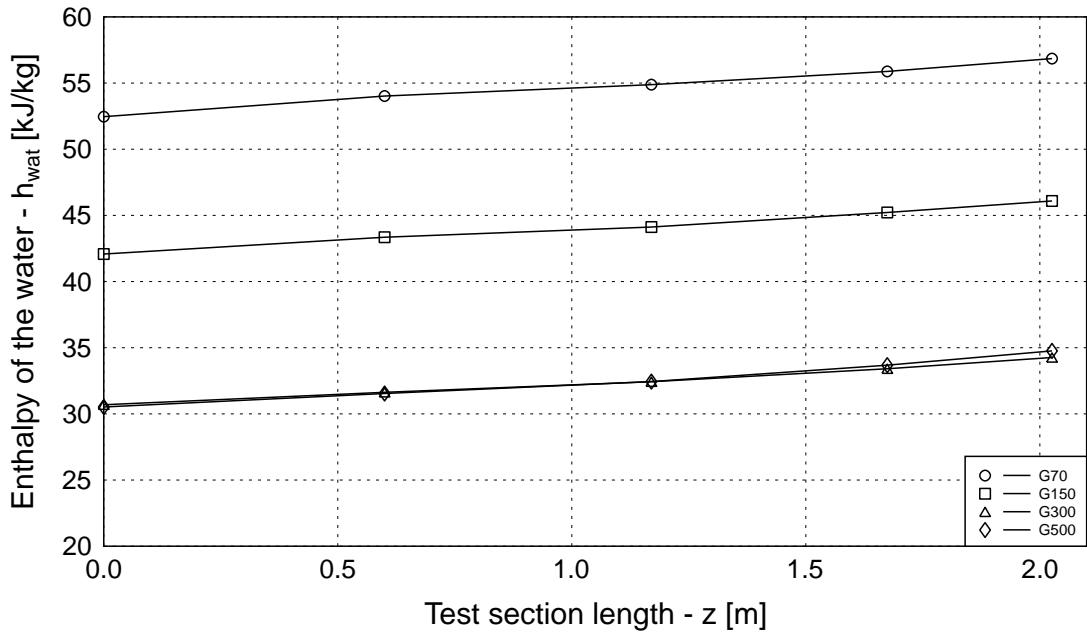


Figure 4.8: Enthalpy profile along the test section for R-22 evaporation tests at  $G = 70, 150, 300$  and  $500 \text{ kg/m}^2\text{s}$ ,  $x = 0.5$ ,  $T_{sat} = 5^\circ\text{C}$ ,  $q = 7.5 \text{ kW/m}^2$ .

refrigerant is calculated as:

$$q(z) = q_{ext} \left( \frac{D_{ext}}{D} \right) = \frac{\dot{M}_{wat}}{\pi D} \left( \frac{dh_{wat}(z)}{dz} \right) \quad (4.6)$$

For mist flow and dryout conditions, the enthalpy profile  $h_{wat}(z)$  cannot be determined accurately along the whole tube length with a second order polynomial applied to all five water measurements points. Compared to other flow regimes, the hot water temperature changes very slowly as mist flow occurs. This phenomenon starts to appear at the end of the refrigerant tube at higher vapor qualities. To determine the enthalpy profile exclusively for mist flow and dryout conditions, only the last three mean water temperatures  $T1_{water}$ ,  $T2_{water}$  and  $T3_{water}$  were used to define the enthalpy profile  $h_{wat}(z)$  at the end of the test section.

#### 4.2.4 Local heat transfer coefficient determination

After measurement and calculation of the local values of wall temperature  $T_{wall}$ , refrigerant saturation temperature  $T_{sat}$  and heat flux at the local measurement position  $q$ , the refrigerant heat transfer coefficient can be determined. Figure 4.9 shows the overall thermal resistance



diagram with the temperature distribution for the local heat transfer measurement test conditions.

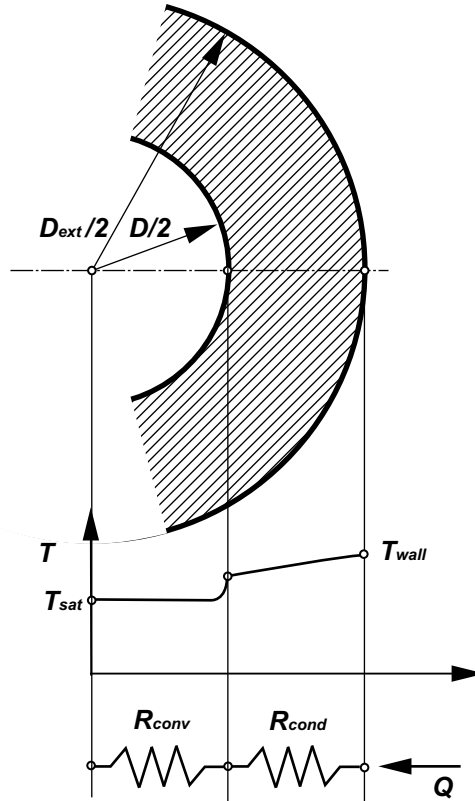


Figure 4.9: Thermal resistance diagram and temperature distribution during evaporation tests.

As can be seen in Figure 4.9, the overall thermal resistance  $R_{tot}$  is the sum of the tube wall conduction resistance  $R_{cond}$  and the convection resistance of the refrigerant  $R_{conv}$ :

$$R_{tot} = R_{cond} + R_{conv} \quad (4.7)$$

The overall thermal resistance  $R_{tot}$  can be also expressed as:

$$R_{tot} = \frac{T_{wall} - T_{sat}}{Q} \quad (4.8)$$

For radial conduction in a cylindrical wall, the thermal resistance  $R_{cond}$  is:

$$R_{cond} = \frac{\ln(D_{ext}/D)}{2\pi L\lambda} \quad (4.9)$$

where  $\lambda$  is the thermal conductivity of copper. The thermal convection resistance  $R_{conv}$  can be calculated as:

$$R_{conv} = \frac{1}{h_{ref}\pi DL} \quad (4.10)$$

and after substituting all terms to equation 4.8, the local heat transfer coefficient is determined from equation 4.12:

$$\frac{T_{wall} - T_{sat}}{Q} = \frac{\ln(D_{ext}/D)}{2\pi L\lambda} + \frac{1}{h_{ref}\pi DL} \quad (4.11)$$

$$\frac{1}{h_{ref}} = \frac{T_{wall} - T_{sat}}{q} - \frac{\ln(D_{ext}/D)D}{2\lambda} \quad (4.12)$$

All calculations of the vapor quality and heat transfer coefficient were calculated and monitored in real time. This allowed adjustments in  $T_{sat}$  and vapor quality  $x$  for each experimental point, before acquisition. Experimental points were calculated as the mean value from ten acquisitions. The experimental points were only saved, if the refrigerant saturation temperature  $T_{sat}$  did not change more than  $\pm 0.05^\circ C$  during an acquisition according to the steady-state criterion.

### 4.3 Vapor quality calculation

To calculate the vapor quality, an energy balance is made over the preheater and the test section. The refrigerant enters the preheater as a subcooled liquid. The temperature of the refrigerant is measured with a thermocouple installed on the tube wall under an insulation layer. In the test section, the vapor quality at any test section position can be calculated from the following equation:

$$x(z) = \frac{P + \dot{M}_{wat} \cdot c_{wat} \cdot (T1water - T_{wat}(z))}{\dot{M}_{ref} \cdot h_{LV}} \quad (4.13)$$

where  $P$  is the electrical power provided from the preheater,  $T1water$  is the temperature of the heating water at the inlet to the test section,  $T_{wat}(z)$  is the heating water temperature at any position along the test section,  $c_{wat}$  is the water specific heat,  $\dot{M}_{wat}$ ,  $\dot{M}_{ref}$  are the water and the refrigerant mass flow, respectively.

For evaporation tests, the most important parameters calculated are the vapor qualities at the local heat transfer measurement position and at the outlet of the test section, where the void fraction measurements are performed.

## 4.4 Void fraction determination

For the void fraction measurements, the upper support described in section 3.2 is used. The video camera and the laser optic fibre head are fixed in the same manner as they were during the calibration procedure. Figure 4.10 shows the upper support structure installed on the calibration support (on the left) and the same structure applied to the dynamic void fraction measurement at the end of the evaporator test section (on the right).

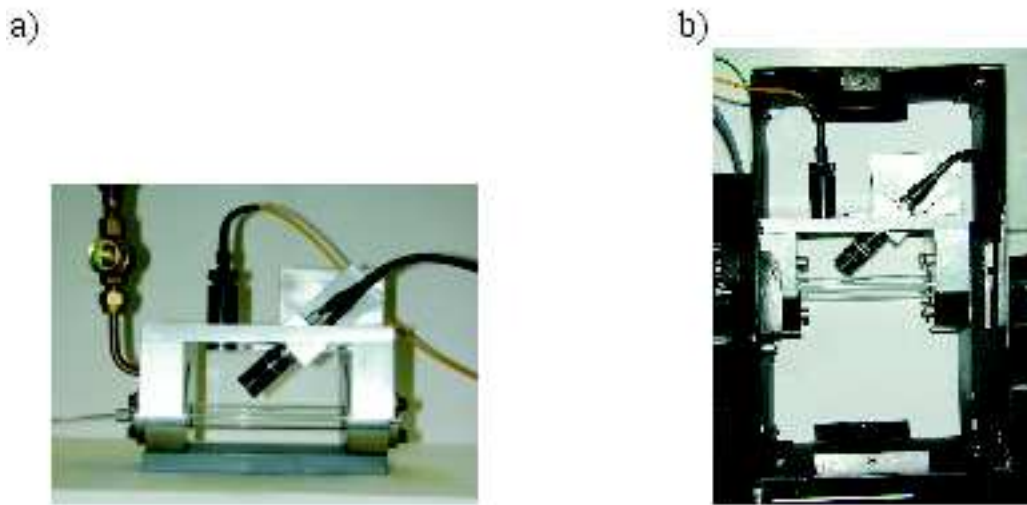


Figure 4.10: Void fraction measurement system a) calibration set-up, b) dynamical void fraction measurement set-up.

The sight glass is a borosilicate glass tube with an external diameter of  $16.00\text{ mm}$  and a wall thickness of  $1.20\text{ mm}$  for the  $13.84\text{ mm}$  test section and an external diameter of  $10.00\text{ mm}$  and a wall thickness of  $1.00\text{ mm}$  for the  $8.00\text{ mm}$  test section. It has a very good degree of roundness ( $\pm 0.02\text{ mm}$ ) for the both tubes and very good optical qualities according to DIN ISO 3585. The camera is equipped with a video card TARGA 2000, which allows a real time acquisition rate of 25 frames per second with an image resolution of  $720 \times 576$  pixels. Because of the interlaced acquisition mode (*i.e.* even lines and odd lines are not exposed and not recorded at the same time), a resampling procedure is performed. The resampling technique consists of segregating even lines from odd lines and recalculating the respective missing lines with a linear interpolation. This operation yields two images from one, increasing artificially the acquisition rate to 50 frames per second and removes the "shadow" effect of interlaced images to achieve sharp interfacial contrast. The calibration procedure described in section 3.2 is simply repeated over both image types.

## 4.5 Accuracy of measurements

To be sure that the entire measurement system is working correctly, liquid-liquid tests have been done with subcooled R-22 and R-410A versus water for both test sections. The accuracy of the energy balance between the heating and cooling fluids, and hence that when evaporating, refrigerant was thus determined. As one can see in Figure 4.11,  $Q_{wat}/Q_{ref}$  varied from 0.98 to 1.02, with a mean error of  $\pm 0.98\%$  for R-410A and  $\pm 0.96\%$  for R-22. Figure 4.12 shows the results of the same test for the 8.00 mm test section. For the liquid-liquid test with R-410A  $Q_{wat}/Q_{ref}$  varied from 0.992 to 1.009 with a mean error of  $\pm 0.7\%$ . For the test with R-22  $Q_{wat}/Q_{ref}$  ranged from 0.993 to 1.012 with a mean error of  $\pm 0.5\%$ . This is *very* accurate for these types of measurements. As a further check on the experimental set-up,

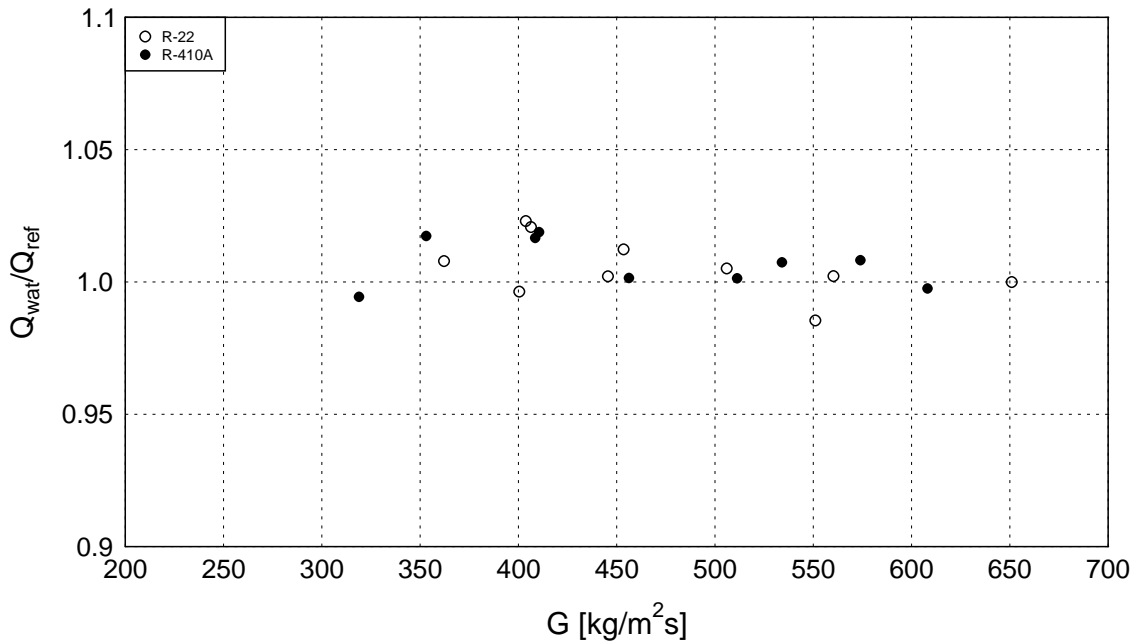


Figure 4.11: Energy balance in the liquid-liquid tests for refrigerants R-22 and R-410A in the 13.84 mm test section.

local values of the single-phase heat transfer coefficient have been measured and compared to the correlations of Dittus-Boelter and Gnielinski, respectively:

$$Nu_L = 0.023 Re_L^{0.8} Pr^{0.4} \quad (4.14)$$

$$Nu_L = \frac{(f/8)(Re_L - 1000) Pr}{1 + 12.7(f/8)^{0.5}(Pr^{0.666} - 1)} \quad (4.15)$$

where  $f$  is the friction factor obtained from the Moody diagram.

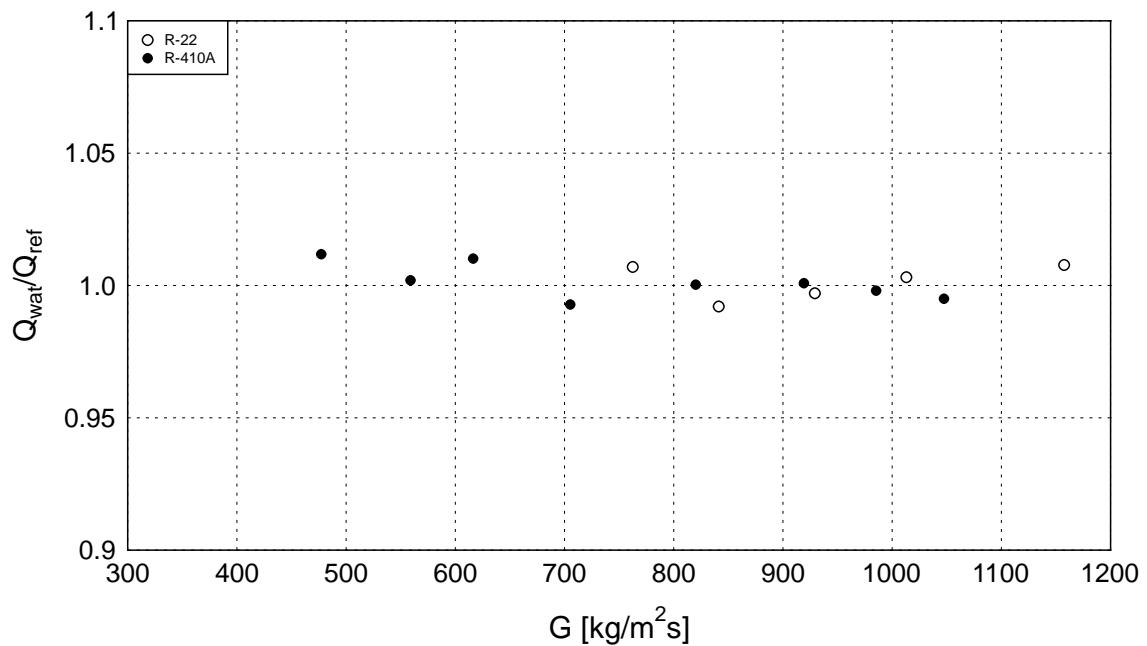


Figure 4.12: Energy balance in the liquid-liquid tests for refrigerants R-22 and R-410A in the 8.00 mm test section.

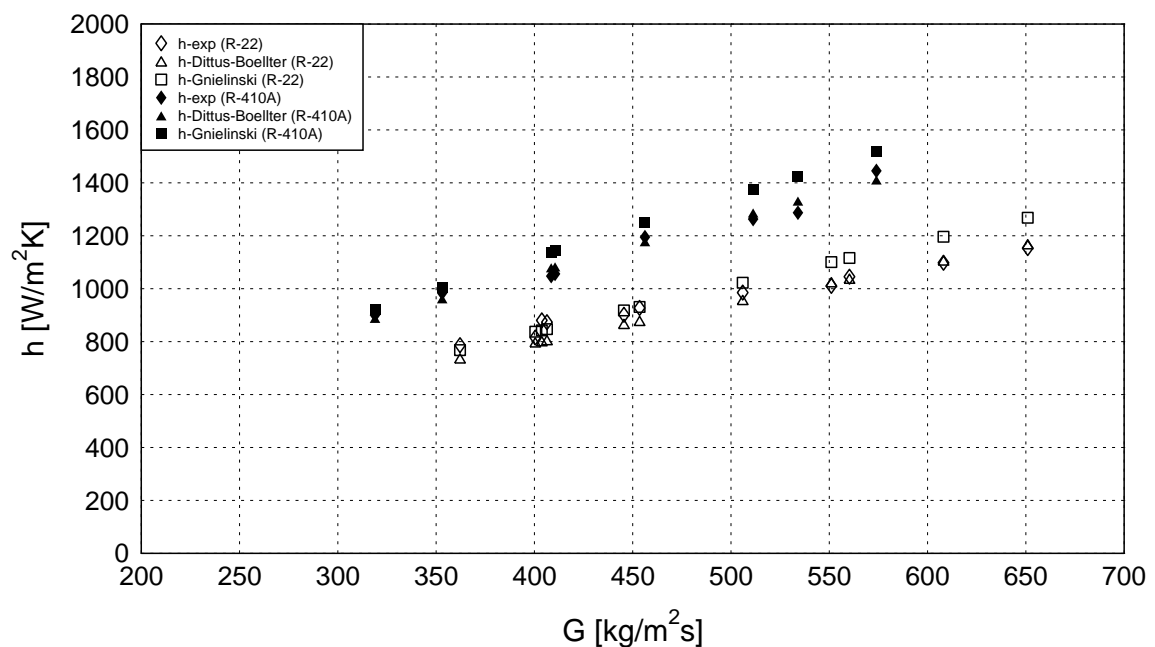


Figure 4.13: Single-phase heat transfer coefficient for refrigerants R-22 and R-410A in the 13.84 mm test section.

The measured heat transfer data are presented in Figure 4.13 and show a very good agreement with the Dittus-Boelter and Gnielinski predictions. The fit of experimental data agrees particularly well with the correlation of Dittus-Boelter at higher mass velocities. Similar type of results were obtained for the heat transfer measurement tests in the 8.00 *mm* test section.

The results of the liquid-liquid tests confirm that the experimental results measured on the flow boiling facility are highly accurate. The very low errors in the energy balances prove that all measurement instruments were precisely calibrated and that all the system was working correctly. The good agreement with the predicted correlations with the local heat transfer measurements shows that the applied solution with water-side thermocouples gave precise results and that the method could be applied in the further experimental work for the flow boiling heat transfer coefficient measurements.

#### 4.5.1 Vapor quality measurement inaccuracy

Assuming that all measured values are linearly independent, the absolute vapor quality error at each position of the evaporator based on the general definition applied to 4.13 can be expressed as:

$$\Delta x(z) = \sqrt{\left(\frac{\partial x}{\partial P} \Delta P\right)^2 + \left(\frac{\partial x}{\partial T_{1water}} \Delta T_{1water}\right)^2 + \left(\frac{\partial x}{\partial T_{wat}(z)} \Delta T_{wat}(z)\right)^2 + \left(\frac{\partial x}{\partial \dot{M}_{wat}} \Delta \dot{M}_{wat}\right)^2 + \left(\frac{\partial x}{\partial \dot{M}_{ref}} \Delta \dot{M}_{ref}\right)^2 + \left(\frac{\partial x}{\partial P_{sat}} \Delta P_{sat}\right)^2} \quad (4.16)$$

The term with the saturation pressure  $P_{sat}$  in the vapor quality error calculation is encountered because the latent heat of refrigerant is determined from the measurement of the saturation pressure.

The absolute uncertainty for the heating power measurements is  $\pm 20$  *W* and the accuracy of the temperature measurements is  $\pm 0.02^\circ C$ . The absolute error of the pressure transducers after calibration has been estimated to be  $\pm 20$  *mbar*. The refrigerant and water mass flow rates are measured with an accuracy of  $\pm 0.15\%$ . After calculating of partial derivatives and substituting all values in equation 4.16, the maximum absolute error for each tested mass velocity has been obtained. The results for the 13.84 *mm* and 8.00 *mm* are presented in Tables 4.7 and Table 4.8, respectively.

These errors are smaller than the errors in the energy balances in some cases. The reason

Mass velocity	70 [ $kg/m^2 s$ ]	150 [ $kg/m^2 s$ ]	300 [ $kg/m^2 s$ ]	500 [ $kg/m^2 s$ ]
R-22	$\pm 0.0139$	$\pm 0.0067$	$\pm 0.0037$	$\pm 0.0025$
R-410A	$\pm 0.0128$	$\pm 0.0062$	$\pm 0.0035$	$\pm 0.0024$

Table 4.7: Absolute error in the vapor quality for the tests in the 13.84 mm test section.

Mass velocity	100 [ $kg/m^2 s$ ]	200 [ $kg/m^2 s$ ]	350 [ $kg/m^2 s$ ]	500 [ $kg/m^2 s$ ]
R-22	$\pm 0.0290$	$\pm 0.0145$	$\pm 0.0082$	$\pm 0.0057$
R-410A	$\pm 0.0265$	$\pm 0.0132$	$\pm 0.0076$	$\pm 0.0052$

Table 4.8: Absolute error in the vapor quality for the tests in the 8.00 mm test section.

is that during liquid-liquid tests with subcooled refrigerant the heating water temperature was very low and some heat gains from surroundings were inevitable. Furthermore, since no evaporation took place in the test section, the  $\Delta T$  of heating water was only below  $1^\circ C$ .

### 4.5.2 Local heat transfer measurement inaccuracy

For the local heat transfer calculation, firstly the local heat flux absolute error has to be determined. Converting the derivative of the enthalpy for the derivative of the temperature of the heating water

$$\frac{dh_{wat}(z)}{dz} = c_{p_{wat}} \frac{dT_{wat}(z)}{dz} \quad (4.17)$$

and substituting into equation 4.6, the heat flux in each point of the test section can be expressed in the following way:

$$q(z) = \frac{\dot{M}_{wat}}{\pi D} c_{p_{wat}} \frac{dT_{wat}(z)}{dz} \quad (4.18)$$

If we assume, that the measurements of the heating water temperature and flow are linearly independent, the absolute error of the heat flux  $\Delta q$  can be calculated from the following expression.

$$\Delta q(z) = \sqrt{\left(\frac{dq(z)}{d\dot{M}_{wat}} \Delta \dot{M}_{wat}\right)^2 + \left(\frac{dq(z)}{dT_{wat}} \Delta T_{wat}\right)^2} \quad (4.19)$$

The absolute uncertainty of the heating water flow measurement was 0.15% and one of the temperature  $\pm 0.02^\circ C$ .

After calculating the partial derivatives in equation 4.19 and substituting the absolute uncertainties of the measured values, absolute and relative errors have been obtained for each

experimental point at the heat transfer measurement position. The calculated mean relative error does not exceed 2% and 1% for the 13.84 mm and 8.00 mm test section, respectively.

Substituting the variable  $R$  for the conductive thermal resistance in the heat transfer calculation:

$$R = \frac{\ln(D_{ext}/D)D}{2\lambda} \quad (4.20)$$

equation 4.12 can be expressed in the following form:

$$h_{ref} = \frac{q}{T_{wall} - T_{sat} - Rq} \quad (4.21)$$

After calculating partial derivatives in equation 4.21 with the assumption that all variables are linearly independent, the absolute error of the local heat transfer measurements is calculated as:

$$\Delta h_{ref} = \sqrt{\left(\frac{-q}{(T_{wall} - T_{sat} - Rq)^2} \Delta T_{wall}\right)^2 + \left(\frac{q}{(T_{wall} - T_{sat} - Rq)^2} \Delta T_{sat}\right)^2 + \left(\frac{(T_{wall} - T_{sat})}{(T_{wall} - T_{sat} - Rq)^2} \Delta q\right)^2} \quad (4.22)$$

The wall temperature measurement uncertainty was  $\pm 0.02^\circ C$ . The error in the saturation temperature determination was  $\pm 0.07^\circ C$  and  $\pm 0.11^\circ C$  for the tests with R-410A and R-22, respectively. The absolute error of the heat flux previously calculated at the heat transfer measurement position was substituted into 4.22.

Tables 4.9 and 4.10 show the relative error of the local heat transfer coefficient for all principal test series in the 13.84 mm and 8.00 mm test sections. For the tests in the 13.84 mm tube, the lowest mean relative error of the heat transfer measurement is encountered at small mass velocities. At  $G = 70 \text{ kg/m}^2\text{s}$  the mean relative error is in the range  $\pm 1.9\%$  for  $q = 7.5 \text{ kW/m}^2$  and  $\pm 1.5\%$  for  $q = 17.5 \text{ kW/m}^2$ . As can be seen, the error rises with the mass velocity. The highest error will occur for the tests at  $G = 500 \text{ kg/m}^2\text{s}$  at the lowest heat flux. The mean relative error there equals  $\pm 5.8\%$  and  $\pm 8\%$  for the R-410A and R-22 tests, respectively. In equation 4.21, it can be seen that the heat transfer coefficient is inversely proportional to the temperature difference between the wall and the refrigerant. As the heat transfer coefficient increases with the mass velocity, for the constant heat flux, the difference between saturation and wall temperature will decrease. This phenomenon is depicted in Figure 4.14.



Relative Error in R-410A tests - $\Delta h_{ref}/h_{ref}[-]$									
G [ $kg/m^2s$ ]	$q = 7.5kW/m^2$			$q = 17.5kW/m^2$			$q = 37.5kW/m^2$		
	Mean	Min	Max	Mean	Min	Max	Mean	Min	Max
<b>G70</b>	0.019	0.015	0.02	0.015	0.008	0.03	-	-	-
<b>G150</b>	0.026	0.019	0.061	0.02	0.017	0.028	0.024	0.009	0.078
<b>G300</b>	0.042	0.024	0.061	0.022	0.014	0.041	0.02	0.01	0.101
<b>G500</b>	0.058	0.029	0.088	0.03	0.022	0.04	0.021	0.012	0.076
Relative Error in R-22 tests - $\Delta h_{ref}/h_{ref}[-]$									
G [ $kg/m^2s$ ]	$q = 7.5kW/m^2$			$q = 17.5kW/m^2$			$q = 37.5kW/m^2$		
	Mean	Min	Max	Mean	Min	Max	Mean	Min	Max
<b>G70</b>	0.017	0.015	0.024	0.013	0.011	0.019	-	-	-
<b>G150</b>	0.03	0.022	0.129	0.017	0.016	0.018	0.013	0.011	0.023
<b>G300</b>	0.059	0.033	0.101	0.028	0.018	0.083	0.019	0.016	0.048
<b>G500</b>	0.08	0.039	0.136	0.032	0.024	0.049	0.03	0.016	0.171

Table 4.9: Relative error in the local heat transfer coefficient in the 13.84 mm test section for R-410A and R-22.

Relative Error in R-410A tests - $\Delta h_{ref}/h_{ref}[-]$									
G [ $kg/m^2s$ ]	$q = 7.5kW/m^2$			$q = 17.5kW/m^2$			$q = 37.5kW/m^2$		
	Mean	Min	Max	Mean	Min	Max	Mean	Min	Max
<b>G100</b>	0.034	0.032	0.036	0.022	0.021	0.022	-	-	-
<b>G200</b>	0.038	0.034	0.042	0.028	0.024	0.03	0.021	0.02	0.022
<b>G350</b>	0.045	0.035	0.052	0.031	0.026	0.033	0.022	0.016	0.024
Relative Error in R-22 tests - $\Delta h_{ref}/h_{ref}[-]$									
G [ $kg/m^2s$ ]	$q = 7.5kW/m^2$			$q = 17.5kW/m^2$			$q = 37.5kW/m^2$		
	Mean	Min	Max	Mean	Min	Max	Mean	Min	Max
<b>G100</b>	0.033	0.03	0.041	0.022	0.022	0.023	-	-	-
<b>G200</b>	0.047	0.042	0.056	0.026	0.024	0.026	0.02	0.019	0.02
<b>G350</b>	0.061	0.025	0.074	0.028	0.018	0.083	0.024	0.019	0.059

Table 4.10: Relative error in the local heat transfer coefficient in the 8.00 mm test section for R-410A and R-22.

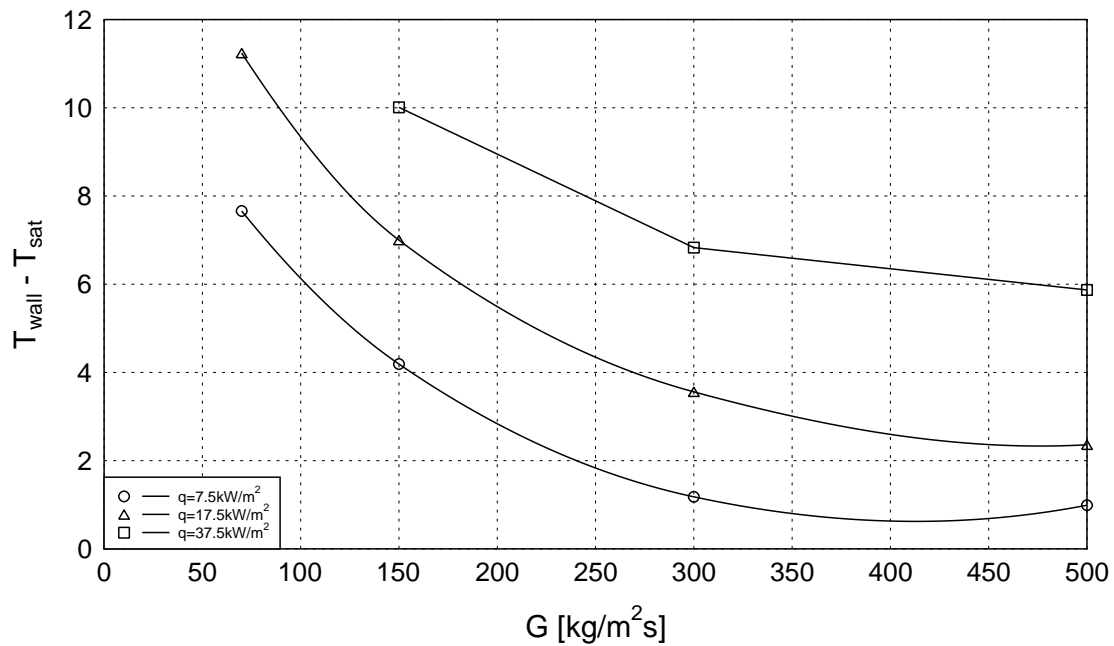


Figure 4.14: Distribution of the difference between the wall and saturation temperature for R-22 tests at  $x = 0.85$ .

As can be seen in Figure 4.14, for the lowest heat flux at the mass velocities  $G = 300$  and  $500 \text{ kg}/\text{m}^2\text{s}$ , the  $\Delta T$  is only about  $1^\circ\text{C}$ . As  $T_{\text{sat}}$  is measured with the accuracy of  $\pm 0.11^\circ\text{C}$  for R-22, it yields a higher value of error compared to the other tests conditions. The mean relative error of the measured heat transfer for the  $8.00 \text{ mm}$  test section shows the same trend in results compared to the  $13.84 \text{ mm}$  test section. The  $\Delta h_{\text{ref}}/h_{\text{ref}}$  increases with increasing mass velocity. The maximum values of the relative error are encountered at  $G = 350 \text{ kg}/\text{m}^2\text{s}$  and equals  $\pm 4.5\%$  and  $\pm 6.1\%$  for R-410A and R-22, respectively.

### 4.5.3 Dynamical void fraction measurement inaccuracy

The accuracy of the dynamic void fraction measurements is assumed to be the same as for the static tests, since no dynamic calibration scheme is accurate enough for this purpose to our knowledge. As it has been shown in subsection 3.2.4 the optical technique has been optimized for stratified types of flow and yields void fractions with a measured precision in absolute value on the order of  $\pm 0.01$  and  $\pm 0.03$  over the vapor quality range from 0.05 to 0.95 for the  $13.84 \text{ mm}$  and  $8.00 \text{ mm}$  test section, respectively.

## Chapter 5

# Dynamic void fraction and dry angles

A new optical void fraction measurement system has been coupled to the flow boiling test facility described in Chapter 4 to obtain dynamic and time-averaged void fractions in a horizontal tube. A series of evaporation tests have been run for two refrigerants in two diameters of glass tube. Using our newly developed image processing system, about 310 000 images have been analyzed in this study to provide the same number of dynamic void fraction measurements. From these images, 238 time-averaged void fraction values have been obtained for vapor qualities from 0.01 to 0.95 for the 13.60 *mm* diameter glass tube and 87 time-averaged void fraction values for the 8.00 *mm* diameter glass tube. The same number of time-averaged dry angles have been obtained for both tubes. The flow pattern oriented heat transfer model proposed by Kattan *et al.* [30, 31, 32] (1998a-c) used the Steiner version of the Taitel-Dukler [53] (1976) void fraction model embedded in the flow pattern identification map and the Rouhani-Axelsson relation [46] (1970) for the heat transfer prediction. As a next step, Thome and El Hajal [55] (2002) proposed to use the Steiner version of the Rouhani-Axelsson void fraction model for both flow pattern and heat transfer prediction (see section 2.2.3) by introducing it into the flow pattern map. In this study, the experimental results of dynamic void fraction measurements will be compared to the model of Taitel-Dukler and to the Steiner version of Rouhani-Axelsson relation. Two other methods will be also compared: the homogeneous model as a limiting case and widely quoted kinetic energy model of Zivi [67] (1964). The dry angle are also measured and compared to the values of  $\theta_{dry}$  used for the definition of tube dry perimeter of the tube in the heat transfer model of Kattan *et al.*

## 5.1 Void fraction models

Void fraction has been described for four different geometrical conditions in section 1.3. In the present study, the focus will be only on the cross-sectional void fraction. As it defines the cross-sectional areas occupied by the vapor and the liquid, it defines the true mean velocities of each phase. It is also the primary parameter in the calculation of pressure drop, flow pattern transitions and heat transfer coefficients. Void fraction models define the variation of void fraction as a function of vapor quality. Numerous void fraction relationships exist in the literature. Surprisingly numerous studies refer to a void fraction model without any physical motivation. It is very difficult to define a void fraction correlation and a lot of different physical approaches are proposed. In this section the homogeneous model, which assumes the same velocity in each phase and the several velocity ratio models will be presented. Furthermore, the model of Taitel-Dukler [53] (1976) used for the prediction of flow pattern transitions and drift flux models will be discussed.

### 5.1.1 Homogeneous model

The homogeneous model is based on the assumption that the vapor and liquid phases flow at the same velocities. After comparison of vapor and liquid velocities defined in equations 1.13 and 1.14, the void fraction can be calculated as:

$$\varepsilon = \left[ 1 + \left( \frac{1-x}{x} \right) \left( \frac{\rho_V}{\rho_L} \right) \right]^{-1} \quad (5.1)$$

This model represents the upper physical limit of the void fraction for horizontal co-current two-phase flows. There is no surprise that the homogeneous model overpredicts the real void fraction for most practical cases, where the vapor phase flows usually at the higher velocity. This expression is reasonably accurate only for bubbly flows and dispersed droplets in mist flows, where the entrained phase travels at nearly the same velocity as the continuous phase. The homogeneous model is also the limiting case as the pressure tends towards the critical pressure, where the difference in the phase densities disappears.

### 5.1.2 Velocity ratio models

The velocity ratio is a concept utilized in separated flow types of models, where it is assumed that the two-phases flow at two different velocities. The velocity ratio is defined as:

$$S = \frac{u_V}{u_L} \quad (5.2)$$

and describes relative mean velocities of the two co-existent phases. The value  $S$  is often referred incorrectly to as the slip ratio, although physically there cannot be a discontinuity in the two velocities at the interface since a boundary layer is formed in both phases. The general velocity ratio model is defined as:

$$\varepsilon = \left[ 1 + \left( \frac{1-x}{x} \right) \left( \frac{\rho_V}{\rho_L} \right) S \right]^{-1} \quad (5.3)$$

For equal velocities of both phases, *i.e.*  $S = 1$  the expression reverts to the homogeneous model. For upward and horizontal co-current flows  $u_V$  is nearly always greater than  $u_L$  such that  $S > 1$ . Numerous analytical and empirical methods have been proposed to calculate the velocity ratio  $S$ . Several will be presented below:

#### Momentum flux model

In this model, the value of the momentum flux is minimized by differentiation of the momentum flux equation with respect to  $\varepsilon$  and set equal to zero, so that:

$$G^2 \left[ \frac{x^2 v_V}{\varepsilon} + \frac{(1-x)^2 v_L}{1-\varepsilon} \right] \frac{d}{d\varepsilon} = 0 \quad (5.4)$$

Comparing the resulting expression to equation 5.3, the velocity ratio for this simple model is:

$$S = \left( \frac{\rho_L}{\rho_V} \right)^{1/2} \quad (5.5)$$

### Kinetic energy model of Zivi

Zivi [67] (1964) proposed a model for annular flow, assuming that no liquid is entrained in the central vapor core. Based on the hypothesis that the total kinetic energy of the two-phases will seek to be a minimum, he obtained his velocity ratio as:

$$S = \left( \frac{\rho_L}{\rho_V} \right)^{1/3} \quad (5.6)$$

### Chisholm model

Chisholm [10] (1973) obtained the following correlation for the velocity ratio:

$$S = \left[ 1 - x \left( 1 - \frac{\rho_L}{\rho_V} \right) \right]^{1/2} \quad (5.7)$$

This relation results from simple annular flow theory and application of the homogeneous theory on the fluid density, producing approximately equal frictional pressure gradients in each phase.

### 5.1.3 Geometric model of Taitel-Dukler

Taitel and Dukler [53] (1976) proposed a model for predicting flow regimes transitions. Starting from a momentum balance of each phase in an equilibrium stratified flow, they obtained:

$$-A_V \left( \frac{dp}{dz} \right)_V - \tau_V P_V - \tau_i P_i + \rho_V A_V g \sin \varphi = 0 \quad (5.8)$$

$$-A_L \left( \frac{dp}{dz} \right)_L - \tau_L P_L + \tau_i P_i + \rho_L A_L g \sin \varphi = 0 \quad (5.9)$$

and assuming the same pressure gradient in both phases, the two equations are reduced as follows:

$$\tau_V \frac{P_V}{A_V} - \tau_L \frac{P_L}{A_L} + \tau_i P_i \left( \frac{1}{A_L} + \frac{1}{A_V} \right) + (\rho_L - \rho_V) g \sin \varphi = 0 \quad (5.10)$$

The shear stresses are evaluated in the conventional manner and the friction factors are a function of the Reynolds number. Interface and vapor friction factors are assumed to be equal. Taitel and Dukler transformed their equations to dimensionless form with the reference variables:  $D$  for length,  $D^2$  for area and the superficial velocities,  $j_L$  and  $j_V$  for the liquid and vapor velocities, respectively. By designating dimensionless quantities by a subscript  $D$ , equation 5.10 takes the form:

$$X_{tt}^2 \left[ (u_{LD} D_{LD})^{-n} u_{LD}^2 \frac{P_{LD}}{A_{LD}} \right] - \left[ (u_{VD} D_{VD})^{-m} u_{VD}^2 \left( \frac{P_{VD}}{A_{VD}} + \frac{P_{iD}}{A_{LD}} + \frac{P_{iD}}{A_{VD}} \right) \right] - 4Y = 0 \quad (5.11)$$

$Y$  is a variable equal to zero if the flow is horizontal ( $\varphi = 0$ ). For turbulent flow, Taitel and Dukler proposed  $n = m = 0.2$  and  $n = m = 1.0$  for laminar flow. Every dimensionless variable shown in equation 5.11 can be expressed as function of the dimensionless liquid height  $h_{LD}$  defined in equation 2.2 as:

$$A_{LD} = \frac{A_L}{D^2} = 0.25 \left[ \pi - \arccos(2h_{LD} - 1) + (2h_{LD} - 1) \sqrt{1 - (2h_{LD} - 1)^2} \right] \quad (5.12)$$

$$A_{VD} = \frac{A_V}{D^2} = 0.25 \left[ \arccos(2h_{LD} - 1) + (2h_{LD} - 1) \sqrt{1 - (2h_{LD} - 1)^2} \right] \quad (5.13)$$

$$P_{LD} = \pi - \arccos(2h_{LD} - 1) \quad (5.14)$$

$$P_{VD} = \arccos(2h_{LD} - 1) \quad (5.15)$$

$$P_{iD} = \sqrt{1 - (2h_{LD} - 1)^2} \quad (5.16)$$

$$D_{LD} = \frac{4A_{LD}}{P_{LD}} \quad (5.17)$$

$$D_{VD} = \frac{4A_{VD}}{P_{VD} + P_{iD}} \quad (5.18)$$

$$A_D = \frac{A}{D^2} = \frac{\pi}{4} \quad (5.19)$$

$$u_{LD} = \frac{u_L}{j_L} = \frac{A_D}{A_{LD}} \quad (5.20)$$

$$u_{VD} = \frac{u_V}{j_V} = \frac{A_D}{A_{VD}} \quad (5.21)$$

After substitution of all parameters equation 5.11 is solved iteratively with respect to  $h_{LD}$ . The Martinelli parameter  $X_{tt}$  is calculated from equation 1.50 for each vapor quality  $0 \leq x \leq 1$  and the void fraction can be obtained finally as:

$$\varepsilon = \frac{A_{VD}}{A_D} \quad (5.22)$$

Thus, from the relationship between void fraction and liquid height, it is possible to define the void fraction of Taitel and Dukler. Continuing the same approach, Steiner [58] (1993) proposed simplified relationships for the dimensionless variables used afterwards in the flow pattern prediction by Kattan and presented in section 2.2.1.

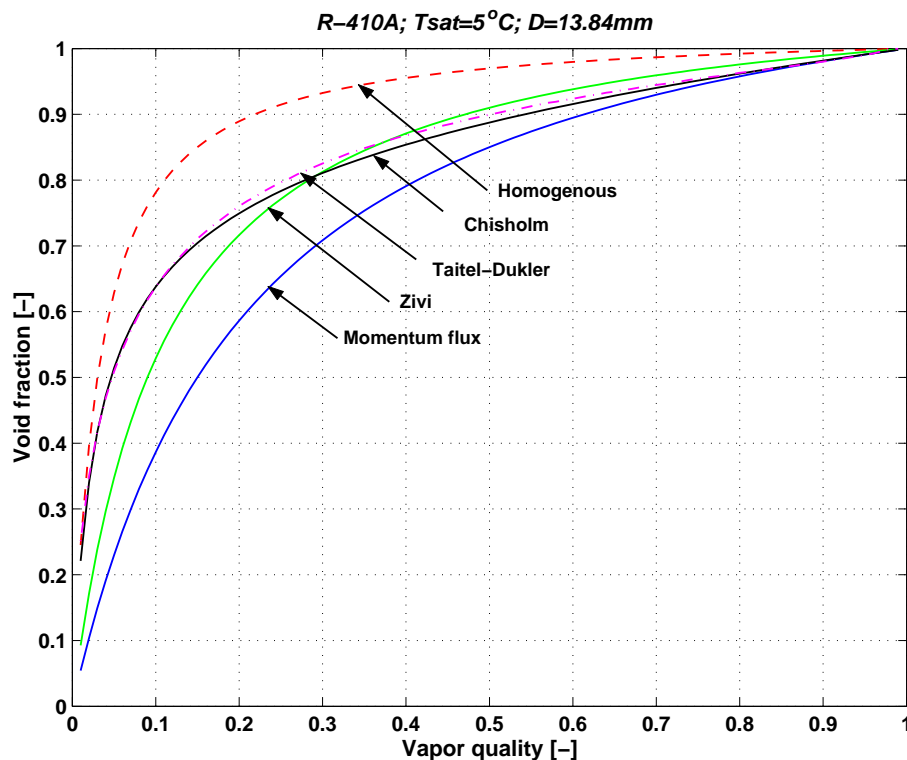


Figure 5.1: Comparison of homogeneous, Taitel-Dukler and velocity ratio void fraction models for refrigerant R-410A at  $T_{sat} = 5^{\circ}\text{C}$ .



Figure 5.1 shows a comparison of the above models for refrigerant R-410A at  $T_{sat} = 5^\circ C$ . As expected, the homogeneous model (dashed curve) gives the highest value of void fraction. The momentum flux model gives the lowest values. The difference between the velocity ratio models (solid curves) is the most significant at low vapor qualities. For the vapor quality  $x = 0.1$ , the disparity in void fraction between the momentum flux model and the Chisholm model is almost 0.25. The geometrical model of Taitel-Dukler (dash-dotted curve) agrees very well with the velocity ratio model of Chisholm and only for the vapor quality range  $0.2 \leq x \leq 0.7$  can a slight shift be observed.

### 5.1.4 Correlations based on the drift flux model

#### The general drift flux model of Zuber and Findlay

Zuber and Findlay [68] (1965) proposed the general form of the drift flux model. This model takes into account both the effect of nonuniform flow and void profiles as well as the effect of the local relative velocity between the phases. The first effect is taken into account by a distribution parameter, whereas the weighted average drift velocity accounts for the latter.

Zuber and Findlay considered a three-dimensional problem and expressed the velocities in terms of vectors. Hence, the volumetric flux densities are defined as:

$$\vec{j}_V = \varepsilon \vec{u}_V \quad (5.23)$$

$$\vec{j}_L = (1 - \varepsilon) \vec{u}_L \quad (5.24)$$

The relative velocity between the two-phases is:

$$\vec{u}_R = \vec{u}_V - \vec{u}_L \quad (5.25)$$

and the diffusion or drift velocities with respect the volumetric flux density of the mixture are:

$$\vec{V}_{Vj} = \vec{u}_V - \vec{j} \quad (5.26)$$

$$\vec{V}_{Lj} = \vec{u}_L - \vec{j} \quad (5.27)$$

and the volumetric flux density of the mixture is defined by:

$$\vec{j} = \vec{j}_V + \vec{j}_L \quad (5.28)$$

Considering the continuity equation for the liquid and gas phase, they concluded that the volumetric flux densities of the two-phases do not depend upon space coordinates but only upon time, thus:

$$\vec{j}_V + \vec{j}_L = \vec{j}(t) \quad (5.29)$$

Zuber and Findlay proposed the average value of a scalar or of a vector quality  $F$  over the cross-sectional area of the duct defined by:

$$\langle F \rangle = \frac{1}{A} \int_A F dA \quad (5.30)$$

Introducing the expressions for the local values of the local velocities  $u_V$  calculated from 5.26 into 5.30, they obtained the average velocities (over the cross-sectional area) of the vapor; thus

$$\langle u_V \rangle = \left\langle \frac{j_V}{\varepsilon} \right\rangle = \langle j \rangle + \langle V_V j \rangle \quad (5.31)$$

However, the system input parameters readily available to a designer or to an experimenter are the average volumetric flux densities defined by

$$\langle j_V \rangle = \langle \varepsilon u_V \rangle = \frac{Q_V}{A} \quad (5.32)$$

In view of these relations, Zuber and Findlay considered the weighted mean value of the quantity  $F$ , defined by:

$$\bar{F} = \frac{\langle \varepsilon F \rangle}{\langle \varepsilon \rangle} = \frac{\frac{1}{A} \int_A \varepsilon F dA}{\frac{1}{A} \int_A \varepsilon dA} \quad (5.33)$$

whence they obtained the weighted mean velocity  $\bar{u}_V$  of the gas phase, which is

$$\bar{u}_V = \frac{\langle u_V \varepsilon \rangle}{\langle \varepsilon \rangle} = \frac{\langle j_V \rangle}{\langle \varepsilon \rangle} \quad (5.34)$$

In view of equation 5.26, the weighted mean velocity also can be expressed as:

$$\bar{u}_V = \frac{\langle \varepsilon j \rangle}{\langle \varepsilon \rangle} + \frac{\langle \varepsilon V_V j \rangle}{\langle \varepsilon \rangle} \quad (5.35)$$

In general, the average velocity  $\langle u_V \rangle$  defined by equation 5.31 is not equal to the weighted mean velocity  $\bar{u}_V$  defined by equation 5.34 and 5.35.

The weighted mean velocity  $\bar{u}_V$  can be cast in several forms which are useful for analysing experimental data and for determining the average volumetric concentration (void fraction)  $\langle \varepsilon \rangle$ . Thus, multiplying and dividing the first term on the right-hand side of equation 5.35 by  $\langle j \rangle$ , we obtain

$$\bar{u}_V = \frac{\langle j_V \rangle}{\langle \varepsilon \rangle} = C_o \langle j \rangle + \frac{\langle \varepsilon V_V j \rangle}{\langle \varepsilon \rangle} \quad (5.36)$$

where the distribution parameter  $C_o$  is defined by:

$$C_o = \frac{\langle \varepsilon j \rangle}{\langle \varepsilon \rangle \langle j \rangle} = \frac{\frac{1}{A} \int_A \varepsilon j dA}{\left[ \frac{1}{A} \int_A j dA \right] \left[ \frac{1}{A} \int_A \varepsilon dA \right]} \quad (5.37)$$

Equation 5.36 can be expressed in a nondimensional form by dividing both sides of  $\langle j \rangle$ , thus

$$\frac{\langle \beta \rangle}{\langle \varepsilon \rangle} = C_o + \frac{\langle \varepsilon V_V j \rangle}{\langle \varepsilon \rangle \langle j \rangle} \quad (5.38)$$

what after rearranging, results in the general expression for predicting the average volumetric concentration (void fraction)  $\langle \varepsilon \rangle$  of the form:

$$\langle \varepsilon \rangle = \frac{\langle \beta \rangle}{C_o + \frac{\langle \varepsilon V_V j \rangle}{\langle \varepsilon \rangle \langle j \rangle}} \quad (5.39)$$

where  $\langle \beta \rangle$  is the average volumetric flow concentration corresponding to the homogeneous void fraction:

$$\langle \beta \rangle = \frac{\langle j_V \rangle}{\langle j \rangle} = \frac{Q_V}{Q_V + Q_L} = \left[ 1 + \left( \frac{1-x}{x} \right) \left( \frac{\rho_V}{\rho_L} \right) \right]^{-1} \quad (5.40)$$

In contrast to previous analyses, Zuber and Findlay derived an expression, which is applicable to any two-phase flow regime. Furthermore, the analysis takes into account both the effect of nonuniform flow and concentration profiles and the effect of the local relative velocity. The first effect is accounted for by the distribution parameter  $C_o$ , whereas the second one is accounted for by the weighted mean drift flux velocity  $\langle \varepsilon V_{Vj} \rangle / \langle \varepsilon \rangle$ . For each particular flow regime, the value of the average volumetric concentration  $\langle \varepsilon \rangle$  can be obtained from the general expression 5.39 by inserting the appropriate velocity and concentration profiles and the appropriate expression for the drift velocity.

Zuber and Findlay showed that the distribution parameter  $C_o$  depends on the flow structure. Analyzing experimental results in the  $\langle j \rangle - \bar{u}_V$  coordinates, they showed linear dependence of the results for slug, bubbly and annular flow regimes. According to equation 5.36, for a particular two-phase flow pattern the slope of such a straight line gives the value of the distribution parameter  $C_o$ , whereas the intercept of this line with the  $\bar{u}_V = \frac{\langle j \rangle}{\langle \varepsilon \rangle}$  axis gives the value of the weighted mean drift velocity  $\bar{V}_{Vj}$ .

Without any references to flow pattern, a mean value of  $C_o = 1.13$  correlated the steam-water mixture data of Zuber *et al.* [69] (1967) at elevated pressures. For vertical slug flow they proposed  $C_o = 1.2$ .

The weighted mean drift flux velocity obtained by Zuber and Findlay for the vertical, slug flow regime is

$$\bar{V}_{Vj} = \frac{\langle \varepsilon V_{Vj} \rangle}{\langle \varepsilon \rangle} = 0.35 \left[ \frac{gpD}{\rho_L} \right]^{0.5} \quad (5.41)$$

and for the vertical, bubbly churn-turbulent regime it is

$$\bar{V}_{Vj} = \frac{\langle \varepsilon V_{Vj} \rangle}{\langle \varepsilon \rangle} = 1.53 \left[ \frac{\sigma gp}{\rho_L^2} \right]^{0.25} \quad (5.42)$$

Zuber *et al.* [69] (1967) proposed for vertical flows of steam-water mixtures at elevated pressure, a mean value of  $\bar{V}_{Vj}$  applicable without any references to flow regime as

$$\bar{V}_{Vj} = \frac{\langle \varepsilon V_{Vj} \rangle}{\langle \varepsilon \rangle} = 1.41 \left[ \frac{\sigma gp}{\rho_L^2} \right]^{0.25} \quad (5.43)$$

As can be seen, the drift flux model of Zuber and Findlay allows one to calculate the void fraction  $\langle \varepsilon \rangle$  taking into account the numerous aspects occurring in two-phase flow. They presented their model for specific flow patterns and hence there is not a continuous transition

in void fraction between different flow regimes.

### The Rouhani-Axelsson model

Rouhani-Axelsson [46] (1970) presented a drift flux model based on that of Zuber and Findlay [68] (1965) in the form of:

$$\varepsilon = \frac{x}{\rho_V} \left[ C_o \left( \frac{x}{\rho_V} + \frac{1-x}{\rho_L} \right) + \frac{\bar{V}_{Vj}}{G} \right]^{-1} \quad (5.44)$$

The weighted mean drift flux velocity and the distribution parameter based on a horizontal configuration are in agreement with experimental data proposed by VDI-Wärmeatlas [58] (1993) using the additional expressions:

$$\bar{V}_{Vj} = 1.18(1-x) \left[ \frac{g\sigma(\rho_L - \rho_V)}{\rho_L^2} \right]^{0.25} \quad (5.45)$$

$$C_o = 1 + 0.12(1-x) \quad (5.46)$$

After substitution into equation 5.44, this results in the expression:

$$\varepsilon = \frac{x}{\rho_V} \left[ (1 + 0.12(1-x)) \left( \frac{x}{\rho_V} + \frac{1-x}{\rho_L} \right) + \frac{1.18(1-x)[g\sigma(\rho_L - \rho_V)]^{0.25}}{G\rho_L^{0.5}} \right]^{-1} \quad (5.47)$$

This form of the Rouhani-Axelsson void fraction model was proposed for general use by Steiner [58] (1993) irrespective of flow pattern but for horizontal flows. This method takes into account effects of concentration distribution and relative velocity and includes the important effects of mass velocity, viscosity and surface tension.

Kattan *et al.* [32] (1998c) and Zürcher [70] (2000) selected the Steiner version of the Rouhani-Axelsson void fraction model for their heat transfer investigation. As it has been shown in section 2.2.3, Thome and El Hajal proposed to also use this form of drift flux model for both flow pattern transition and heat transfer predictions.

Figure 5.2 shows the Rouhani-Axelsson drift flux model for refrigerant R-410A at four mass velocities: 70, 150, 300 and 500  $kg/m^2s$ . As can be seen, the predicted void fraction value increases with increasing mass velocity. The effect of mass velocity becomes less significant

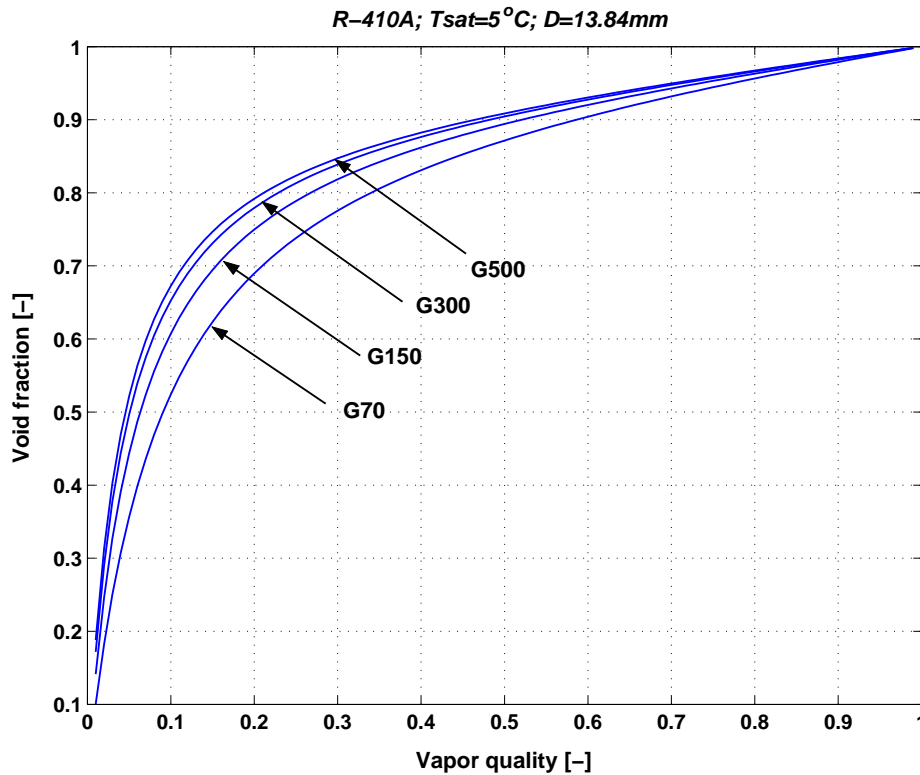


Figure 5.2: Rouhani-Axelsson drift flux void fraction model for R-410A at  $T_{sat} = 5^{\circ}\text{C}$ .

at higher mass velocities. It can be seen that the difference in prediction of void fraction between  $G = 300 \text{ kg/m}^2\text{s}$  and  $G = 500 \text{ kg/m}^2\text{s}$  is more or less negligible.

## 5.2 Dynamic void fraction measurements

The dynamic void fraction experimental set-up is located at the outlet of the evaporator test section and it is described in section 4.4. The cross-sectional image sequences were simultaneously acquired with all the heat transfer parameters. The images were processed on a PC with a Pentium 3 processor (455 MHz) as described in section 3.2. All together, 325 experimental points have been acquired corresponding to almost 310 000 images. Due to optical perturbations, some sequences had to be removed as they were not processable. The best image quality in terms of the contrast between the vapor and the liquid phase is obtained at low vapor qualities and low mass velocities (*i.e.* for low liquid phase velocities). On the other hand, at high vapor qualities, occasionally some droplets of liquid were carried away by the high velocity vapor, which resulted in additional reflections and secondary refraction of

the light. Moreover, for high vapor quality tests, the rhodamineB powder deposited on the upper "dry" internal perimeter of the tube. As a result, very intense white spots sometimes appear on the acquired image (overexposed images). This problem is partially avoided by regularly "washing" the tube wall with high frequency waves at higher mass velocities before returning to the test conditions. Finally, condensation of moisture in the room air on the external surface of the glass tube was removed with a dry air jet to avoid blurred images.

### 5.2.1 Experimental conditions

In the 13.84 mm test section, experimental tests were run for two refrigerants at four mass velocities over nearly the entire range of vapor quality  $0.01 \leq x \leq 0.95$ . R-22 was tested at mass velocities of 70, 100, 150 and 200  $kg/m^2s$  and R-410A for 70, 150, 200 and part of the range for 300  $kg/m^2s$ . In the 8.00 mm test section, R-22 was tested at mass velocities 100, 150, 200  $kg/m^2s$  and R-410A at 100 and 200  $kg/m^2s$ . Due to the flow instabilities in the 8.00 mm test section at low mass velocities, the void fraction over the entire vapor quality range was only measured at 200  $kg/m^2s$ . For lower mass velocities the tested range of vapor quality was  $0.01 \leq x \leq 0.55$ . The saturation temperature was  $5^\circ C$  and the heat fluxes in the heat transfer section ranged from 2.0 to 7.5  $kW/m^2$  (low heat fluxes were used to avoid nucleate boiling and its entrained bubbles in the flow). The minimum heat flux was applied especially for the lower void fractions measurements to obtain low vapor qualities at the outlet of the heat transfer test section. A computerised data acquisition system was used to record all data and to insure that steady-state conditions were reached. The criteria for steady-state conditions was the refrigerant saturation temperature, which should not change more than  $\pm 0.05^\circ C$ .

### 5.2.2 Results and discussion

Each test case of void fraction measurement can be presented as a function of time, but due to the large number of measurements, only a few cases are shown here. The first case is for a R-410A stratified-wavy flow in the 13.60 mm sightglass tube (see Figure 5.3) at the exit of the 13.84 mm heat transfer test section with the void fraction of each sequential image plotted versus time. The mass velocity is  $G = 70 kg/m^2s$  and vapor quality is  $x = 0.200$ . The characteristic cyclic variation observable corresponds to waves passing through the cross-section and the time in-between corresponds to their period. The void fractions equal to 0.0

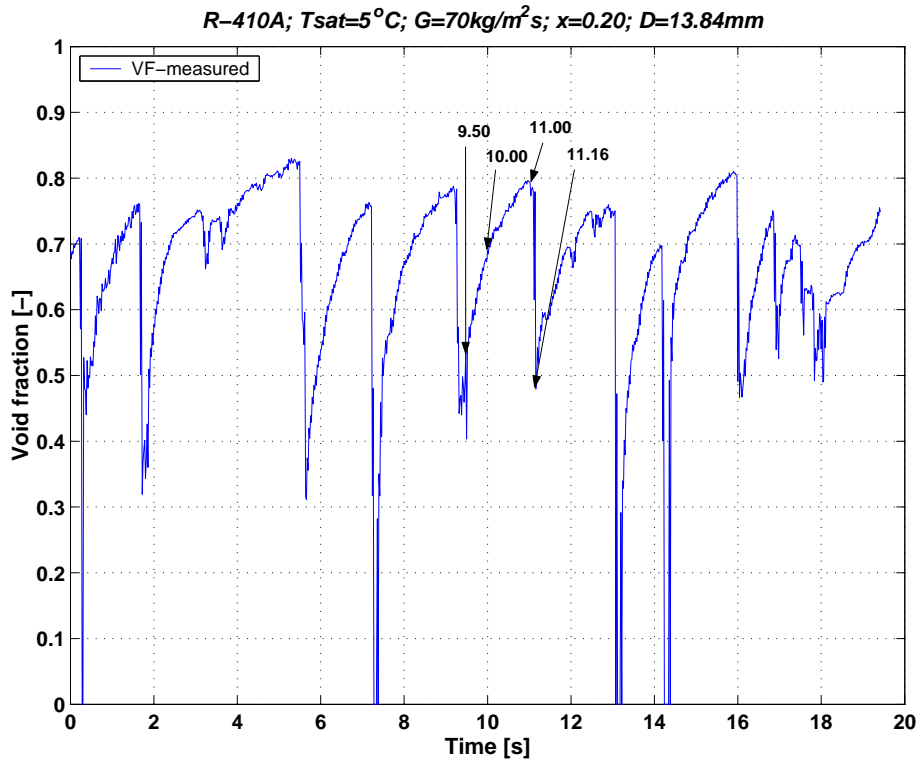


Figure 5.3: Void fraction evolution for stratified-wavy flow with intermittent flow: R-410A,  $G = 70 \text{ kg/m}^2\text{s}$ ,  $T = 5^\circ\text{C}$ ,  $x=0.200$ ,  $D = 13.60 \text{ mm}$ .

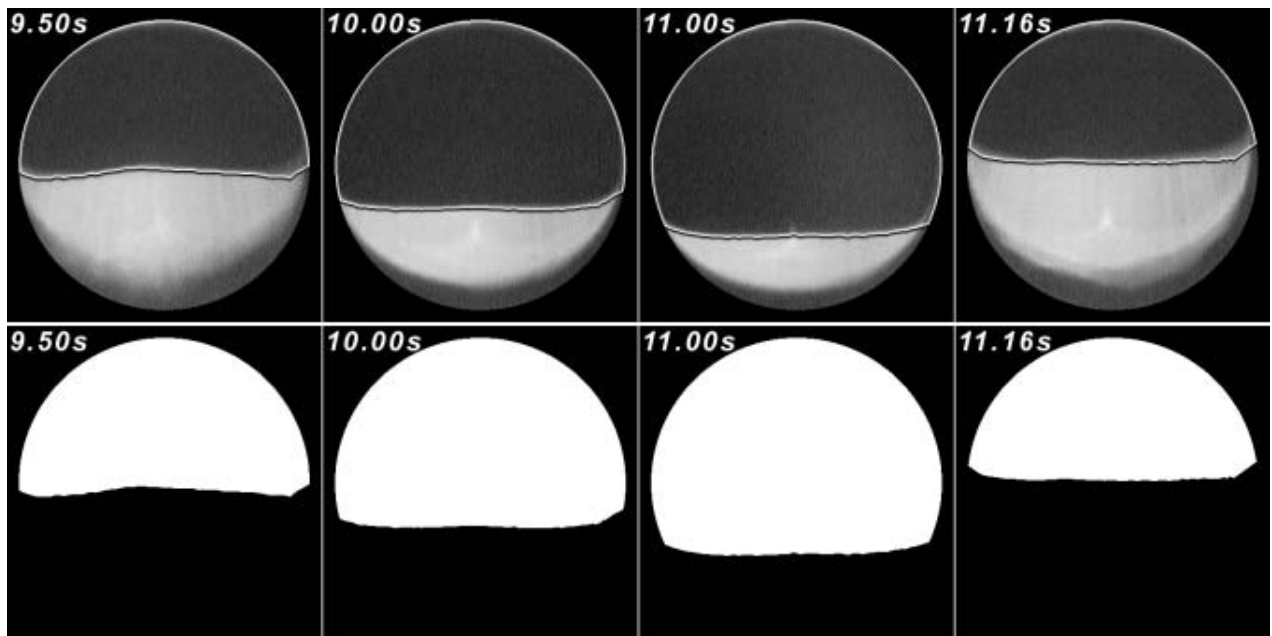


Figure 5.4: Variation of the liquid interface during one wave cycle (from 9.50 to 11.16 seconds): R-410A,  $G = 70 \text{ kg/m}^2\text{s}$ ,  $T = 5^\circ\text{C}$ ,  $x = 0.200$ ,  $D = 13.60 \text{ mm}$ . Transformed images with detected interface (upper part) and final processed images used for void fraction calculation (bottom part).



represent the passage of liquid slugs that fill the entire channel. Figure 5.4 shows selected cross-sectional images within the time interval of 9.50 to 11.16 *seconds*, which correspond to the passage of a wave with respective void fractions of 0.537, 0.685, 0.794 and 0.479. There are two groups of images corresponding to two different steps of the image processing. The first group (top) is obtained after optical transformation and interfacial detection (black curves). As can be seen, the position of interface is precise and parameters like the dry angle and the liquid height can be very accurately determined. The second group (bottom) illustrates the final black and white processed images used for void fraction calculation. The cross-sectional area below the gas/liquid interface is filled with black color and represents the liquid phase. Inversely, the white color corresponds to the gas phase. The cross-sectional void fraction is thus calculated from the ratio of the white pixels to the total number of pixels of the channel.

The second case is presented in Figure 5.5 for a slug flow with R-410A. The mass velocity is  $G = 150 \text{ kg/m}^2\text{s}$  and vapor quality is  $x = 0.103$ . The interfacial profile changes more rapidly compared to the previous case. Indeed, the periods of waves are shorter and the whole tube perimeter is wetted more frequently by liquid slugs. The recorded sequence contains about 20 large amplitude wave passages that should give a good representation of the time-averaged void fraction value. The transformed images in the upper part of Figure 5.6 depict specific cross-sectional views due to passage of a liquid slug. For this very high frequency phenomenon (only 0.06 *seconds* between first and last image), the dynamic interface detection between gas and liquid remains accurate, even if a very small vapor zone has not been detected (the "tooth" in the 2.82 *seconds* image in the upper group). Concerning the same image, the interface detected seems to be very rough, especially close to the internal tube surface at the right side. The surface detection technique is directly based on the absolute luminance signal. If the distinction of the interface is locally perturbed by a shadow (issued from a rhodamineB deposit or from a moisture droplet), the detection will be directly influenced and such a rough interface (which probably has no fluid dynamic sense) will appear. A smoothing function could be applied on the interface profile to eliminate these minor anomalies, but the influence in terms of void fraction measurement error is very low, and thus the technique remains very accurate without such an intervention. Concerning the lower images in Figure 5.6, the corresponding black-and-white images used to identify the surface of the vapor zone are shown, which are used for the void fraction calculation.

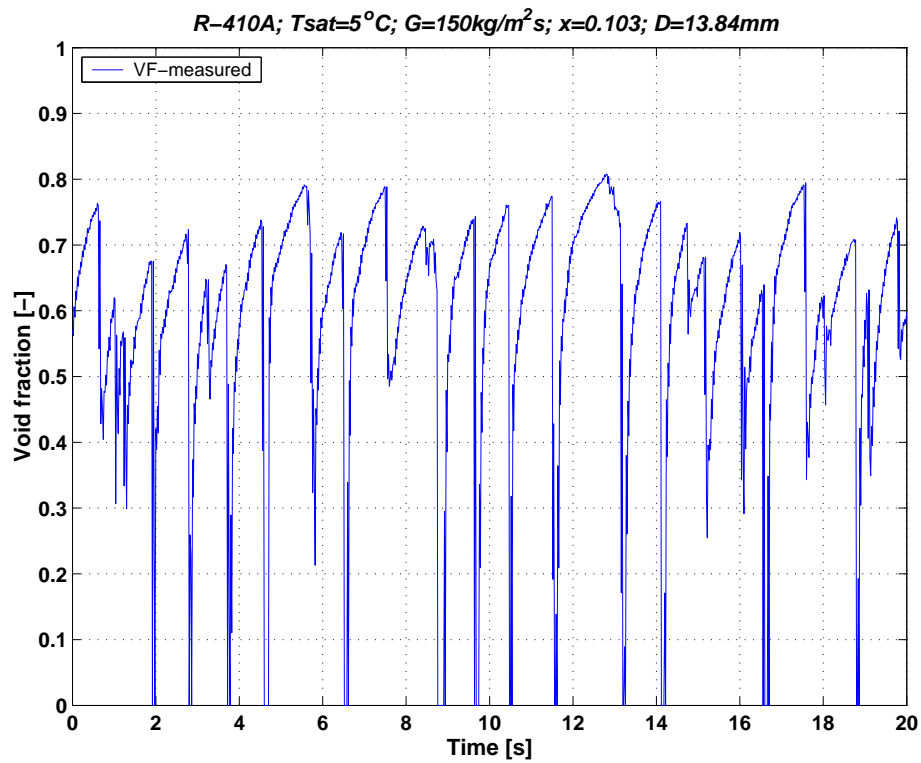


Figure 5.5: Void fraction distribution for slug flow: R-410A,  $G = 150 \text{ kg/m}^2\text{s}$ ,  $T = 5^\circ\text{C}$ ,  $x = 0.103$ ,  $D = 13.60 \text{ mm}$ .

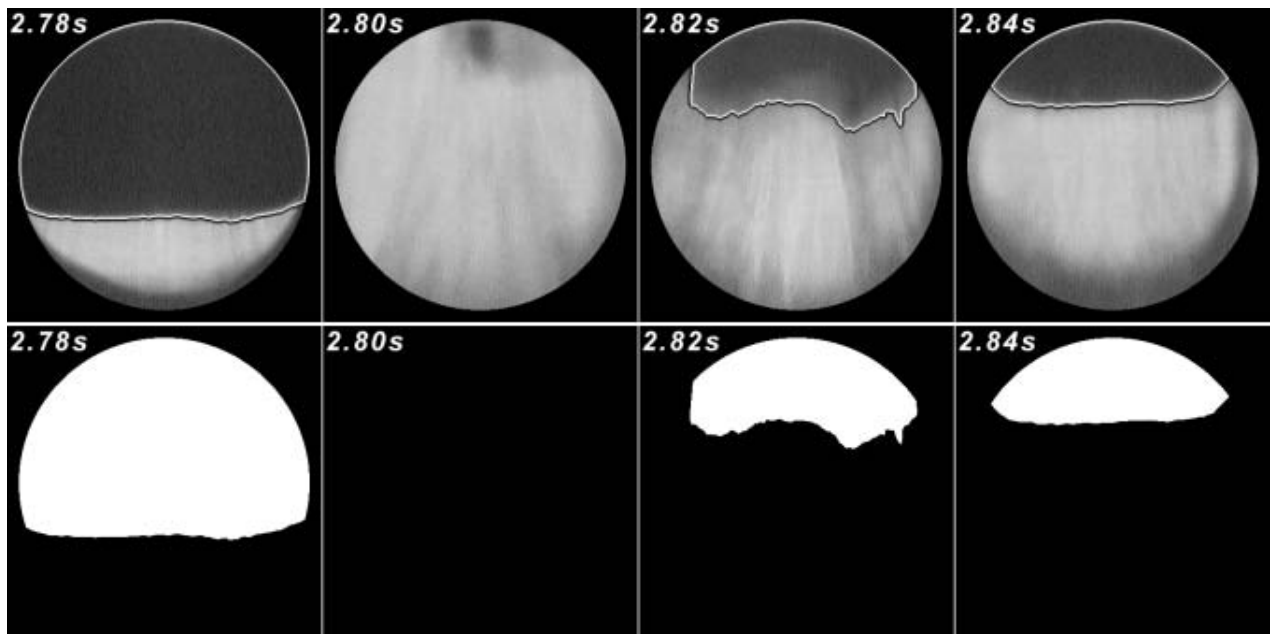


Figure 5.6: Variation of the liquid interface for slug flow: R-410A,  $G = 150 \text{ kg/m}^2\text{s}$ ,  $T = 5^\circ\text{C}$ ,  $x = 0.103$ ,  $D = 13.60 \text{ mm}$ . Transformed images with detected interface (upper part) and final processed images used for void fraction calculation (bottom part).

Reviewing the literature, nearly all slug flow length and frequency data and prediction methods are for air-water and air-oil adiabatic flows, which are quite different that the current test conditions, chosen specifically for examining evaporating flows of refrigerants, *e.g.* a widely used industrial process in refrigeration and air-conditioning systems. Extrapolating, the method of Tronconi [56] (1990) for instance to the present conditions, where his slug frequency  $\omega$  is predicted to be:

$$\omega = 0.61 \frac{\rho_V u_V}{\rho_L (D - h_L)} \quad (5.48)$$

it overpredicts a sampling of slug frequencies, deduced from our measurements, by a factor of 2 to 3. Hence, one can conclude that air-water data and prediction methods for slug frequency are not representative for typical working fluids (refrigerants and hydrocarbons) that have much lower surface tensions and contact angles.

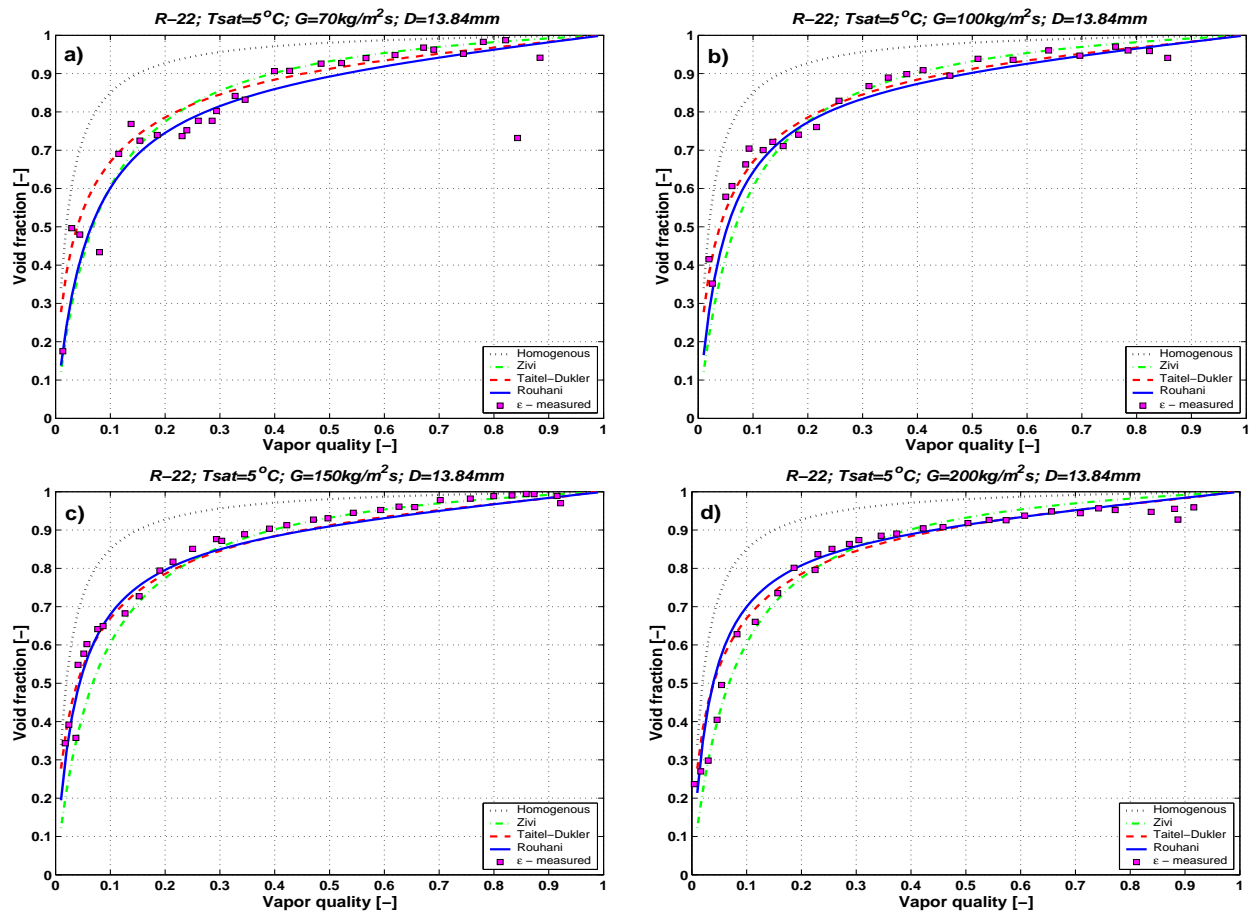


Figure 5.7: Evolution of the void fraction as a function of vapor quality for R-22 in the 13.60 mm sightglass at four mass velocities: a) 70, b) 100, c) 150 and d) 200  $\text{kg/m}^2\text{s}$ .

Based on the 238 image sequences obtained experimentally in the 13.60 mm sightglass tube, 238 time-averaged values of void fraction were determined. The results obtained for R-22 and R-410A are shown in Figure 5.7 and Figure 5.8, respectively. The experimental time-averaged void fractions are presented as a function of vapor quality (square points) and are compared with the homogeneous model (dotted line), the Zivi model (dash-dotted line), the Taitel-Dukler model (dashed line) and the Steiner version of the Rouhani-Axelsson drift flux void fraction model (solid line).

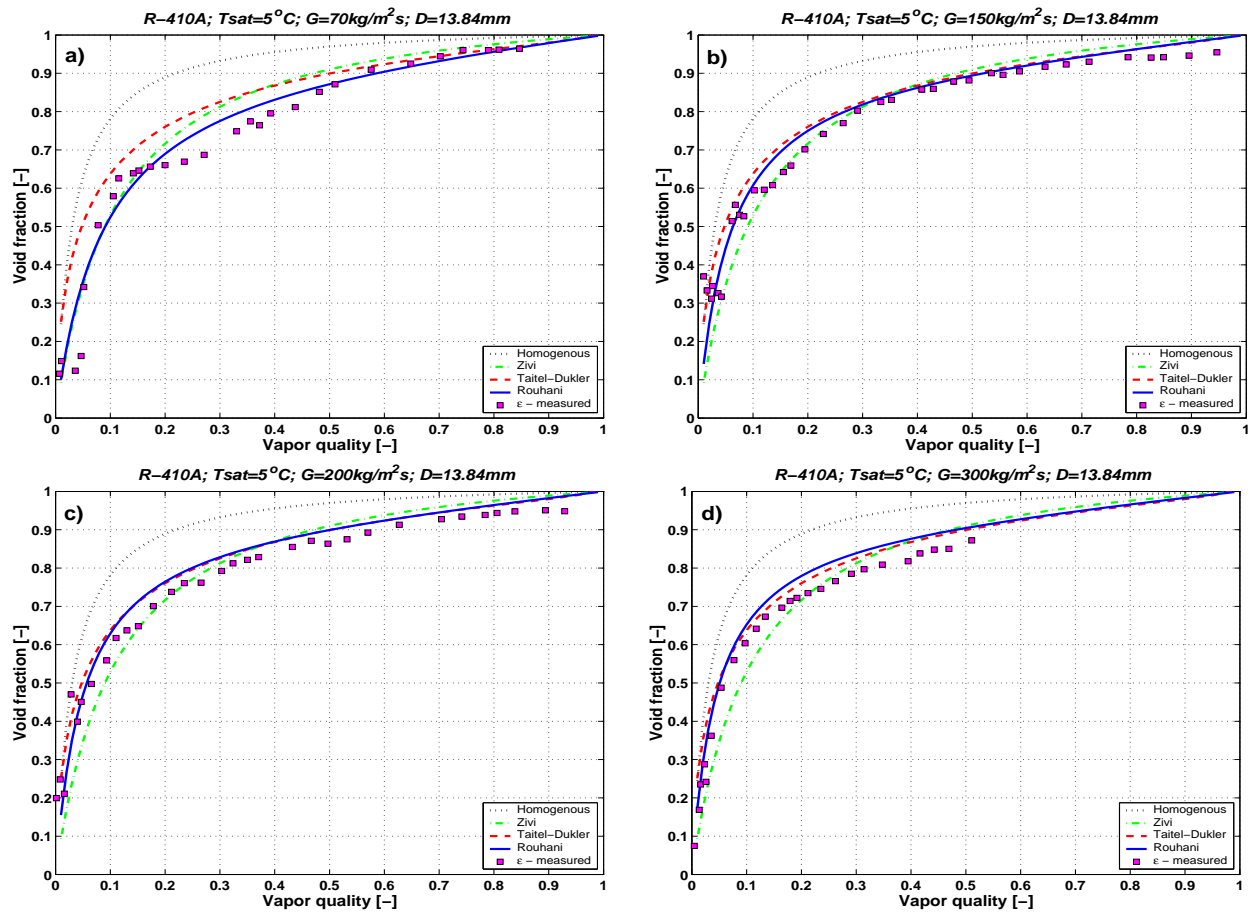


Figure 5.8: Evolution of the void fraction as a function of vapor quality for R-410A in the 13.60 mm sightglass at four mass velocities: a) 70, b) 150, c) 200 and d) 300  $kg/m^2s$ .

The comparison with the homogeneous model has been presented as the limiting case in which vapor and liquid travel with the same velocity. As expected, there is a huge difference between measured and homogeneous void fraction in all tests. The second void fraction model used for comparison is the correlation of Zivi presented in section 5.1.2. As can be seen in Figure 5.7 and Figure 5.8, kinetic energy model of Zivi significantly underpredicts void fraction almost for all tests in the vapor quality range  $0 \leq x \leq 0.2$ . For higher vapor

qualities the model of Zivi predicts void fraction correctly and particularly well for the R-22 tests. The predicted void fraction using the models of Taitel-Dukler and Rouhani-Axelsson is similar for the mass velocities  $G \geq 100 \text{ kg/m}^2\text{s}$  and it shows good agreement with the experimental results. The model of Rouhani-Axelsson, contrary to that of Taitel-Dukler, is a function of mass velocity. This effect was presented for refrigerant R-410A in Figure 5.2. It shows that the void fraction decreases with decreasing mass velocity and the difference between void fraction calculated for  $G = 70 \text{ kg/m}^2\text{s}$  and  $G = 150 \text{ kg/m}^2\text{s}$  is quite significant.

To allow a quantitative comparison between experimental results and the four void fraction models, the results are now compared to the methods through three statistical errors.

The relative error between the predicted and measured void fraction is:

$$\varepsilon_i = \frac{(\varepsilon_{model} - \varepsilon_{meas})}{\varepsilon_{meas}} \quad (5.49)$$

The average deviation is:

$$\bar{\varepsilon} = \frac{1}{n} \sum_{i=1}^n \varepsilon_i \quad (5.50)$$

and defines how centered is prediction to measured points.  $\bar{\varepsilon} = 0$ , if the data are exactly centered.

The mean deviation is:

$$|\bar{\varepsilon}| = \frac{1}{n} \sum_{i=1}^n |\varepsilon_i - \bar{\varepsilon}| \quad (5.51)$$

and defines the intensity of deviation by the global sum of each local deviation. It shows how large is the scattering of the experimental points with respect to prediction.

The standard deviation is:

$$\sigma = \sqrt{\frac{1}{n-1} \sum_{i=1}^n (\varepsilon_i - \bar{\varepsilon})^2} \quad (5.52)$$

and calibrates for  $\bar{\varepsilon} \pm \sigma$  the location of  $\approx 68\%$  of statistical occurrence. Twice the standard deviation value  $\pm 2\sigma$  increases the statistical occurrence to  $\approx 96\%$ .

Test	Model	$\bar{\varepsilon}$ (%)	$ \bar{\varepsilon} $ (%)	$\sigma$ (%)
<b>R-22</b> , $G = 70 \text{ kg/m}^2\text{s}$	Homogenous	22.0	16.7	28.2
	Zivi	1.2	7.5	13.0
	Taitel-Dukler	6.8	10.4	18.2
	Rouhani	-1.2	6.6	11.7
<b>R-22</b> , $G = 100 \text{ kg/m}^2\text{s}$	Homogenous	15.8	10.5	13.6
	Zivi	-5.8	9.6	12.8
	Taitel-Dukler	-0.1	3.5	5.6
	Rouhani	-4.1	4.8	7.7
<b>R-22</b> , $G = 150 \text{ kg/m}^2\text{s}$	Homogenous	14.7	13.0	17.8
	Zivi	-6.7	8.9	11.9
	Taitel-Dukler	-0.4	3.6	7.3
	Rouhani	-1.6	3.3	6.7
<b>R-22</b> , $G = 200 \text{ kg/m}^2\text{s}$	Homogenous	18.0	17.4	25.7
	Zivi	-3.8	7.7	15.1
	Taitel-Dukler	3.4	7.6	13.0
	Rouhani	2.9	7.6	15.1
<b>R-410A</b> , $G = 70 \text{ kg/m}^2\text{s}$	Homogenous	47.2	43.4	77.6
	Zivi	8.7	16.3	32.1
	Taitel-Dukler	30.6	37.5	61.8
	Rouhani	7.0	16.6	33.8
<b>R-410A</b> , $G = 150 \text{ kg/m}^2\text{s}$	Homogenous	20.4	15.6	20.7
	Zivi	-6.8	13.0	18.4
	Taitel-Dukler	6.5	7.7	12.6
	Rouhani	0.1	7.4	14.3
<b>R-410A</b> , $G = 200 \text{ kg/m}^2\text{s}$	Homogenous	14.9	13.9	22.5
	Zivi	-8.6	15.9	23.1
	Taitel-Dukler	3.7	6.4	14.7
	Rouhani	-1.1	9.8	18.8
<b>R-410A</b> , $G = 300 \text{ kg/m}^2\text{s}$	Homogenous	31.5	16.3	21.9
	Zivi	-9.0	12.5	15.0
	Taitel-Dukler	17.3	19.3	28.5
	Rouhani	9.6	5.5	8.8
<b>Overall statistical results</b>	Homogenous	23.1	18.3	28.5
	Zivi	-3.9	11.4	17.7
	Taitel-Dukler	8.5	12.0	20.2
	Rouhani	1.5	7.7	14.6

Table 5.1: Statistical analysis of the void fraction results in the 13.60 mm sightglass.

Table 5.1 shows the statistical analysis of the void fraction results in the 13.60 mm sightglass. The results shows that the drift flux model of Rouhani-Axelsson predicts the void fraction with the lowest values of average, mean and standard deviation in most of the tests. Also quite accurate prediction is obtained with the model of Taitel-Dukler, which in four from eight tests produces the smallest standard deviation. The mean value of standard deviation of Taitel-Dukler method calculated for all eight tests is 20.21% is much higher compared to 14.61% of Rouhani-Axelsson.

Regarding to the experimental points of time-averaged void fractions, which follow those predicted by the model of Rouhani-Axelsson, Taitel-Dukler and Zivi for higher  $x$ , it is surprising to see quite high values of standard deviation. The reason of this are the measurements at low vapor quality ( $x < 0.1$ ), where some successive points present a discontinuous evolution of time-averaged void fraction, especially for measurements at low mass velocity ( $G = 70 \text{ kg/m}^2\text{s}$  for R-22 and R-410A, Figure 5.7a and Figure 5.8a, respectively). For example, referring to the values of  $x \approx 0.05$  in Figure 5.8a, which are too low relative to expectations. Two specific parameters can explain such deviations, a non-representative acquisition time period (an issue discussed below) and the maximum errors  $\pm 2\%$  in energy balances discussed in section 4.5.

Figure 5.9 shows void fraction as a function of time for R-410A at  $G = 70 \text{ kg/m}^2\text{s}$  (a relatively low mass velocity) and  $x = 0.051$ . Two different trends appear on this graph and seem to be due to two different types of flows. The first is characterized by short slugs (each lasting about 0.5 seconds) and the second represents a long wave (lasting almost 4 seconds). The short slug phenomenon appears to repeat itself (beginning at time 13 seconds) with relatively small void fraction values, but the long wave phenomenon appears completely only one time within the sampling period of 19 seconds in Figure 5.9 with much larger values. This indicates that in this case, the measurement sampling period was too short to capture several cycles of the repeating flow phenomena (not known at the time the sequence was obtained in the experiments), yielding a time-averaged void fraction measurement below the real value in a video sequence dominated by the short slug phenomenon. However, as can be observed for higher mass velocity (Figure 5.5,  $G = 150 \text{ kg/m}^2\text{s}$ ,  $x = 0.103$ ) or for higher vapor quality (Figure 5.3,  $G = 70 \text{ kg/m}^2\text{s}$ ,  $x = 0.200$ ) the acquisition time of 18 seconds to 20 seconds is sufficient to be representative of their time-averaged void fraction values. The points at low vapor quality ( $x < 0.1$ ) give the highest values of relative error. For above experimental point where the measurement sampling period was too short to capture several cycles of the repeating flow phenomena, the relative error ( $\bar{\epsilon}$ ) calculated with respect to the

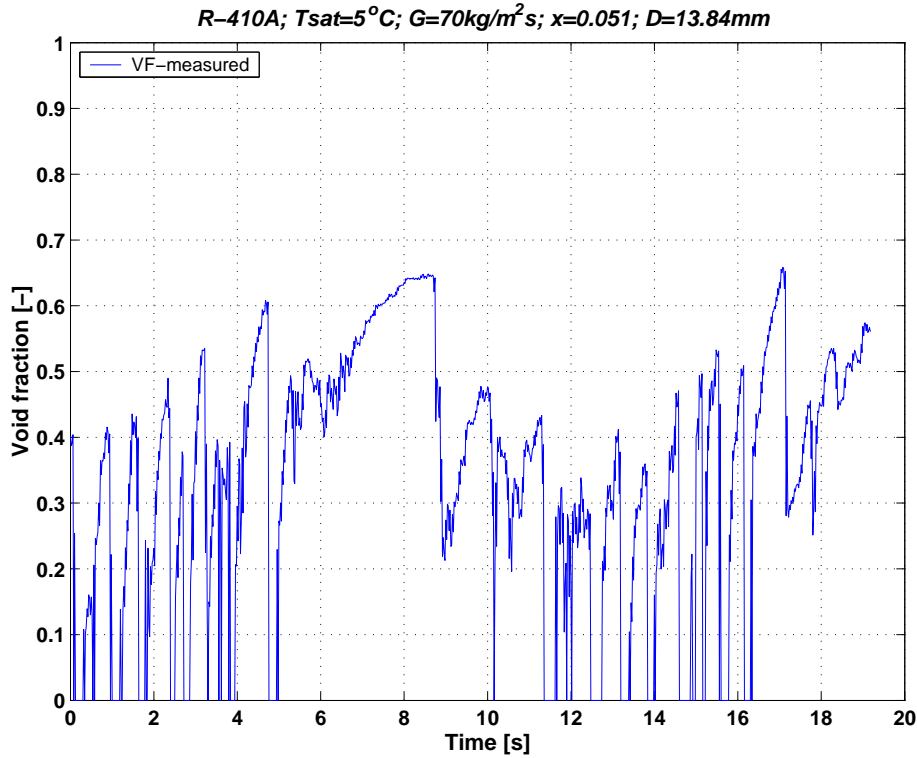


Figure 5.9: Void fraction as a function of time for R-410A,  $G = 70 \text{ kg/m}^2\text{s}$ ,  $T = 5^\circ\text{C}$ ,  $x = 0.051$ ,  $D = 13.60 \text{ mm}$ .

Rouhani-Axelsson model equals 110.9%. As the standard deviation ( $\sigma$ ) calibrates for  $\bar{\varepsilon} \pm 3\sigma$  the location of  $\approx 99.6\%$  statistical occurrence, it is not surprising that for the R-410A test at  $G = 70 \text{ kg/m}^2\text{s}$ ,  $\sigma = 33.8\%$  and  $\bar{\varepsilon} = 7.0\%$ . Making the same statistical analysis for experimental points in the vapor quality range  $0.1 \leq x < 1$ , mean and standard deviations of only 0.88% and 4.9%, will be respectively obtained for the Rouhani-Axelsson model.

The accuracy in the void fraction prediction of the Rouhani-Axelsson model for low vapor qualities ( $x < 0.1$ ) increases with increasing mass velocity and is particularly good for the R-410A test at  $G = 300 \text{ kg/m}^2\text{s}$  presented in Figure 5.8 d. But in this test, in contrast to all the other tests, the time-averaged void fraction measurements for  $x > 0.2$  are noticeably less than those calculated with 5.47. Moreover, due to the quality of the images, the image processing was stopped for  $x > 0.5$ . The reason was the type of flow, *i.e.* annular. In fact, for  $x < 0.5$ , an annular flow was already present, but the film thickness was too thin to be detected by the image processing. By viewing the original image sequences, it is possible to imagine an annular flow, because local deposits of rhodamineB with their characteristic white spots are immediately washed away by the flow. However, at this mass velocity and



for  $x \approx 0.4$ , the flow field is clearly not characterized by slugs nor by stratified-wavy flow. The internal surface of the tube is washed only in the presence of an annular flow. Thus, the presence of a very thin liquid film modifies the optical reflection of light through the glass tube and as a result, the interface is incorrectly measured as being higher than it actually is. Consequently, the measured void fraction is slightly lower than the real value. Concerning the images for  $x > 0.5$ , either they appear completely blurred or the image processing detected a liquid film at the top and the measured void fractions tend to zero, which is not feasible. As noted in section 3.2, the present method is not currently applicable to annular flow, nor to slug flows with significant entrainment of bubbles, and neither when bubbles support a liquid film on the upper perimeter.

For the tests in stratified types of flow at high vapor quality (where  $x > 0.4$ ), deposition of rhodamineB on the internal surface of the tube produced some spurious bright spots on the acquired images. These intense white spots disturbed the interface detection process and they were very often identified incorrectly by the image processing program as a limit of the liquid phase. Because the spots are systematically located on the "dry" upper perimeter of the tube, when this deposition occurs the resulting void fraction measurements tend to yield lower time-averaged values than the actual ones (images with such spots tend to give void fractions of about zero). These difficulties start to appear at  $x \approx 0.5$ , and become much more important for  $x > 0.9$ . Thus, for some tests, a filtering procedure of the results was required to remove the sporadic appearance of these spotted images. To do this, a void fraction threshold was fixed by optically analysing the superposition of the transformed images and the respective detected interfaces (like the images in the upper series of the Figures 5.4 and 5.6). Below the threshold, all the results are automatically suppressed. Figure 5.10 shows the void fraction distribution before and after such filtering for R-410A,  $G = 200 \text{ kg/m}^2\text{s}$  and vapor quality  $x = 0.497$ . In this case, the void fraction threshold was set at 0.6 and only 21 values have been deleted from the 885 total (no liquid slugs occupying a large fraction of the channel are seen visually in these flows and hence it is clear that these 21 images do not represent the flow but only occasional "sparkling" on the upper perimeter). The most intensive filtering was required for vapor qualities above 0.9. For these test conditions, the fraction of the remaining liquid phase is extremely small and the deposition of rhodamineB from evaporated refrigerant forms a thin layer on the upper dry perimeter of the glass tube. Therefore, the highest void fraction threshold processed was 0.9 and in the worst case only 25% of the images were suitable for the mean void fraction calculation (*i.e.* about 250 images).

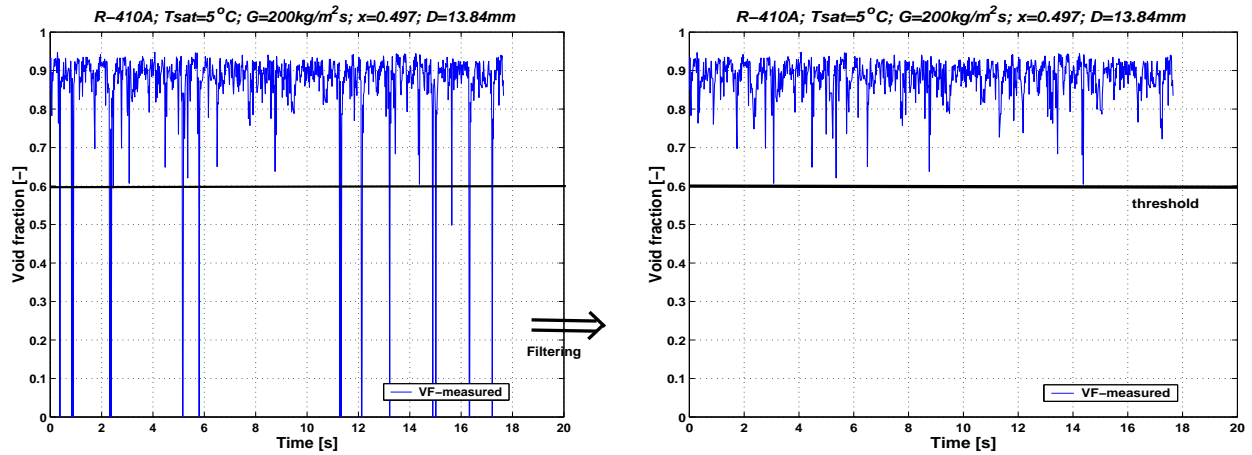


Figure 5.10: Filtering of void fraction signal for R-410A,  $G = 200 \text{ kg/m}^2\text{s}$ ,  $T = 5^\circ\text{C}$ ,  $x = 0.497$ ,  $D = 13.60 \text{ mm}$ .

For tests in the  $8.00 \text{ mm}$  sightglass, liquid slugs and high amplitude-waves tend to leave a liquid film behind on the top of the tube. This liquid film is thicker compared to the  $13.60 \text{ mm}$  sightglass and causes a perturbation in the liquid interface detection. Figure 5.11 shows a sequence acquired during the test with R-22 at mass velocity  $G = 150 \text{ kg/m}^2\text{s}$  and vapor quality  $x = 0.676$  with successive steps of image processing. As it can be seen in Figure 5.11a, the acquired image is badly blurred by the upper film of the liquid (bright white arc around upper perimeter).

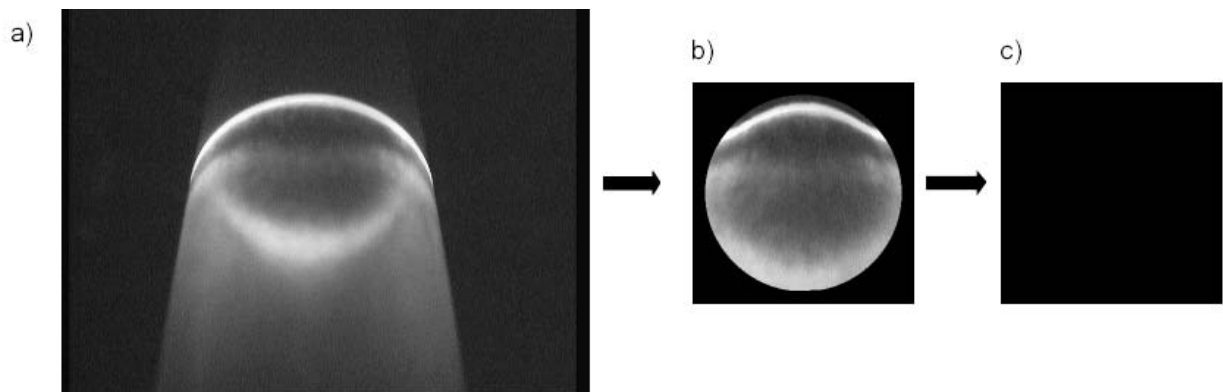


Figure 5.11: Images for test: R-22,  $G = 150 \text{ kg/m}^2\text{s}$ ,  $T = 5^\circ\text{C}$ ,  $x = 0.676$  in the  $8.00 \text{ mm}$  test section. a) Acquired image of the cross-section at  $2.36 \text{ seconds}$  of acquisition, b) Transformed image, c) Final processed image used for void fraction calculation.

Figure 5.11b and 5.11c show the acquired image after optical transformation and the processed image used for void fraction calculation. As can be expected, as detected by the image

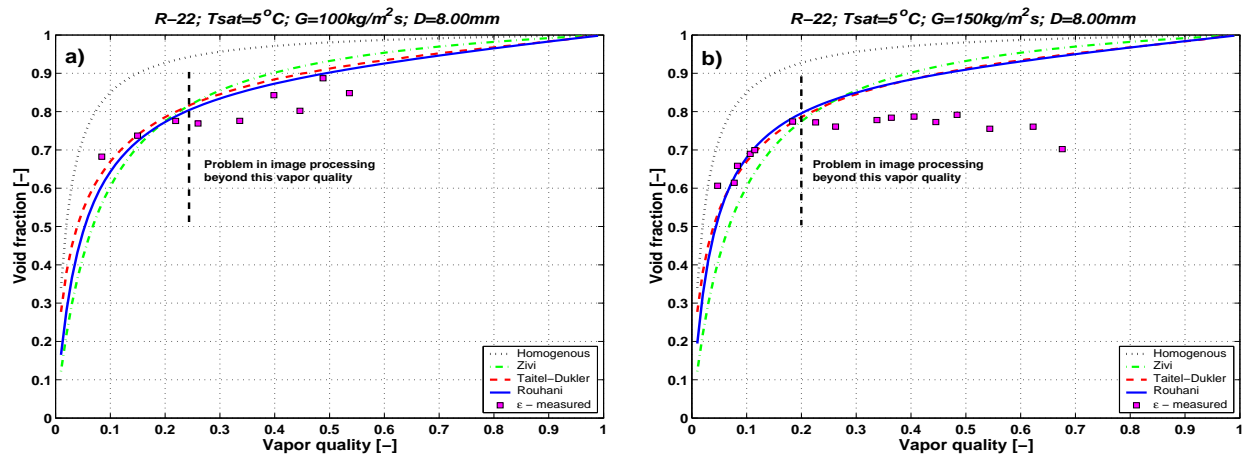


Figure 5.12: Evolution of the void fraction as a function of vapor quality for R-22 in the 8.00 mm sightglass at two mass velocities: a) 100, b) 150  $kg/m^2s$ .

processing program, the void fraction for this point equals 0, what is of course not true. The presence of the liquid film on the upper perimeter of the tubular sightglass creates an additional refraction in viewing of the interface by the camera. If this film is extremely thin and its interface is smooth, then the measurement technique is not noticeably affected. However, if the film is not so thin and not smooth, then the image is blurred and the location of the stratified liquid cannot be determined. Consequently, this is a limitation of the range of application of this technique. A second important issue of tests in the 8.00 mm sightglass is the smaller resolution of transformed images. The resolution of any transformed image from the 8.00 mm sightglass is 301x301 pixels while that for the 13.60 mm sightglass is 421x421 pixels. This gives a 48.8% decrease in effective pixels with void fraction information. Furthermore, obtaining quality images suitable for image processing was more difficult due to higher curvature of the smaller tube. Hence, while numerous videos were taken for R-22 and R-410A at several mass velocities each, only a very limited number were able to be processed reliably.

Figure 5.12 shows the results of two tests in the 8.00 mm test section for refrigerant R-22 at mass velocities  $G = 100$  and  $150 kg/m^2s$ . The result of the test at  $G = 200 kg/m^2s$  for R-22 and two other tests for refrigerant R-410A provided poor quality images influenced by the presence of the thin liquid layer on the tube's upper wall. The vapor quality beyond which image processing problems started has been indicated with the vertical dashed lines. All results for vapor qualities above this point are strongly effected by the presence of the liquid film on the upper perimeter of the sightglass and even a filtration process of the

images could not eliminated the false detection of the stratified liquid interface. Hence, for this reason in the 8.00 mm sightglass, only a limited data range can be considered as correct. The data on the right side of the vertical line are not valid and are only shown to illustrate the problem; from 87 acquired points, only 9 points at lowest vapor qualities and mass velocities represent real void fractions. Table 5.2 shows results of statistical analysis for those 9 experimental points. As it can be seen, the lowest values of average, mean and standard deviation are obtained for the Taitel-Dukler and the Rouhani-Axelsson models. The model of Zivi underpredicts void fraction at low vapor quality like in the tests in the 13.60 mm sightglass. The homogeneous model as a limiting case overpredicts void fraction significantly with the the overall average deviation of 22.4%.

Test	Model	$\bar{\varepsilon}$ (%)	$ \bar{\varepsilon} $ (%)	$\sigma$ (%)
<b>R-22</b> , $G = 100 \text{ kg/m}^2\text{s}$	Homogenous	21.1	0.6	0.8
	Zivi	-6.6	7.7	10.5
	Taitel-Dukler	-1.0	3.6	4.9
	Rouhani	-3.9	4.9	6.6
<b>R-22</b> , $G = 150 \text{ kg/m}^2\text{s}$	Homogenous	23.8	3.5	5.0
	Zivi	-13.7	7.2	10.6
	Taitel-Dukler	-2.8	3.4	4.9
	Rouhani	-2.1	4.3	6.4
<b>Overall statistical results</b>	Homogenous	22.4	2.1	2.9
	Zivi	-10.2	7.4	10.5
	Taitel-Dukler	-1.9	3.5	4.9
	Rouhani	-3.0	4.6	6.5

Table 5.2: Statistical analysis of the void fraction results in the 8.00 mm sightglass.

### 5.3 Dynamic dry angle measurements

It has been observed during experiments that the liquid film climbing on the sides of tube above the stratified bulk liquid after passage of a slug or wave was very thin and this film was not always detected by the optical void fraction measurement system. Thus, the optical method finds rather dry angles produced by the stratified liquid bulk than the "real dry angles" defining the dry tube perimeter. Figures 5.13 and 5.14 present the experimental values of dry angle obtained from processing the videos. The dry angles shown are time-averaged values. The maximum feasible dry angle can be predicted by assuming a completely

stratified flow, that is  $\theta_{strat}$  calculated from the expression of Biberg presented in equation 2.35 using the Steiner version of Rouhani-Axelsson void fraction - equation 5.47. As can be

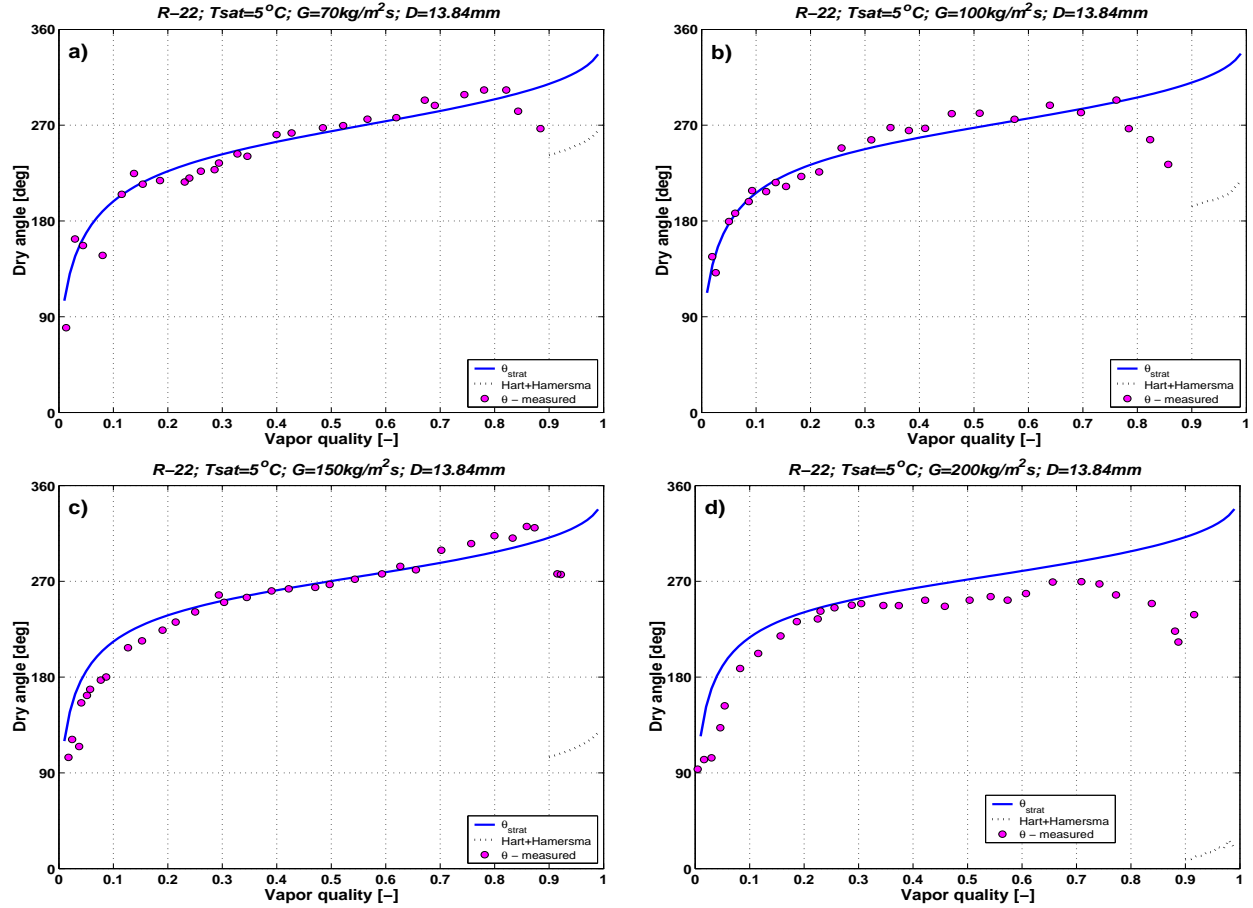


Figure 5.13: Evolution of the dry angle as a function of vapor quality for R-22 in the 13.84 mm test section at four mass velocities: a) 70, b) 100, c) 150 and d) 200  $kg/m^2s$ .

seen, most of the measured values are equal to or less than this maximum value, and are quite well represented by this simple prediction. In Figure 5.14d, annular flow as encountered at  $x = 0.52$  and hence no data for  $x > 0.52$  are measurable using our technique.

Also shown in Figures 5.13 and 5.14 is a comparison to the dry angle prediction method proposed by Hart *et al.* [23] (1989). This method is only applicable at high liquid holdups and is seen to give much lower values than observed here (it was developed from air-water data). Even with our measurement limitations at high vapor qualities as noted above, visual observations show that they were certainly not as low as Hart's predictions shown in Figure 5.13(c,d) and 5.14(b,c). This illustrates the significant difference between refrigerants and water in such flows and demonstrates why air-water flows are not often representative of

most working fluids, which have much smaller surface tension and contact angles.

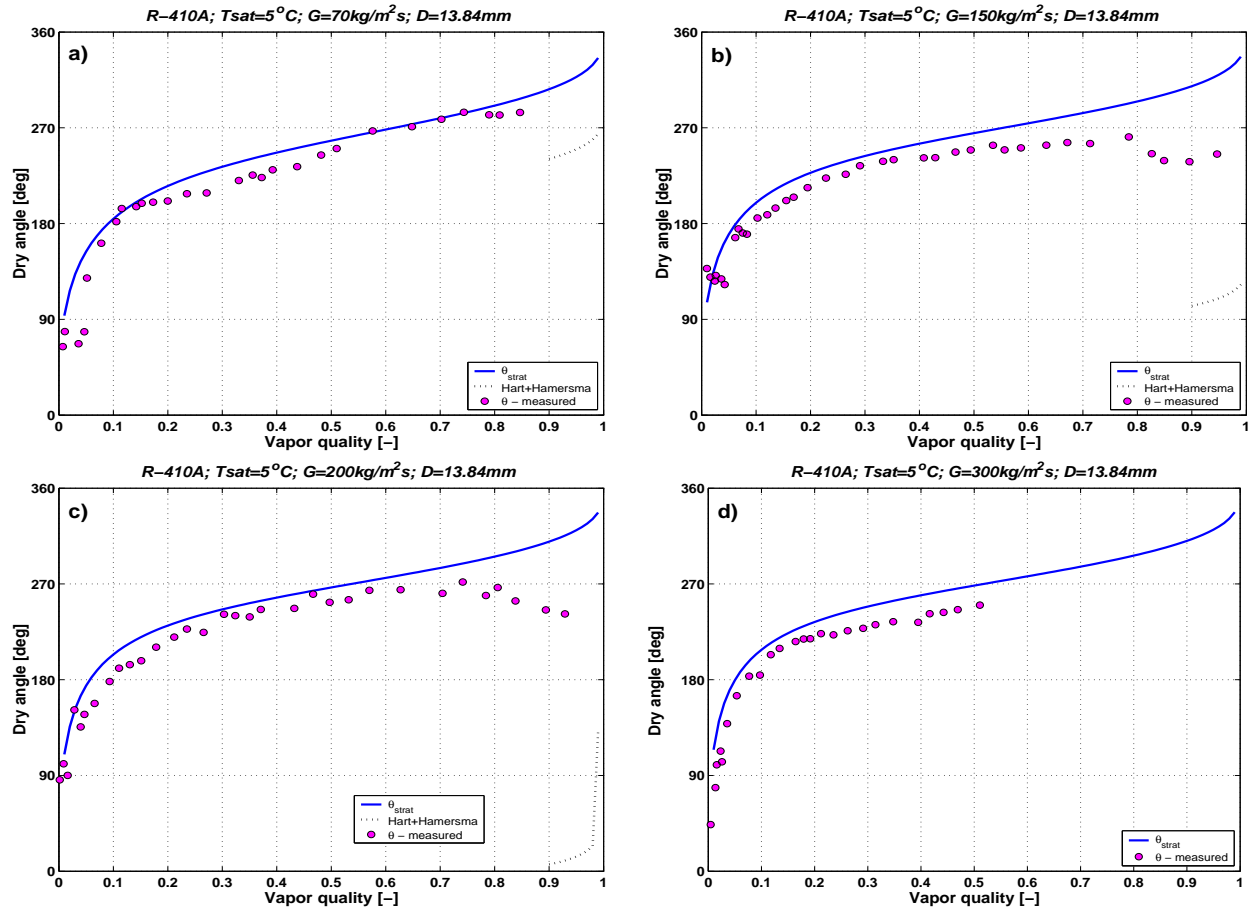


Figure 5.14: Evolution of the dry angle as a function of vapor quality for R-410A in the 13.60 mm test section at four mass velocities: a) 70, b) 150, c) 200 and d) 300  $kg/m^2s$ .

Figure 5.15 shows the measured dry angles in the 8.00 mm sightglass compared to  $\theta_{strat}$ . Only valid values not influenced by a presence of the liquid layer on the top of the tube are presented. As for the dry angle calculations, the same video sequences as for the void fraction calculation are used and similar problems in the image processing are encountered, *i.e.* blurred images and higher optical deformation. Thus, the accuracy of the measurement method for the 8.00 mm sightglass is only about  $\pm 0.03$  in void fraction. Even if the accuracy is lower than for tests in the 13.60 mm sightglass, experimental points in Figure 5.15a follow  $\theta_{strat}$ . In the test at  $G = 150 kg/m^2s$  (Figure 5.15b), the liquid film tends to ride up the side walls, reducing the dry angle.

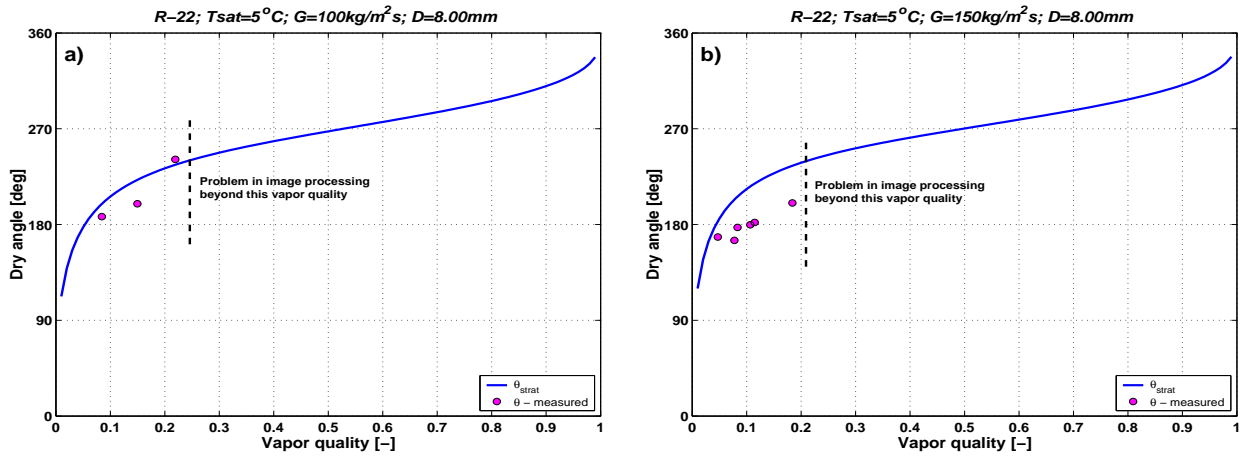


Figure 5.15: Evolution of the dry angle as a function of vapor quality for R-22 in the 8.00 mm test section at two mass velocities: a) 100, b) 150  $\text{kg/m}^2\text{ s}$ .

## 5.4 Conclusions

The tests in the 13.60 mm sightglass provided very good quality video sequences. Using the image processing technique presented in section 3.2, 310 000 images have been analysed to supply the same number of dynamic void fractions measured with the frequency 50 Hz and accuracy of about  $\pm 0.01$ . From these images, 238 time-averaged void fraction values have been obtained for the 13.60 mm sightglass in eight series of tests (two liquids and four mass velocities for each), and are most accurately predicted by the Steiner version of the Rouhani-Axelsson model, whose average and standard deviations are 1.5% and 14.6%, respectively. The larger errors occur mostly for vapor qualities  $x < 0.1$ , for which the acquisition time was too short to capture the cyclic nature of the slugs (discussed in section 5.2.2). For comparison, the average and standard deviations calculated for the measured points at  $x > 0.1$  for the Rouhani-Axelsson model are only 1.57% and 3.89%. For the Zivi and the Taitel-Dukler models at  $x > 0.1$ , the average and standard deviations are: 0.80%, 5.45% and 2.82%, 4.08%, respectively. This confirms that even considering only higher vapor qualities, the prediction of the Rouhani-Axelsson model is the most accurate and that the choice of this model to calculate the geometry of the flow for the flow pattern transitions as well as for the heat transfer prediction is very appropriate. For the tests in the 8.00 mm sightglass, only 9 points have been obtained, due to the presence of a liquid layer on the top of the tube for higher vapor qualities. In these tests, the accuracy of the image processing method was lower compared to the 13.60 mm sightglass test due to smaller image size and higher optical deformation. The same number of time-average dry angles has been obtained

as dynamic void fraction. As the extremely thin liquid film climbing on the sides of the tube wall above the stratified bulk of liquid could not be detected by the void fraction measurement technique, the measured angle corresponds rather to the dry angle produced by the stratified liquid bulk than to the "real dry angle" representing the dry tube perimeter. The measured dry angles show very good agreement compared to  $\theta_{strat}$  calculated from the void fraction model of Rouhani-Axelsson (equations 2.35, 5.47).



# Chapter 6

## Heat transfer coefficient in stratified-wavy flow

The heat transfer model of Kattan-Thome-Favrat was developed for vapor qualities higher than 0.15. According to the last version of the flow pattern map presented in Figure 2.6, all points below vapor quality 0.15 and  $G_{wavy}$  are identified as stratified-wavy and for the lowest mass velocities as stratified flow. In his study, Kattan suggested that the wave frequency in this region is very important and the all wet or partially wet thresholds are the deciding factors for the prediction of heat transfer coefficient. He proposed in the future to divide this zone into two subzones according to an all wet or partially wet criteria. The final version of the heat transfer model of Kattan -Thome-Favrat for the stratified-wavy flow assumes linear variation between 0 for  $G_{wavy}$  and  $\theta_{strat}$  for  $G_{strat}$  according to equation 2.53. Zürcher did not make any changes in the heat transfer model in the stratified-wavy region even if in his study some experimental data points at the lowest vapor qualities are clearly underpredicted by the model of Kattan. A new correlation has been proposed by El Hajal *et al.* [16] (2003b) for calculation of the dry angle in stratified-wavy flow in their new condensation heat transfer model. They assumed a quadratic interpolation between its maximum value of  $\theta_{strat}$  at  $G_{strat}$  and its minimum value of 0 at  $G_{wavy}$  as:

$$\theta_{dry} = \left[ \frac{(G_{wavy} - G)}{(G_{wavy} - G_{strat})} \right]^{0.5} \theta_{strat} \quad (6.1)$$

In this chapter the focus will be on the improving of the heat transfer model of Kattan-Thome-Favrat for stratified-wavy flow based on the new experimental data and observations

made by a dynamic void fraction measurements system. Several improvements will be proposed to the flow pattern map to take into account the observed phenomena and to more correctly calculate the dry angle for stratified-wavy flow for the whole range of vapor qualities.

## 6.1 New approach to dry angle in stratified-wavy flow

As it has been mentioned in section 5.3, it was not possible to obtain directly the dry angle from the optical measurements of void fractions. The measured angles correspond very close to the stratified angles because the liquid film climbing on the sides of the tube wall above the stratified bulk of liquid is extremely thin and was not detected by the optical measurement system described in section 3.2. But along with the dynamic void fraction, the experimental results provide very important information concerning flow structures in tested regions.

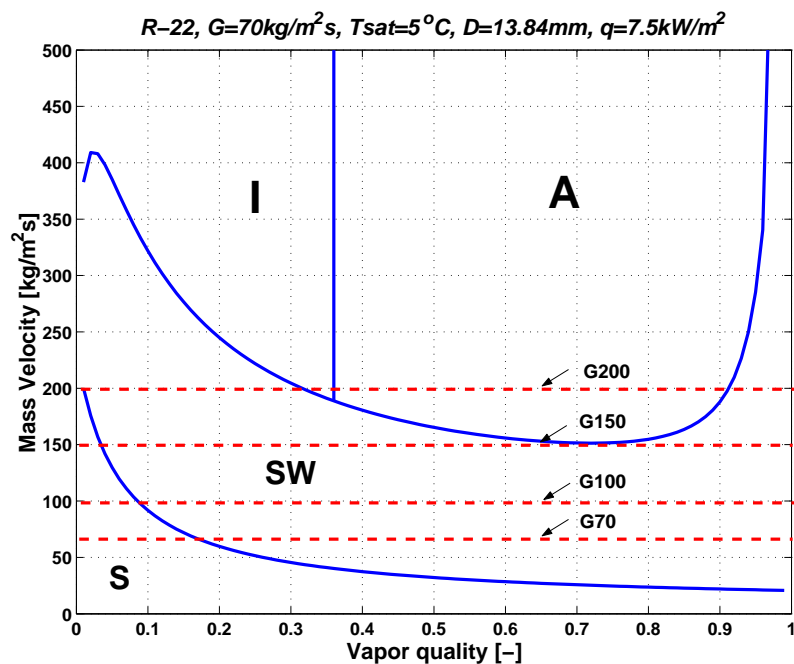


Figure 6.1: Flow pattern map of Thome-El Hajal for R-22 at  $T_{sat} = 5^{\circ}C$  in the 13.84 mm test section at  $G = 70 \text{ kg/m}^2\text{s}$ .

Figure 6.1 shows the Thome-El Hajal version of flow map for R-22 at  $T_{sat} = 5^{\circ}C$  in the 13.84 mm test section with the traced lines at mass velocities the optical measurements of void fraction were performed. As it can be seen at the mass velocity  $G = 70 \text{ kg/m}^2\text{s}$ , the

flow pattern map predicts stratified flow below a vapor quality of 0.15 and above 0.15 it gives stratified-wavy flow. At the highest mass velocity tested  $G = 200 \text{ kg/m}^2\text{s}$ , stratified-wavy flow is predicted in the vapor quality range from 0 to 0.3 and in the partial dryout region at high vapor qualities. For these two mass velocities some experimental data will be discussed.

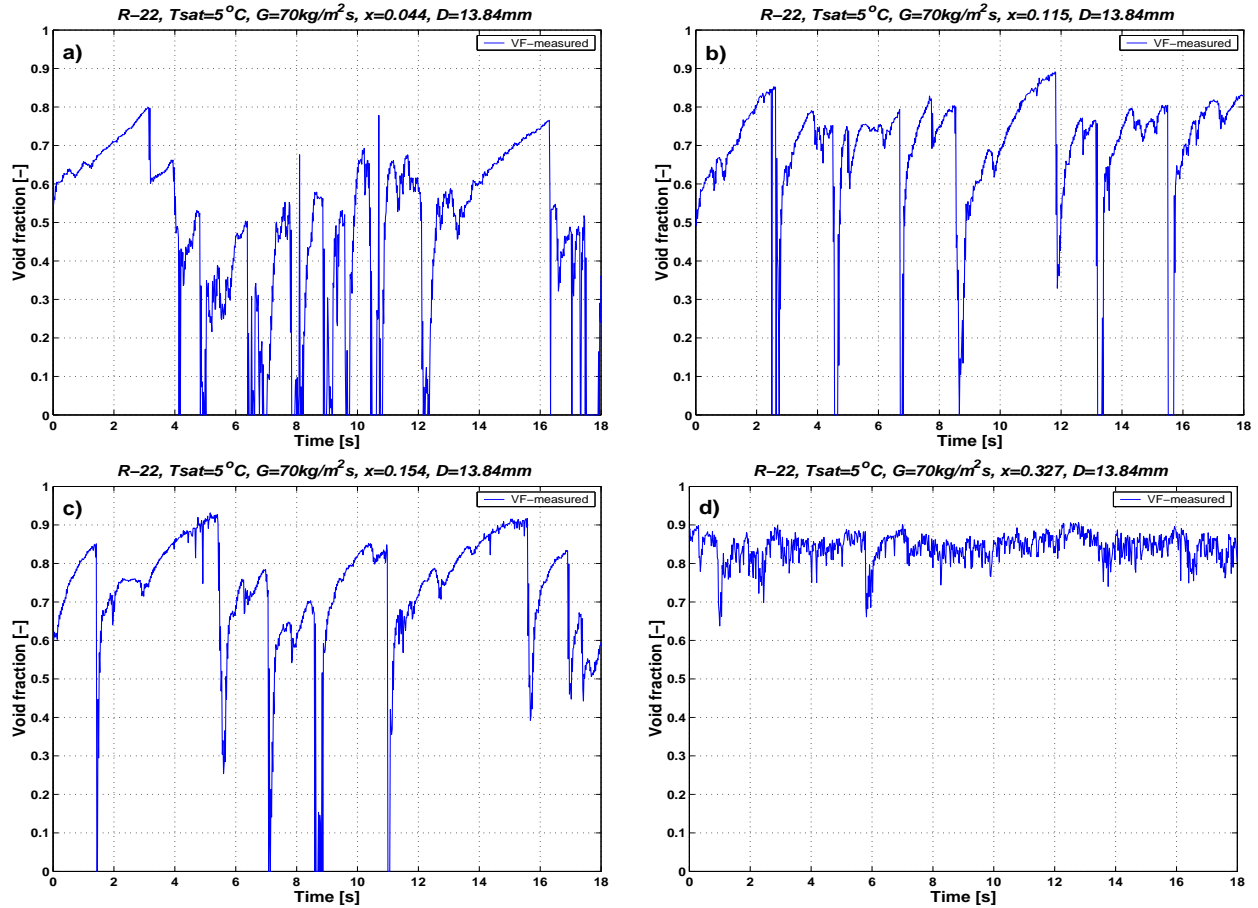


Figure 6.2: Void fraction as a function of time for R-22,  $G = 70 \text{ kg/m}^2\text{s}$ ,  $T = 5^\circ\text{C}$ ,  $D = 13.84 \text{ mm}$  at vapor qualities: a)  $x = 0.044$ , b)  $x = 0.115$ , c)  $x = 0.154$ , d)  $x = 0.327$ .

Figures 6.2a-d show experimental results of void fraction as a function of time for R-22 tested at  $G = 70 \text{ kg/m}^2\text{s}$  and vapor qualities: 0.044, 0.115, 0.154 and 0.327, respectively. For the test at  $x = 0.044$ , two different flow structures can be distinguished: the first one is a long wave lasting almost 4 seconds and the second is the short slugs appearing in-between (each lasting about 1 second). Increasing the vapor quality to  $x = 0.115$ , the slug duration becomes longer (each slug lasts about 2 seconds). Further increasing the vapor quality to  $x = 0.154$  results in fewer slugs with waves becoming dominant. As can be seen in Figure 6.2c, the fluctuations of void fraction are lower and only a few slugs are observed in the test period of 18 seconds (distinguish by void fraction going to zero). At the last vapor quality

with  $x = 0.327$ , fully developed stratified-wavy flow has appeared, which was observed until complete evaporation ( $x \rightarrow 0.95$ ) at the test mass velocity  $G = 70 \text{ kg/m}^2\text{s}$ .

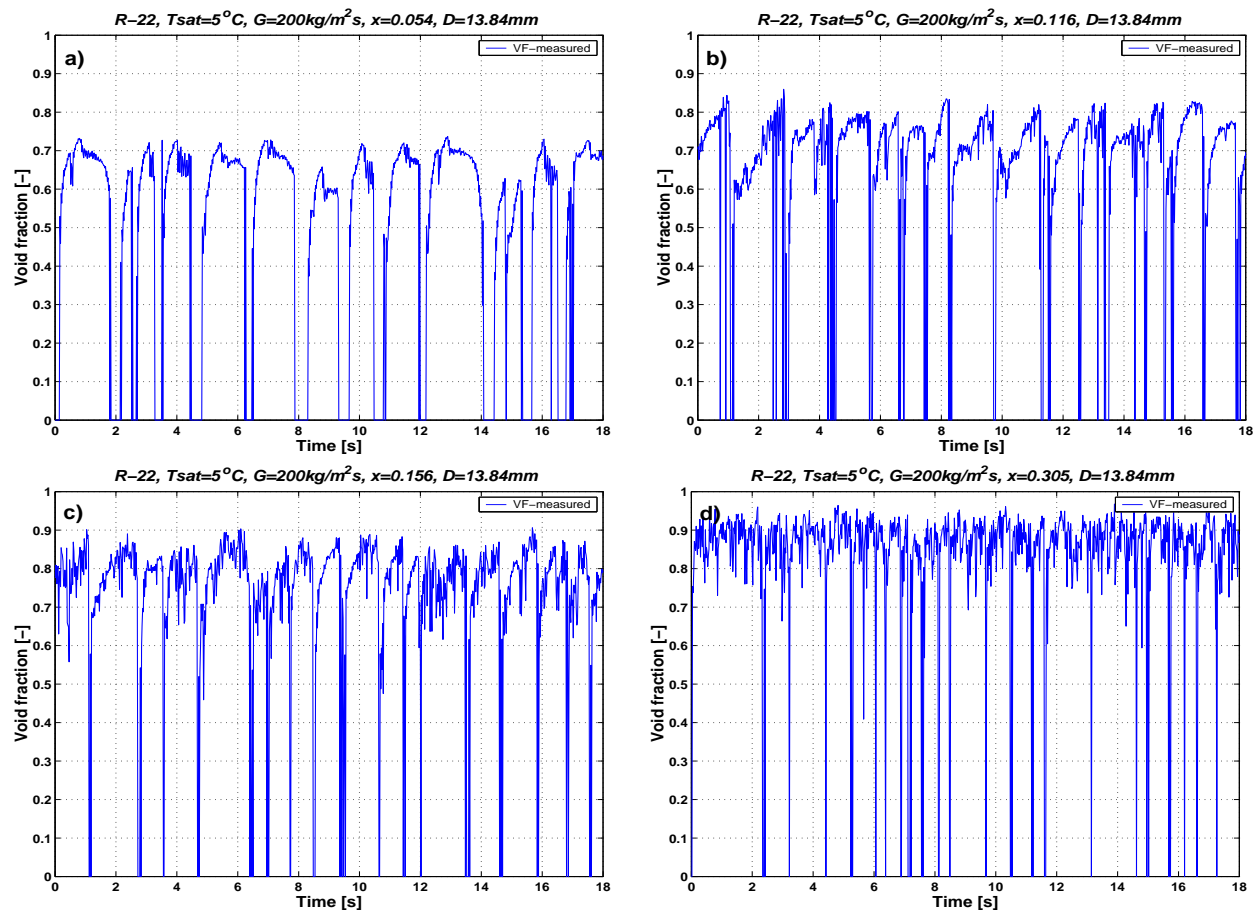


Figure 6.3: Void fraction as a function of time for R-22,  $G = 200 \text{ kg/m}^2\text{s}$ ,  $T = 5^\circ\text{C}$ ,  $D = 13.60 \text{ mm}$  at vapor qualities: a)  $x=0.054$ , b)  $x=0.118$ , c)  $x=0.156$ , d)  $x=0.305$ .

As a comparison Figures 6.3a-d show experimental results of void fraction as a function of time for R-22 tested at  $G = 200 \text{ kg/m}^2\text{s}$  and vapor qualities: 0.054, 0.116, 0.156 and 0.305, respectively. As it can be seen in 6.3a-c, the frequency of slugs systematically increases. The period of slugs can be clearly distinguished and there are no long wave structures between the slugs as detected in the tests at lower mass velocities. At the vapor quality  $x = 0.305$ , slugs start disappearing and a very thin liquid layer appears around the perimeter of sightglass.

Following conclusions can be drawn from above observations and other similar results:

1. Stratified flow was not detected at any tested mass velocity.
2. In the vapor quality range  $0 < x < x_{IA}$ , a mixed flow structure of slug, stratified-wavy

was observed.

3. The transition from slug/stratified-wavy to fully stratified-wavy flow appears approximately at  $x_{IA}$ .
4. Only slug flow was observed in the zone identified by the Thome-El Hajal map to be stratified-wavy in the region when  $G > G_{wavy}(x_{IA})$ .

Based on these observations, the Thome-El Hajal version of map has been modified as:

1.  $G_{strat} = G_{strat}(x_{IA})$  at  $x < x_{IA}$  (creates a horizontal transition line to the left of  $x_{IA}$ ).
2. Stratified-wavy region has been divided into three zones:
  - At  $G > G_{wavy}(x_{IA})$ , this becomes the SLUG ZONE.
  - At  $G_{strat} < G < G_{wavy}(x_{IA})$  and  $x < x_{IA}$ , this becomes the SLUG/STRATIFIED-WAVY ZONE.
  - At  $x \geq x_{IA}$ , this remains as the STRATIFIED-WAVY ZONE.

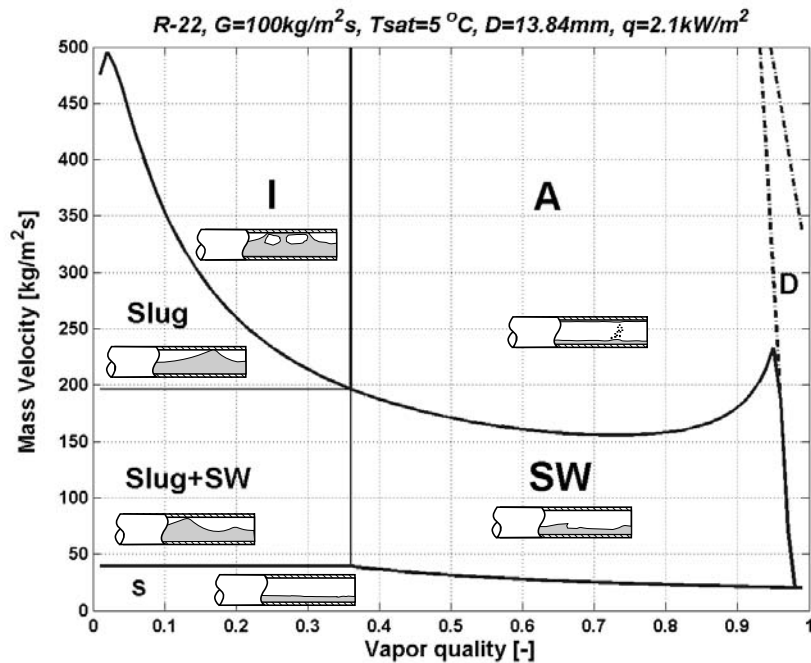


Figure 6.4: New flow pattern map for R-22 at  $T_{sat} = 5^{\circ}C$  in the 13.84 mm test section at  $G = 100 \text{ kg/m}^2\text{s}$  and  $q = 2.1 \text{ kW/m}^2$ .

Figure 6.4 depicts the new flow pattern map evaluated for R-22 at  $T_{sat} = 5^\circ C$  in the 13.84 mm test section at  $G = 100 \text{ kg/m}^2\text{s}$  and  $q = 2.1 \text{ kW/m}^2$ . As can be seen, modifications have been applied to the Thome-El Hajal version of Kattan-Thome-Favrat flow pattern map to better describe the actual character of the flow. The dash-pointed lines correspond to the new dryout and mist flow transitions curves described in the next chapter.

Based on the modifications in flow pattern map, changes to the prediction of dry angles are also desirable. Thus, the following new procedure is proposed for the dry angle calculations in the three new zones:

**SLUG ZONE (Slug):**

The high frequency slugs maintain continuously a thin liquid layer on the tube's upper perimeter. Thus, similarly to the intermittent flow regime:

$$\theta_{dry} = 0 \quad (6.2)$$

**STRATIFIED-WAVY ZONE (SW):**

As it has been mentioned before, a new correlation was proposed by El Hajal *et al.* [16] (2003b) for calculation of the dry angle in stratified-wavy flow in their new condensation heat transfer model. They proposed a quadratic interpolation between its maximum value of  $\theta_{strat}$  at  $G_{strat}$  and its minimum value of 0 at  $G_{wavy}$ . Based on the present experimental heat transfer data for this region, better agreement has been found with an exponent of 0.61 as follows:

$$\theta_{dry} = \left[ \frac{(G_{wavy} - G)}{(G_{wavy} - G_{strat})} \right]^{0.61} \theta_{strat} \quad (6.3)$$

and applied when  $x > x_{IA}$ .

**SLUG/STRATIFIED-WAVY ZONE (Slug+SW):**

In the slug/stratified-wavy zone both low amplitude (which do not reach the top of the tube) waves and liquid slugs washing the top of the tube are observed. With increasing vapor quality in this region, the frequency of slugs decreases and the waves become dominant. The slugs disappear completely approximately at a vapor quality of  $x_{IA}$ . To capture this phenomenon, the following correlation is proposed:

$$\theta_{dry} = \frac{x}{x_{IA}} \left[ \frac{(G_{wavy} - G)}{(G_{wavy} - G_{strat})} \right]^{0.61} \theta_{strat} \quad (6.4)$$

and applied when  $x \leq x_{IA}$ .

All presented modifications assure a smooth transition in the determination of dry angle between respective zones and also a smooth transition in the heat transfer coefficient from zone to zone.

## 6.2 Heat transfer results for stratified-wavy flow

The new flow pattern map presented in the previous section will be applied to the heat transfer calculations. The experimental heat transfer data will be compared with the original model of Kattan and with a new method taking into account the new procedures for  $\theta_{dry}$  calculation and a new nucleate boiling suppression factor described later in section 7.5. The liquid film thickness  $\delta$  is calculated as proposed by El Hajal *et al.* [16] (2003b) from solving of the following geometrical expression:

$$A_L = \frac{(2\pi - \theta_{dry})}{8} [D^2 - (D - 2\delta)^2] \quad (6.5)$$

to give

$$\delta = \frac{D}{2} - \sqrt{\left(\frac{D}{2}\right)^2 - \frac{2A_L}{(2\pi - \theta_{dry})}} \quad (6.6)$$

When the liquid occupies more than one-half of the cross-section of the tube at low vapor quality, this expression would yield a value of  $\delta > D/2$ , what is not geometrically realistic. Hence, whenever equation 6.6 gives  $\delta > D/2$ ,  $\delta$  is set equal to  $D/2$ .

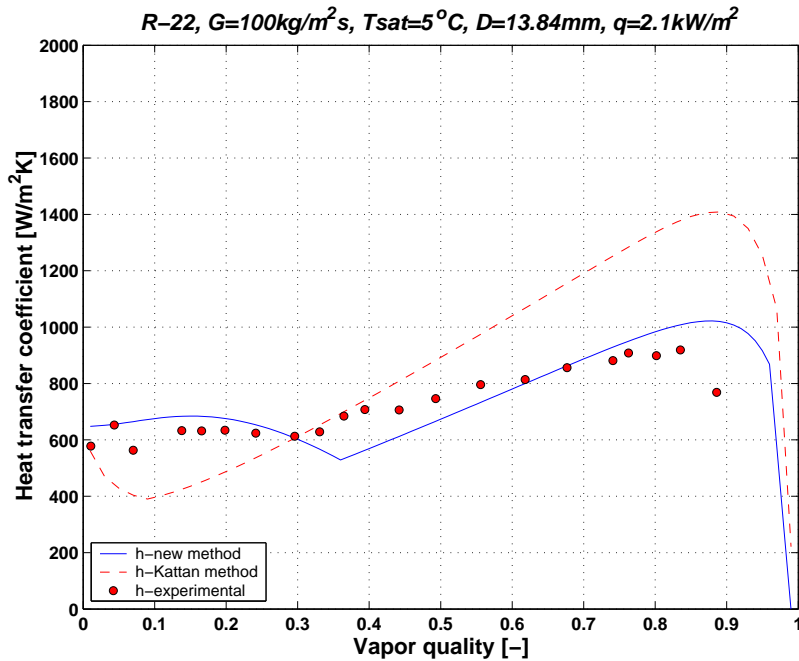


Figure 6.5: Comparison of the experimental heat transfer data with the model of Kattan and the new prediction method for tests with R-22 at mass velocity  $G = 100 \text{ kg/m}^2\text{s}$  and heat flux  $q = 2.1 \text{ kW/m}^2$ .

Figure 6.5 shows the heat transfer results for R-22 tested at a mass velocity  $G = 100 \text{ kg/m}^2\text{s}$  and heat flux  $q = 2.1 \text{ kW/m}^2$  measured simultaneously during the void fraction measurements at the end of evaporator. Much better agreement has been found between the experimental points and the new prediction method in the slug/stratified-wavy zone ( $x < 0.36$ ) as well as in the stratified-wavy region ( $x \geq 0.36$ ).

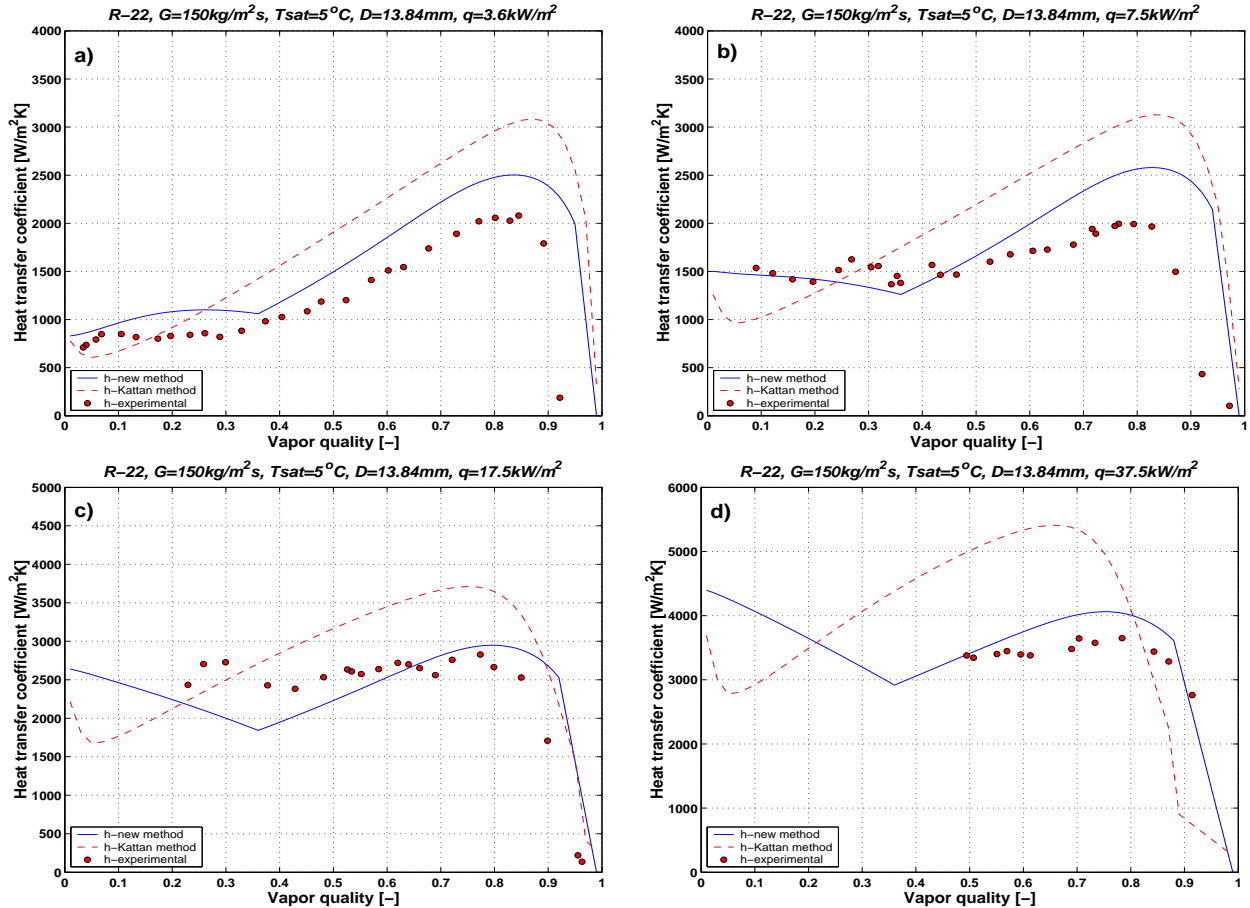


Figure 6.6: Comparison of the experimental heat transfer data with the model of Kattan and the new prediction method for tests with R-22 at mass velocity  $G = 150 \text{ kg/m}^2\text{s}$  and heat fluxes: a)  $q = 3.6 \text{ kW/m}^2$ , b)  $q = 7.5 \text{ kW/m}^2$ , c)  $q = 17.5 \text{ kW/m}^2$ , d)  $q = 37.5 \text{ kW/m}^2$ .

Figures 6.6a-d depict the experimental heat transfer data compared with the model of Kattan and the new prediction method for tests with R-22 at a mass velocity  $G = 150 \text{ kg/m}^2\text{s}$  and heat fluxes of  $3.6 \text{ kW/m}^2$ ,  $7.5 \text{ kW/m}^2$ ,  $17.5 \text{ kW/m}^2$  and  $37.5 \text{ kW/m}^2$ , respectively. The heat transfer data could be obtained experimentally only in the slug/stratified-wavy zone for the lowest heat fluxes. They show very good agreement with the new model in this zone. In the stratified-wavy zone ( $x \geq 0.36$ ), the new prediction is more accurate for higher heat fluxes than for  $q = 3.6 \text{ kW/m}^2$  and  $q = 7.5 \text{ kW/m}^2$ . The reason of this could be an effect of heat



flux, which is not considered in the dry angle correlation presented in equation 6.3. But even without taking into account the heat flux effect in the dry angle calculation, the new method predicts reasonable heat transfer values in the stratified-wavy zone, even for very low heat fluxes and seems to be a significant improvement compared to the original method of Kattan, who in fact limited application of his method to  $x > 0.15$ .

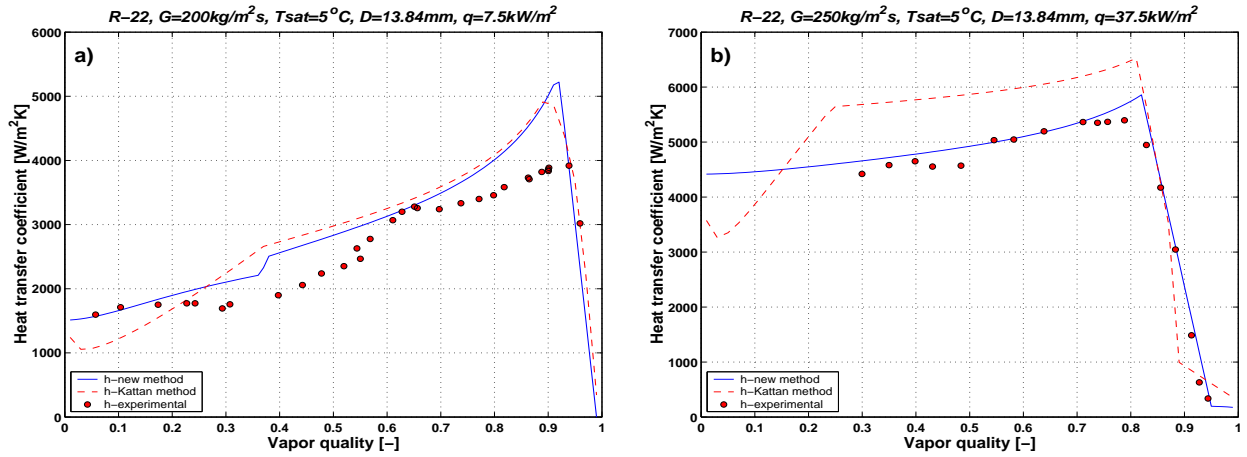


Figure 6.7: Comparison of the experimental heat transfer data with the model of Kattan and the new prediction method for tests with R-22 at: a)  $G = 200 \text{ kg/m}^2\text{s}$ ,  $q = 3.6 \text{ kW/m}^2$ , b)  $G = 250 \text{ kg/m}^2\text{s}$ ,  $q = 37.5 \text{ kW/m}^2$ .

The last results discussed in this section are from tests with R-22 at  $G = 200 \text{ kg/m}^2\text{s}$ ,  $q = 7.5 \text{ kW/m}^2$  and at  $G = 250 \text{ kg/m}^2\text{s}$ ,  $q = 37.5 \text{ kW/m}^2$  and are presented in Figures 6.7a and 6.7b, respectively. As can be seen in the slug region ( $x < 0.36$ ), the heat transfer coefficient is accurately predicted in the test at  $G = 200 \text{ kg/m}^2\text{s}$ . After vapor quality exceeds  $x_{IA}$ , the predicted heat transfer increases rapidly because annular flow is reached. For the data depicted in Figure 6.7b, the transition between slug and intermittent flow happens at a vapor quality  $x = 0.25$ . The new method in contrast to the model of Kattan predicts a smooth transition between these two flow regimes and the agreement with experimental data is much better. The results of statistical analysis for the model of Kattan and a new method for the tests at mass velocities below  $300 \text{ kg/m}^2\text{s}$  are presented in Tables 6.1-6.4, where  $\bar{\varepsilon}$ ,  $|\bar{\varepsilon}|$  and  $\sigma$  are the average, mean and standard deviations, respectively, and  $n$  - corresponds to the number of experimental points.

G	q	$\bar{\varepsilon}_{Kattan}$	$ \bar{\varepsilon} _{Kattan}$	$\sigma_{Kattan}$	$\bar{\varepsilon}_{new}$	$ \bar{\varepsilon} _{new}$	$\sigma_{new}$	n
( $kg/m^2 s$ )	( $kW/m^2$ )	(%)	(%)	(%)	(%)	(%)	(%)	
70	7.5	-6.09	11.92	16.60	-29.36	8.30	10.59	21
70	17.5	-6.35	2.40	3.14	-34.71	3.60	4.45	16
100	2.1	11.19	26.24	31.94	1.53	9.79	12.95	21
150	3.0	30.91	25.98	30.14	22.66	5.18	6.90	28
150	7.5	47.02	44.27	102.33	24.73	35.21	84.76	27
150	17.5	24.31	12.17	17.27	-2.85	12.76	18.44	19
150	37.5	37.25	21.61	28.92	9.19	3.75	4.57	12
200	4.4	16.47	21.07	26.36	25.54	16.95	20.08	27
200	7.5	15.73	13.30	17.74	15.46	9.30	10.91	29
250	37.5	21.28	4.39	4.88	2.93	2.11	2.61	12
Summary		19.17	18.34	27.93	3.51	10.70	17.63	212

Table 6.1: Statistical analysis of heat transfer data obtained during evaporation of refrigerant R-22 in the 13.84 mm test section compared to the model of Kattan and to the new method.

G	q	$\bar{\varepsilon}_{Kattan}$	$ \bar{\varepsilon} _{Kattan}$	$\sigma_{Kattan}$	$\bar{\varepsilon}_{new}$	$ \bar{\varepsilon} _{new}$	$\sigma_{new}$	n
( $kg/m^2 s$ )	( $kW/m^2$ )	(%)	(%)	(%)	(%)	(%)	(%)	
150	7.5	-9.38	18.30	21.95	-14.30	10.99	13.50	12
200	7.5	0.84	11.66	14.31	1.42	11.58	13.44	20
200	17.5	6.51	11.00	13.29	2.08	17.31	19.89	13
200	37.5	-3.93	1.35	1.79	-17.85	1.72	2.33	5
Summary		-1.49	10.58	12.84	-7.16	10.40	12.29	50

Table 6.2: Statistical analysis of heat transfer data obtained during evaporation of refrigerant R-22 in the 8.00 mm test section compared to the model of Kattan and to the new method.

G	q	$\bar{\varepsilon}_{Kattan}$	$ \bar{\varepsilon} _{Kattan}$	$\sigma_{Kattan}$	$\bar{\varepsilon}_{new}$	$ \bar{\varepsilon} _{new}$	$\sigma_{new}$	n
( $kg/m^2 s$ )	( $kW/m^2$ )	(%)	(%)	(%)	(%)	(%)	(%)	
150	7.5	59.72	54.15	93.22	31.16	38.61	71.37	18
150	17.5	11.46	27.13	55.54	-10.93	24.46	54.48	19
150	37.5	8.19	13.91	19.16	-17.63	19.82	27.77	14
200	7.5	39.14	40.70	82.07	37.92	34.23	74.34	33
Summary		29.63	33.97	62.50	10.13	29.28	56.99	84

Table 6.3: Statistical analysis of heat transfer data obtained during evaporation of refrigerant R-410A in the 13.84 mm test section compared to the model of Kattan and to the new method.

G	q	$\bar{\varepsilon}_{Kattan}$	$ \bar{\varepsilon} _{Kattan}$	$\sigma_{Kattan}$	$\bar{\varepsilon}_{new}$	$ \bar{\varepsilon} _{new}$	$\sigma_{new}$	n
( $kg/m^2s$ )	( $kW/m^2$ )	(%)	(%)	(%)	(%)	(%)	(%)	
100	7.5	-50.88	3.26	4.07	-54.78	5.37	6.58	9
100	17.5	-35.68	3.70	4.83	-55.02	2.35	2.96	7
200	10.5	-21.53	12.62	16.91	-24.48	13.55	17.81	19
200	17.5	-17.17	17.69	21.17	-18.78	27.77	37.30	13
200	37.5	-26.30	1.30	1.85	-36.17	3.92	5.22	8
Summary		-30.31	7.72	9.77	-37.84	10.59	13.97	56

Table 6.4: Statistical analysis of heat transfer data obtained during evaporation of refrigerant R-410A in the 8.00 mm test section compared to the model of Kattan and to the new method.

### 6.3 Comparison of the new model to independent data

Most of papers presenting flow boiling heat transfer data for R-22 and R-410A are focused on the heat transfer enhancement of microfin tubes. They present few experimental points for plain tubes comparing them with some enhanced data and calculate the heat transfer enhancement factor. For example, Seo-Kim [48] (2000) and Kim *et al.* [35] (2001) show only five experimental points over the entire vapor quality range for all tests with R-22 and R-410A. Wang *et al.* [59] (1998) present quasi-local heat transfer coefficients during evaporation of R-22 and R-410A at mass velocities of  $G = 100$  and  $400 \text{ kg/m}^2s$  in a smooth 6.4 mm ID tube. Analysing their experimental points for R-410A at  $G = 400 \text{ kg/m}^2s$  and  $q = 5.0 \text{ kW/m}^2$  in the vapor quality range from 0.1 to 0.9, it has been noted that reported heat transfer coefficient varies in this range only from  $2000 \text{ W/m}^2K$  to  $3000 \text{ W/m}^2K$ . Considering the high mass velocity, intermittent/annular flow regime and the fact that most models in the literature predict a variation of heat transfer coefficient for these conditions from  $3000 \text{ W/m}^2K$  to  $10000 \text{ W/m}^2K$ , it raises some doubts about the precision of the experimental set-up used in their work. Lallemand *et al.* [38] (2001) investigated flow boiling heat transfer coefficients during evaporation of R-22 and R-407C in both a smooth tube and a microfin tube at mass velocities from 100 to  $300 \text{ kg/m}^2s$ . They presented quite an extensive database for this mass velocity range, denoting clear trends in the evolution of the heat transfer coefficient. Figures 6.8a-b show the comparison of the experimental heat transfer data of Lallemand *et al.* [38] (2001) with the new prediction method at mass velocities of 150 and 250 with the corresponding flow pattern maps. According to the flow pattern map at mass velocity  $150 \text{ kg/m}^2s$ , the transition from slug/stratified-wavy to stratified-wavy flow takes place at  $x_{IA} = 0.38$ . It can be seen in Figure 6.8a that the predicted heat transfer coefficient

is in very good agreement with the experimental values. It confirms that the transition from slug/stratified-wavy to stratified-wavy flow is correctly identified and the proposed heat transfer model predicts very accurate heat transfer data for both flow regimes. Figure 6.8b shows experimental heat transfer coefficient for the test at  $G = 250 \text{ kg/m}^2\text{s}$ . In these experimental conditions, slug, intermittent and annular flows are encountered before dryout appears. It can be observed that the prediction shows a smooth transition between the respective flow patterns, similar to the experimental heat transfer data. The new model corresponds very well to the experimental values at vapor qualities below 0.8, where in contrary to the prediction, experimental heat transfer data start decreasing. This can be explained as the consequence of "non-controlled wall temperature increase" in their electrically heated test section. This issue is described in section 7.4.2.

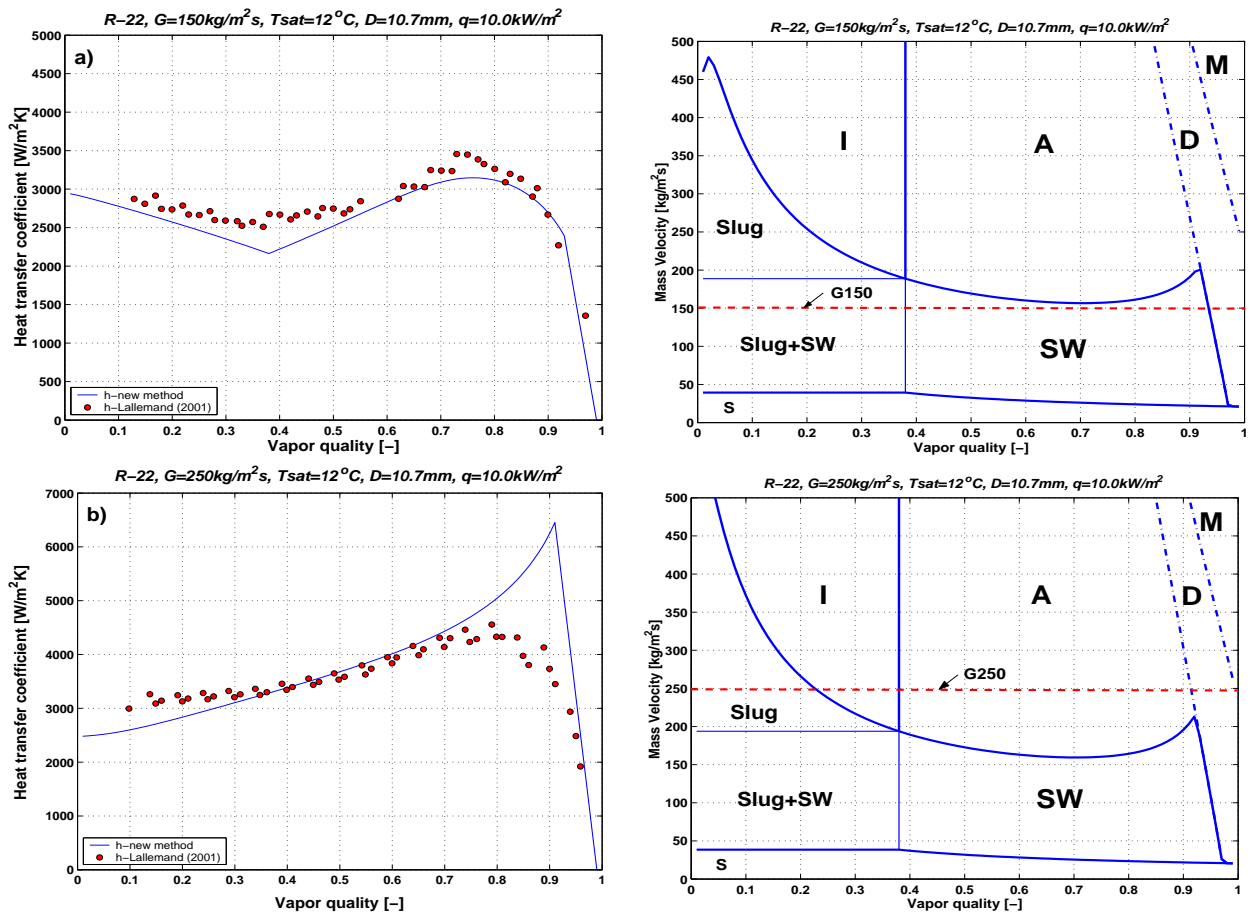


Figure 6.8: Comparison of the experimental heat transfer data of Lallemand *et al.* [38] (2001) with the new prediction method (on left) and corresponding flow pattern maps (on right). Tests with R-22,  $T_{sat} = 5^\circ\text{C}$ ,  $D = 10.7 \text{ mm}$ ,  $q = 10.0 \text{ kW/m}^2$  at mass velocities: a)  $G = 150 \text{ kg/m}^2\text{s}$ , b)  $G = 250 \text{ kg/m}^2\text{s}$ .

The new prediction method shows similar agreement with the heat transfer results of Lallemand *et al.* at mass velocities 200 and 300  $kg/m^2s$  as in the two examples presented above.

## 6.4 Conclusions

Several improvements have been proposed to the latest version of Kattan flow pattern map after analysing the phenomena observed during optical measurements of void fraction. Since stratified flow was not observed for the lowest mass velocity  $G = 70 kg/m^2s$  tested, the transition curve  $G_{strat}$  has been adjusted for vapor qualities below  $x_{IA}$ . Furthermore, the stratified-wavy region in the flow pattern map of Kattan has been divided into three zones: slug, slug/stratified-wavy and stratified-wavy zones. A new method for the dry angle -  $\theta_{dry}$  calculation has been proposed for these three zones. This new approach provides a notable improvement in the accuracy in prediction of heat transfer in stratified types of flow, as has been proven in comparison with experimental results. The heat transfer model has also been extended to vapor qualities below 0.15 and compared to independent data of Lallemand *et al.* [38] (2001), showing very good agreement with them.



# Chapter 7

## Dryout and mist flow heat transfer

The regime of post dryout is encountered when the heated wall becomes dry before complete evaporation. For example, this regime is reached when an evaporating annular film dries out and the remaining liquid is entrained as droplets, such that the vapor quality  $x$  is large but less than 1.0. It also refers to heat transfer from the point at which the critical heat flux has been reached. In this case, the vapor quality  $x$  is smaller or close to 0.0 and the remaining liquid in the flow is still subcooled.

In general, the post dryout heat transfer regime may be reached from the wet wall regime by passing through one of three different transitions in the evaporation process:

- Critical heat flux. The heat flux at the wall or the imposed wall superheat is so high that a continuous vapor film is formed on the wall.
- Dryout of the liquid film. The liquid within an annular film may completely evaporate, leaving the entrained liquid droplets in the vapor to still be evaporated.
- Entrainment of the liquid film. Under high vapor shear stress on the liquid film, the film may be completely removed and all the liquid entrained in the vapor phase.

However, in the post dryout heat transfer regime, the wall may not actually always be dry. Entrained liquid droplets can impinge on the wall and momentarily wet it locally before either evaporating or be re-entrained into the vapor phase. Furthermore, only a portion of the heated periphery of the flow channel may be dry, particularly in horizontal flows and in channels with a wide variation in the peripheral heat flux. In the present study mist flow conditions were obtained due to dryout and entrainment of the liquid film at higher

vapor qualities and mass velocities, yielding 71 mist heat transfer values measured in the 13.84 mm test section for two tested fluids (R-22 and R-410A). The onset of mist flow has been observed at five mass velocities ( $G = 300, 400, 500, 600, 700 \text{ kg/m}^2\text{s}$ ) at heat fluxes of  $q = 37.5 \text{ kW/m}^2$  and  $57.5 \text{ kW/m}^2$  for both tested fluids. The onset of mist flow has been also verified in the 8.00 mm test section for the refrigerant R-410A. In this chapter, the main heat transfer mechanisms in the mist flow and existing heat transfer models in the post dryout zone will be presented. Based on experimental values, the mist flow heat transfer model of Groeneveld has been modified for hydrocarbons.

## 7.1 Heat transfer mechanisms in post dryout

The first principal type of evaporation process encountered in post dryout heat transfer is dispersed flow. In this regime the vapor phase becomes the continuous phase and all the liquid is entrained as dispersed droplets (see Figure 7.1a). The dispersed flow typically occurs after dryout or entrainment of an annular flow. At the dryout location the vapor is assumed to be at saturation. Downstream of dryout the vapor temperature is controlled by wall-vapor and vapor droplet heat exchange. Due to the low superheat of the vapor near the dryout location, the vapor-droplet heat exchange is small and almost all of the heat transferred from the wall is used for superheating the vapor. At a certain distance downstream from the dryout location, however, an equilibrium vapor superheat is reached. It means that the amount of heat transferred from the wall to the vapor is then approximately equal to the amount of heat absorbed by the evaporating droplets. Near a heated surface the heat exchange between vapor and droplets is enhanced due to the temperature in the thermal boundary layer being well above that of the vapor core. If the temperature of the heated surface is below the Leidenfrost temperature, some wetting of the wall may occur, resulting in an appreciable fraction of the droplets being evaporated. At temperatures above the Leidenfrost temperature only dry collisions can take place (collisions where a vapor blanket is always present between surface and droplet). Little heat transfer take place to small droplets which resist deformation and bounce back into the bulk flow, following a dry collision. However, the dry collisions disturb the boundary layer, thus improving the wall-vapor heat transfer. Larger droplets are much more deformable, and tend to spread considerably, thus improving both the wall-vapor and vapor-droplet heat exchange. This spreading may lead to a breakup into many smaller droplets if the impact velocity is sufficiently high. The vapor film thickness separating the stagnated droplets from the heated surface is difficult to estimate but must



be greater than the mean free path of the vapor molecules in order to physically separate the liquid from the heated surface - Groeneveld [20] (1975). Attempts to evaluate the direct heat flux to the droplets due to the interaction with the heated surface have resulted in the postulation of many simplifying assumptions, *e.g.* Bailey [3] (1972), Groeneveld [18] (1972) and Plummer [43]. These assumptions may be questionable when applied to liquid-deficient cooling. However, due to lack of direct measurement of droplet-wall interaction during forced-convective post dryout conditions, no other approach can be taken.

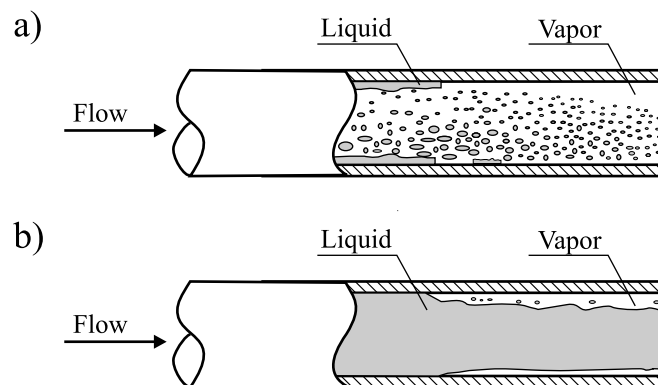


Figure 7.1: Principal mist flow configuration in horizontal tubes: a) dispersed flow, b) inverted annular flow.

The second type of post dryout evaporation process for very high heat fluxes is inverted annular flow. In the inverted annular flow regime shown in Figure 7.1b, few entrained droplets are present, as the bulk of the liquid is in the form of a continuous liquid core, which may contain entrained bubbles. At dryout the continuous liquid core suddenly becomes separated from the wall by a low viscosity vapor layer which can accommodate steep velocity gradients. The velocity distribution across the liquid core is fairly uniform. Once a stable vapor blanket has formed, the heat is transferred from the wall to the vapor, and subsequently from the vapor to the liquid core. Heat transfer across the wavy vapor-liquid interface takes place by forced convective evaporation. This mode of heat transfer is much more efficient than the single phase convective heat transfer between a smooth wall and vapor. Hence, it is assumed that the bulk of the vapor is at or close to the liquid core temperature (*i.e.* saturation temperature). The low viscosity, low-density vapor flow experiences a higher acceleration than the dense core flow. This results in an increased velocity differential across the interface (which may lead to liquid entrainment from the wavy interface) and a reduction in heated surface temperature. If the temperature of heating wall is below the Leidenfrost temperature rewetting occurs. Due to the high CHF in the inverse annular flow regime

at pressures less than 100 *bar*, the post dryout temperatures encountered are high. Hence, experimental measurements are rare since only a cumbersome temperature-controlled system permits safe operation at these conditions. No satisfactory method of predicting post dryout temperatures is available at these conditions, even in simple geometries - Groeneveld [20] (1975). For horizontal and inclined tubes, dryout does not occur uniformly around the tube perimeter. Only the upper part of the tube wall may be in the post dryout heat transfer regime while the lower remains wet.

## 7.2 Departure from thermodynamic equilibrium

A very important issue in the post dryout region is the departure from thermodynamic equilibrium in post dryout. During wet wall evaporation, the wall temperature remains close to the local wall temperature corresponding to the saturation pressure. In the post dryout regime, where there is no permanent liquid contact with the wall, the temperature of the heating wall becomes significantly higher than the saturation temperature and hence departure from thermodynamic equilibrium occurs. Figure 7.2 illustrates two limiting cases for post dryout heat transfer.

The first case is complete departure from equilibrium and heat is transferred only to the continuous vapor phase that is in contact with the heated wall, which results in superheating of the vapor. If the rate of the heat transfer from the superheated vapor phase to the entrained droplets is so slow that their presence may be ignored, the vapor temperature  $T_V(z)$  downstream of the dryout point may be calculated with the assumption that all heat superheats the vapor. In this case,  $T_{wall}$  can be calculated using a single-phase heat transfer correlation, giving the profile illustrated in Figure 7.2a. The other limiting case is complete thermodynamic equilibrium as shown in 7.2b. In this case, the rate of heat transfer from the vapor phase to the entrained droplets is assumed to be so effective that the vapor temperature  $T_V(z)$  remains at the saturation temperature until all the droplets have been completely evaporated. The downstream wall temperature  $T_{wall}$  may vary nonlinearly and a maximum may be reached, in part because of the cooling effect of impingement of liquid droplets on the heated wall. The post dryout heat transfer process tends towards the case of thermal non-equilibrium at low mass velocities and low pressures. At the other extreme, the process tends towards thermal equilibrium at high mass velocities and high pressures. A typical thermodynamic path of the process is illustrated in Figure 7.3, where the local temperature is

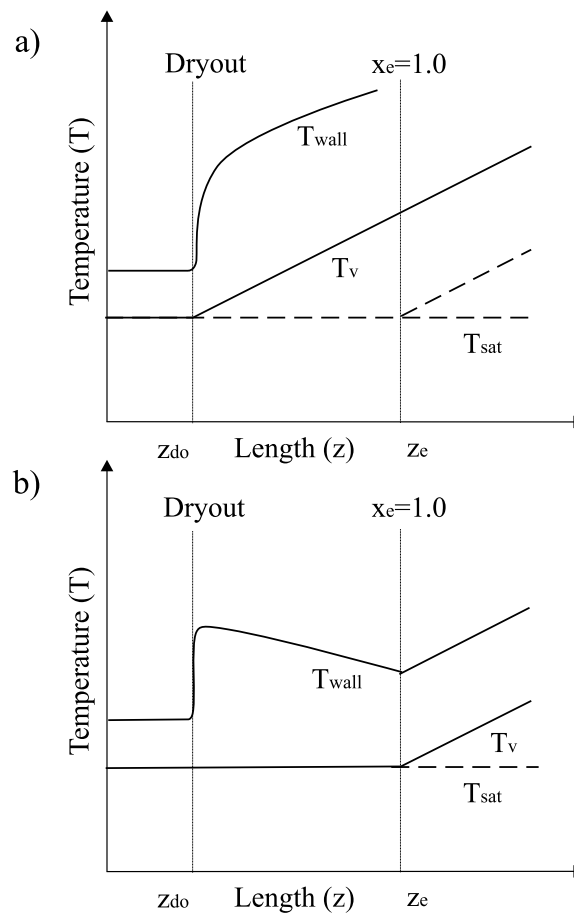


Figure 7.2: Limiting conditions for post dryout heat transfer - based on Collier, Thome [11]  
a) Complete lack of thermodynamic equilibrium, b) Complete thermodynamic equilibrium.

lower than the maximum occurring during complete non-equilibrium, but is still significantly above the local saturation temperature of the complete equilibrium case. Hence, in post dryout heat transfer the local bulk temperature of the vapor is unknown and becomes an added complication in describing and modelling the process. Another complicating aspect of post dryout heat transfer is the determination of the local vapor quality. Thermodynamic equilibrium as shown in Figure 7.2b means that all transferred heat is utilised to evaporate the liquid and hence the local equilibrium vapor quality is  $x_e(z)$ . On the other hand, if all the heat is used to superheat the vapor after the onset of dryout as in Figure 7.2a, the vapor quality remains fixed at that at the dry out point  $x_{do}(z)$ . In reality, the actual local vapor quality  $x_a(z)$  is less than that estimated from complete thermodynamic equilibrium and hence it follows that  $x_{do}(z) < x_a(z) < x_e(z)$ .

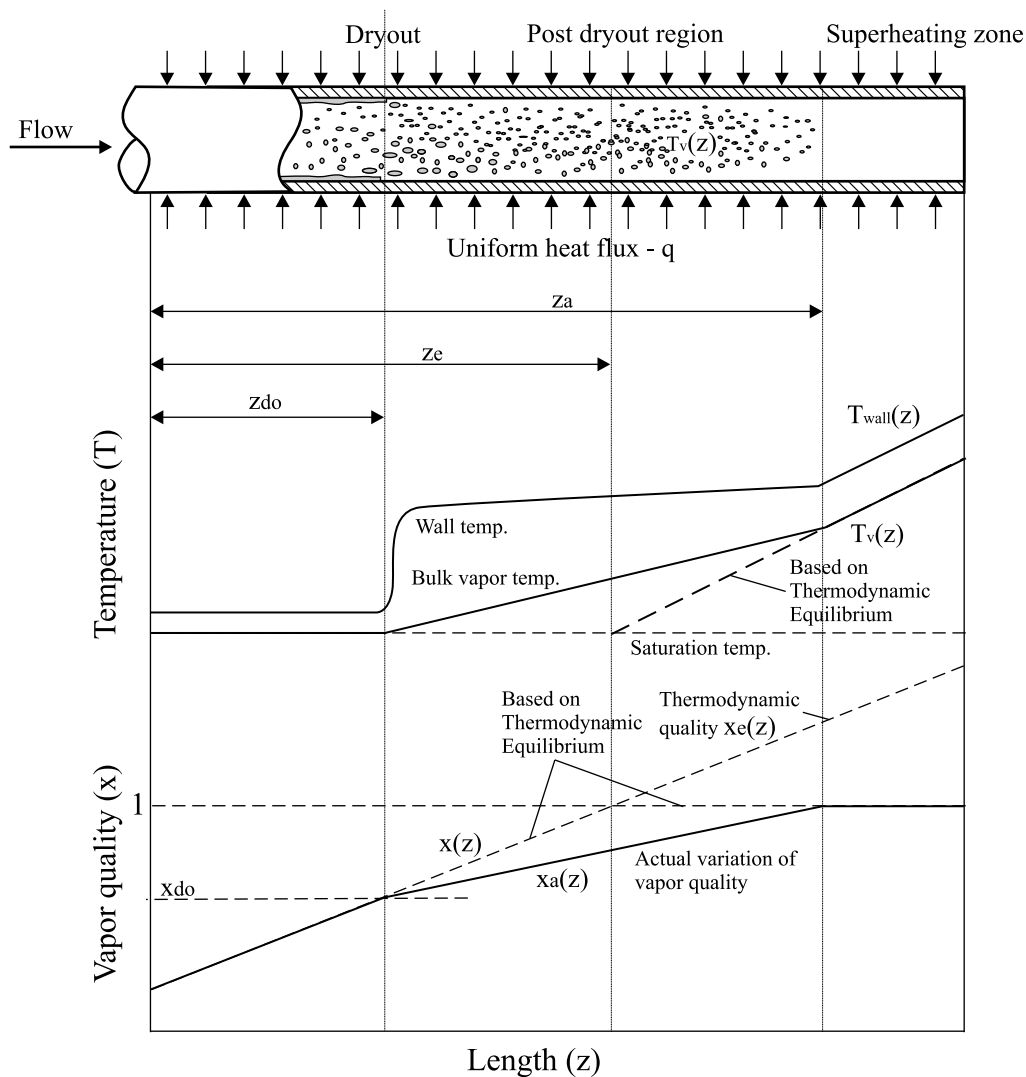


Figure 7.3: Departure from thermodynamic equilibrium in post dryout - based on Collier, Thome [11].

Figure 7.3 depicts post dryout in a tube of internal diameter  $D$  heated uniformly with a heat flux of  $q$ . Dryout occurs at a length  $z_{do}$  from the inlet, and it is assumed that thermodynamic equilibrium exists at the dryout point. If complete equilibrium is maintained after dryout, all the liquid will be evaporated when the point  $z_e$  is reached. In the other case only a fraction  $\kappa$  of the surface heat flux is used to evaporate the remaining liquid in the post dryout region, while the remainder is used to superheat the bulk vapor. The liquid is thus completely evaporated only when a downstream distance of  $z_a$  is reached. If we assume that the total heat flux  $q(z)$  is subdivided into two components: the heat associated with droplet evaporation  $q_L(z)$  and the heat flux associated with vapor superheating  $q_V(z)$ , then

a fraction of heat used only for evaporation can be obtained as:

$$\kappa = \frac{q_L(z)}{q(z)} \quad (7.1)$$

For simplicity,  $\kappa$  is considered independent of tube length, although this is not the case in general, and the profiles of the actual bulk vapor temperature  $T_V$  and actual vapor quality  $x_a$  are shown as linear in Figure 7.2. The variation in the thermodynamic vapor quality with tube length for  $z < z_e$  is given by an energy balance:

$$x(z) - x_{do} = \frac{4q}{DGh_{LV}}(z - z_{do}) \quad (7.2)$$

The location of point  $z_e$  is given by:

$$z_e = \left[ \frac{DGh_{LV}}{4q}(1 - x_{do}) \right] + z_{do} \quad (7.3)$$

The actual vapor quality  $x_a(z)$  for  $z < z_a$  can be calculated as:

$$x_a(z) - x_{do} = \frac{4\kappa q}{DGh_{LV}}(z - z_{do}) \quad (7.4)$$

and  $z_a$  is given by

$$z_a = \left[ \frac{DGh_{LV}}{4\kappa q}(1 - x_{do}) \right] + z_{do} \quad (7.5)$$

By combining equation 7.2 with 7.4 and equation 7.3 with 7.5, the resulting expression for the heat fraction used for liquid evaporation is:

$$\kappa = \left[ \frac{x_a(z) - x_{do}}{x(z) - x_{do}} \right] = \left[ \frac{z_a - z_{do}}{z_e - z_{do}} \right] \quad (7.6)$$

Similarly, the actual bulk vapor temperature  $T_V(z)$  is obtained as:

$$T_V(z) = T_{sat} + \left[ \frac{4(1 - \kappa)q(z - z_{do})}{Gc_{pV}D} \right] \quad (7.7)$$

for  $z < z_a$  while for  $z > z_a$  as:

$$T_V(z) = T_{sat} + \left[ \frac{4q(z - z_e)}{Gc_{pV}D} \right] \quad (7.8)$$

The two limiting cases illustrated in Figure 7.2 are clearly recognized by setting  $\kappa = 0$  and  $\kappa = 1$ , respectively, in the above equations. In reality,  $\kappa$  is probably not independent of tube length and must be predicted from the actual experimental conditions.

## 7.3 Mist flow heat transfer models

As mentioned in section 7.1 due to lack of direct measurement of droplet-wall interaction during forced-convective post dryout conditions, only empirical correlations are used to describe the very complex process of the heat transfer in mist (dispersed) flow. These are described below.

### 7.3.1 Thermal equilibrium correlations

These correlations assume that the liquid is in thermal equilibrium with the vapor, and the heated surface is cooled by forced convection to the vapor only. These correlations are basically forced convective correlations where the vapor velocity  $u_V$  is evaluated by assuming either homogeneous flow ( $S = 1$ ) or by using a suitable slip ratio  $S$ .

One of the equilibrium methods which assumes homogeneous flow is the correlation of **Dougall - Rohsenow** [14] (1963). They proposed to calculate the mean velocity of the fluid as the homogeneous velocity of two-phases  $u_H$ :

$$u_H = \frac{G}{\rho_h} = G \left( \frac{x}{\rho_V} + \frac{1-x}{\rho_L} \right) \quad (7.9)$$

The definition of the homogeneous vapor Reynolds number is thus

$$Re_H = \frac{GD}{\mu_V} \left( x + \frac{\rho_V}{\rho_L}(1-x) \right) \quad (7.10)$$

Hence, assuming homogeneous flow, their mist flow heat transfer correlation is:

$$Nu_V = \frac{h_{mist}D}{\lambda_V} = 0.023 Re_H^{0.8} Pr_V^{0.4} \quad (7.11)$$

The vapor quality  $x$  to use in the expression is the equilibrium vapor quality  $x_e$  and all properties are evaluated at the saturation temperature. A similar result can be obtained making the same modification to the well-known Gnielinski correlation that covers the transition and turbulent flow regimes such that

$$Nu_V = \frac{(f/2)(Re_H - 1000)Pr_V}{1 + 12.7(f/2)^{1/2}(Pr_V^{2/3} - 1)} \quad (7.12)$$

where the friction factor  $f$  is obtained from:

$$f = (1.58 \ln Re_H - 3.28)^{-2} \quad (7.13)$$

The limitations of this type of approach are:

- All other heat transfer mechanisms in mist flow, except for wall-to-vapor heat transfer, are ignored.
- The nonequilibrium effects of superheating the vapor driving the convection process is neglected.

In the approach of Dougall-Rohsenow, the definition of the Reynolds number is not actually consistent with homogeneous flow theory because some gas properties are used with conjunction with the homogeneous density when only homogeneous properties should be used. To correct this, **Groeneveld** [19] (1973) added another multiplying factor  $Y$  defined as:

$$Y = 1 - 0.1 \left[ \left( \frac{\rho_L}{\rho_V} - 1 \right) (1 - x) \right]^{0.4} \quad (7.14)$$

The new correlation for the Nusselt number is then:

$$Nu_V = \frac{h_{mist}D}{\lambda_V} = aRe_H^b Pr_V^c Y^d \quad (7.15)$$

The empirical constants giving the best fit to the database of Groeneveld are:  $a=0.00327$ ,  $b=0.901$ ,  $c=1.32$  and  $d=-1.5$ . The most significant change is to the exponent of the Prandtl number. The database of Groeneveld used to optimise empirical factors covers the following

conditions:

$$2.5 \text{ mm} < D < 25 \text{ mm}$$

$$34 \text{ bar} < P < 215 \text{ bar}$$

$$700 \text{ kg/m}^2\text{s} < G < 5300 \text{ kg/m}^2\text{s}$$

$$0.1 < x < 0.9$$

$$120 \text{ kW/m}^2 < q < 2100 \text{ kW/m}^2$$

Such big values of pressures, heat fluxes and mass velocities are typical to power boilers. This correlation is applicable to vertical and horizontal tubes and to vertical annuli and its use beyond above specified conditions was not verified.

As can be seen in Figure 7.7, thermal equilibrium correlations assume the extreme value of actual vapor quality  $x_a$  in post dryout region, which equals to equilibrium vapor quality  $x_e$ , which in most of applications is not true but only convenient to assume.

### 7.3.2 No evaporation after dryout - "frozen droplets" model

These are correlations which assume that no evaporation takes place in the post dryout region, and the heating tube wall is cooled by forced convection to the vapor only. Although here the same forced convective correlation is used as above, the predicted temperature is much higher, since the vapor becomes progressively more superheated:

$$T_{Va} = T_{sat} + (x_e - x_{do})h_{LV}/c_{pV} \quad (7.16)$$

The degree of vapor superheat can be determined from a heat balance. The no-evaporation assumption also results in the Reynolds number remaining virtually constant in the post dryout region, since  $x = x_{do}$ . This type of correlation is pessimistic, but it can be used to predict an upper boundary for the heated surface temperature. In contrast to the thermal equilibrium correlations, the "frozen droplet" model assumes the minimum extreme value of the actual vapor quality  $x_a$ , which does not change in the post dryout region and is fixed to  $x_{do}$ .



### 7.3.3 Models predicting non-equilibrium effects

Taking into account non-equilibrium effects in the post dryout zone, **Groeneveld - De-lorme** [21] (1976) proposed two new empirical correlations. After analysis they found that the simpler version presented below predicted their data quite well:

$$\frac{h_{mist}D}{\lambda_{Vf}} = \frac{qD}{(T_{wall} - T_{Va})\lambda_{Vf}} = 0.008348 \left[ \left( \frac{GD}{\mu_{Vf}} \right) x_a + \frac{\rho_V}{\rho_L} (1 - x_a) \right]^{0.8774} Pr_{Vf}^{0.6112} \quad (7.17)$$

Notably, the actual non-equilibrium temperature  $T_{Va}$  and actual vapor quality  $x_a$  are utilized rather than the saturation temperature  $T_{sat}$  and equilibrium vapor quality  $x_e$ . The subscript  $Vf$  in this expression indicates that the vapor properties should be evaluated at the film temperature defined as:

$$T_{Vf} = (T_{wall} - T_{Va})/2 \quad (7.18)$$

To determine the values of  $T_{Va}$  and  $x_a$ , an energy balance is used where  $h_{Va}$  is the actual vapor enthalpy and  $h_L$  is the enthalpy of saturated liquid while  $x_e$  is the equilibrium vapor quality and  $h_{LV}$  is the latent heat of evaporation. Thus, the actual vapor quality is obtained from:

$$x_a = \frac{h_{LV}x_e}{h_{Va} - h_L} \quad (7.19)$$

The change in the vapor enthalpy is calculated from:

$$h_{Va} - h_L = h_{LV} + \int_{T_{sat}}^{T_{Va}} cp_V dT_V \quad (7.20)$$

The most important issue in this correlation is the prediction of the difference between the actual vapor enthalpy  $h_{Va}$  and the equilibrium vapor enthalpy  $h_{Ve}$ . The following expression has been proposed to calculate this relationship:

$$\frac{h_{Va} - h_{Ve}}{h_{LV}} = e^{-\tan(\psi)} \quad (7.21)$$

To correlate this function, Groeneveld and Delorme proposed a parameter  $\psi$  defined as follows:

$$\psi = a_1 Pr_V^{a_2} Re_H^{a_3} \left( \frac{q D c_{pV}}{\lambda_L h_{LV}} \right)^{a_4} \sum_{i=0}^2 b_i x_e^i \quad (7.22)$$

which is valid for  $0 \leq \psi \leq \pi/2$ , when  $\psi < 0$ , its value is set to 0.0; when  $\psi > \pi/2$ , it is set to  $\pi/2$ . The empirical values determined from a database of 1402 points for water are:  $a_1 = 0.13864$ ,  $a_2 = 0.2031$ ,  $a_3 = 0.20006$ ,  $a_4 = -0.09232$ ,  $b_0 = 1.3072$ ,  $b_1 = -1.0833$ ,  $b_2 = 0.8455$

The homogeneous Reynolds number in above expression is calculated from equation 7.10.

For  $0 \leq x_e \leq 1$ , the equilibrium vapor enthalpy  $h_{V_e}$  is that of saturated vapor, *i.e.*

$$h_{V_e} = h_V \quad (7.23)$$

and for  $x_e > 1$ , the equilibrium vapor enthalpy  $h_{V_e}$  is calculated as:

$$h_{V_e} = h_V + (x_e - 1)h_{LV} \quad (7.24)$$

Figure 7.4 shows the evolution of Groeneveld-Delorme correlation function  $e^{-\tan(\psi)}$ , which predicts the variation of the enthalpy of superheated vapor.

Rearranging equation 7.21, the actual enthalpy of the vapor is calculated as:

$$h_{V_a} = e^{-\tan(\psi)} h_{LV} + h_{V_e} \quad (7.25)$$

Accordingly to Figure 7.4, the correlation function  $e^{-\tan(\psi)}$  does not start from 0, for the onset of dryout and the initial value of the function is 0.0488. It will result in the predicted enthalpy jump what will cause an increase of predicted temperatures and a step decrease of actual vapor quality  $x_a$ . These phenomena are presented in Figures 7.5 and 7.7, respectively.

It can be seen in Figure 7.5 that the method of Groeneveld-Delorme (1976) predicts the rapid increase of  $T_{V_a}$  from  $5^\circ C$  to  $17.7^\circ C$  as the onset of dryout appears. This jump decreases with increasing of vapor quality. The dashed line in Figure 7.7 presents the variation of the actual vapor quality  $x_a$  calculated with the correlation of Groeneveld-Delorme (1976) as a function of equilibrium vapor quality  $x_e$ . The predicted decrease of actual vapor quality for the onset of dryout is about 3.7%, which seems to be not realistic in the practical case.

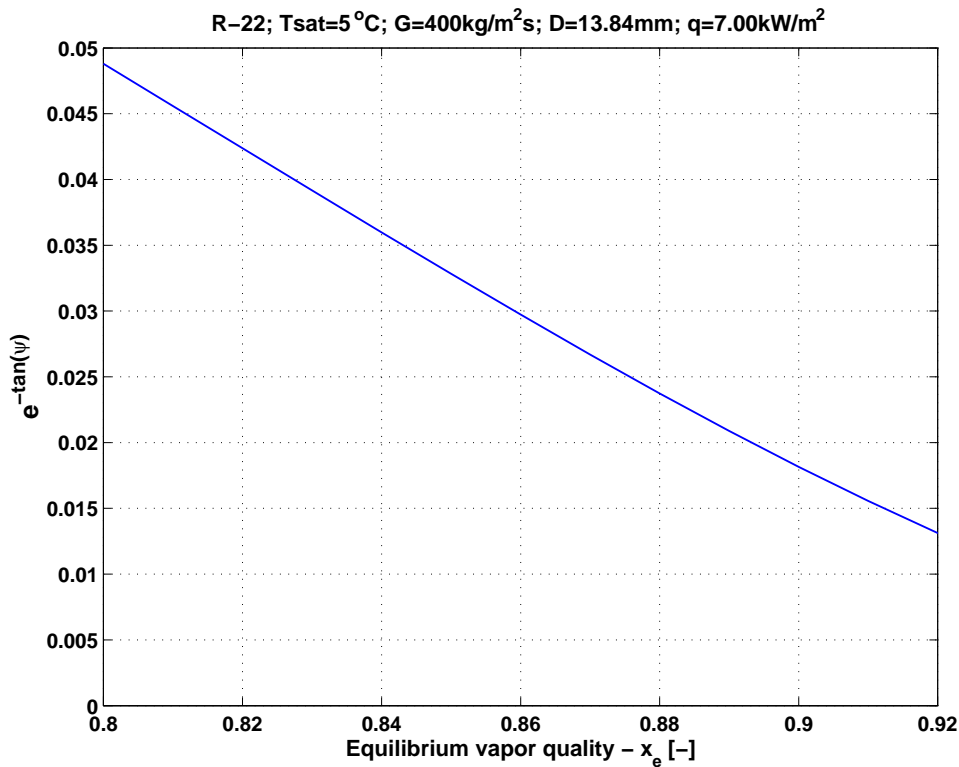


Figure 7.4: Correlation function of Groeneveld-Delorme  $e^{-\tan(\psi)}$  for the mist flow conditions during evaporation of R-22 in  $D = 13.84 \text{ mm}$  tube for equilibrium.

To find the values of:  $h_{mist}$ ,  $T_{Va}$  and  $x_a$  when given those of  $G$ ,  $x_e$  and  $q$ , the following procedure has to be implement:

- Estimate an initial value of  $T_{Vf}$  to evaluate the fluid properties.
- Use equation 7.22 to determine  $\psi$ .
- Utilize either equation 7.23 or 7.24 together with 7.21 to obtain  $h_{Va}$ .
- Input the value of  $h_{Va}$  into 7.19 to obtain  $x_a$ .
- Solve equation 7.20 to find  $T_{Va}$ .
- Input the resulting values into equation 7.17 to determine the wall temperature  $T_{wall}$  and then the heat transfer coefficient  $h_{mist}$ .
- A new film temperature  $T_{Vf}$  may now be calculated with 7.18 and the whole procedure is repeated until the iteration reaches a stable result.

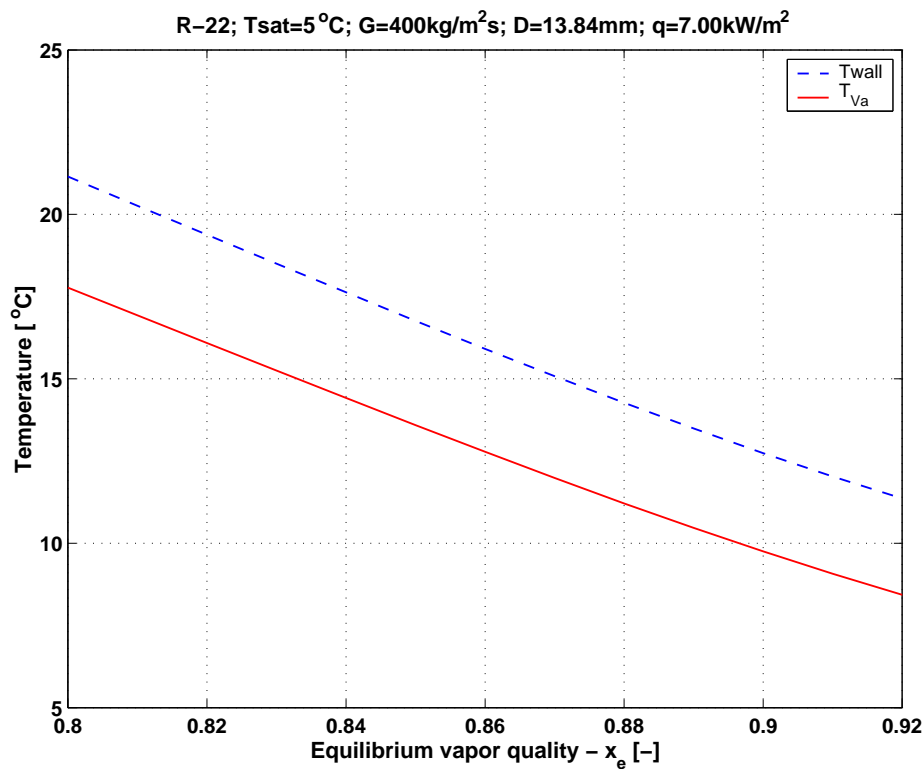


Figure 7.5: Prediction of wall temperature and actual vapor temperature using the method of Groeneveld-Delorme (1976) for the mist flow conditions during evaporation of R-22 in  $D = 13.84 \text{ mm}$  tube.

Groeneveld and Delorme evaluated the actual vapor enthalpy based on the following assumptions:

- The liquid phase does not participate directly in the cooling of the heated surface.
- Radiative heat transfer to the droplets is negligible.
- The flow is homogeneous.
- Heat transfer at the wall can be predicted by a superheated vapor correlation.

Mori *et al.* [41] (2000) presented a new post dryout heat transfer model for refrigerant flowing in horizontal tubes. In their method, equation 7.12 of Gnielinski is applied to calculate the convective heat transfer from the wall to the superheated vapor in the post dryout region using Reynolds number for vapor flow and friction factor as follows:

$$Re = \frac{Gx_a D}{\mu_{Va}} \quad (7.26)$$

$$f = (3.64 \log Re - 3.28)^{-2} \quad (7.27)$$

The actual vapor quality is calculated like in equation 7.19 of Groeneveld and Delorme and the convection heat transfer (wall-vapor) is defined as:

$$h_{wall-V} = \frac{q}{(T_{wall} - T_{Va})} \quad (7.28)$$

Based on the measured data of wall temperature  $T_{wall}$ , the value of the actual quality  $x_a$  was obtained by Mori *et al.* by combining of above equation with the value of the convective heat transfer coefficient of Gnielinski. The relation between the calculated actual quality  $x_a$  and the thermodynamic equilibrium quality  $x_e$  was found by Mori *et al.* to be reproduced fairly well by Saha's [47] (1980)  $K_1$  correlation developed for vertical tubes. Therefore, by modifying Saha's  $K_1$  correlation, they developed the following expression for the actual vapor quality in a horizontal smooth tube:

$$\frac{dx_a}{dx_e} = \frac{D\Gamma_{Va}h_{LV}}{4q} \quad (7.29)$$

$$\Gamma_{Va} = K \frac{\lambda_{Va}(1 - \varepsilon)(T_{Va} - T_{sat})}{D^2 h_{LV}} \quad (7.30)$$

$$K = 2600 \left(1 - \frac{P}{P_{cr}}\right)^2 \left[ \left(\frac{Gx_a}{\varepsilon}\right)^2 \frac{D}{\rho_{Va}\sigma} \right]^{0.5} \quad (7.31)$$

where  $\Gamma_{Va}$  is the rate of vapor generation,  $\varepsilon$  is the void fraction and  $P$  and  $P_{cr}$  are the pressure and the critical pressure of the fluid, respectively. Two modifications were made by Mori to Saha's correlations: The void fraction was estimated using the slip ratio of Ahmad's [1] (1970) correlation, and the constant in the equation for the parameter  $K$  was changed to 2600. The slip ratio of Ahmads is equal to  $S = (\rho_L/\rho_V)^{0.2}$ . In the post dryout region for a horizontal tube, Mori *et al.* considered that the bulk vapor of the vapor-liquid mixture begins to be superheated at the point of the dryout. The actual vapor quality  $x_a$  can be estimated by solving equation 7.29 with the initial condition of:

$$x_a = x_{do} \text{ at } x_e = x_{do}$$

By the use of this actual vapor quality value, the wall temperature  $T_{wall}$  is calculated from the Gnielinski correlation with equations 7.27, 7.26, 7.19 and 7.28. Then the heat transfer coefficient can be calculated, for a given set of pressure, tube diameter, mass velocity and heat flux from:

$$h_{mist} = \frac{q}{(T_{wall} - T_{Lb})} \quad (7.32)$$

where  $T_{Lb}$  is the liquid bulk temperature.

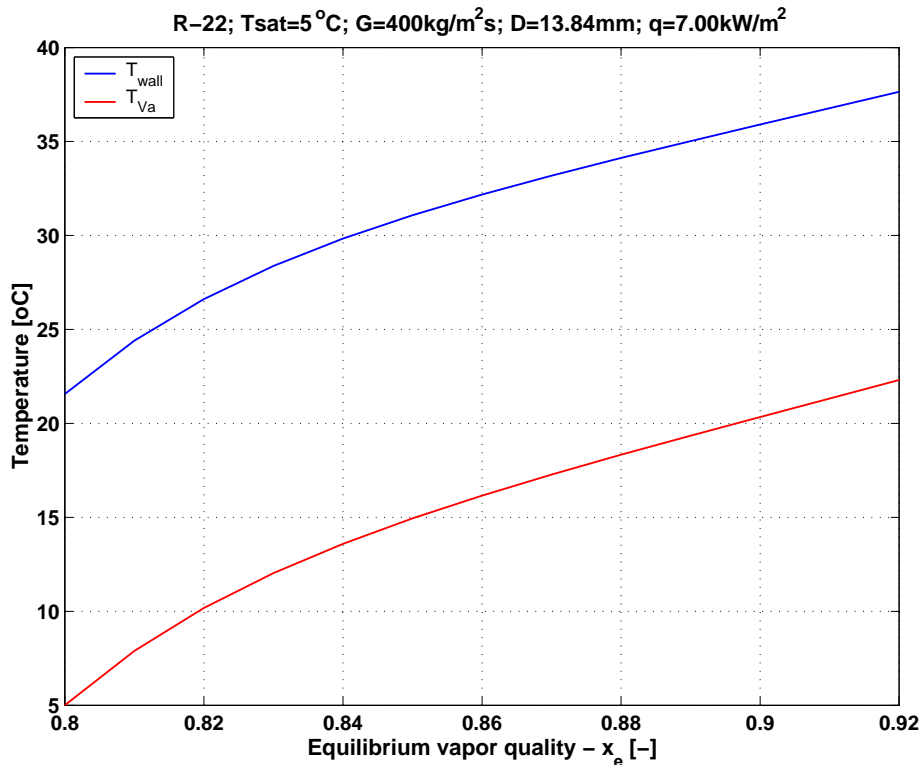


Figure 7.6: Prediction of wall temperature and actual vapor temperature using the method of Mori *et al.* (2000) for the mist flow during evaporation of R-22 in  $D = 13.84 \text{ mm}$  tube.

Mori *et al.* found an agreement within  $\pm 10\%$  with their measurements in their electrically heated test section. Figure 7.6 shows predicted wall and actual vapor temperatures using the method of Mori *et al.* (2000) in the dryout zone during evaporation of R-22 in the present  $D = 13.84 \text{ mm}$  tube. In distinction to the method of Groeneveld-Delorme (1976), the actual vapor temperature  $T_{Va}$  starts rising from the saturation temperature  $T_{Va}$  due to the effect of vapor superheating. The difference between the temperature  $T_{wall}$  and  $T_{Va}$  decrease slightly with the increasing of vapor quality.

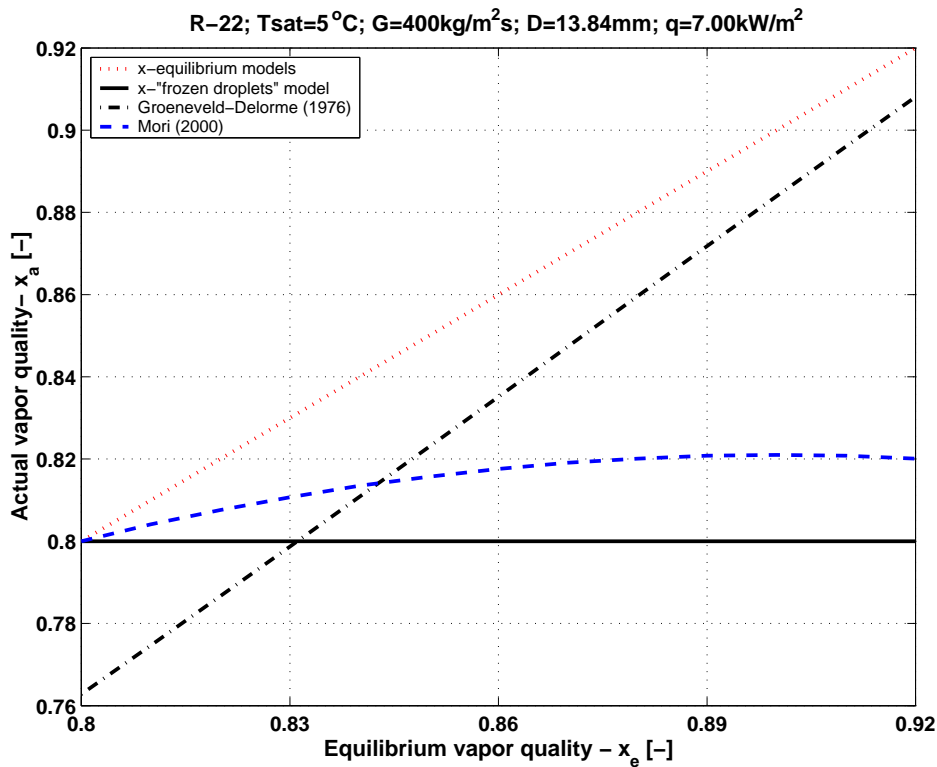


Figure 7.7: Prediction of actual vapor quality for mist flow conditions during evaporation of R-22 in  $D = 13.84 \text{ mm}$  tube for equilibrium, "frozen droplets" and non-equilibrium models.

The dashed curve in Figure 7.7 corresponds to the predicted actual vapor quality  $x_a$  using the correlation of Mori *et al.* (2000). As mentioned before the dotted line represents equilibrium models, which are the upper limiting case obtained with the assumption that all enthalpy transferred to the vapor is used to evaporate dispersed liquid droplets. The opposite case is the "frozen droplets" approach where all enthalpy is assumed to superheat the vapor and no further evaporation occurs. The dash-dotted curve is the actual vapor quality prediction based on the correlation of Groeneveld-Delmore (1976). This method does not predict the correct actual vapor quality (*i.e.* the equilibrium quality) at the dryout point.

It can be concluded that the non-equilibrium methods predict quite different values of actual vapor qualities  $x_a$  and temperatures  $T_{Va}$  and  $T_{wall}$ . That results, of course, in a big difference in the predicted heat transfer coefficient. Most of these correlations were developed for water at high pressures to calculate the wall temperature in the post dryout regime for the design of steam generators and cannot be directly applied to refrigerants. It has to be emphasized that non-equilibrium methods require knowing the heat flux value to predict the heat transfer coefficient contrary to the equilibrium models.

## 7.4 A new heat transfer model for dryout and mist flow

The good performance of flow boiling heat transfer in an evaporator tube is limited by the onset of dryout. At this point, thin liquid annular film is disturbed due to evaporation and entrainment by the high velocity vapor. Also the nucleation in the liquid film facilitates the dryout process. The knowledge of the heat transfer coefficient is essential for the design or performance evolution of evaporators. Even if a lot of studies have been made for dryout heat transfer in vertical tubes, these results cannot be directly applied to a horizontal evaporator tube in a heat pump or refrigeration system due to the stratification effect of gravity. Only few studies concerning refrigerant heat transfer in the dryout region of horizontal tubes have been reported. First tests were made with R-22 and R-12 by Lavin and Young [39] (1965). They proposed a new transition between annular and mist flow regime based on the Weber number. Chaddock and Varma [8] (1979) made tests with R-22 in the mass velocity range from 157.3 to 835  $kg/m^2s$  in the dryout region. The test section consisted of three 3.00 m lengths of 8.00 mm internal diameter stainless steel tubes heated by passing an electric current. The onset of dryout was made to occur in the beginning of the third tube. To simulate the heating conditions of a fluid-to-fluid evaporator, the heat flux in the third tube was set lower than that in the preceding sections. Heat fluxes from 6.3 to 31.55  $kW/m^2$  were investigated and 40 experiments were run. Dryout occurred at vapor qualities between 0.89 and 0.99. It started at the top of the tube, continued down the sides and finally arrived at the bottom in a progression along the tube. The onset was usually marked by a rapid and relatively small increase in local heat transfer coefficients, followed immediately by an order of magnitude decrease.

The most recent experimental data for R-22 and R-134A evaporating in horizontal tubes were reported by Mori *et al.* [41] (2000). They ran tests at mass velocities from 100 to 600  $kg/m^2s$  at heat fluxes ranging from 5.0 to 50.0  $W/m^2$ . They tested internal tube diameters of 6.34 mm and 10.70 mm. Mori *et al.* proposed a new post dryout heat transfer model for refrigerant flowing in horizontal tubes presented in section 7.3.3 and correlations of the dryout inception and the dryout completion qualities. The test section was heated electrically with constant heat flux. In this condition, the tube wall temperature has to increase correspondingly. This could create physical conditions quite different than that of heat transfer from a second fluid outside the tube, as it occurs in most practical refrigeration applications.



### 7.4.1 Heat transfer for high mass velocities and high heat fluxes

In the present study mist flow conditions were obtained due to dryout and entrainment of the liquid film at relatively high vapor qualities and mass velocities: 71 mist heat transfer values have been measured in the 13.84 mm test section for two tested fluids (R-22 and R-410A). The onset of mist flow has been observed at five mass velocities ( $G = 300, 400, 500, 600, 700 \text{ kg/m}^2\text{s}$ ) at initial heat flux of  $q = 57.5 \text{ kW/m}^2$  prior to dryout for both fluids. Due to the protection system of the preheater, mist flow conditions could be obtained at initial heat flux  $q = 37.5 \text{ kW/m}^2$  at mass velocities of 300, 400 and 500  $\text{kg/m}^2\text{s}$ , only. For lower initial heat fluxes in the test section, more heat has to be supplied from the preheater to obtain the same vapor quality at the heat transfer measurement location. This causes operating near the critical heat flux conditions in the preheater, which would result in a dramatic increase of the preheater wall temperature. Thus, the protection system of the preheater shuts down the power supply when the wall temperature exceeds  $25^\circ\text{C}$ . An initial heat flux means the heat flux measured before the onset of dryout occurs (prior to dryout). In the fluid-to-fluid evaporator test section for the same heating water temperature at the inlet of an evaporator, the heat flux as dryout progresses along the tube decreases rapidly downstream of where the onset of dryout appears.

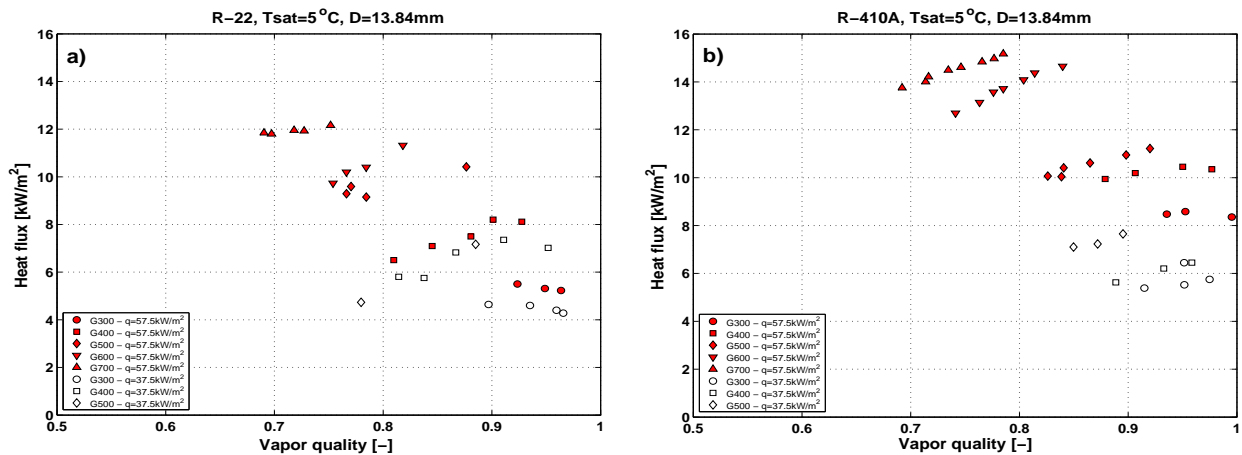


Figure 7.8: Post dryout heat flux evolution for initial condition  $q = 37.5 \text{ kW/m}^2$  and  $q = 57.5 \text{ kW/m}^2$  in the 13.84 mm test section for refrigerants: a) R-22, b) R-410A.

Figures 7.8a and 7.8b show the post dryout heat fluxes in the 13.84 mm test section for R-22 and R-410A, respectively. The initial heat fluxes were  $q = 37.5 \text{ kW/m}^2$  and  $q = 57.5 \text{ kW/m}^2$ . As can be seen for the initial heat flux  $q = 37.5 \text{ kW/m}^2$ , the post dryout heat flux varies between  $4.3 \div 7.4 \text{ kW/m}^2$  for R-22 and  $5.4 \div 7.7 \text{ kW/m}^2$  for R-410A. For the initial heat

flux  $q = 57.5 \text{ kW/m}^2$ , the post dryout heat flux varies in the range  $5.2 \div 12.2 \text{ kW/m}^2$  for R-22 and  $8.4 \div 15.2 \text{ kW/m}^2$  for R-410A. The decrease from the initial heat flux is lower as the mass velocity increases.

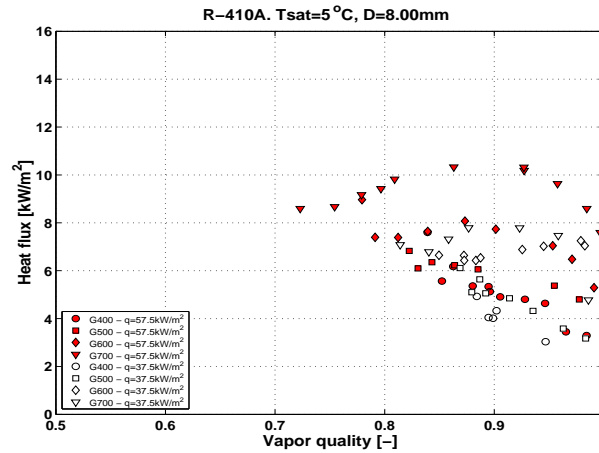


Figure 7.9: Post dryout heat flux evolution for initial condition  $q = 37.5 \text{ kW/m}^2$  and  $q = 57.5 \text{ kW/m}^2$  in the  $8.00 \text{ mm}$  test section for refrigerant R-22.

Figure 7.9 illustrates post dryout heat flux during evaporation of R-410A in the  $8.00 \text{ mm}$  test section. For the same initial heat flux conditions in the wetted perimeter evaporation, the heat flux in post dryout regime is lower by 30 to 60% than in the  $13.84 \text{ mm}$  test section. Furthermore, in all tests, the heat flux continues to decrease for  $x > 0.95$ , what is caused by the non-equilibrium effect.

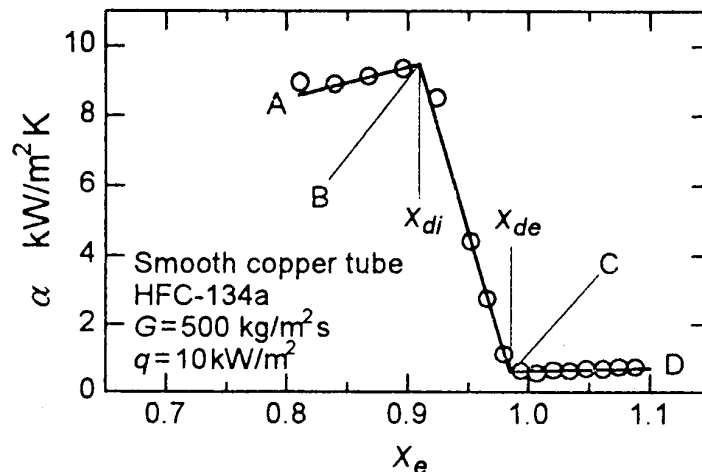


Figure 7.10: Approximation of heat transfer coefficient in the neighborhood of dryout - Mori *et al.* [41] (2000).

There is no surprise that so big a drop in the heat flux results in a rapid decrease of the heat transfer coefficient relative to that prior to dryout. The heat transfer coefficient falls over a limited quality range and then becomes nearly constant in value. This variation as shown in Figure 7.10 has been traced by Mori *et al.* [41] (2000) by three straight lines. The point of intersection B indicates the inception point of dryout at the top of the horizontal tube, at which the heat transfer begins to become worse, and the point of intersection C indicates the point at which the dryout is complete around the tube perimeter, where the deterioration of the heat transfer ends. The qualities at the respective points are denoted  $x_{di}$  and  $x_{de}$ . The distinction of these two points is caused by the shift of the dryout position from the top to the bottom along the tube perimeter with increasing quality and also by the irregular fluctuations of the axial dryout position. The same effect of nearly linear reducing of heat transfer coefficient over a certain vapor quality range was clearly observed during the present evaporation tests, which will now be presented below.

Figures 7.11, 7.12 and 7.13 show experimental results of the local heat transfer coefficient measurements in the 13.84 mm test section for R-22 at the initial heat fluxes  $q = 57.5, 37.5$  and  $17.5 \text{ kW/m}^2$ , respectively. Like in the approach of Mori, three lines trace the variation of heat transfer. In the annular flow close to dryout, heat transfer coefficient increases with increasing of the vapor quality almost linearly. The dryout inception -  $x_{di}$  is determined by the last heat transfer point after which the initial heat flux started decreasing. The heat transfer drop in the transition zone (between annular and mist flow) can be modelled by a steep line, which intersects nearly horizontal line representing mist flow heat transfer. The experimental point at which the decline of heat transfer coefficient ends is considered to be end of dryout and is denoted as -  $x_{de}$ . More details concerning selection of qualities  $x_{di}$  and  $x_{de}$  are described at the end of this section. It can be observed that the dryout inception -  $x_{di}$  appears at lower vapor qualities as the mass velocity increases. For example, for the initial heat flux  $q = 57.5 \text{ kW/m}^2$ ,  $x_{di}$  varies between 0.52 and 0.72 at the mass velocities  $G = 700 \text{ kg/m}^2\text{s}$  and  $G = 300 \text{ kg/m}^2\text{s}$ , respectively. For the same conditions, the end of dryout -  $x_{de}$  varies between 0.68 and 0.92. As it can be seen in Figures 7.12 and 7.13 at lower initial heat fluxes,  $x_{di}$  and  $x_{de}$  move to higher vapor qualities and the transition zone between them becomes smaller.

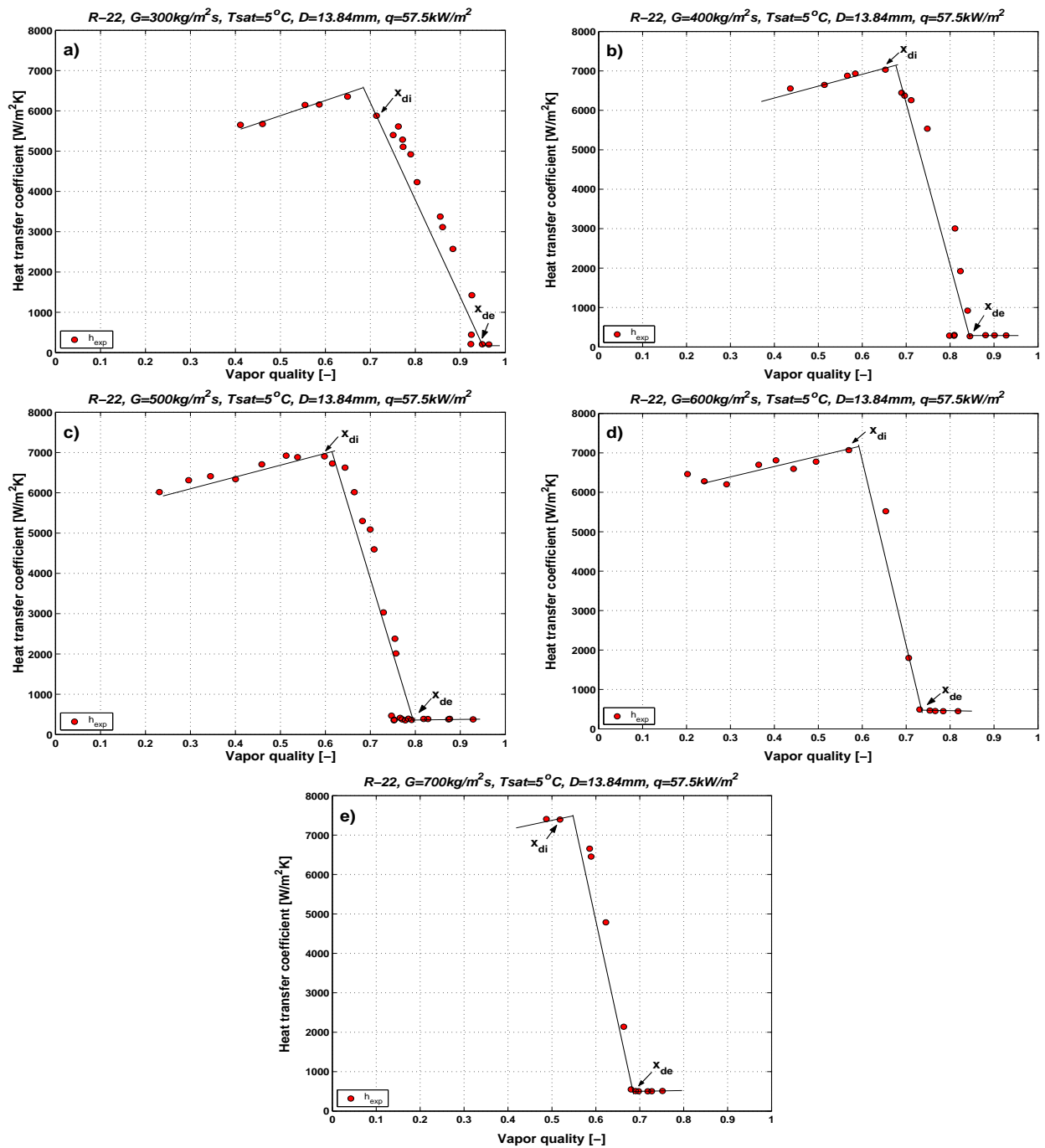


Figure 7.11: Experimental heat transfer coefficients in the 13.84 mm test section for R-22,  $T_{sat} = 5^{\circ}C$ ,  $q = 57.5 kW/m^2$ , at mass velocities: a)  $300 kg/m^2s$ , b)  $400 kg/m^2s$ , c)  $500 kg/m^2s$ , d)  $600 kg/m^2s$ , e)  $700 kg/m^2s$ .

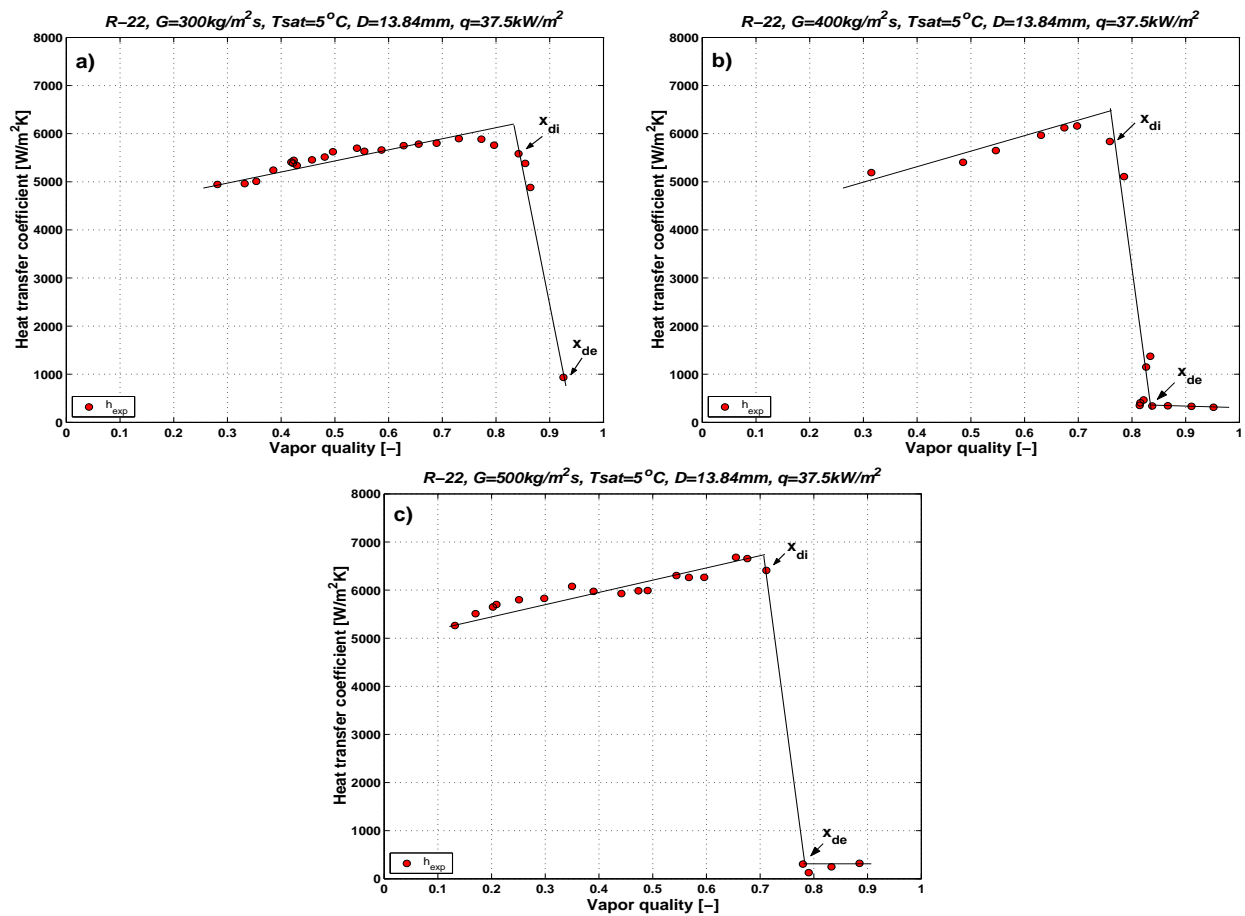


Figure 7.12: Experimental heat transfer coefficients in the 13.84 mm test section for R-22,  $T_{sat} = 5^\circ\text{C}$ ,  $q = 37.5 \text{ kW/m}^2$ , at mass velocities: a)  $300 \text{ kg/m}^2\text{s}$ , b)  $400 \text{ kg/m}^2\text{s}$ , c)  $500 \text{ kg/m}^2\text{s}$ .

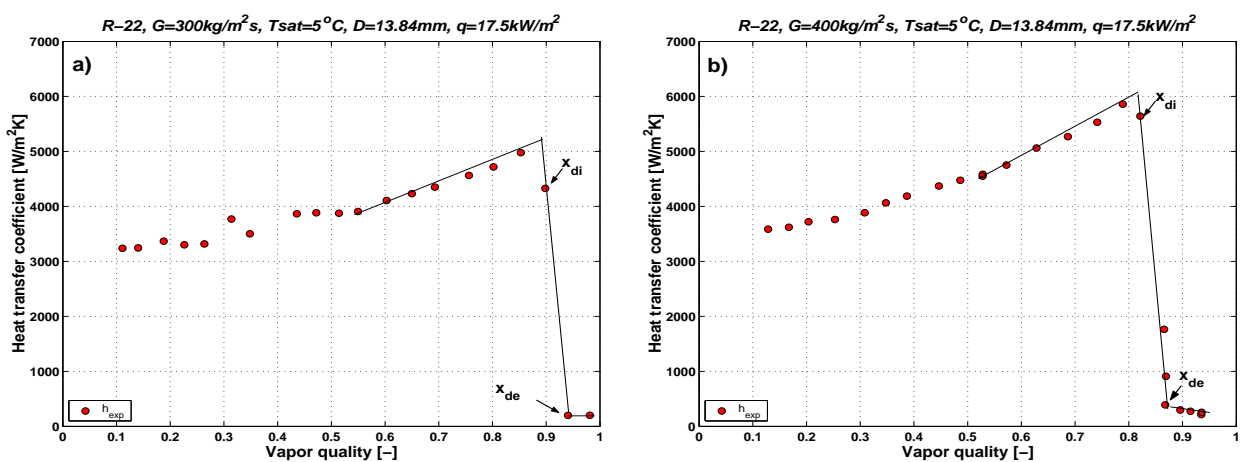


Figure 7.13: Experimental heat transfer coefficients in the 13.84 mm test section for R-22,  $T_{sat} = 5^\circ\text{C}$ ,  $q = 17.5 \text{ kW/m}^2$ , at mass velocities: a)  $300 \text{ kg/m}^2\text{s}$ , b)  $400 \text{ kg/m}^2\text{s}$ .

Similar phenomena are observed in the tests with R-410A. The results for the 13.84 mm test section are presented in Figures 7.14, 7.15, 7.16 for initial heat fluxes  $q = 57.5, 37.5$  and  $17.5 \text{ kW/m}^2$ , respectively. Compared to the experimental results of R-22, the line modelling heat transfer coefficient in the annular flow is much more flat in the R-410A tests. The average heat transfer coefficient for R-410A is higher than that in the R-22 tests of 22%, 26% and 42.5% for the initial heat fluxes  $q = 57.5, 37.5$  and  $17.5 \text{ kW/m}^2$ , respectively. It is caused by the higher reduced pressure of R-410A, which results in increasing of the nucleate boiling contribution. Comparing the onsets of dryout for both liquids presented in Figure 7.19a and 7.19b, it can be seen that  $x_{di}$  appears at the initial heat flux  $q = 57.5 \text{ kW/m}^2$  at highest mass velocities earlier for R-410A than for R-22. This can be explained that a liquid film with more nucleation sites can more easily become entrained by the high velocity vapor. The nucleate boiling contribution of R-410A is 30% greater than that of R-22. Figures 7.17 and 7.18 show heat transfer coefficients for R-410A evaporated in the 8.00 mm test section at initial heat fluxes  $q = 57.5$  and  $37.5 \text{ kW/m}^2$ . In annular flow, lines representing heat transfer are either flat or even slightly decreasing with increasing of vapor quality. The heat transfer coefficient is on average 35% higher than in the 13.84 mm test section. Figure 7.19c show the onsets and the ends of dryout for evaporation tests of R-410A in the 8.00 mm test section. Comparing the ends of dryout in the 8.00 mm tube with those from Figure 7.19b in the 13.84 mm tube, it can be said that in both tests  $x_{de}$  has similar values. However, the onsets of dryout -  $x_{di}$  in smaller diameter tube do not increase with decreasing of G for four tested mass velocities. It has to be said that the heat transfer coefficient was measured for the discrete vapor qualities. The increase of vapor quality between two successive experimental points was from 0.03 to 0.05. The dryout inception -  $x_{di}$  was identified as the last point after which the heat flux dropped more than 10% from its initial value. It was resulting in the selection of point, which was sometimes at the intersection of lines tracing heat transfer coefficient or close to it. The end of dryout -  $x_{de}$  was selected as the first point of mist flow. The accuracy of the vapor quality determination is presented in section 4.5.1.

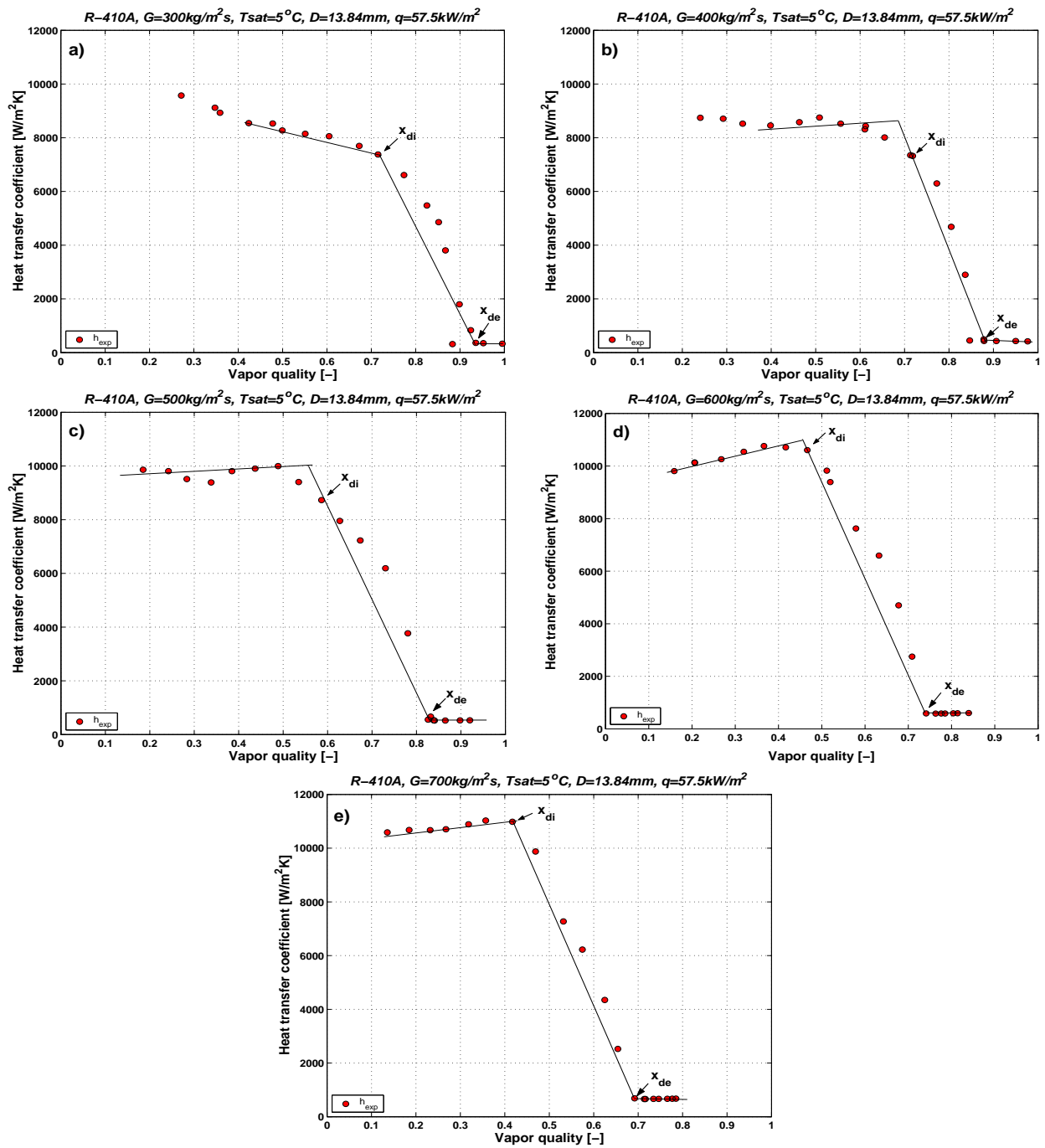


Figure 7.14: Experimental heat transfer coefficients in the 13.84 mm test section for R-410A,  $T_{sat} = 5^\circ C$ ,  $q = 57.5 kW/m^2$ , at mass velocities: a) 300  $kg/m^2s$ , b) 400  $kg/m^2s$ , c) 500  $kg/m^2s$ , d) 600  $kg/m^2s$ , e) 700  $kg/m^2s$ .

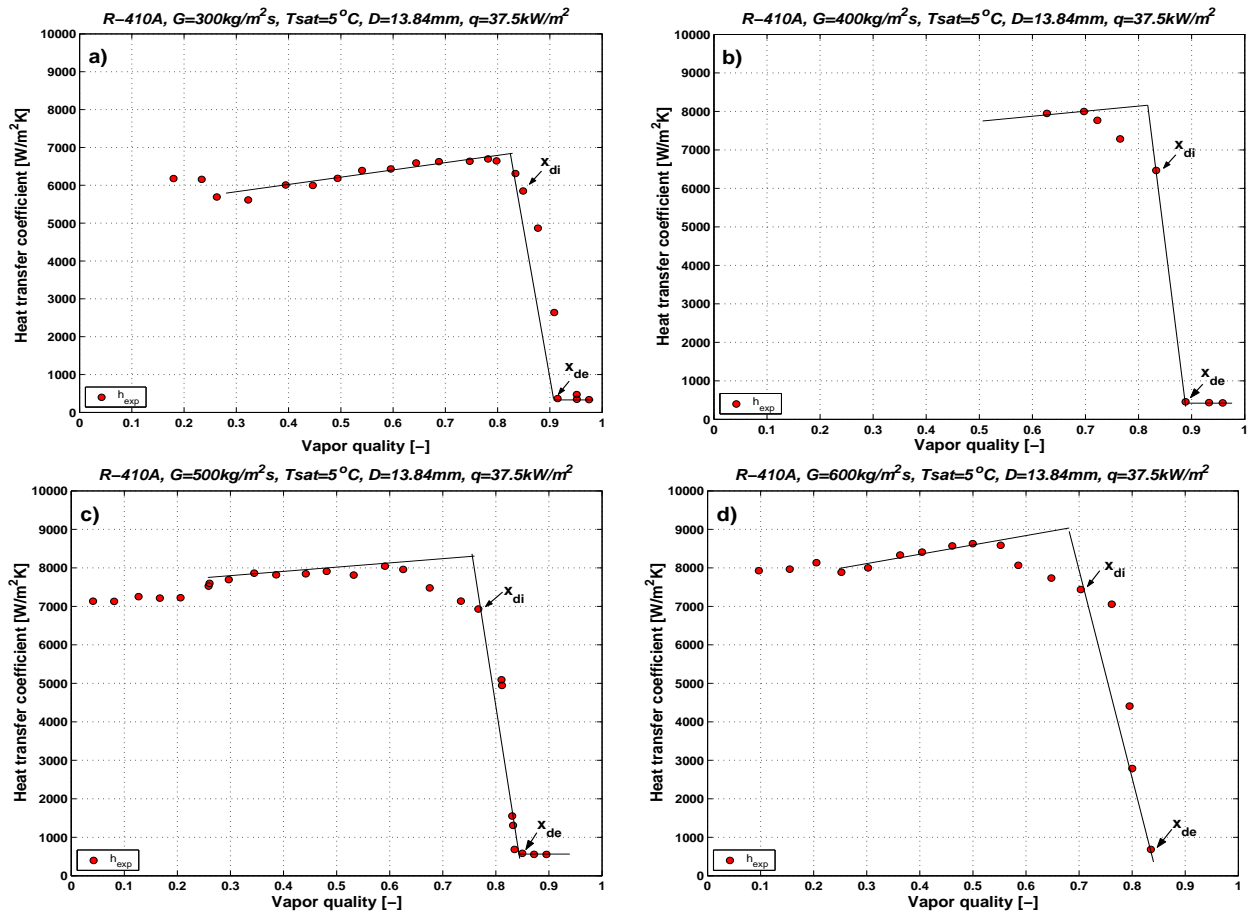


Figure 7.15: Experimental heat transfer coefficients in the 13.84 mm test section for R-410A,  $T_{sat} = 5^\circ C$ ,  $q = 37.5 kW/m^2$ , at mass velocities: a)  $300 kg/m^2s$ , b)  $400 kg/m^2s$ , c)  $500 kg/m^2s$ , d)  $600 kg/m^2s$ .

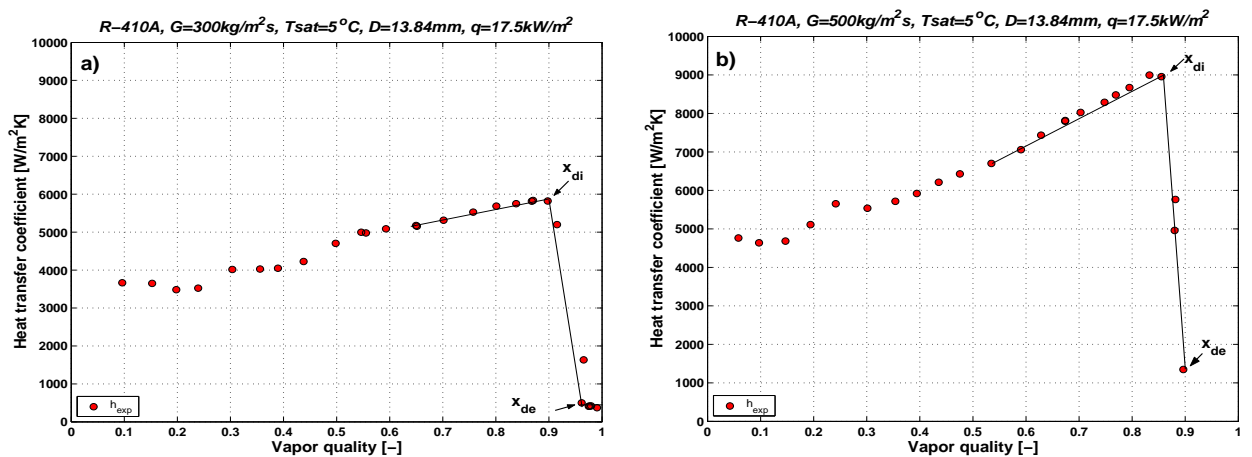


Figure 7.16: Experimental heat transfer coefficients in the 13.84 mm test section for R-410A,  $T_{sat} = 5^\circ C$ ,  $q = 17.5 kW/m^2$ , at mass velocities: a)  $300 kg/m^2s$ , b)  $500 kg/m^2s$ .



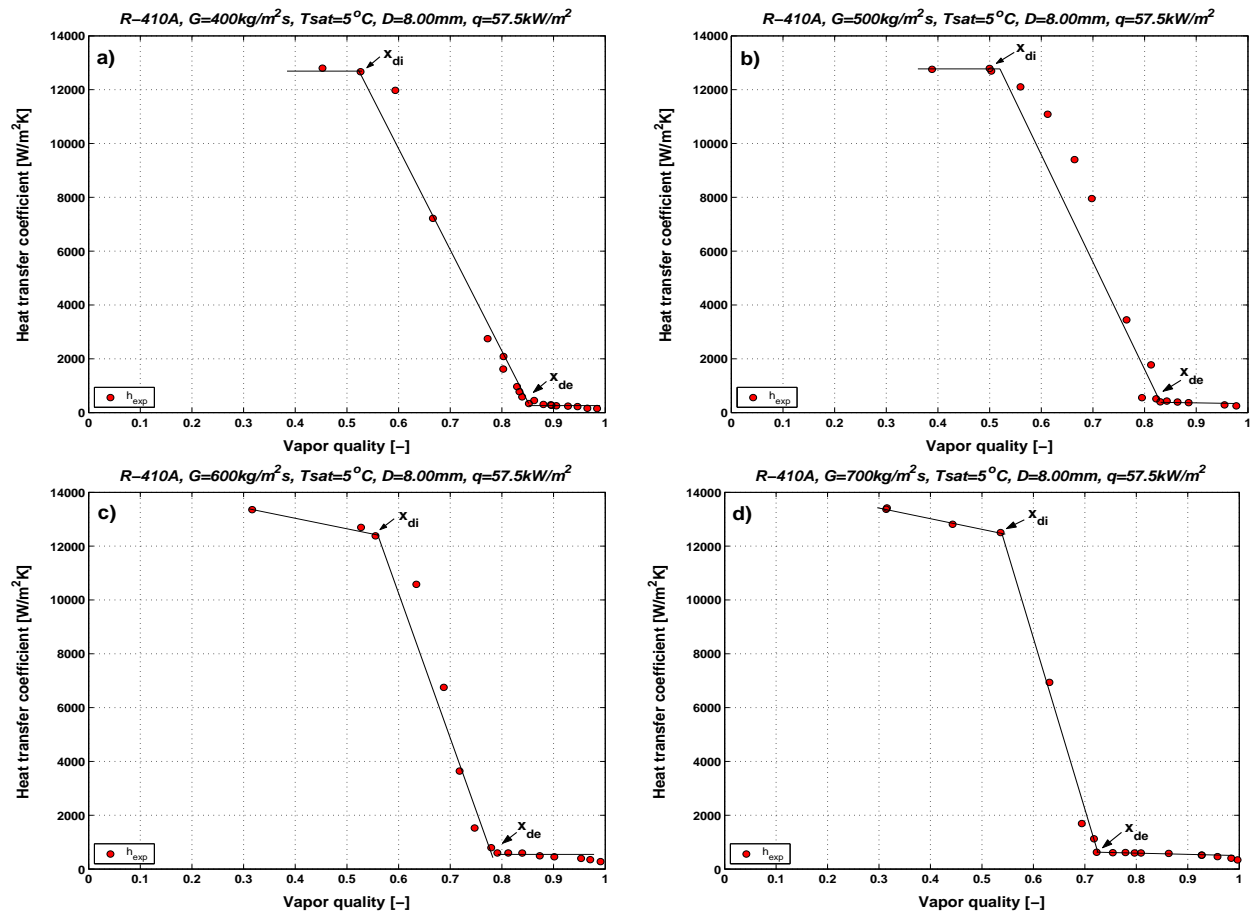


Figure 7.17: Experimental heat transfer coefficients in the 8.00 mm test section for R-410A,  $T_{sat} = 5^\circ\text{C}$ ,  $q = 57.5 \text{ kW/m}^2$ , at mass velocities: a)  $400 \text{ kg/m}^2\text{s}$ , b)  $500 \text{ kg/m}^2\text{s}$ , c)  $600 \text{ kg/m}^2\text{s}$ , d)  $700 \text{ kg/m}^2\text{s}$ .

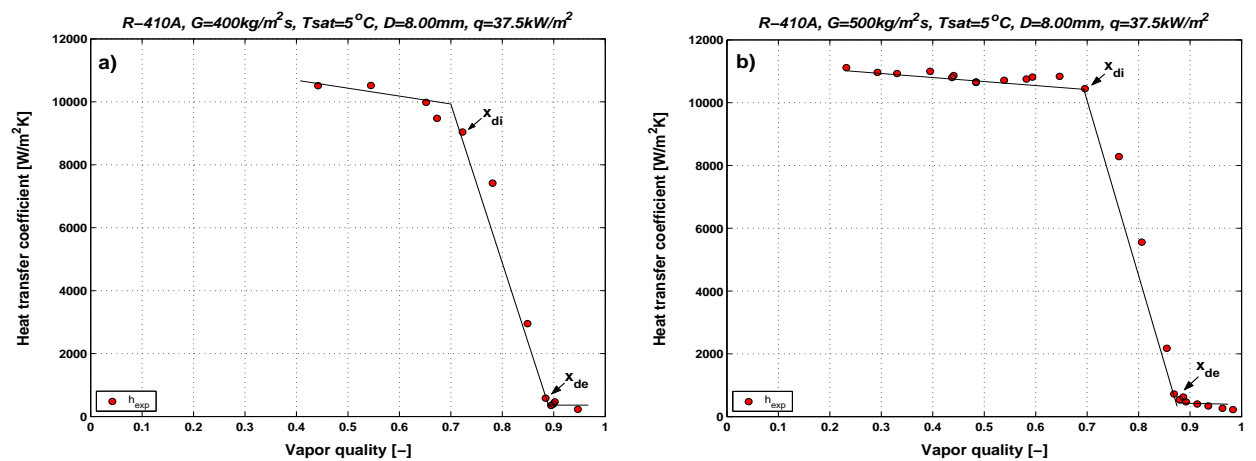


Figure 7.18: Experimental heat transfer coefficients in the 8.00 mm test section for R-410A,  $T_{sat} = 5^\circ\text{C}$ ,  $q = 37.5 \text{ kW/m}^2$ , at mass velocities: a)  $400 \text{ kg/m}^2\text{s}$ , b)  $500 \text{ kg/m}^2\text{s}$ .

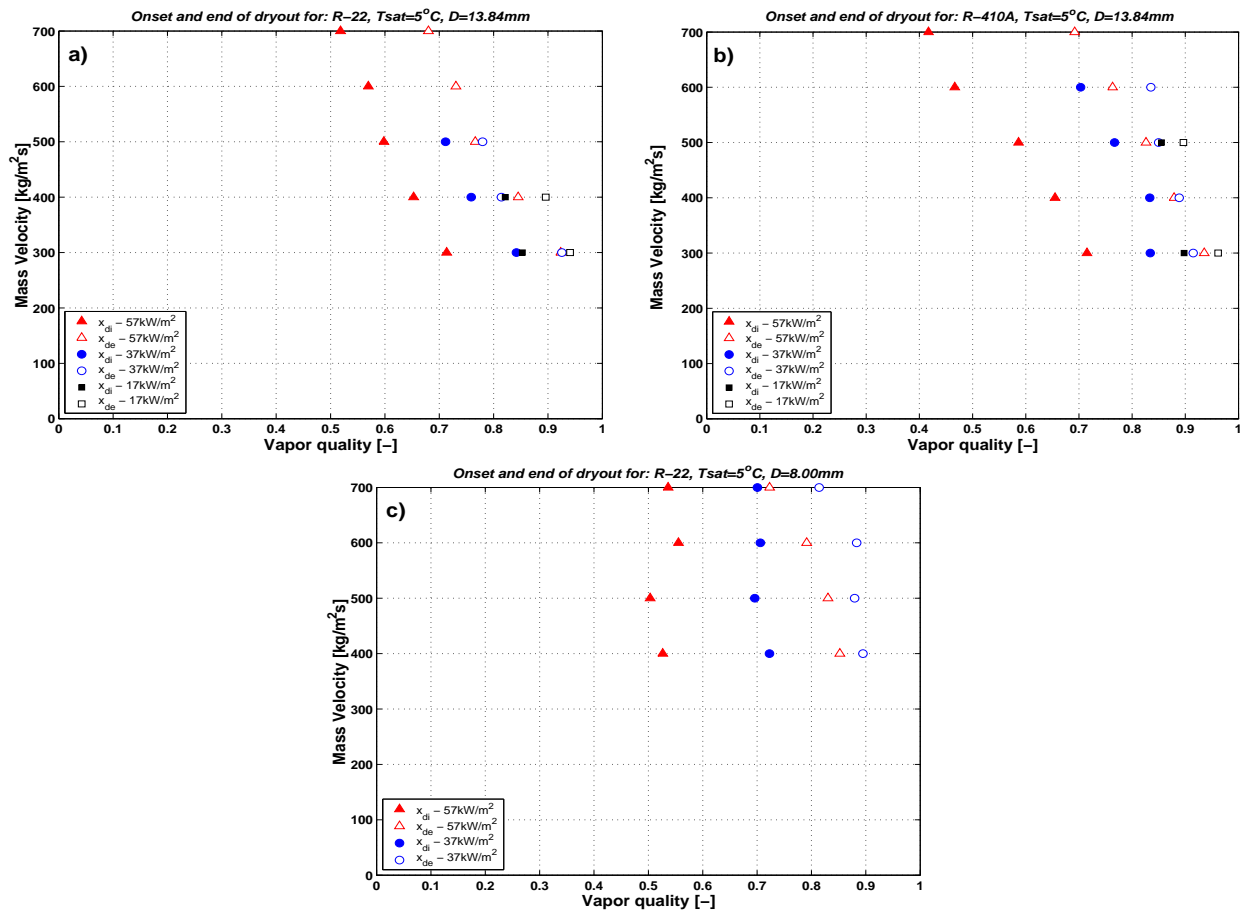


Figure 7.19: Dryout inception -  $x_{di}$  and dryout completion -  $x_{de}$  for tests: a)  $R - 22, D = 13.84 \text{ mm}$ , b)  $R - 410A, D = 13.84 \text{ mm}$ , c)  $R - 410A; D = 8.00 \text{ mm}$ .

## 7.4.2 New transitions: Annular-Dryout and Dryout-Mist flow

Analysing experimental results presented in the previous section and from observation in the sight glass, it is obvious that there is no step-wise transition from Annular to Mist flow. As depicted in Figure 7.20, dryout occurred at the top of the tube first (cross-section A-A), where the liquid film is thinner and progresses downward around the perimeter until reaching the bottom (cross-section B-B). The process of dryout thus takes place over a range of vapor qualities and ends at the bottom of the tube when the fully developed mist flow regime is reached as presented in cross-section C-C. This regime between points  $x_{di}$  and  $x_{de}$  will be called dryout.

First attempt to model the annular-dryout transition during evaporation in horizontal tubes was made by Lavin and Young [39] (1965). They proposed a new transition between the

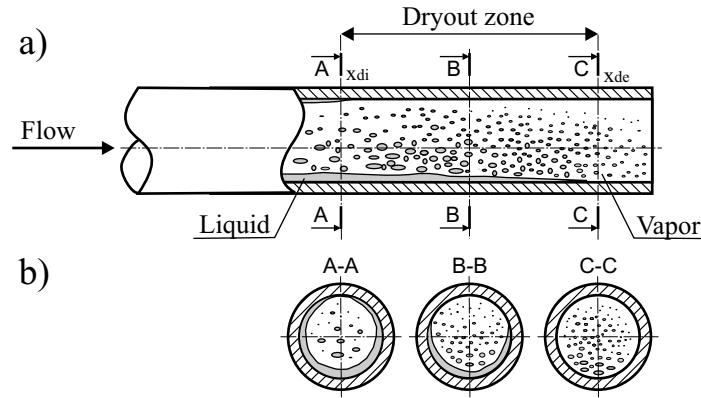


Figure 7.20: a) Dryout zone during evaporation in horizontal tube; b) Cross sections: A-A onset of dryout in annular flow; B-B dryout; C-C end of dryout and beginning of mist flow.

annular and dryout zones based on the Weber number for R-22 and R-12. Lavin and Young observed the dryout, but with the apparatus used, they could not obtain the heat transfer coefficient within the dryout regime nor study the conditions under which the dryout regime ends and stable mist flow was established. Kattan *et al.* (see section 2.2.1) used the Steiner version of the Taitel-Dukler "A-M" curve to predict the transition from annular to mist flow. He added a criterion to avoid the possibility of a mist flow reverting back again to annular flow with increasing vapor quality. This approach does not distinguish between annular-dryout and dryout-mist flow transitions and predicts the annular-mist flow transition only by one curve, which in horizontal diabatic flow is not appropriate as shown above. It has to be noted that this transition boundary has not been investigated experimentally in the work of Kattan. Since dryout proceeds over a certain vapor quality range, Mori *et al.* [41] (2000) defined dryout inception -  $x_{di}$  and completion -  $x_{de}$  classified into three characteristic regimes S1, S2 and S3 defined as follows:

Regime-S1 (High G (approx. over  $300 \text{ kg/m}^2\text{s}$ ) and low  $q/G$  (approx. below  $0.03 \text{ kJ/kg}$ ):

$$x_{di1} = 0.94 - 1.75 \cdot 10^{-6} (Re_V Bo)^{1.75} (\rho_V / \rho_L)^{-0.86} \quad (7.33)$$

$$x_{de1} = 1.02 - 1.75 \cdot 10^{-6} (Re_V Bo)^{1.75} (\rho_V / \rho_L)^{-0.86} \quad (7.34)$$

Regime-S2 (High G (approx. over  $300 \text{ kg/m}^2\text{s}$ ) and medium  $q/G$  (approx. between 0.03 and  $0.08 \text{ kJ/kg}$ ):

$$x_{di2} = 0.58 e^{[0.52 - 2.1 \cdot 10^{-5} We_V^{0.96} Fr_V^{-0.02} (\rho_V / \rho_L)^{-0.08}] \quad (7.35)$$

$$x_{de2} = 0.61 e^{[0.57 - 2.65 \cdot 10^{-5} We_V^{0.94} Fr_V^{-0.02} (\rho_V / \rho_L)^{-0.08}] \quad (7.36)$$

Regime-S3 (High G (approx. over  $300 \text{ kg/m}^2\text{s}$ ) and high  $q/G$  (approx. over  $0.08 \text{ kJ/kg}$ ), or low G (approx. below  $300 \text{ kg/m}^2\text{s}$ )):

$$x_{di3} = \min(x_{di3a}, x_{di3b}) \quad (7.37)$$

$$x_{de3} = \min(x_{de3a}, x_{de3b}) \quad (7.38)$$

where

$$x_{di3a} = 0.98 Fr_V^{0.05} Bo^{-0.05} (\rho_V/\rho_L)^{0.16} \quad (7.39)$$

$$x_{di3b} = 0.172 Fr_V^{0.04} Bo^{-0.40} We_V^{-0.09} (\rho_V/\rho_L)^{0.21} \quad (7.40)$$

$$x_{de3a} = 1.01 \quad (7.41)$$

$$x_{de3b} = 0.69 Fr_V^{0.02} Bo^{-0.22} We_V^{-0.09} (\rho_V/\rho_L)^{0.16} \quad (7.42)$$

The nondimensional numbers have been defined by Mori as:

$$Fr_V = G^2/[gD\rho_V(\rho_L - \rho_V)] \quad (7.43)$$

$$Re_V = GD/\mu_V \quad (7.44)$$

$$We_V = G^2D/(\rho_V\sigma) \quad (7.45)$$

The definition of the boiling number -  $Bo$  corresponds to the definition in equation 1.44.

For a given set of conditions, the dryout inception vapor quality has to be determined from the above equations for Regime-S1, S2, S3 and will be denoted as  $x_{di1}$ ,  $x_{di2}$  and  $x_{di3}$ , respectively. Then the dryout vapor quality  $x_{di}$  is determined as:

$$\left. \begin{aligned} x_{di} &= x_{di3} \quad \text{when } x_{di2} \geq x_{di3} \\ x_{di} &= x_{di2} \quad \text{when } x_{di2} < x_{di3} \quad \text{and } x_{di2} \geq x_{di1} \\ x_{di} &= x_{di1} \quad \text{when } x_{di2} < x_{di3} \quad \text{and } x_{di2} < x_{di1} \end{aligned} \right\} \quad (7.46)$$

The dryout completion vapor quality  $x_{de}$  is determined by the same procedure where  $x_{di}$  in equation 7.46 has to be replaced by  $x_{de}$ , and the values of  $x_{de1}$ ,  $x_{de2}$  and  $x_{de3}$  for Regime-S1, S2, S3 are calculated from equations 7.34, 7.36 and 7.38, respectively.

Figures 7.21a and 7.21b show the comparison of the experimental dryout inception and completion data with the prediction of Mori for initial heat fluxes of  $57.5 \text{ kW/m}^2$  and  $37.5 \text{ kW/m}^2$ , respectively. The test liquid was R-22, the diameter of the test section  $D = 13.84 \text{ mm}$  and  $T_{sat} = 5^\circ\text{C}$ . The solid curves show the transition of Mori and originates from

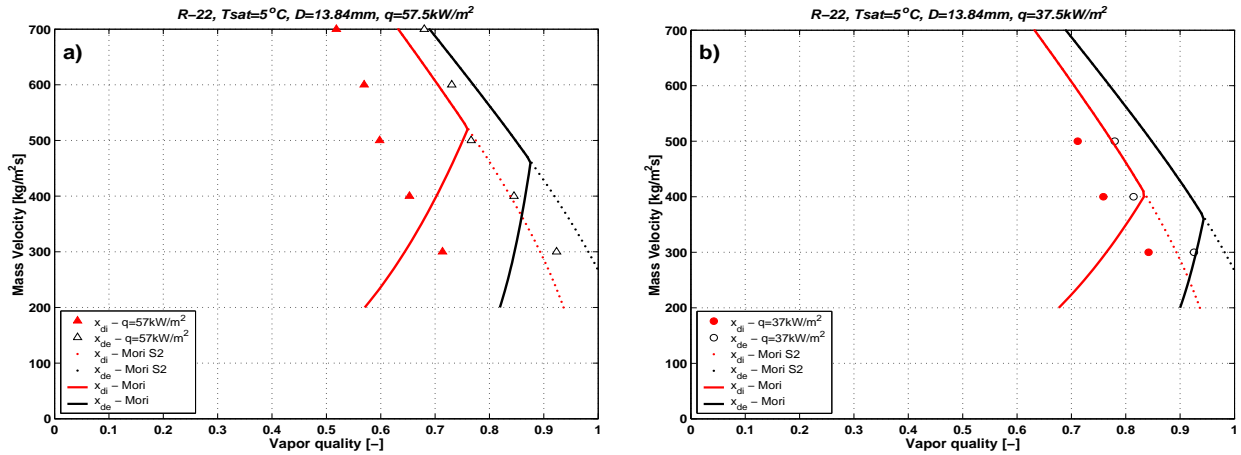


Figure 7.21: Comparison of experimental dryout inception and completion with the prediction of Mori for: R-22,  $D = 13.84 \text{ mm}$  and initial heat fluxes: a)  $57.5 \text{ kW/m}^2$ , b)  $37.5 \text{ kW/m}^2$ .

the intersection of curves representing Regime-S2 (dotted curves - equations 7.35, 7.36) and Regime-S3 (bottom part of the solid curves - equations 7.37, 7.38). The Regime-S3 in the prediction of Mori is a function of heat flux. The higher the initial heat flux, the higher mass velocity at which intersection points appear. Starting from the intersection points, dryout inception and completion qualities decrease with decreasing of the mass velocity. Analysing all experimental dryout inception and completion qualities presented in Figure 7.19 it is clear that  $x_{di}$  and  $x_{de}$  are a function of the heat flux for each mass velocity, also above the intersection points. In contrary to the approach of Mori, the experimental points do not create any "V shape". The dryout inception and completion quality always increase as the mass velocity decreases and show the same trend as the predictions for Regime-S2. The effect of "V shape" in the prediction method of Mori can be probably explained as the consequence of his using electrical heating for his test section.

Figure 7.22 shows the results of two independent evaporation tests with R-22 at mass velocity  $G = 200 \text{ kg/m}^2\text{s}$ . The circles corresponds to the heat transfer coefficient measured by Lallemand et al. [38] (2001) at  $T_{sat} = 12^\circ\text{C}$  using an electrically heated tubes and the squares illustrate the heat transfer coefficient measured during actual evaporation tests at  $T_{sat} = 5^\circ\text{C}$  using fluid-to-fluid heating described in section 4.1. The heat transfer coefficient measured in the fluid-to-fluid heated test section is lower compared to the results of Lallemand for the vapor qualities below 0.3. It is caused by the lower  $T_{sat}$  and thereby smaller nucleate boiling contribution in the heat transfer process. In the vapor quality range from 0.3 to 0.8 the heat

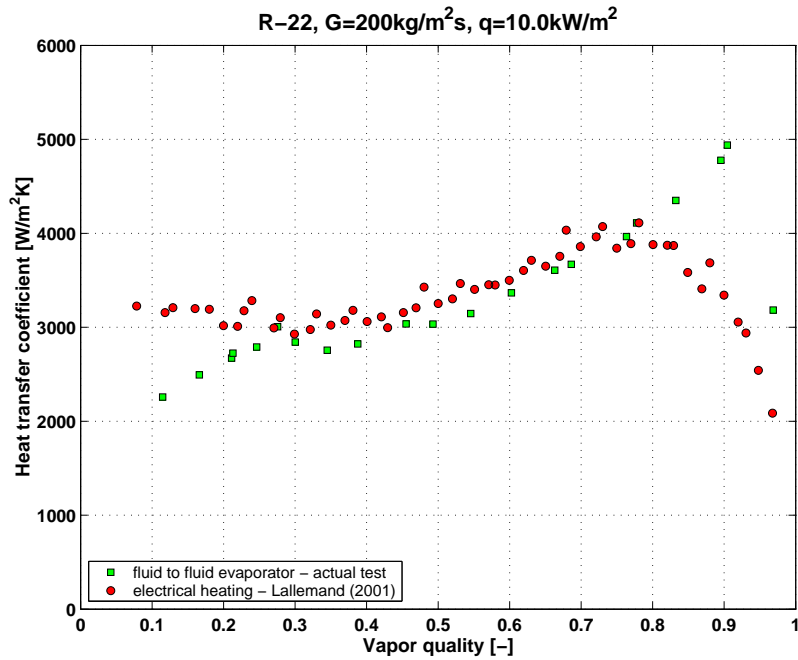


Figure 7.22: Effect of electrical heating on the onset of dryout compared to the fluid-to-fluid evaporator.

transfer coefficients measured in both tests have almost the same values. After exceeding a vapor quality of 0.8, the heat transfer coefficient in the electrical heated section of Lallemand starts decreasing, what means that the onset of dryout appears. In contrary in the fluid-to-fluid evaporator, the heat transfer coefficient increases to the vapor quality of 0.90, where the dryout begins. The dryout inception at lower vapor quality in the electrical heated test section can be explained as an effect of "non-controlled wall temperature increase". During evaporation the liquid film becomes thinner with the increase of the vapor quality. Due to gravity forces the liquid film is much thinner on the top of the tube than on the bottom. If the liquid film on the upper part of the tube will be entrained by the high velocity vapor or will completely evaporate, the wall temperature will rapidly increase, what preventing rewetting of the surface. It means that the electrical heating does not represent the real operating conditions of the fluid evaporators particularly at the high vapor qualities and in stratified flows.

As it has been already pointed out, the dryout inception and completion quality always increase as the mass velocity decreases and show the same trend as the predictions for Regime-S2. Thus, it has been decided to extend equations 7.35 and 7.36 by the heat flux effect. Furthermore, new empirical factors have been found to fit curves with all measured

dryout inception and completion qualities for both tested fluids. After optimizing using the least square error method, new limits of dryout can be calculated from the following equations:

$$x_{di} = 0.58e^{[0.52 - 0.235 \cdot We_V^{0.17} Fr_V^{0.37} (\rho_V / \rho_L)^{0.25} (q/q_{crit})^{0.70}]} \quad (7.47)$$

$$x_{de} = 0.61e^{[0.57 - 5.8 \cdot 10^{-3} We_V^{0.38} Fr_V^{0.15} (\rho_V / \rho_L)^{-0.09} (q/q_{crit})^{0.27}]} \quad (7.48)$$

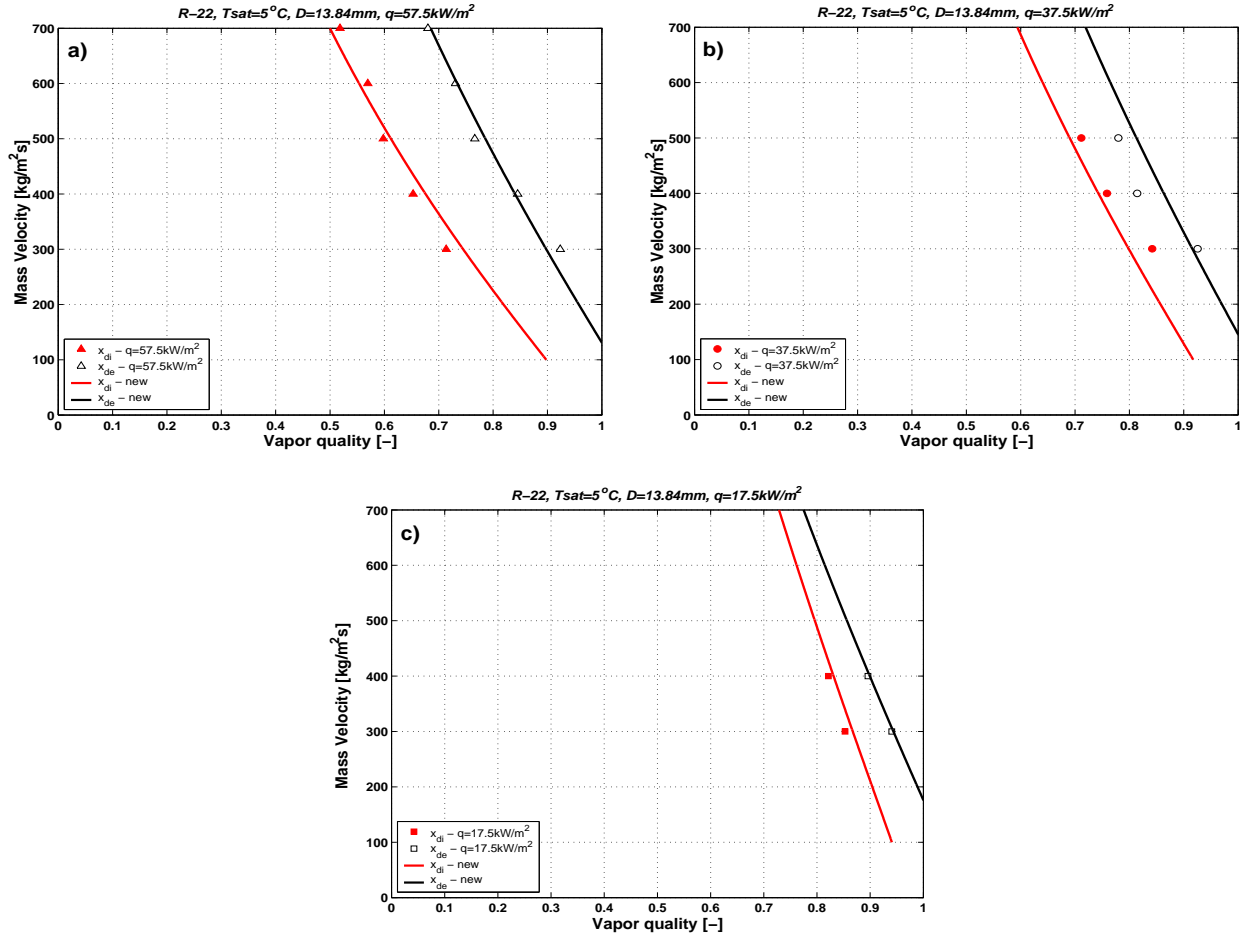


Figure 7.23: New prediction of dryout inception and completion compared to the experimental results of R-22 in the 13.84 mm test section at initial heat fluxes: a) 57.5 kW/m<sup>2</sup>, b) 37.5 kW/m<sup>2</sup>, c) 17.5 kW/m<sup>2</sup>.

Figure 7.23 shows new transition curves calculated from equations 7.47 and 7.48 compared to  $x_{di}$  and  $x_{de}$  obtained during evaporation tests with R-22 in the 13.84 mm test section. As can be seen, very good agreement has been found between the prediction and experimental points for all three initial heat fluxes. Similar results have been obtained for the evaporation tests with R-410A.

### 7.4.3 Updating of flow pattern map of Thome-El Hajal for dryout effects

As the first step in developing of a heat transfer model for the dryout and mist flow regimes, the existing flow pattern map has to be updated. In the previous section, the dryout regime has been defined with two boundaries: annular-dryout "A-D" and dryout-mist flow "D-M". The new transition curves are functions of heat flux and capture the heat transfer effect in the high vapor quality range. In the flow pattern map of Kattan-Thome-Favrat, the heat transfer effect was taken into account using empirical exponents  $F_1(q)$  and  $F_2(q)$  defined in equations 2.19 and 2.20. As presented in section 2.2.3, Thome and El Hajal reduced the heat transfer effect proposed by Kattan by the factor of 2 and simplified the method by eliminating all iteration. Even if Thome and El Hajal recommended using Zürcher transitions "S-SW" and "SW-I/A" developed for ammonia, better agreement of experimental points has been found with the original transitions proposed by Kattan and those will be used here. Based on the present void fraction measurements "S-SW" curve has been adjusted in the vapor quality below  $x_{IA}$  as described in section 6.1. Furthermore, the stratified-wavy region from flow pattern map of Kattan has been divided into: slug, slug/stratified-wavy and stratified-wavy zone. To combine the new transition curves "A-D" and "D-M" with the Thome-El Hajal flow pattern map, the following procedure is proposed:

1. Calculate geometrical parameters  $\varepsilon$ ,  $A_{LD}$ ,  $A_{VD}$ ,  $\theta_{strat}$ ,  $h_{LD}$  and  $P_{iD}$  from equations 5.47, 2.31, 2.32, 2.35, 2.33 and 2.34, respectively.
2. As the effect of heat flux for high vapor quality is captured by the "A-D" and "D-M" transitions, the following adiabatic version of the original Kattan-Thome-Favrat boundary is proposed for prediction of "SW-I/A" transition:

$$G_{wavy} = \left\{ \frac{16A_{VD}^3 g D \rho_L \rho_V}{x^2 \pi^2 (1 - (2h_{LD} - 1)^2)^{0.5}} \left[ \frac{\pi^2}{25h_{LD}^2} \cdot \left( \frac{We}{Fr} \right)_L^{-1} + \frac{1}{\cos \varphi} \right] \right\}^{0.5} + 50 \quad (7.49)$$

where inclination angle  $\varphi = 0$  for horizontal tubes.

Stratified-wavy region has been divided into three zones:

- At  $G > G_{wavy}(x_{IA})$  - SLUG ZONE.
- At  $G_{strat} < G < G_{wavy}(x_{IA})$  and  $x < x_{IA}$  - SLUG/STRATIFIED-WAVY ZONE.
- At  $x \geq x_{IA}$  STRATIFIED-WAVY ZONE has been unchanged.



3. "S-SW" transition is calculated from equation 2.14 with following modification  $G_{strat} = G_{strat}(x_{IA})$  at  $x < x_{IA}$ .
4. "I-A" transition is calculated from equation 2.23.
5. "A-D" boundary is calculated as:

$$G_{dryout} = \left[ \frac{1}{0.235} \cdot \left( \ln \left( \frac{0.58}{x} \right) + 0.52 \right) \left( \frac{D}{\rho_V \sigma} \right)^{-0.17} \left( \frac{1}{gD\rho_V(\rho_L - \rho_V)} \right)^{-0.37} \left( \frac{\rho_V}{\rho_L} \right)^{-0.25} \left( \frac{q}{q_{crit}} \right)^{-0.70} \right]^{0.926} \quad (7.50)$$

6. "D-M" boundary is calculated as:

$$G_{dryout} = \left[ \frac{1}{0.0058} \cdot \left( \ln \left( \frac{0.61}{x} \right) + 0.57 \right) \left( \frac{D}{\rho_V \sigma} \right)^{-0.38} \left( \frac{1}{gD\rho_V(\rho_L - \rho_V)} \right)^{-0.15} \left( \frac{\rho_V}{\rho_L} \right)^{0.09} \left( \frac{q}{q_{crit}} \right)^{-0.27} \right]^{0.943} \quad (7.51)$$

7. The following conditions have to be fulfilled clearly to define transitions in the high vapor quality range:

If  $G_{strat} \geq G_{dry}$  then  $G_{dry} = G_{strat}$

If  $G_{wavy} \geq G_{dry}$  then  $G_{dry} = G_{wavy}$

In the above procedure,  $G_{dryout}$  and  $G_{mist}$  have been extracted from equations 7.47 and 7.48. Figure 7.24 shows new flow pattern maps for R-22 in the  $D = 13.84 \text{ mm}$  test section at heat fluxes:  $57.5 \text{ kW/m}^2$ ,  $37.5 \text{ kW/m}^2$ ,  $17.5 \text{ kW/m}^2$  and  $7.5 \text{ kW/m}^2$ . Comparing to the initial Kattan-Thome-Favrat map modified by Thome-El Hajal, a new flow regime can be distinguished on the updated map. This is denoted by "D" for the dryout regime, which becomes smaller with decreasing of heat flux and determines a transition zone between annular, stratified-wavy and mist flow. Figure 7.25 and 7.26 show new flow pattern maps for R-410A at different heat fluxes in the  $8.00 \text{ mm}$  and  $13.84 \text{ mm}$  test section, respectively.

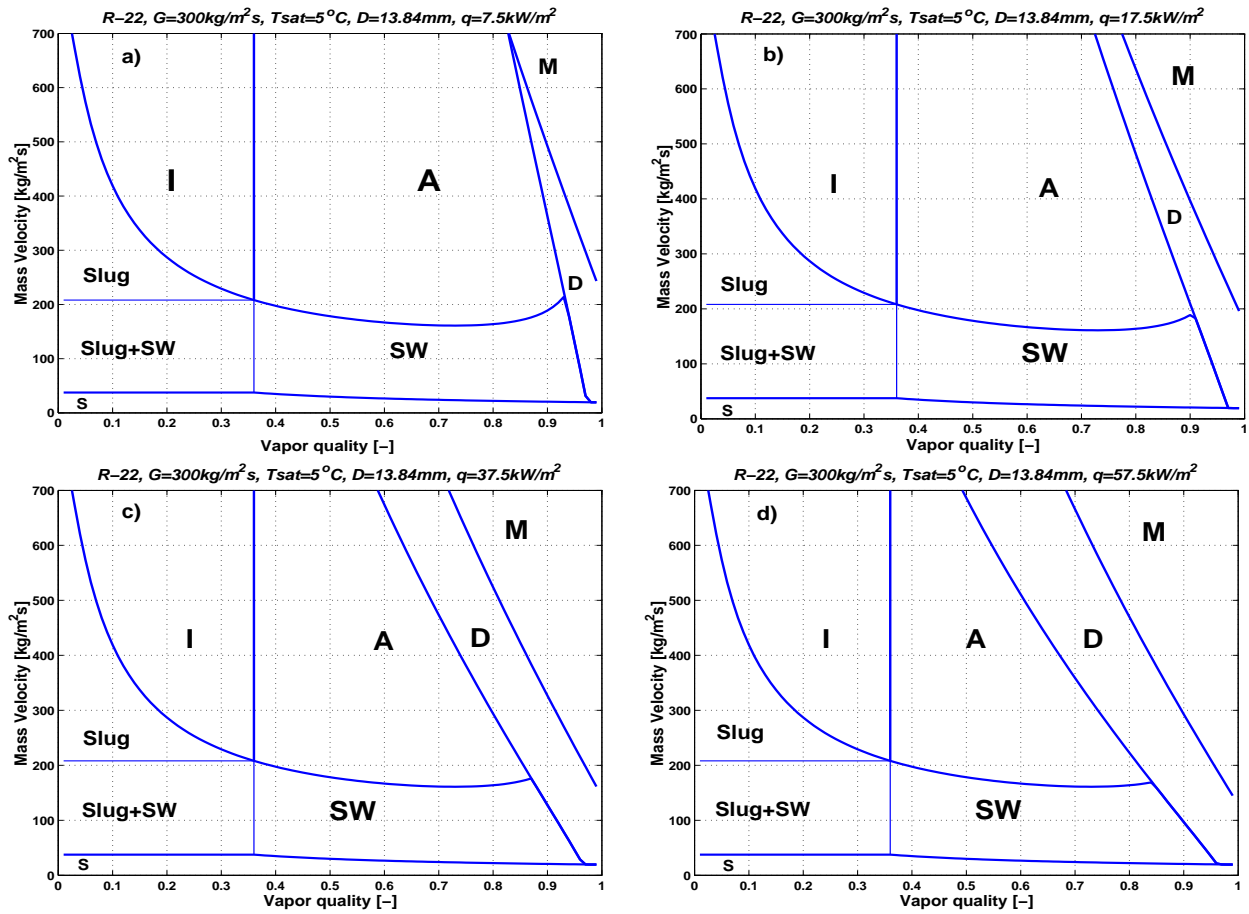


Figure 7.24: New flow pattern maps for R-22,  $T_{\text{sat}} = 5^\circ\text{C}$ ,  $D = 13.84 \text{ mm}$  at  $G = 300 \text{ kg/m}^2\text{s}$  and heat fluxes: a)  $7.5 \text{ kW/m}^2$ , b)  $17.5 \text{ kW/m}^2$ , c)  $37.5 \text{ kW/m}^2$ , d)  $57.5 \text{ kW/m}^2$ .

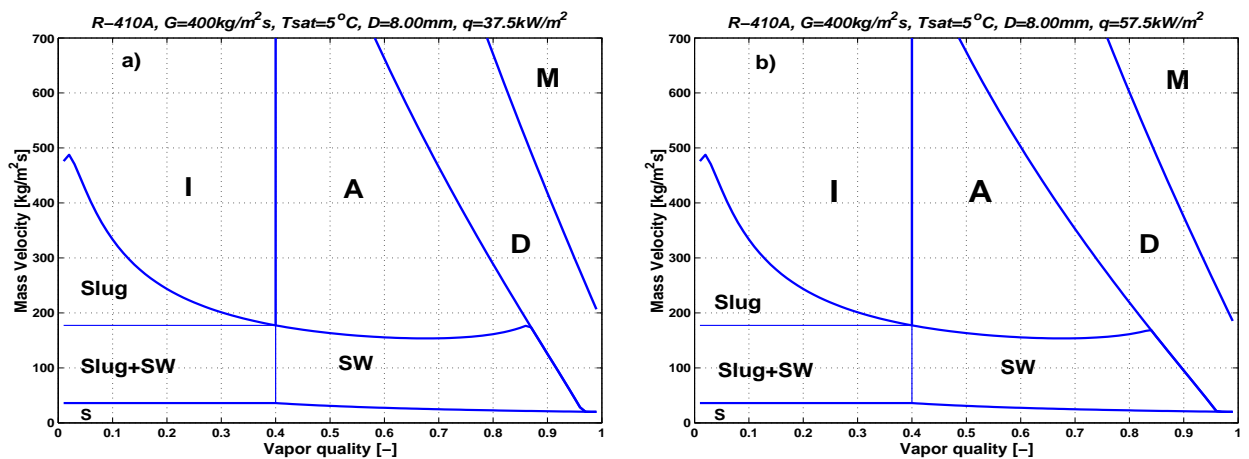


Figure 7.25: New flow pattern maps for R-410A,  $T_{\text{sat}} = 5^\circ\text{C}$ ,  $D = 8.00 \text{ mm}$  at  $G = 400 \text{ kg/m}^2\text{s}$  and initial heat fluxes: a)  $37.5 \text{ kW/m}^2$ , b)  $57.5 \text{ kW/m}^2$ .

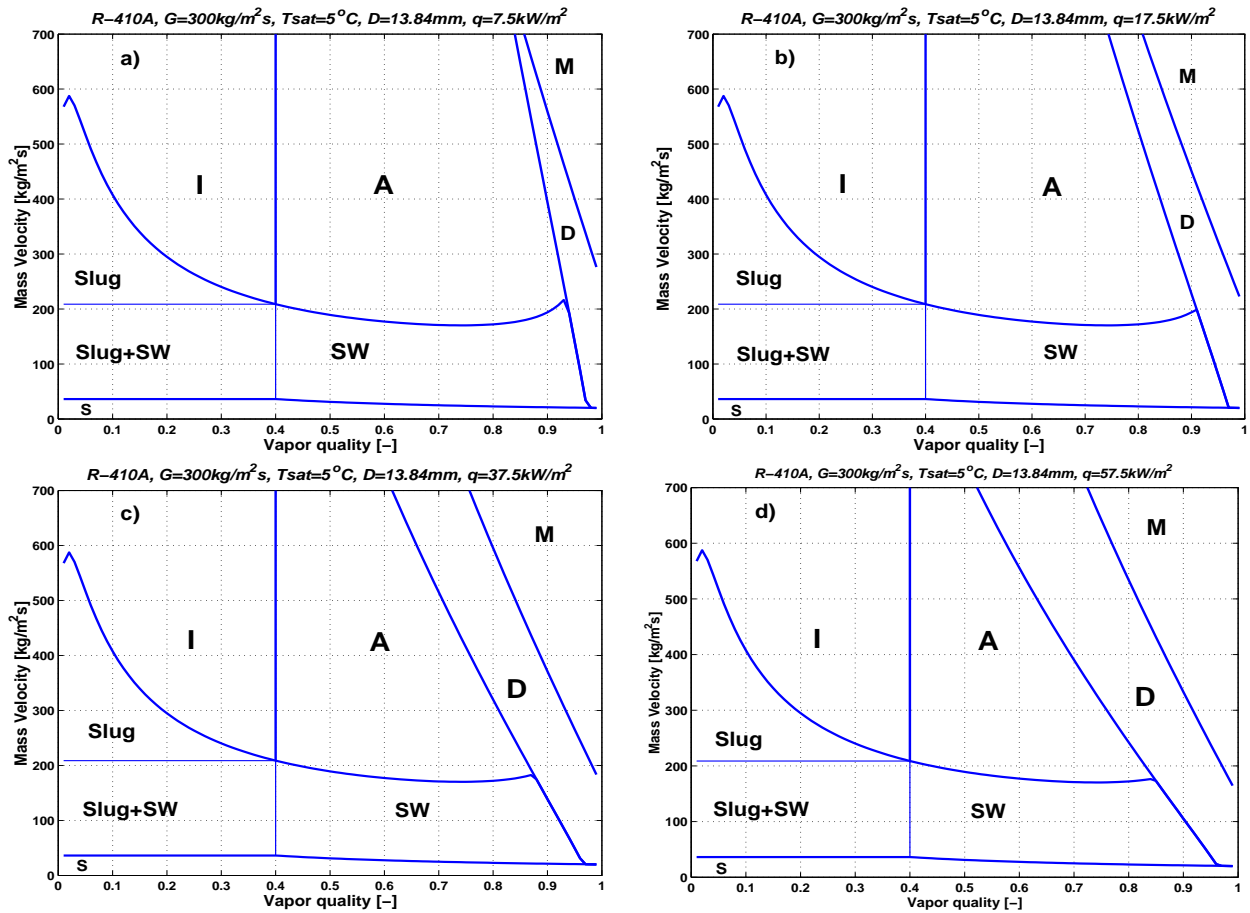


Figure 7.26: New flow pattern maps for R-410A,  $T_{sat} = 5^{\circ}\text{C}$ ,  $D = 13.84 \text{ mm}$  at  $G = 300 \text{ kg/m}^2\text{s}$  and initial heat fluxes: a)  $7.5 \text{ kW/m}^2$ , b)  $17.5 \text{ kW/m}^2$ , c)  $37.5 \text{ kW/m}^2$ , d)  $57.5 \text{ kW/m}^2$ .

#### 7.4.4 New heat transfer model for mist flow and dryout zone

The flow pattern oriented model of Kattan-Thome-Favrat described in section 2.4.4 does not cover neither the new dryout nor the mist flow regimes because of their lack of dryout and mist flow heat transfer data at the time. Also Zürcher [70] (2000) in his ammonia tests investigated mostly the heat transfer coefficient in stratified and stratified-wavy flow regimes. The present study will focus on extending of flow pattern oriented heat transfer model of Kattan-Thome-Favrat to the dryout and mist flow regimes. In the previous section, the new flow pattern map has been described. Two new transition curves  $G_{dryout}$  and  $G_{mist}$  have been defined based on observations and numerous heat transfer data presented in Figures 7.11 - 7.18. All mist flow heat transfer results obtained in the  $13.84 \text{ mm}$  test sections, are presented in Figures 7.27a and 7.27b for refrigerants R-22 and R-410A, respectively. The

initial heat fluxes were  $q = 37.5 \text{ kW/m}^2$  and  $57.5 \text{ kW/m}^2$  and decreased in the mist flow regime to the values presented in Figure 7.8. As has already been shown in section 7.4.1, the measured heat transfer coefficients do not vary with increasing of the vapor quality and are almost linear for each tested mass velocity. For both refrigerants, mist flow heat transfer coefficients increase with increasing of mass velocity and do not show any significant difference in value between tests at initial heat fluxes of  $q = 37.5 \text{ kW/m}^2$  and  $57.5 \text{ kW/m}^2$ . The controlled vapor saturation temperature in the mist flow regime corresponded always to the saturation pressure. This means that no vapor superheating effect was observed in the  $13.84 \text{ mm}$  fluid-to-fluid evaporator. The evaporation of refrigerants at higher mass velocities could not be tested because of limitations in the electrical preheater.

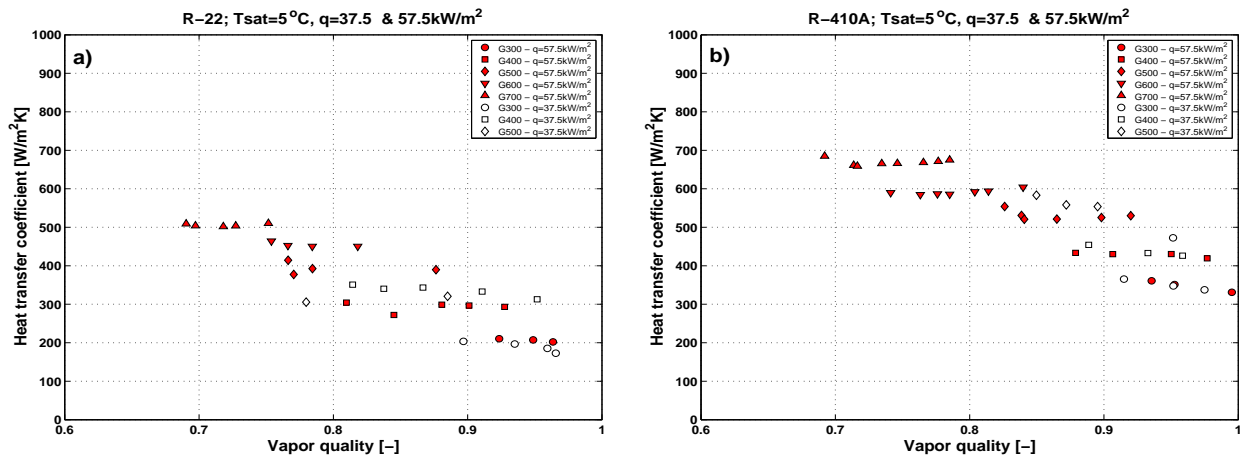


Figure 7.27: Mist flow heat transfer results obtained in the  $13.84 \text{ mm}$  test section at initial heat fluxes  $q = 37.5 \text{ kW/m}^2$  and  $57.5 \text{ kW/m}^2$  for tests with: a) R-22, b) R-410A.

In the  $8.00 \text{ mm}$  test section, a vapor superheating effect was observed only at vapor qualities above 0.95 at the lowest mass velocities tested. All other experimental mist flow heat transfer data displayed an almost linear trend as in the larger lube. The mist flow data in the  $8.00 \text{ mm}$  test section will not be used in the developing of the new mist flow heat transfer model, because the thermocouple placed on the top of the tube was broken and could influence measured values.

Since vapor and liquid phases were in thermal equilibrium during evaporation in the mist flow, the measured heat transfer coefficients can be predicted with a thermal equilibrium correlation. Figure 7.28 illustrates the comparison of the mist flow heat transfer results measured in the  $13.84 \text{ mm}$  test section with the correlations of Dougall-Rohsenow (equation 7.11) and Groeneveld (equation 7.15). It can be seen that the approach of Groeneveld shows

good agreement with the R-22 heat transfer data and overpredicts these for refrigerant R-410A. The values calculated with the Dougall-Rohsenow correlation are considerable higher than the experimental results.

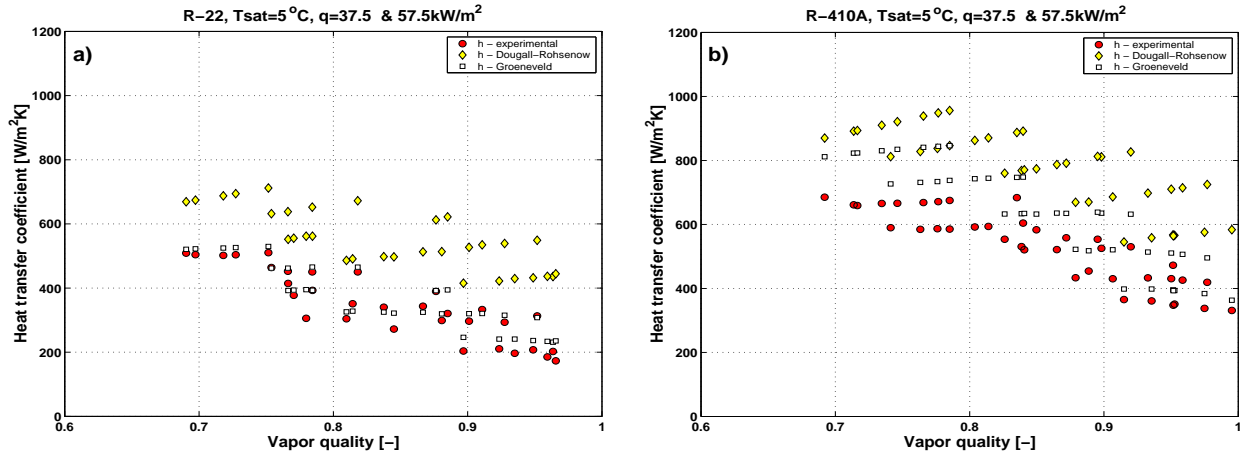


Figure 7.28: Comparison of the mist flow heat transfer results measured in the 13.84 mm test section with the correlations of Dougall-Rohsenow and Groeneveld for: a) R-22, b) R-410A.

As described in section 7.3.1, the database of Groeneveld used to optimise his empirical factors covered only very high mass velocities, saturation pressures and heat fluxes, mostly for water. Based on the new experimental data, the correlation of Groeneveld has been reoptimized for prediction of the mist flow heat transfer coefficient during evaporation of *refrigerants*. The new version of the Groeneveld correlation is as follows:

$$h_{mist} = 0.0117 Re_H^{0.79} Pr_V^{1.06} Y^{-1.83} \frac{\lambda_V}{D} \quad (7.52)$$

Compared to the original version, the values of exponents and leading constant were changed. Figure 7.29 shows the comparison of the mist flow heat transfer results measured in the 13.84 mm test section with the new method for both refrigerants. The agreement of the experimental and predicted points is very good and the statistical analysis of this relationship is presented in Table 7.1.

	$\bar{\varepsilon}$ (%)	$ \bar{\varepsilon} $ (%)	$\sigma$ (%)
Groeneveld	13.6	9.0	10.7
Groeneveld optimized	-0.04	6.31	8.32

Table 7.1: Statistical analysis of the mist flow heat transfer in the 13.84 mm test section.

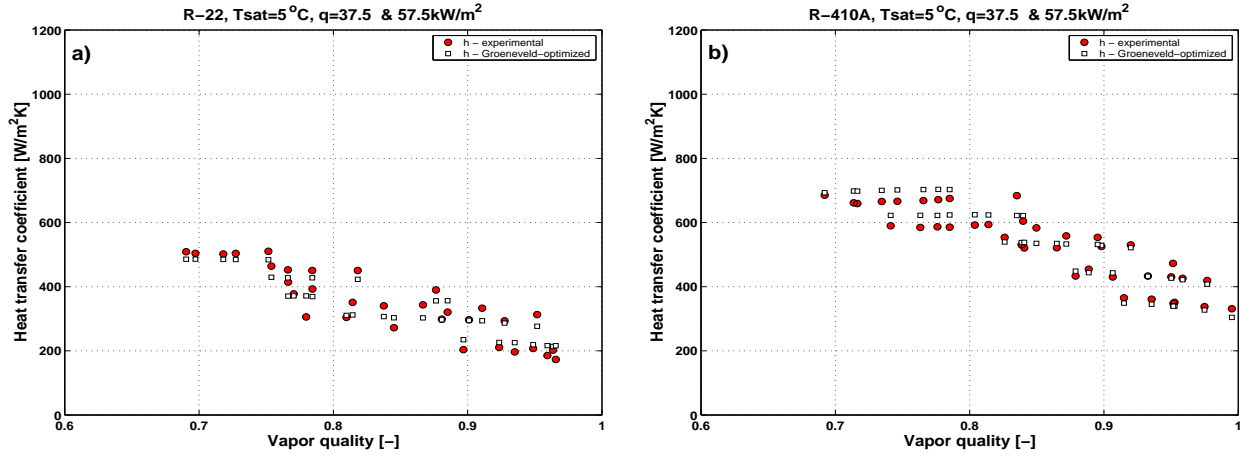


Figure 7.29: Comparison of the mist flow heat transfer results measured in the 13.84 mm test section with the optimized version of Groeneveld for: a) R-22, b) R-410A.

As can be seen in Table 7.1, the average deviation -  $\bar{\varepsilon}$ , the mean deviation -  $|\bar{\varepsilon}|$  and the standard deviation  $\sigma$  for all 71 experimental points are only  $-0.04\%$ ,  $6.31\%$  and  $8.32\%$ , respectively. The new method predicts 93% of experimental results obtained for the two refrigerants at five different mass velocities and two different heat fluxes within  $\pm 15\%$  error. It is proposed in this study to use the optimized method of Groeneveld presented in equation 7.52 for the calculation of heat transfer coefficient in the mist flow region. Seeing that the vapor superheating effect was only observed in some points at vapor qualities above 0.95, using an assuming thermal equilibrium seems to be reasonable.

As has been shown in Figures 7.11 - 7.18, the heat transfer coefficient falls over a limited quality range and then becomes nearly constant in value in mist flow. The vapor quality range over which heat transfer falls linearly corresponds to the dryout zone and the heat transfer coefficient can be calculated for this region from the following correlation:

$$h_{dryout} = h_{tp}(x_{di}) - \frac{x - x_{di}}{x_{de} - x_{di}} [h_{tp}(x_{di}) - h_{mist}(x_{de})] \quad (7.53)$$

where  $h_{tp}$  is the two-phase flow heat transfer coefficient calculated from Kattan-Thome-Favrat equation 2.51 at the dryout inception quality -  $x_{di}$  and  $h_{mist}$  is the mist flow heat transfer coefficient calculated from equation 7.52 at the dryout completion quality -  $x_{de}$ . This simple correlation assumes a linear variation of the heat transfer coefficient in the dryout zone between the maximum value at dryout inception quality -  $x_{di}$  and the minimum value at dryout completion quality -  $x_{de}$ . This approach predicts very accurately experimental data

and smoothly links the heat transfer coefficient in the annular and the mist flow regimes.

## 7.5 Heat transfer results at high mass velocities

In this section, the experimental data obtained at the mass velocities  $G \geq 300 \text{ kg/m}^2\text{s}$  and all heat fluxes tested will be presented for refrigerants: R-22 and R-410A. The experimental heat transfer data will be compared with the initial heat transfer model of Kattan and the new model proposed here, which is an extended version of his approach. The new method is based on the updated flow pattern map. Two new transition curves have been introduced to the updated map to identify the Annular-Dryout and Dryout-Mist transitions.

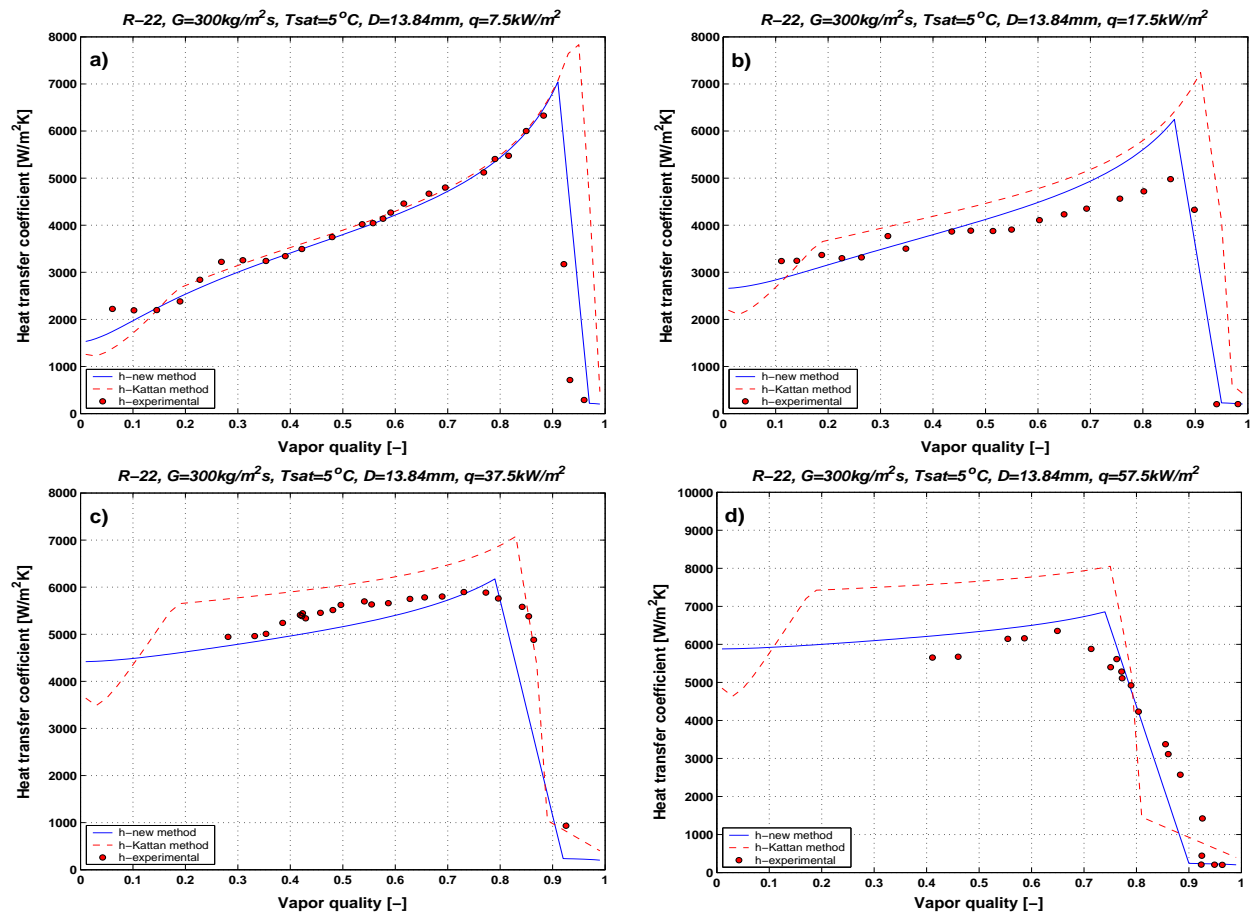


Figure 7.30: Comparison of the experimental heat transfer data with the model of Kattan and the new prediction method for tests with R-22 at mass velocity  $G = 300 \text{ kg/m}^2\text{s}$  and heat fluxes: a)  $7.5 \text{ kW/m}^2$ , b)  $17.5 \text{ kW/m}^2$ , c)  $37.5 \text{ kW/m}^2$ , d)  $57.5 \text{ kW/m}^2$ .

Figures 7.30 - 7.35 show the comparison of the experimental heat transfer data with the model of Kattan (dashed curve) and the new prediction method (solid curve) for tests at mass velocities of 300, 400 and 500  $kg/m^2s$  at all tested heat fluxes. Figures 7.36 and 7.37 show only the comparison of experimental heat transfer data with the new method. The reason is, that at mass velocity of  $G = 600 kg/m^2s$  the flow pattern map of Kattan *et al.* predicts some flows to be in the mist flow region, where his heat transfer model is not applicable. It has to be noted that the heat fluxes cited here refer to the initial heat fluxes along the tube prior to the dryout location. The post dryout heat fluxes for all experimental conditions are presented in Figure 7.19.

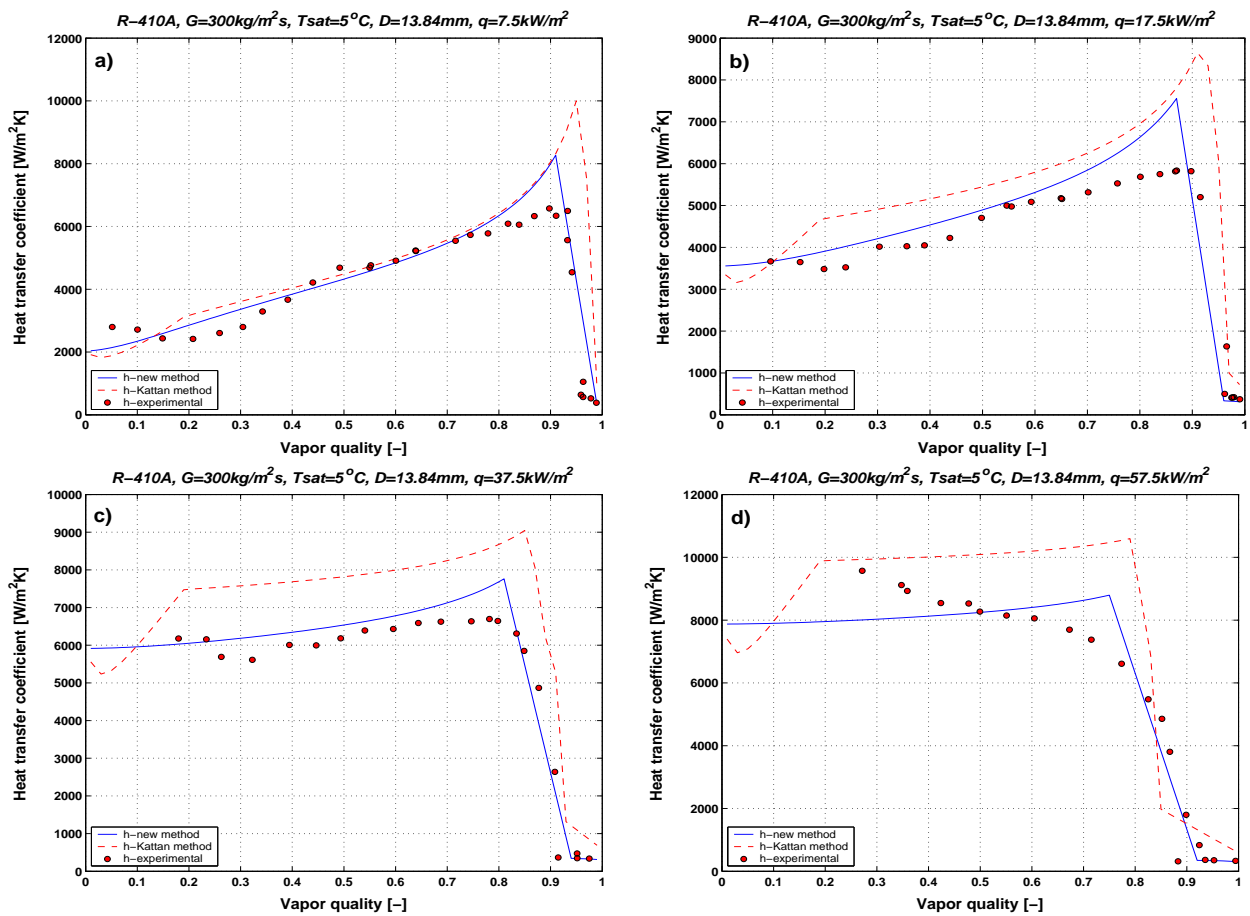


Figure 7.31: Comparison of the experimental heat transfer data with the model of Kattan and the new prediction method for tests with R-22 at mass velocity  $G = 300 kg/m^2s$  and heat fluxes: a)  $7.5 kW/m^2$ , b)  $17.5 kW/m^2$ , c)  $37.5 kW/m^2$ , d)  $57.5 kW/m^2$ .

One modification has been made in the calculation of nucleate boiling contribution compared to the method of Kattan. As can be seen in Figures 7.30 - 7.31 and 7.34 - 7.36, the method of Kattan predicts accurate heat transfer coefficients at the heat flux  $q = 7.5 kW/m^2$  in the



annular flow regime at all tested mass velocities. However, with increasing heat flux, the method systematically overpredicts the measured heat transfer coefficients. As the deviation increases with increasing heat flux it can be concluded that the nucleate boiling contribution in the flow boiling heat transfer model is too high. Based on analysis of the experimental data, it has been estimated that the nucleate boiling heat transfer coefficient calculated from the pool boiling correlation of Cooper should be reduced by 20% to obtain good agreement with experimental values. Consequently, it is recommended in a new method to use a nucleate boiling suppression factor  $S = 0.8$  and thus to calculate the nucleate boiling contribution as:

$$h_{nb,new} = S \cdot h_{nb,Cooper} \quad (7.54)$$

where  $h_{nb,Cooper}$  is the nucleate pool boiling heat transfer of Cooper defined in equation 2.47.

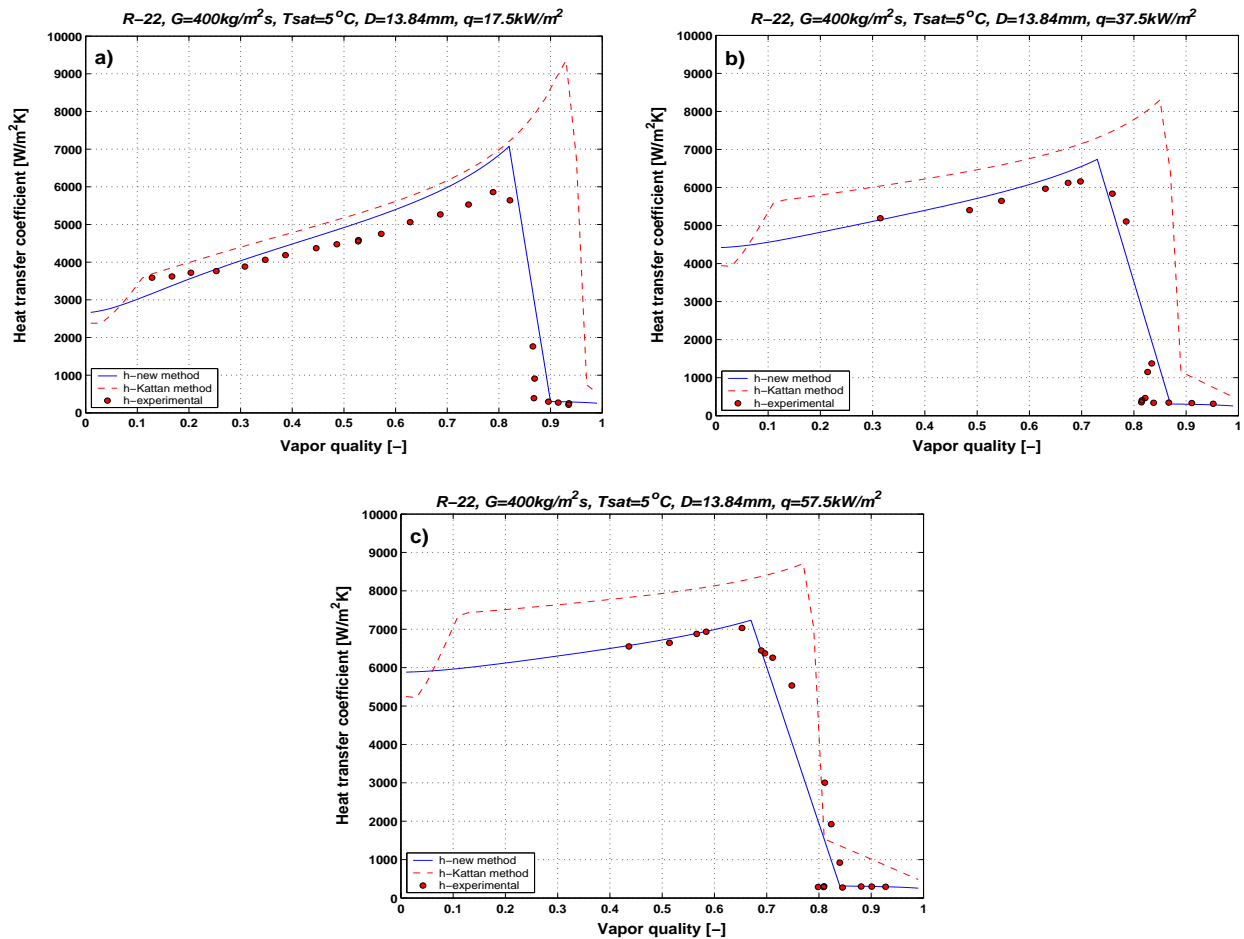


Figure 7.32: Comparison of the experimental heat transfer data with the model of Kattan and the new prediction method for tests with R-22 at mass velocity  $G = 400 \text{ kg/m}^2 \text{ s}$  and heat fluxes: a)  $17.5 \text{ kW/m}^2$ , b)  $37.5 \text{ kW/m}^2$ , c)  $57.5 \text{ kW/m}^2$ .

It can be observed that the new method predicts more accurately the experimental points, particularly for higher heat flux values. Statistical analysis of all experimental results is presented in Tables 7.2 - 7.5. The analysis of experimental results has been done separately for the wetted zone (Stratified Wavy-Annular Flow) and for the Dryout-Mist flow regimes. The heat transfer coefficient drops across in the dryout zone to approximately from 1/15 to 1/20 times of the annular flow values. Thus, if the dryout inception is predicted at slightly too high of a vapor quality, the relative error defined in equation 5.49 can rise to even 2000% !!! This explains the very high statistical errors if the dryout zone is not correctly identified even for few experimental points. One more very important explanation for high statistical errors in the dryout zone is the effect of vapor quality hysteresis. After mist flow conditions are reached, the following increase of the inlet vapor quality generates the occurrence of the mist flow in the zone preceding the local heat transfer measurement position. This reduces significantly the overall heat transfer performance from the heating fluid (water) to the refrigerant and results in a decrease of vapor quality at the local heat transfer measurement position. Consequently, measured mist flow heat transfer values created by this hysteresis in the dryout region boundary will create very high relative error. This effect can be observed very clearly in Figure 7.34c for the tests with R-22 at  $G = 500 \text{ kg/m}^2\text{s}$  and heat flux  $q = 37.5 \text{ kW/m}^2$ . As it can be seen, the dryout inception and onset of mist flow are correctly identified. Two heat transfer points at vapor qualities below vapor quality 0.8 moved backward from the mist flow region due to the hysteresis effect described above. In this particular test there are only three other points taken at "normal" conditions and hence there is no surprise that the mean deviation  $|\bar{\epsilon}|$  raises to 243.9% and standard deviation  $\sigma$  to 326.9%. Even if all experimental points were taken into account in the statistical analysis, the improvement of the new method in the dryout heat transfer prediction compared to the method of Kattan is evident.

The statistical results have also been presented for tests in the 8.00 mm test section (Table 7.5), although as mentioned before, the wall thermocouple on the top of the tube was broken and could considerably influence the measured heat transfer values. A big improvement in the heat transfer prediction in the Dryout-Mist flow zone can be observed also for these experimental conditions.

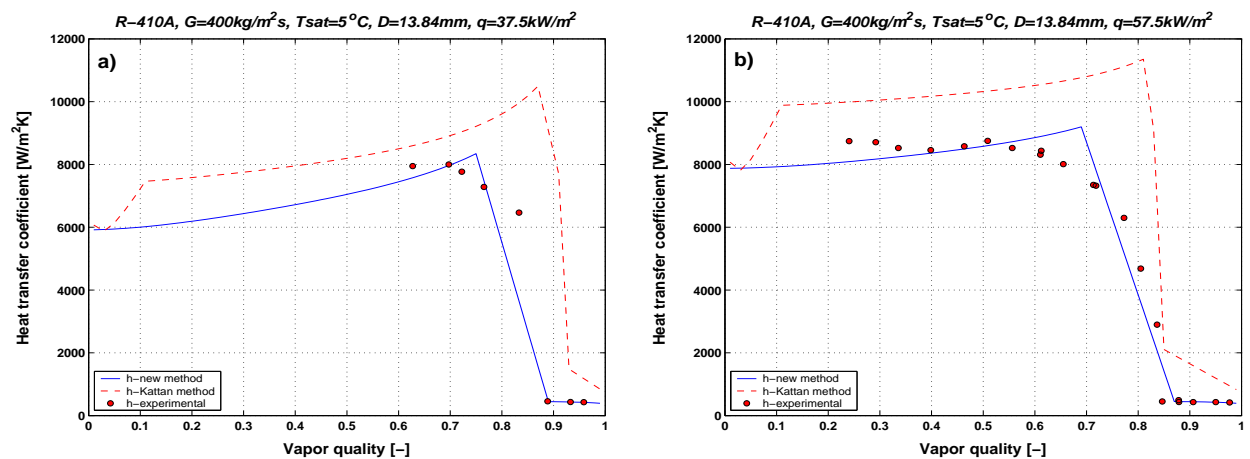


Figure 7.33: Comparison of the heat transfer data with the Kattan model and the new prediction for: R-410A,  $G = 400 \text{ kg/m}^2\text{s}$  at heat fluxes: a)  $37.5 \text{ kW/m}^2$ , b)  $57.5 \text{ kW/m}^2$ .

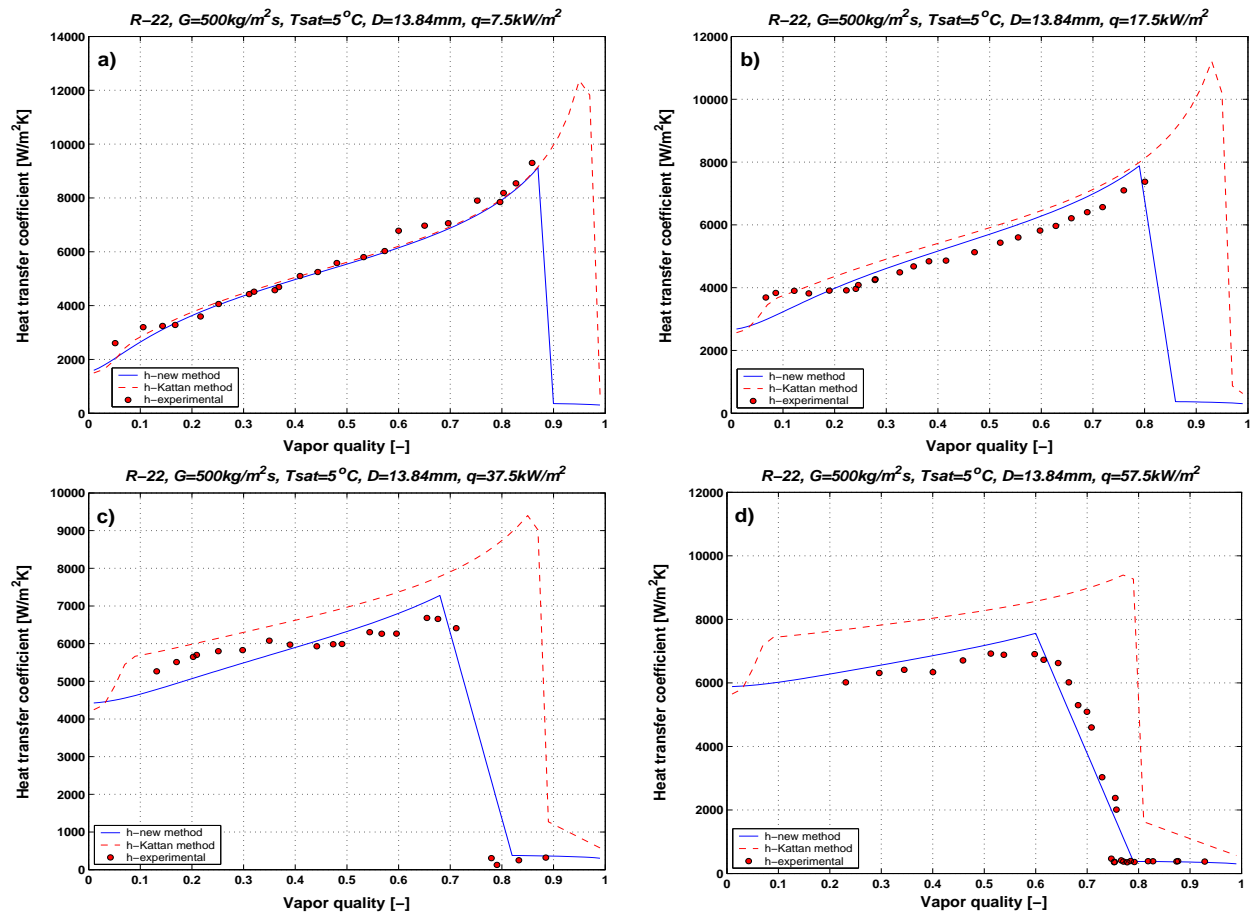


Figure 7.34: Comparison of the experimental heat transfer data with the model of Kattan and the new prediction method for tests with R-22 at mass velocity  $G = 500 \text{ kg/m}^2\text{s}$  and heat fluxes: a)  $7.5 \text{ kW/m}^2$ , b)  $17.5 \text{ kW/m}^2$ , c)  $37.5 \text{ kW/m}^2$ , d)  $57.5 \text{ kW/m}^2$ .

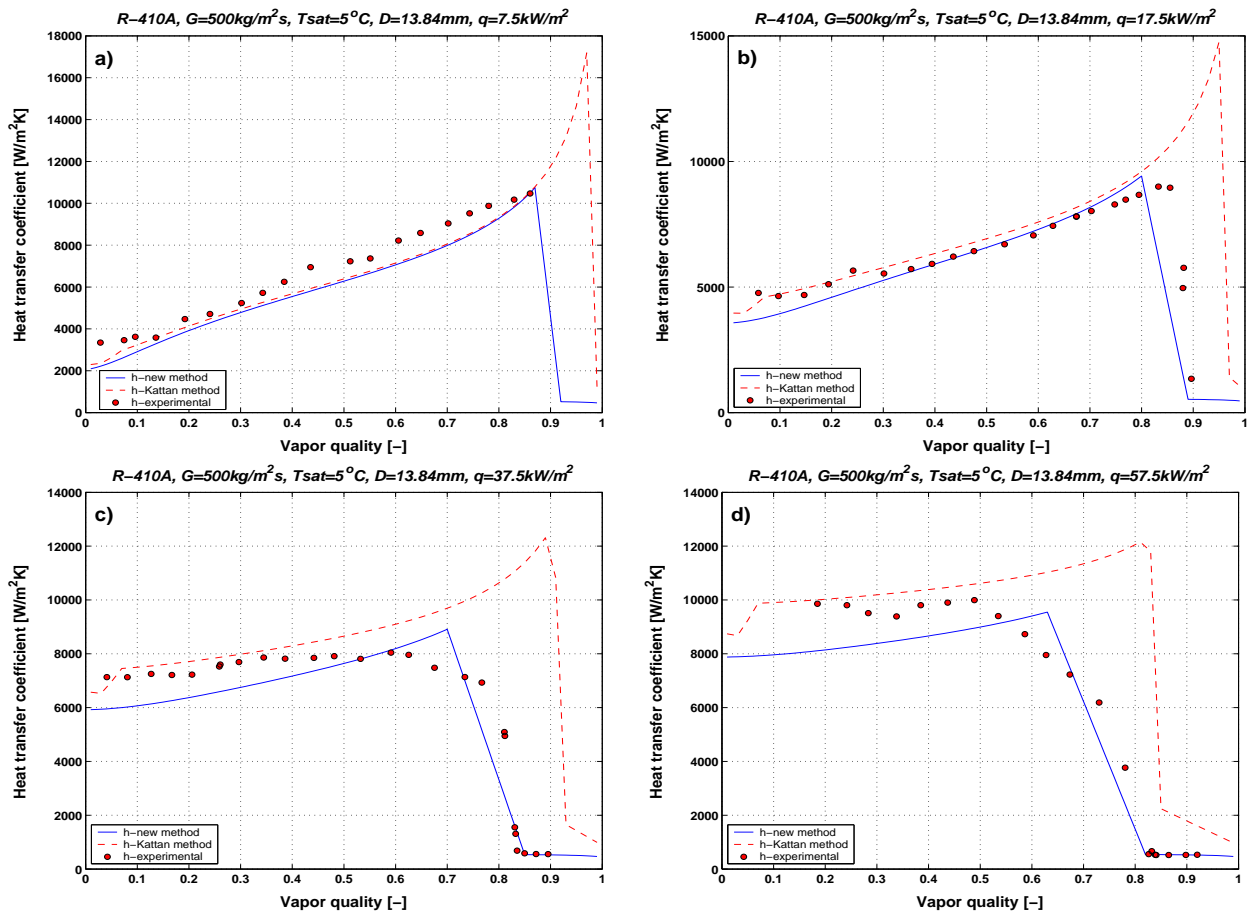


Figure 7.35: Comparison of the experimental heat transfer data with the model of Kattan and the new prediction method for tests with R-410A at mass velocity  $G = 500 \text{ kg/m}^2\text{s}$  and heat fluxes: a)  $7.5 \text{ kW/m}^2$ , b)  $17.5 \text{ kW/m}^2$ , c)  $37.5 \text{ kW/m}^2$ , d)  $57.5 \text{ kW/m}^2$ .

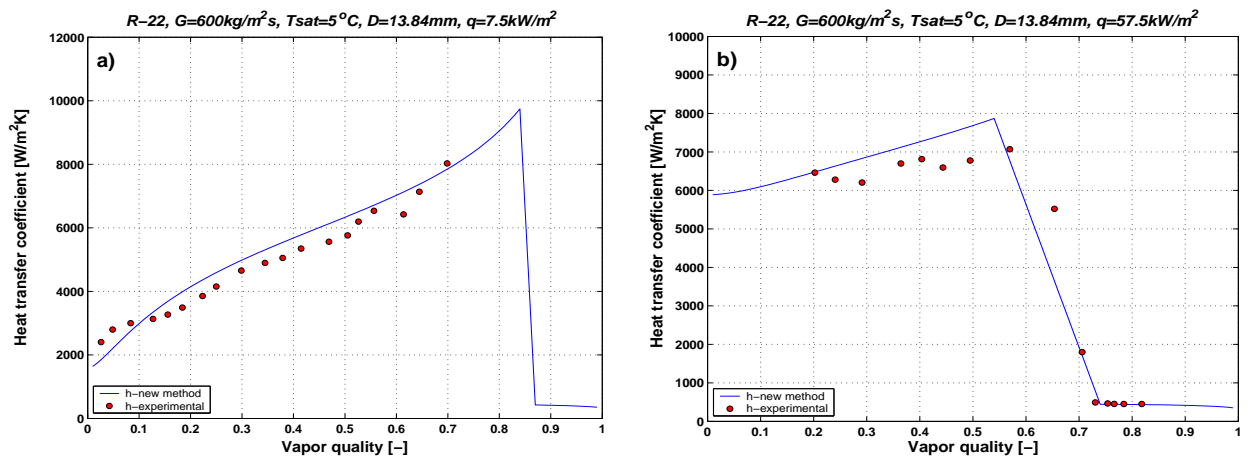


Figure 7.36: Comparison of the experimental heat transfer data with the new prediction method for: R-22,  $G = 600 \text{ kg/m}^2\text{s}$  at heat fluxes: a)  $7.5 \text{ kW/m}^2$ , b)  $57.5 \text{ kW/m}^2$ .

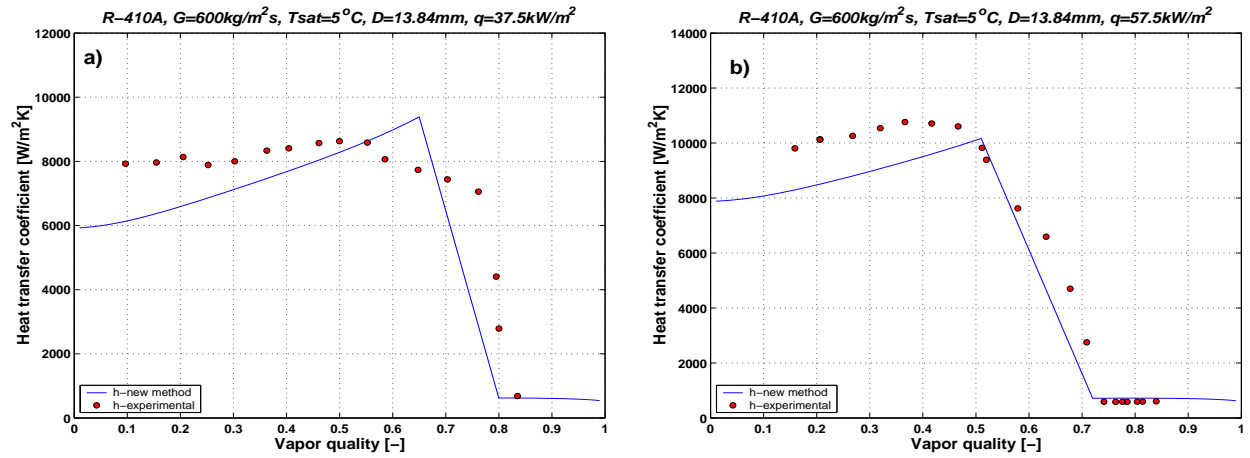


Figure 7.37: Comparison of the experimental heat transfer data with the new prediction method for tests with R-410A at mass velocity  $G = 600 \text{ kg/m}^2\text{s}$  and heat fluxes: a)  $37.5 \text{ kW/m}^2$ , b)  $57.5 \text{ kW/m}^2$ .

R-22, D=8.00mm; Stratified Wavy-Annular Flow (Wetted Perimeter)								
G	q	$\bar{\epsilon}_{Kattan}$	$ \bar{\epsilon} _{Kattan}$	$\sigma_{Kattan}$	$\bar{\epsilon}_{new}$	$ \bar{\epsilon} _{new}$	$\sigma_{new}$	n
( $\text{kg/m}^2\text{s}$ )	( $\text{kW/m}^2$ )	(%)	(%)	(%)	(%)	(%)	(%)	(-)
350	9.5	12.97	4.72	5.73	10.25	5.10	6.37	18
350	17.5	5.75	2.43	3.36	0.46	4.28	5.91	13
350	37.5	-5.58	6.48	8.12	-15.74	7.51	9.33	10
Summary		4.38	4.54	5.74	-1.68	5.63	7.20	41
R-22, D=8.00mm; Dryout Conditions								
G	q	$\bar{\epsilon}_{Kattan}$	$ \bar{\epsilon} _{Kattan}$	$\sigma_{Kattan}$	$\bar{\epsilon}_{new}$	$ \bar{\epsilon} _{new}$	$\sigma_{new}$	n
( $\text{kg/m}^2\text{s}$ )	( $\text{kW/m}^2$ )	(%)	(%)	(%)	(%)	(%)	(%)	(-)
350	9.50	4.33	24.11	35.85	-61.20	29.41	35.45	5
350	17.50	-19.37	28.23	36.30	-73.52	22.06	27.97	7
350	37.50	-33.08	30.14	34.75	-61.65	22.21	28.56	8
Summary		-16.04	27.49	35.63	-65.45	24.56	30.66	20

Table 7.2: Statistical analysis of heat transfer data obtained during evaporation of refrigerant R-22 in the 8.00 mm test section compared to the model of Kattan and to the new method.

<b>R-22, D=13.84mm; Stratified Wavy-Annular Flow (Wetted Perimeter)</b>								
G	q	$\bar{\epsilon}_{Kattan}$	$ \bar{\epsilon} _{Kattan}$	$\sigma_{Kattan}$	$\bar{\epsilon}_{new}$	$ \bar{\epsilon} _{new}$	$\sigma_{new}$	n
( $kg/m^2s$ )	( $kW/m^2$ )	(%)	(%)	(%)	(%)	(%)	(%)	[-]
300	7.5	-1.44	5.55	9.95	-2.47	3.87	5.66	23
300	17.5	12.97	6.81	9.75	4.84	8.08	9.95	17
300	37.5	11.03	2.33	3.00	-4.88	2.34	2.95	19
300	57.5	29.77	4.80	5.34	8.22	3.70	4.41	6
350	37.5	15.53	3.53	4.63	4.29	3.94	5.24	3
400	17.5	13.92	3.36	5.28	7.00	6.40	8.75	17
400	37.5	16.34	1.14	1.62	3.87	1.64	2.57	6
400	57.5	18.10	1.20	1.40	0.83	0.67	0.79	5
500	7.5	-1.46	4.39	6.64	-3.09	4.07	5.95	23
500	17.5	9.41	3.82	5.62	2.98	6.05	8.35	23
500	37.5	11.23	3.92	4.38	-1.19	6.70	7.42	16
500	57.5	23.67	1.94	2.58	5.89	1.59	2.02	8
550	57.5	3.44	2.41	3.19	-11.36	3.46	4.51	9
600	7.5	6.48	7.57	10.26	4.21	7.67	10.46	19
600	57.5	25.13	2.87	3.45	7.68	3.54	4.49	7
Summary		12.94	3.71	5.14	1.79	4.25	5.57	201
<b>R-22, D=13.84mm; Dryout Conditions</b>								
G	q	$\bar{\epsilon}_{Kattan}$	$ \bar{\epsilon} _{Kattan}$	$\sigma_{Kattan}$	$\bar{\epsilon}_{new}$	$ \bar{\epsilon} _{new}$	$\sigma_{new}$	n
( $kg/m^2s$ )	( $kW/m^2$ )	(%)	(%)	(%)	(%)	(%)	(%)	[-]
300	7.5	1110.44	744.37	1054.65	341.25	170.13	242.66	3
300	17.5	825.34	952.62	1238.43	111.78	157.01	204.29	3
300	37.5	5.18	9.49	13.51	-36.21	16.60	26.48	5
300	57.5	48.46	80.36	107.42	-13.94	28.85	33.11	14
350	37.5	542.04	602.54	750.94	87.66	139.19	200.71	10
400	17.5	2213.43	1022.71	1234.13	137.54	161.84	228.68	7
400	37.5	1018.36	834.88	912.83	205.11	245.69	284.51	11
400	57.5	294.58	301.87	536.02	88.44	164.76	212.59	14
500	37.5	1642.39	1481.92	1750.97	181.04	243.92	326.19	5
500	57.5	960.49	1004.89	1080.61	71.96	112.49	144.35	22
550	57.5	1384.92	942.66	1075.27	15.21	39.32	64.24	8
600	57.5	-	-	-	0.55	16.33	28.20	8
700	57.5	-	-	-	-6.77	17.65	26.70	11
Summary		834.45	686.19	831.31	91.05	116.45	155.59	120

Table 7.3: Statistical analysis of heat transfer data obtained during evaporation of refrigerant R-22 in the 13.84 mm test section compared to the model of Kattan and to the new method.

<b>R-410A, D=13.84mm; Stratified Wavy-Annular Flow (Wetted Perimeter)</b>								
G	q	$\bar{\epsilon}_{Kattan}$	$ \bar{\epsilon} _{Kattan}$	$\sigma_{Kattan}$	$\bar{\epsilon}_{new}$	$ \bar{\epsilon} _{new}$	$\sigma_{new}$	n
( $kg/m^2s$ )	( $kW/m^2$ )	(%)	(%)	(%)	(%)	(%)	(%)	[-]
300	7.5	7.75	11.86	15.86	4.93	10.21	12.85	23
300	17.5	21.37	7.46	9.28	10.86	6.38	8.55	20
300	37.5	26.50	3.52	4.51	6.65	3.63	4.90	14
300	57.5	20.83	8.74	11.27	-1.04	8.06	10.41	10
400	37.5	12.00	2.80	3.98	-0.07	3.04	4.51	3
400	57.5	21.34	4.40	5.72	0.72	5.02	6.35	10
500	7.5	-9.64	4.16	6.45	-12.70	4.90	7.41	19
500	17.5	4.30	2.65	3.91	-2.82	6.26	7.87	19
500	37.5	7.59	4.92	7.28	-7.39	7.07	9.14	16
500	57.5	11.49	8.55	11.65	-6.55	8.76	11.73	10
600	37.5	6.02	7.21	10.24	-6.89	9.39	12.74	12
600	57.5	3.21	4.67	6.44	-13.26	5.31	7.01	10
700	57.5	-	-	-	-16.21	4.65	6.97	8
Summary		10.16	5.76	7.90	-3.37	6.36	8.50	174
<b>R-410A, D=13.84mm; Dryout Conditions</b>								
G	q	$\bar{\epsilon}_{Kattan}$	$ \bar{\epsilon} _{Kattan}$	$\sigma_{Kattan}$	$\bar{\epsilon}_{new}$	$ \bar{\epsilon} _{new}$	$\sigma_{new}$	n
( $kg/m^2s$ )	( $kW/m^2$ )	(%)	(%)	(%)	(%)	(%)	(%)	[-]
300	7.5	616.74	537.02	610.88	158.40	158.76	197.21	8
300	17.5	184.42	191.39	314.10	-29.65	13.92	21.53	8
300	37.5	262.86	269.85	440.63	47.96	103.67	167.96	8
300	57.5	97.21	113.49	151.81	50.01	117.62	207.59	10
400	37.5	478.90	567.48	797.86	-8.95	12.73	17.80	5
400	57.5	183.84	89.45	110.54	13.45	36.88	68.75	11
500	17.5	207.86	230.61	325.99	-58.60	12.15	17.86	5
500	37.5	890.77	734.60	831.96	-3.94	22.06	31.80	10
500	57.5	867.55	818.38	887.79	-6.63	11.32	13.86	10
600	37.5	-	-	-	-48.71	30.14	35.87	5
600	57.5	-	-	-	37.00	45.74	71.54	11
700	57.5	-	-	-	55.33	54.72	77.57	12
Summary		421.13	394.70	496.84	17.14	51.64	77.45	103

Table 7.4: Statistical analysis of heat transfer data obtained during evaporation of refrigerant R-410A in the 13.84 mm test section compared to the model of Kattan and to the new method.

<b>R-410A, D=8.00mm; Stratified Wavy-Annular Flow (Wetted Perimeter)</b>								
G	q	$\bar{\epsilon}_{Kattan}$	$ \bar{\epsilon} _{Kattan}$	$\sigma_{Kattan}$	$\bar{\epsilon}_{new}$	$ \bar{\epsilon} _{new}$	$\sigma_{new}$	n
( $kg/m^2 s$ )	( $kW/m^2$ )	(%)	(%)	(%)	(%)	(%)	(%)	[-]
350	10.5	-8.15	12.52	16.97	-12.13	14.64	19.41	16
350	17.5	-20.92	11.71	14.75	-26.40	13.54	16.95	17
350	37.5	-32.48	3.43	4.42	-41.80	4.45	5.61	11
400	37.5	-6.58	9.14	11.80	-15.58	9.76	12.49	5
400	57.5	-14.21	3.42	4.61	-27.04	3.46	4.73	3
500	37.5	-15.72	5.75	7.05	-24.28	6.81	8.42	12
500	57.5	-12.16	2.92	4.18	-23.98	3.07	4.57	4
600	37.5	-9.41	6.53	8.50	-17.00	7.87	10.14	4
600	57.5	-13.28	6.11	8.64	-24.29	7.01	9.91	2
700	37.5	-8.97	7.86	11.02	-16.29	9.09	12.65	4
700	57.5	-14.10	4.22	5.48	-24.88	4.71	6.12	3
Summary		-14.18	6.69	8.86	-23.06	7.67	10.09	81
<b>R-410A, D=8.00mm; Dryout Conditions</b>								
G	q	$\bar{\epsilon}_{Kattan}$	$ \bar{\epsilon} _{Kattan}$	$\sigma_{Kattan}$	$\bar{\epsilon}_{new}$	$ \bar{\epsilon} _{new}$	$\sigma_{new}$	n
( $kg/m^2 s$ )	( $kW/m^2$ )	(%)	(%)	(%)	(%)	(%)	(%)	[-]
350	10.5	-13.09	31.43	44.95	-71.56	25.41	34.30	4
350	17.5	-21.67	44.89	48.90	-68.20	20.35	24.71	8
350	37.5	-51.56	25.86	29.64	-73.54	16.02	19.49	7
400	37.5	607.24	469.11	607.12	132.45	86.59	115.03	7
400	57.5	381.69	133.60	157.51	178.73	90.00	121.88	17
500	37.5	712.63	575.44	665.88	23.63	46.79	58.45	12
500	57.5	431.58	244.87	485.13	104.02	98.29	131.09	13
600	37.5	919.96	846.75	920.60	-0.68	29.84	35.48	14
600	57.5	629.31	570.71	728.27	48.96	47.67	57.32	14
700	37.5	835.76	824.00	976.02	-0.69	43.68	58.24	13
700	57.5	1016.45	889.18	994.11	63.05	45.17	66.86	15
Summary		495.30	423.26	514.38	30.56	49.98	65.71	124

Table 7.5: Statistical analysis of heat transfer data obtained during evaporation of refrigerant R-410A in the 8.00 mm test section compared to the model of Kattan and to the new method.



## 7.6 Conclusions

New flow pattern transition curves have been proposed to define the Annular-Dryout and Dryout-Mist flow transitions based on experimental data and observations. It has been found that the operational conditions of fluid-fluid heated test section are different from those with electrical heating particularly at high vapor qualities. Post dryout heat transfer models have been described for both thermal equilibrium and thermal non-equilibrium conditions. The non-equilibrium correlations of Mori and Groeneveld-Delorme have been applied to predict wall temperature, actual vapor temperature and actual vapor quality. Both methods predict at simulated experimental conditions wall temperatures  $T_{wall}$  higher than the temperatures of the heating water used in our experiments. Hence, it is evident that the methods were developed for an electrical heated tube and cannot be applied to fluid heated evaporators. As the non-equilibrium effect was only observed here for a few experimental points for vapor qualities above 0.95, the thermal equilibrium model of Groeneveld has been adapted to predict the heat transfer coefficient for *refrigerants*. The new method predicts 93% of experimental results obtained for two refrigerants at five different mass velocities and two different initial heat fluxes within  $\pm 15\%$  error. For the dryout zone heat transfer prediction, a simple correlation has been proposed, which assumes a linear variation of the heat transfer coefficient between the maximum value at dryout inception quality -  $x_{di}$  and the minimum value at dryout completion quality -  $x_{de}$ . This approach predicts very accurately many of the experimental data and links the heat transfer coefficient in the annular and the mist flow. One change has been made in the heat transfer coefficient calculation in the wetted region compared to the model of Kattan. Based on the experimental data analysis, it has been estimated that the nucleate boiling heat transfer coefficient calculated from the pool boiling correlation of Cooper should be reduced by 20% to obtain better agreement with experimental values at high heat fluxes. All experimental data have been compared with the model of Kattan and the new prediction method. Statistical analysis has been done separately for wetted and dryout-mist flow region and show improvement in heat transfer predictions particularly at higher heat fluxes and in the Dryout-Mist flow region.



# Chapter 8

## General conclusions

A new optical measurement technique to dynamically measure cross-sectional void fractions in stratified types of two-phase flow in horizontal tubes has been developed. The new method was nonintrusive and allowed measurements of the void fraction through a glass tube in a cross-sectional view perpendicular to the flow. The new optical void fraction measurement system was coupled to the flow boiling test facility to obtain dynamic and time-averaged void fractions simultaneously with local heat transfer coefficients. Using our newly developed image processing system, about 310 000 images have been analysed in this study to obtain the same number of dynamic void fraction measurements. From these images, 238 and 87 time-averaged void fraction values have been obtained for the 13.60 mm and 8.00 mm diameter glass tubes, respectively. The experimental results show very good agreement with the Steiner version of the Rouhani-Axelsson model, what confirms that the use of this void fraction model for calculation of flow geometries and flow pattern transitions in the heat transfer model of Kattan *et al.* is appropriate. Several improvements of the flow pattern map of Kattan *et al.* have been proposed after analysing the phenomena observed during optical measurements of void fraction. The stratified-wavy region has been subdivided into three zones: slug, slug/stratified-wavy and stratified-wavy. A new method for predicting the dry angle -  $\theta_{dry}$  has been proposed for each new zone. Furthermore, the transition curve stratified/stratified-wavy flow has been adjusted for vapor qualities below  $x_{TA}$ . This new approach provides a notable improvement in the accuracy in prediction of heat transfer coefficients in stratified types of flow as has been proven in comparison with the present and independent experimental results. The proposed modification extends the heat transfer

model to vapor qualities below 0.15.

Based on the heat transfer data for higher mass velocities, new flow pattern transition curves have been proposed to define the annular/dryout and dryout/mist flow transitions. As the non-equilibrium effect was only observed here for a few experimental points for vapor qualities above 0.95, the thermal equilibrium mist flow heat transfer model of Groeneveld has been adapted to predict heat transfer coefficients for refrigerants in mist flow. For the new dryout zone in the flow pattern map, a simple heat transfer correlation has been proposed, which assumes a linear variation of the heat transfer coefficient between the maximum value at dryout inception quality -  $x_{di}$  and the minimum value at dryout completion quality -  $x_{de}$ .

It has been observed at high heat fluxes that the pool boiling correlation of Cooper overpredicts the nucleate boiling contribution by about 20% on average. Thus, a fixed nucleate boiling suppression factor of  $S = 0.8$  has been proposed for the calculation of the nucleate boiling contribution, that significantly improves heat transfer predictions at heat fluxes above  $17.5 \text{ kW/m}^2$ .

After modifications presented above, the improved heat transfer model can successfully be used for the flow boiling heat transfer predictions over the whole vapor quality range ( $0 < x < 1.0$ ) in all flow regimes (with the exception of bubbly flows) and at heat fluxes ranging from 2.0 to  $57.5 \text{ kW/m}^2$ . This experimental work extends our flow boiling heat transfer database with over 1250 new experimental points for R-22 and R-410A at mass velocities from 70 to  $700 \text{ kg/m}^2\text{s}$  and heat fluxes from 2.0 to  $57.5 \text{ kW/m}^2$ . 368 experimental points have been measured in dryout and mist flow conditions, that fulfil the gap in our heat transfer database.

# Chapter 9

## Nomenclature

### 9.1 Latin

Symbol	Description	Units
$A$	Cross Section Area	$m^2$
$a_k$	Parameters Coupling Real and Synthetic Grids ( $k= 1, 2, \dots$ )	-
$A_L$	Cross Section Area of Liquid Phase	$m^2$
$A_{LD}$	Non-dimensional Area of Liquid Phase - $[A_L/D]$	-
$A_V$	Cross Section Area of Vapor Phase	$m^2$
$A_{VD}$	Non-dimensional Area of Vapor Phase - $[A_V/D]$	-
$Bi$	Biot Heat Transfer Number	-
$Bo$	Boiling Number	-
$C$	Empirical Constant	-
$C_o$	Distribution Parameter in the Drift-Flux Model	-
$c_{pL}$	Liquid Specific Heat	$J/kgK$
$c_{pV}$	Vapor Specific Heat	$J/kgK$
$c_{p_{wat}}$	Heating Water Specific Heat	$J/kgK$
$C_{sf}$	Empirical Constant in Rohsenow correlation	-
$d$	Vapor Core Diameter	$m$
$D$	Internal Tube Diameter	$m$
$D_{ext}$	External Tube Diameter	$m$
$D_h$	Hydraulic Diameter	$m$

$E$	Enhancement Factor	-
$E_1, E_2$	Empirical Factors in the Superposition Model	-
$f_L$	Liquid Friction Factor	-
$f_V$	Vapor Friction Factor	-
$Fr_L$	Liquid Froude Number	-
$g$	Acceleration of Gravity	$m/s^2$
$G$	Mass Velocity	$kg/m^2 s$
$h$	Heat Transfer Coefficient	$W/m^2 K$
$h$	Enthalpy per Unit of Mass	$J/kg$
$h_{cb}$	Convective Boiling Heat Transfer Coefficient	$W/m^2 K$
$h_{cb,crit}$	Heat Transfer Coefficient in Zürcher ONB Criterion	$W/m^2 K$
$h_{dryout}$	Dryout Heat Transfer Coefficient	$W/m^2 K$
$h_L$	Liquid Height in the Tube	$m$
$h_{LD}$	Non-dimensional Liquid Height in the Tube - $[h_L/D]$	-
$h_L$	Liquid Enthalpy	$J/kg$
$h_{L,cb}$	Liquid Convective Boiling Heat Transfer Coefficient	$W/m^2 K$
$h_{LV}$	Latent Heat of Vaporisation	$J/kg$
$h_{mist}$	Mist Flow Heat Transfer Coefficient	$W/m^2 K$
$h_{nb}$	Nucleate Boiling Heat Transfer Coefficient	$W/m^2 K$
$h_{ref}$	Local Heat Transfer Coefficient	$W/m^2 K$
$h_{tp}$	Two-Phase Flow Heat Transfer Coefficient	$W/m^2 K$
$h_V$	Vapor Convective Heat Transfer Coefficient	$W/m^2 K$
$h_{Va}$	Actual Vapor Enthalpy	$J/kg$
$h_{Ve}$	Equilibrium Vapor Enthalpy	$J/kg$
$h_{wall-V}$	Heat Transfer Coefficient (Wall-Vapor)	$W/m^2 K$
$h_{wat}$	Enthalpy of the Heating Water per Unit of Mass	$J/kg$
$h_{wet}$	Heat Transfer Coefficient for the Wet Perimeter	$W/m^2 K$
$i$	Horizontal Grid Line Indices	-
$i_1, i_2$	Incident Angle and Refracted Angle	-
$j$	Vertical Grid Line Indices	-
$j$	Total Superficial Velocity	$m/s$
$j_L$	Liquid Superficial Velocity	$m/s$
$j_{Lj}$	Liquid Drift Flux	$m/s$
$j_{LV}$	Liquid Drift Flux Relative to Vapor	$m/s$
$j_V$	Vapor Superficial Velocity	$m/s$

$j_{Vj}$	Vapor Drift Flux	$m/s$
$j_{VL}$	Vapor Drift Flux Relative to Liquid	$m/s$
$K$	Parameter in Mori Correlation	-
$L$	Luminance Value of a Pixel	-
$L$	Characteristic Length	$m$
$L_L$	Liquid Phase Length	$m$
$L_{mean}$	Mean Luminance Value over Pixel Area whose Luminance is Higher than Luminance Threshold	-
$L_V$	Vapor Phase Length	$m$
$m$	Empirical Constant	-
$M$	Molecular Weight	$g/mol$
$\dot{M}$	Total Mass Flow Rate	$kg/s$
$\dot{M}_L$	Liquid Mass Flow Rate	$kg/s$
$\dot{M}_{ref}$	Refrigerant Mass Flow Rate	$kg/s$
$m_T$	Total Mass of Refrigerant Inside Calibration Setup	$kg$
$\dot{M}_V$	Vapor Mass Flow Rate	$kg/s$
$\dot{M}_{wat}$	Heating Water Mass Flow Rate	$kg/s$
$n$	Active Nucleation Sites Density	$sites/m^2$
$n$	Empirical Constant	-
$n_1, n_2$	Refraction Indices of the First and Second Medium	-
$Nu$	Nusselt Number	-
$P$	Pressure	$bar$
$P$	Preheater Power	$W$
$P_{crit}$	Critical Pressure	$bar$
$P_i$	Liquid Interface	$m$
$P_{iD}$	Non-dimensional Liquid Interface - $[P_i/D]$	-
$P_{local}$	Saturation Pressure on the Local Heat Transfer Measurement Position	$bar$
$P_L$	Wetted Perimeter	$m$
$P_{LD}$	Non-dimensional Wetted Perimeter - $[P_L/D]$	-
$P_r$	Reduced Pressure - $[P/P_{crit}]$	-
$P_{sat}$	Saturation Pressure	$bar$
$P_V$	Dry Perimeter	$m$
$P_{VD}$	Non-dimensional Dry Perimeter - $[P_V/D]$	-
$Pr$	Prandtl Number	-

$Pr_L$	Prandtl Number of Liquid Phase	-
$Pr_V$	Prandtl Number of Vapor Phase	-
$Pr_{Vf}$	Prandtl Number of Film	-
$q$	Heat Flux	$W/m^2$
$q_{crit}$	Critical Heat Flux	$W/m^2$
$q_{ext}$	External Heat Flux	$W/m^2$
$q'$	Heat Input per Unit Length	$W/m$
$\dot{Q}_L$	Liquid Volumetric Flow Rate	$m^3/s$
$q_{ONB}$	Onset of Nucleate Boiling Heat Flux	$W/m^2$
$\dot{Q}_V$	Vapor Volumetric Flow Rate	$m^3/s$
$R$	Internal Tube Radius	$m$
$R_{cond}$	Conductive thermal resistance	$K/W$
$R_{conv}$	Convective thermal resistance	$K/W$
$r_{crit}$	Critical Bubble Radius	$m$
$R_p$	Surface Roughness Factor in Cooper Correlation	$\mu m$
$R_{tot}$	Overall thermal resistance	$K/W$
$Re$	Reynolds Number	-
$Re_H$	Homogeneous Reynolds Number	-
$Re_L$	Reynolds Number in Liquid Phase	-
$Re_V$	Reynolds Number in Vapor Phase	-
$Re_\delta$	Reynolds Number in Liquid Film	-
$S$	Slip ratio	-
$S$	Nucleate Boiling Suppression Factor	-
$t$	Time	$s$
$T$	Temperature	$K$
$T_{crit}$	Critical Temperature	$K$
$T_{Lb}$	Liquid Bulk Temperature	$K$
$T_r$	Reduced Temperature $[T/T_{crit}]$	-
$T_{sat}$	Saturation Temperature	$K$
$T_V$	Saturated Vapor Temperature	$K$
$T_{Va}$	Actual Vapor Temperature	$K$
$T_{Vf}$	Film Temperature	$K$
$T_{wall}$	Wall Temperature	$K$
$T_{wat}$	Heating Water Mean Temperature	$K$
$\Delta T$	Difference between Wall and Saturation Temperature	$K$



$u_H$	Homogenous Velocity of Two-Phases	$m/s$
$u_L$	Mean Velocity of Liquid Phase	$m/s$
$u_V$	Mean Velocity of Vapor Phase	$m/s$
$V$	Internal Glass Tube Volume	$m^3$
$v_L$	Liquid Phase Specific Volume	$m^3/kg$
$V_L$	Liquid Phase Volume	$m^3$
$V_{Lj}$	Local Liquid Drift Velocity	$m/s$
$V_T$	Total Calibration Setup Volume	$m^3$
$v_V$	Vapor Phase Specific Volume	$m^3/kg$
$V_V$	Vapor Phase Volume	$m^3$
$V_{Vj}$	Local Vapor Drift Velocity	$m/s$
$\bar{V}_{Vj}$	Weighted Mean Drift Velocity	$m/s$
$We_L$	Liquid Weber Number	-
$x$	Horizontal Coordinate in Image Plane	-
$x$	Vapor Quality	-
$x_a$	Actual Vapor Quality	-
$x_{de}$	Dryout Completion Quality	-
$x_{di}$	Dryout Inception Quality	-
$x_{do}$	Onset of Dryout Quality	-
$x_e$	Equilibrium Vapor Quality	-
$x_{IA}$	Vapor Quality at Intermittent-Annular Flow Transition	-
$X_{tt}$	Martinelli Parameter	-
$y$	Vertical Coordinate in Image Plane	-
$Y$	Multiplying Factor in Groeneveld's Correlation	-
$z_h$	Heated Tube Length from Inlet to Local Heat Transfer Measurement Position	$m$
$z_i$	Local Position on the Heated Tube Length	$m$
$z_t$	Total Heated Tube Length	$m$
$( )_{real}$	Concerns the Real (Distorted) Image	-
$( )_{synth}$	Concerns the Synthetic Image	-

## 9.2 Greek

Symbol	Description	Units
$\langle\beta\rangle$	Average Volumetric Flow Concentration	-
$\Gamma_{Va}$	Rate of Vapor Generation	$kg/s$
$\delta$	Liquid Film Thickness	$m$
$\delta_{crit}$	Liquid Film Thickness in Zürcher ONB Criterion	$m$
$\varepsilon$	Cross-Sectional Void Fraction	-
$\bar{\varepsilon}$	Average Deviation	%
$ \bar{\varepsilon} $	Mean Deviation	%
$\langle\varepsilon\rangle$	Volumetric Void Fraction	-
$\varepsilon_{Ch}$	Chordal Void Fraction	-
$\varepsilon_i$	Relative Error	%
$\varepsilon_{ip}$	Cross-Sectional Void Fraction Measured by Image Processing	-
$\varepsilon_{ref}$	Reference Cross-Sectional Void Fraction	-
$\varepsilon_T$	Total Void Fraction of Calibration System	-
$\Delta\varepsilon$	Void Fraction Measurement Error	-
$\theta_{dry}$	Dry Angle	$rad$
$\theta_{strat}$	Stratified Angle	$rad$
$\theta_{wet}$	Wetting Angle	$rad$
$\lambda_L$	Thermal Conductivity of Liquid Phase	$W/mK$
$\lambda_V$	Thermal Conductivity of Vapor Phase	$W/mK$
$\lambda_{Vf}$	Thermal Conductivity of Film	$W/mK$
$\kappa$	Heat Fraction Used for Liquid Evaporation	-
$\mu_L$	Dynamic Viscosity of Liquid	$Pa \cdot s$
$\mu_V$	Dynamic Viscosity of Vapor	$Pa \cdot s$
$\mu_{Va}$	Actual Dynamic Viscosity of Vapor	$Pa \cdot s$
$\mu_{Vf}$	Dynamic Viscosity of Film	$Pa \cdot s$
$\xi$	Stratified-Wavy Angle in Zürcher ONB Criterion	$rad$
$\rho_L$	Density of Liquid	$kg/m^3$
$\rho_T$	Total Density of Two-Phase Mixture	$kg/m^3$
$\rho_V$	Density of Vapor	$kg/m^3$
$\rho_{Va}$	Actual Density of Vapor	$kg/m^3$
$\sigma$	Surface Tension	$N/m$

$\sigma$	Standart Deviation	%
$\varphi$	Tube Inclination Angle	<i>rad</i>
$\varphi$	Moon Angle in Zürcher ONB Criterion	<i>rad</i>
$\psi$	Half Wetting Angle in Zürcher ONB Criterion	<i>rad</i>
$\psi$	Paremeter in Correlation of Groeneveld-Delorme	—
$\omega$	Slug Frequency	<i>Hz</i>



# Bibliography

- [1] S.Y. Ahmad, *Axial distribution of bulk temperature and void fraction in a heated channel with inlet subcooling*, Trans. ASME, J. Heat Transfer **92** (1970), 595–609.
- [2] Refrigerating American Society of Heating and Inc. Air-Conditioning Engineers, *ASHRAE Handbook - Fundamentals*, SI Ed., Atlanta, 1997.
- [3] N.A. Bailey, *The interaction of droplet and forced convection in the post dryout heat transfer at high subcritical pressures*, European Two-Phase Flow Group Meeting, Rome (1972).
- [4] O. Baker, *Design of pipe lines for simultaneous flow of oil and gas*, Oil and Gas Journal **53** (1954), 185–190.
- [5] D. Biberg, *An explicit approximation for the wetted angle in two-phase stratified pipe flow*, Canadian J. Chemical Engineering **77** (1999), 1221–1224.
- [6] A. Cartellier, *Optical probes for local void fraction measurements: Characterization of performance*, Rev. Sci. Instrum. **61** (1990), 874–886.
- [7] ———, *Measurement of gas phase characteristics using new monofiber optical probes and real-time signal processing*, Nuclear Engineering and Design **184** (1998), 393–408.
- [8] J.B. Chaddock and H.K. Varma, *An experimental investigation of dry-out with R-22 evaporating in a horizontal tube*, ASHRAE Trans. **85** (1979), 105–121, part 2.
- [9] J.C. Chen, *A correlation for boiling heat transfer to saturated fluids in convective flow.*, ASME preprint 63-HT-34 presented at 6<sup>th</sup> National Heat Transfer Conference, Boston, 11-14 August, (1963).
- [10] D. Chisholm, *Void fraction during 2-phase flow*, J. of Mechanical Engineering Science **15** (1973), no. 3, 235–236.

- [11] J.G. Collier and Thome J.R., *Convective boiling and condensation*, 3<sup>rd</sup> ed., Oxford University Press, 1994.
- [12] M.K. Cooper, *Saturated nucleate pool boiling: A simple correlation*, 1<sup>st</sup> U.K. National Heat Transfer Conference **2** (1984), 785–793.
- [13] G. Costigan and P.B. Whalley, *Slug flow regime identification from dynamic void fraction measurements in vertical air-water flows*, Int. J. Multiphase Flow **23** (1997), 263–282.
- [14] R.S. Dougall and W.M. Rohsenow, *Film boiling on the inside of vertical tubes with upward flow of the fluid at low vapor qualities*, MIT Report (1963), no. 9079-26.
- [15] J. El Hajal, J.R. Thome, and A. Cavallini, *Condensation in horizontal tubes, part 1: Two-phase flow pattern map*, Int. J. of Heat and Mass Transfer **46** (2003a), no. 18, 3349–3363.
- [16] J. El Hajal, J.R. Thome, and A. Cavallini, *Condensation in horizontal tubes, part 2: New heat transfer model based on flow regimes*, Int. J. of Heat and Mass Transfer **46** (2003b), no. 18, 3365–3387.
- [17] E.J. Fordham, A. Holmes, R.T. Ramos, S. Simonian, S-M. Huang, and Lenn C.P., *Multiphase-fluid discrimination with local fibre-optical probes: I. liquid/liquid flows*, Meas. Sci. Technol. **10** (1999), 1329–1337.
- [18] D.C. Groeneveld, *The thermal behaviour of a heated surface at and beyond dryout*, EAEL-4309 (1972).
- [19] ———, *Post-dryout heat transfer at reactor operating conditions*, Report AECL-4513 (ANS topical meeting on Water Reactor Safety, Salt Lake City) (1973).
- [20] ———, *Post-dryout heat transfer: Physical mechanisms and a survey of prediction methods*, Nuclear Engineering and Design **32** (1975), 283–294.
- [21] D.C. Groeneveld and G.G.J. Delorme, *Prediction of the thermal non-equilibrium in the post-dryout regime*, Nuclear Engineering and Design **36** (1976), 17–26.
- [22] K.E. Gungor, Winterton, and R.H.S., *A general correlation for flow boiling in tubes and annuli*, Int. J. Heat Mass Transfer **29** (1986), 351–358.

- [23] J. Hart, P.J. Hamersma, and J.M.H. Fortuin, *Correlations predicting frictional pressure drop and liquid holdup during durig horizontal gas-liquid pipe-flow with a small liquid holdup*, Int. J. Multiphase Flow **15** (1989), no. 6, 947–964.
- [24] G.D. Harvel, K. Hori, K. Kawanishi, and J.S. Chang, *Real-time cross-sectional void fraction measurements in vertical annulus gas-liquid two-phase flow by neutron radiography and X-ray tomography techniques*, Nuclear Instruments and Methods in Physics Research **371** (1996), 544–552.
- [25] ———, *Cross-sectional void fraction distribution measurements in a vertical annulus two-phase flow by high speed X-ray computed tomography and real-time neutron radiography techniques*, Flow Measurement and Instrumentation **10** (1999), 259–266.
- [26] K. Hashizume, *Flow pattern and void fraction of refrigerant two-phase flow in a horizontal pipe*, Bulletin of JSME **26** (1983), no. 219, 1597–1602.
- [27] H.T. Huang, H.E. Fiedler, and J.J. Wang, *Limitation and improvement of PIV: Part II: Particle image distortion, a novel technique*, Exp. Fluids **15** (1993), 263–273.
- [28] D.S. Jung, M. McLiden, and Didion D. Radermacher R., *A study of flow boiling heat transfer with refrigerant mixtures*, Int. J. Heat Mass Transfer **32** (1989), no. 9, 1791–1764.
- [29] N. Kattan, *Contributon to the heat transfer analysis of substitute refrigerants in evaporator tubes with smooth or enhanced tube surfaces*, Ph.D. thesis, Swiss Federal Institute of Technology - Lausanne, Thesis No. 1498, 1996.
- [30] N. Kattan, J.R. Thome, and D. Favrat, *Flow boiling in horizontal tubes. part 1: Development of a diabatic two-phase flow pattern map*, J. Heat Transfer **120** (1998a), 140–147.
- [31] ———, *Flow boiling in horizontal tubes. part 2: New heat transfer data for five refrigerants*, J. Heat Transfer **120** (1998b), 148–155.
- [32] ———, *Flow boiling in horizontal tubes. part 3: Development of a new heat transfer model based on flow patterns*, J. Heat Transfer **120** (1998c), 156–165.
- [33] Y. Katto and H. Ohne, *An improved version of the generalized correlation of critical heat flux for forced convection boiling in uniformly heated vertical tubes*, Int. J. Heat Mass Transfer **27** (1984), 1641–1648.

- [34] A.A. Kendoush and Z.A. Sarkis, *Void fraction measurement by X-ray absorption*, Experimental Thermal and Fluid Science **25** (2001), 615–621.
- [35] Y. Kim, K. Seo, and J.T. Chung, *Evaporation heat transfer characteristics of R-410A in 7 and 9.52 mm smooth/micro-fin tubes*, Int. J. of Refrigeration **25** (2002), 716–730.
- [36] E. Krepper, A.-K. Krüßenberg, H.-M. Prasser, and A. Schaffrath, *High resolution void fraction measurements for the validation of flow maps and CFD codes*, Two-Phase Flow Modelling and Experimentation (1999), 1371–1378, Edizioni ETS, Pisa.
- [37] S. S. Kutateladze, *On the transition to film boiling under natural convection*, Kotloturbostroenie **3** (1948), no. 10.
- [38] M. Lallemand, C. Branescu, and P. Haberschill, *Local heat transfer coefficients during boiling of R-22 and R-407C in horizontal smooth and microfin tubes*, Int. J. of Refrigeration **24** (2001), 57–72.
- [39] J.G. Lavin and E.H. Young, *Heat transfer to evaporating refrigerants in two-phase flow*, AIChE J. **11** (1965), no. 6, 1124–1132.
- [40] R.C. Lockhardt, R.W. and Martinelli, *Proposed correlation of data for isothermal two-phase, two-component flow in pipes*, Chemical Engineering Progress **45** (1949), 39–48.
- [41] H. Mori, S. Yoshida, K. Ohishi, and Y. Kokimoto, *Dryout quality and post-dryout heat transfer coefficient in horizontal evaporator tubes*, Proc. of 3<sup>rd</sup> European Thermal Sciences Conference (2000), 839–844.
- [42] I.L. Piro, *Experimental evaluation of constants for the Rohsenow pool boiling correlation*, J. Heat Transfer **42** (1998), 2003–2013.
- [43] D.N. Plummer, *Post critical heat transfer to flowing liquid in a vertical tube*, Ph.D. thesis, MIT, Dept. of Mechanical Engineering, 1973.
- [44] S. Richter, M. Aritomi, H.-M. Prasser, and R. Hampel, *Approach towards spatial phase reconstruction in transient bubbly flow using a wire-mesh sensor*, International Journal of Heat and Mass Transfer **45** (2002), 1063–1075.
- [45] W.M. Rohsenow, *A method of correlating heat transfer data for surface boiling liquids*, Trans. ASME **74** (1962), 969–975.



- [46] S.Z. Rouhani and E. Axelsson, *Calculation of volume void fraction in subcooled and quality region*, Int. J. Heat Mass Transfer **13** (1970), 383–393.
- [47] P. Saha, *A nonequilibrium heat transfer model for dispersed droplet post-dryout regime*, Int. J. Heat Mass Transfer **23** (1980), 483–492.
- [48] K. Seo and Y. Kim, *Evaporation heat transfer and pressure drop of R-22 in 7 and 9.52 mm smooth/micro-fin tubes*, Int. J. of Heat and Mass Transfer **43** (2000), 2869–2882.
- [49] M.M. Shah, *Chart correlation for saturated boiling heat transfer: Equations and further study*, ASHRAE Trans. **88** (1982), 285–196.
- [50] C.-H. Song, M.K. Chung, and H.C. No, *Measurements of void fraction by an improved multi-channel conductance void meter*, Nuclear Engineering and Design **184** (1998), 269–285.
- [51] K. Spindler and E. Hahne, *An experimental study of the void fraction distribution in adiabatic water-air two-phase flows in an inclined tube*, Int. J. Therma. Sci. **38** (1999), 305–314.
- [52] D. Steiner and J. Taborek, *Flow boiling heat transfer in vertical tubes correlated by an asymptotic model*, Heat Transfer Engng. **13** (1992), no. 2, 43–69.
- [53] Y. Taitel and A.E. Dukler, *A model for predicting flow regime transitions in horizontal and near horizontal gas-liquid flow*, AIChE Journal **22** (1976), no. 1, 47–55.
- [54] J.R. Thome, G. Dunkel, and L. Wojtan, *Optical measurement of void fraction*, 2<sup>nd</sup> Japanese-European Two-Phase Flow Group Meeting, Tsukuba, Japan (2000), (attendance by invitation only).
- [55] J.R. Thome and J. El Hajal, *Two-phase flow pattern map for evaporation in horizontal tubes: Latest version*, 1<sup>st</sup> Int. Conf. On Heat Transfer, Fluid Mechanics and Thermodynamics, Kruger Park, South Africa, April 8-10 **1** (2002), 182–188.
- [56] E. Tronconi, *Prediction of slug frequency in horizontal two-phase slug flow*, AIChE Journal **36** (1990), no. 5, 701–709.
- [57] T. Ursenbacher, L. Wojtan, and J.R. Thome, *Interfacial measurements in stratified types of flow. part I: New optical measurement technique and dry angle measurements*, Int. J. of Multiphase Flow **30** (2004), 107–124.

- [58] Verein Deutscher Ingenieure VDI-Wärmeatlas (VDI Heat Atlas), *Chapter HBB*, VDI-Gesellschaft Verfahrenstechnik und Chemieingenieurwesen (GVC), Düsseldorf, 1993.
- [59] C.C. Wang, J.G. Yu, S.P. Lin, and D.C. Lu, *An experimental study of convective boiling of refrigerants R-22 and R-410A*, ASHRAE Trans. **104** (1998), 1144–1150.
- [60] J. Westerweel, *Fundamentals of digital particle image velocimetry*, Meas. Sci. Technol. **8** (1997), 1379–1392.
- [61] L. Wojtan and J.R. Thome, *New results for R-410A and R-134A compared to R-22*, 21<sup>st</sup> IIR International Congress of Refrigeration, Washington, D.C., USA (2003), Paper ICR044.
- [62] L. Wojtan, T. Ursenbacher, and J.R. Thome, *Technique for measurement of void fraction in horizontal tubes*, 3<sup>rd</sup> International Conference on Enhancement Technology for the Process Industries, Davos, Switzerland (2001).
- [63] ———, *Measurement of dynamic void fractions in stratified types of flow*, 3<sup>rd</sup> European-Japanese Two-Phase Flow Group Meeting, Siena, Italy (2003).
- [64] ———, *Interfacial measurements in stratified types of flow. part II: Measurements for R-22 and R-410A*, Int. J. of Multiphase Flow **30** (2004), 125–137.
- [65] ———, *Measurement of dynamic void fractions in stratified types of flow*, Experimental Thermal and Fluid Science **28** (in press).
- [66] K. Yamagata, F. Kirano, K. Nishiwaka, and H. Matsuoka, *Nucleate boiling of water on the horizontal heating surface*, Mem. Fac. Eng. Kyushu **15** (1955), 98.
- [67] S.M. Zivi, *Estimation of steady-state steam void fraction by means of the principle of minimum entropy production*, J. Heat Transfer **86** (1964), 247–252.
- [68] N. Zuber and J.A. Findlay, *Average volumetric concentration in two-phase flow systems*, J. Heat Transfer **87** (1965), 453–468.
- [69] N. Zuber, F.W. Staub, G. Bijwaard, and P.G. Kroeger, *Steady state and transient void fraction fraction in two-phase flow systems*, GEAP 5417 (1967).
- [70] O. Zürcher, *Contributon to the heat transfer analysis of natural and substitute refrigerants evaporated in a smooth horizontal tubes*, Ph.D. thesis, Swiss Federal Institute of Technology - Lausanne, Thesis No. 2122, 2000.

- [71] O. Zürcher, J.R. Thome, and D. Favrat, *Evaporation of ammonia in a smooth horizontal tube: Heat transfer measurements and predictions*, J. Heat Transfer **121** (1999), 89–101.
- [72] ———, *An onset of nucleate boiling criterion for horizontal flow boiling*, Int. J. of Thermal Sciences **39** (2000), 909–918.
- [73] ———, *Development of a diabatic two-phase flow pattern map for horizontal flow boiling*, Int. J. Heat Mass Transfer **45** (2002), 291–301.



# Curriculum Vitae

## PERSONAL DATA:

Name: **Leszek WOJTAN**  
Date of Birth: 02.10.1973  
Birthplace: Starachowice - Poland  
Marital Status: Married to Magdalena PARLINSKA-WOJTAN  
Nationality: Polish

## EDUCATION & CAREER:

1988 - 1993 The St. Dubois Secondary Technical School in Starachowice - Poland, Construction Department of Combustion Engines  
05.1993 The Secondary School Certificate  
  
1993 - 1998 The University of Mining and Metallurgy in Cracow, Poland  
Department of Mechanical Engineering and Robotics  
30.06.1998 Master of Science and Engineer; Master's Thesis Title:  
„Application of Computer-Aided Measurements with Double-Sided Contact in Cylindrical Gears”  
  
1998 - 2000 Position of Design and Commercial Engineer by KSB Pumps  
  
2000 - 2004 PhD-Student at the Laboratory of Heat and Mass Transfer at The Swiss Federal Institute of Technology - Lausanne under the Direction of Professor J.R. Thome; Main Research Interests: Two-Phase Flow, Flow Boiling Heat Transfer, Measurements of Void Fraction.